# Computational Multiscale Models for Microdosimetric Investigations of Skin Tissues under Electromagnetic Exposure

Von der Fakultät für Ingenieurwissenschaften,
Abteilung Elektrotechnik und Informationstechnik,
der Universität Duisburg-Essen

zur Erlangung des akademischen Grades
Doktor der Ingenieurwissenschaften (Dr.-Ing.)

genehmigte Dissertation

von

**Karsten Jerbic**

aus

Duisburg

1. Gutachter: Prof. Dr. sc. techn. Daniel Erni

2. Gutachter: Prof. Dr.-Ing. Jan C. Balzer

Tag der Disputation: 23. Februar 2024

**DOI:** 10.17185/duepublico/81973
**URN:** urn:nbn:de:hbz:465-20240611-091102-0

**Computational Multiscale Models for Microdosimetric Investigations of Skin Tissues under Electromagnetic Exposure**

A dissertation submitted to the

Faculty of Engineering of
the Department of Electrical Engineering and Information Technology of
the University of Duisburg-Essen

for the degree of
Doctor of Engineering (Dr.-Ing.)
by **Karsten L. K. Jerbic, M.Sc.**
from Duisburg

Date of submission: 18th of August 2023
Date of defense: 23rd of February 2024

Supervisor of the doctorate:
**Prof. Dr. sc. techn. Daniel Erni**
General and Theoretical Electrical Engineering

Co-examiner of the dissertation:
**Prof. Dr.-Ing. Jan C. Balzer**
Communication Systems

This dissertation was funded by the Swiss Research Foundation for Electricity and Mobile Communication (FSM) at the ETH Zurich within the FSM project no. A2019-01 and by the German Research Foundation (DFG) under project 287022738 of the CRC/TRR 196 MARIE as part of project M03.

“The mystery of life is not a problem to solve, but a reality to experience.
A process that cannot be understood by stopping it.
Understanding must move with the flow of the process, must join it and flow with it."
- Frank Herbert, Dune

# Abstract

As ambitious projects such as Industry 4.0 and the Internet of Things evolve, the consequent drive towards next-generation telecommunication standards (i.e., 5G) implies increasing exposure to electromagnetic (EM) radiation at higher frequencies (2.5 – 6 GHz and 24 – 52 GHz) compared to those currently implemented (600 MHz up to 2.5 GHz, i.e., 2G-4G). This frequency shift brings into focus the absorption of EM energy in the outermost millimeters of the body, and especially in the skin. This highlights the need for both a reevaluation of current exposure guidelines and for refined methodological approaches that allow the dedicated assessment of EM absorption in tissue microstructures down to the cellular level in order to determine precisely where in the subcellular structure EM energy is converted to heat.

In response to this challenge, the research presented here introduced scale-back projection, a top-down, multiscale approach that accounts for the intricate interplay between tissue morphology, histochemical composition, and EM absorption at the cellular level. For this approach to be effectively applied, a tailored material description that is adapted to the specific tissue anatomy was required. To this end, a hierarchical bottom-up model of the epidermis was developed, offering a coherent representation of material properties at both macroscopic and microscopic scales. Central to the epidermal model is its detailed representation of the life cycle of keratinocytes, modeling the differentiation of epidermal cells across 24 cell layers by capturing changes in cell geometry, internal structure, and histochemical composition.

Scale-back projection allows a deeper exploration into EM exposure within individual cell microvolumes, precisely quantifying EM absorption relative to the specific location of individual epidermal cells. Using this innovative approach reveals a surprisingly high level of variability of EM fields induced in the cellular microstructure of such cells by up to 71 %, and exposure values which are up to 45 % higher than previously predicted by conventional dosimetric studies considering skin exposure on only a macroscopic scale. By providing more accurate exposure profiles across the epidermis, scale-back projection not only offers a detailed exposure map, but also emerges as a promising tool to complement and enhance conventional multiphysics simulation techniques currently used in EM dosimetry.

# Kurzfassung

Angetrieben durch ehrgeizige Projekte wie Industrie 4.0 und das Internet der Dinge führt die konsequente Umstellung auf Telekommunikationsstandards der nächsten Generation (d. h. 5G) zu einer erhöhten Exposition durch elektromagnetische (EM) Strahlung bei höheren Frequenzen (2,5 – 6 GHz und 24 – 52 GHz) im Vergleich zu derzeit verwendeten Standards (600 MHz bis 2,5 GHz, d. h. 2G-4G). Diese Frequenzverschiebung rückt die Absorption von EM Energie in den äußersten Millimetern des Körpers und insbesondere in der Haut in den Mittelpunkt. Daraus folgt, dass sowohl eine Neubewertung der derzeitigen Expositionsrichtlinien als auch verfeinerte methodische Ansätze erforderlich sind, die eine gezielte Bewertung der EM Absorption in den Mikrostrukturen des Gewebes bis hinunter auf die Zellebene ermöglichen, um genau zu bestimmen, wo in der subzellulären Struktur EM Energie in Wärme umgewandelt wird.

Als Antwort auf diese Herausforderung wurde in der hier vorgestellten Forschungsarbeit die Scale-Back-Projektion eingeführt, ein top-down Multiskalen-Ansatz, der die komplexen Wechselwirkungen zwischen Gewebemorphologie, histochemischer Zusammensetzung und EM Absorption auf zellulärer Ebene berücksichtigt. Um diesen Ansatz effektiv anwenden zu können, ist eine maßgeschneiderte Materialbeschreibung erforderlich, die an die spezifische Gewebeanatomie angepasst ist. Zu diesem Zweck wurde ein hierarchisches Bottom-up-Modell der Epidermis entwickelt, das eine konsistente Darstellung der Materialeigenschaften sowohl auf makroskopischer als auch auf mikroskopischer Ebene ermöglicht. Im Mittelpunkt des Epidermismodells steht die detaillierte Darstellung des Lebenszyklus der Keratinozyten, wobei die Differenzierung dieser epidermalen Zellen in 24 Zellschichten durch die Erfassung von Veränderungen der Zellgeometrie, der inneren Struktur und der histochemischen Zusammensetzung modelliert wird.

Die Scale-Back-Projektion ermöglicht eine detailliertere Untersuchung der EM Exposition innerhalb einzelner Zellmikrovolumina durch die genaue Quantifizierung der EM Absorption in Abhängigkeit von der spezifischen Position einzelner epidermaler Zellen. Die Anwendung dieses innovativen Ansatzes zeigt sowohl eine überraschend hohe Variabilität der in die zelluläre Mikrostruktur solcher Zellen induzierten EM Felder von bis zu 71 % als auch Expositionswerte, die um bis zu 45 % höher liegen als bisher durch konventionelle dosimetrische Studien vorhergesagt, die die Hautexposition nur auf makroskopischer Ebene betrachten. Durch die Ermittlung genauerer Expositionsprofile über die Epidermis liefert die Scale-Back-Projektion nicht nur eine detaillierte Expositionsbewertung,

sondern erweist sich auch als vielversprechendes Werkzeug zur Ergänzung und Verbesserung konventioneller multiphysikalischer Simulationstechniken, die derzeit in der EM Dosimetrie eingesetzt werden.

# Contents

# 1 Introduction

Ambitious projects such as Industry 4.0 and the Internet of Things require high data rates and low latencies, thus driving network expansion towards 5G. Depending upon future technological and regulatory changes, this means that people may become increasingly exposed to electromagnetic (EM) radiation at higher frequencies (24 GHz to 52 GHz) compared to those currently implemented by telecommunication standards (2G at 1.9 GHz, 3G at 2.1 GHz and 4G from 600 MHz up to 2.5 GHz). EM exposure will therefore not be limited primarily to public spaces, as has been the case in the past, but will also have a massive impact on the workplace or remote areas such as those used for agriculture implementing smart farming. The resulting increase in the duration of exposure to EM fields at frequencies that are currently absent or only present at very low extents in our environment necessitates a more detailed reassessment of existing radiation guidelines, as anticipated by the International Commission on Non-Ionizing Radiation Protection (ICNIRP) [1]. This shift to higher frequencies thereby draws attention to absorption in the outermost millimeters of the body surface, especially in the skin and the eyes, and raises the question of exactly where in a tissue microstructure EM energy is absorbed and converted into thermal energy. In order to perform microdosimetric investigations to predict the effects at this scale, new methodological approaches are needed.

The primary objective of prevailing exposure guidelines is to impose restrictions on anthropogenic EM radiation, aiming to maintain levels below thresholds that prevent thermal damage by limiting the heat generated in exposed tissues [1, 2, 3]. To comply with ethical standards and avoid potential harm, in vivo experiments on human subjects are explicitly excluded from determining these limits. Instead, multiphysics simulations are used to determine cause-and-effect relationships between environmental exposure, EM energy absorbed by the tissue, and resulting temperature increases, which form the scientific basis for establishing these guidelines [4, 5, 6, 7, 8, 9, 10, 11, 12]. The exposed tissues in such simulations are commonly represented as homogeneous bulk materials, enabling efficient numerical predictions of EM absorption across an exposed body (i.e., organ or body part). This representation, however, is inherently limited as it does not allow the consideration of the intricate interactions between the EM fields and the microstructure of the irradiated tissues at the cellular level. As this research will demonstrate, these interactions play a crucial role in the precise determination of EM absorption within individual tissue-specific cells and their subcellular structures. Therefore, the overarching objective of this work is to develop a methodological framework that extends the existing multiphysics simulation approach, allowing for a comprehensive assessment of the energy absorption in high-resolution tissue models.

However, the development of such tissue models is challenging because biological tissues are highly symbiotic systems consisting of a multitude of complex structural features at all possible length scales [13]. This is particularly true for the skin, which can be considered an organ system with a profoundly intricate stratified topology, encompassing various tissues and is divided into three distinct sublayers: the epidermis, dermis, and hypodermis. Furthermore, the skin exhibits a complex arrangement of macroanatomical cross-layer features, further increasing the level of complexity. As a result, the development of a performant computational model that captures the skin in its entirety is impossible. In order to still be able to describe the interaction of EM fields and our skin, a useful approach is to decompose the overall system into definable subsystems that are hierarchically organized according to their spatial dimensions. Following this approach, the representation of the skin can be broadly divided into a macroscopic scale, which captures its overall topology and macroanatomical features, and a microscopic scale, which focuses on the microstructure of individual cells. The primary challenge in implementing this approach is to maintain consistency in the essential properties of all subsystems between these two scales.

The methodological framework to address this challenge is a bottom-up multiscale modeling approach published in [14], where a comprehensive skin model was synthesized by applying analytical mixing rules and numerical simulations to derive the dielectric properties of skin tissues on a microscopic scale. The modeling approach presented there was developed in the context of diagnostic applications in the frequency range between 10 and 100 MHz, i.e., in a frequency range where the dielectric signature of biological tissues is predominantly determined by Maxwell-Wagner interfacial polarization. With this polarization as a primary effect, it was acceptable in [15] to consider only the geometry of the cell exterior when developing cell models at the microscopic scale and consequently to neglect the cell interior. However, at the frequencies used for mobile communication, research has shown that EM fields penetrate significantly into the interior of cells and that the membranes of the organelles contained therein contribute significantly to the energy absorption process [16, 17, 18]. Therefore, it is essential to develop cell models that represent the internal structure of the cell according to its anatomical features with a sufficient level of detail in a way that takes into account two crucial aspects: (1) a realistic quantification of the absorption and (2) an adequate localization of this absorption within the cell.

To accommodate the symbiotic nature of biological systems within the skin model developed in this thesis, consideration is given to physiological variations occurring within tissues, distinguishing it from existing modeling approaches. Consequently, unlike [14], the representation of a specific tissue at the microscopic scale does not rely on a single prototypical cell model. Instead, a series of parametric cell models are used that differ in shape, size, internal structure, and histochemical composition depending on their intended position within the tissue model. In order to achieve this, a broad spectrum of detailed knowledge in the fields of histoanatomy and cytoanatomy must be translated into computer models that coherently represent the intertwined relationship between the macroscopic and microscopic scales, which, applied to all tissue types of the skin, is

beyond the scope of this work. For this reason, the development of a bottom-up tissue model will be limited to only the top layer of the skin, i.e. the epidermis, here.

By incorporating the aforementioned innovations into bottom-up multiscale modeling, the epithelial tissue of the epidermis is represented at the microscopic scale using its predominant cell type, the keratinocyte. At the macroscopic scale, the epidermis is conceptualized as a sequence of cell layers, enabling the modeling of the entire life cycle of cells, including their formation, maturation, and eventual death. Consequently, the underlying biochemical processes driving this life cycle can be reconstructed and translated into effective material parameters. This highly detailed model of the epidermis facilitates dosimetric investigations of the skin, specifically considering the unique position of the epidermis as the outermost layer in terms of potential impedance matching effects, as recently discussed in [19]. Moreover, the availability of a cell-layer-specific model of the epidermis allows targeted dosimetric examinations of the basal and subbasal rows (i.e. the bottommost cell layers), which hold particular significance for two main reasons. Firstly, these layers are crucial for skin resurfacing as they contain the proliferative pool of the epidermis. Excessive EM exposure in these layers carries the risk of adverse health effects if mitotic activity is negatively affected. Secondly, the proliferative pool is situated above the basement membrane, an aggregation of proteins and structures separating the epidermis from the dermis, which contributes significantly to skin thermoregulation and metabolic transport. For these anatomical reasons, the epidermis/dermis interface has been explicitly identified by ICNIRP as heat-sensitive under exposure to EM radiation, making it an area of particular interest [1].

In order to conduct comprehensive dosimetric studies of the skin and to thoroughly evaluate the influence of physiological variations within the epidermis on the absorbed EM energy, it is necessary to verify and integrate the bottom-up tissue model of the epidermis into a realistic and comprehensive skin model. These steps are based on a modular modeling approach presented by Sasaki et al. in [4,5], where the dispersive material properties of each skin layer (i.e., epidermis, dermis, and hypodermis) are represented using experimental data obtained from in vitro measurements on fractionated skin. Adapting the experimental data enables the verification of the effective macroscopic material properties of the individual cell layers considered in the bottom-up model of the epidermis and facilitates the construction of modular skin models encompassing all sublayers. As a result, two different skin models can be created. The first model, which closely follows the specifications presented in [4], serves as a reference model in this thesis. It is considered a reference because of its wide recognition and acceptance in the scientific community, its significant influence on the currently accepted exposure limits [1], and its high degree of realism as an empirical model. The second model represents a modified version of the reference model in which the metrologically recorded representation of the epidermis is replaced by the bottom-up model developed in this thesis. This modified model thus combines methodologically derived representations of the skin layers with the numerically derived representations of the epidermis and is therefore considered a hybrid model. By subjecting both skin models to a generic exposure scenario involving plane EM waves, it is possible to determine the influence of physiological variations on the ab-

sorbed EM energy through comparison, in particular within the individual cell layers of the epidermis.

Using the hybrid skin model, the primary objective of this thesis is now achievable: the development of a methodological framework for the assessment of EM energy absorption at the microscopic scale. This framework follows a twofold top-down multiscale approach. In the first step, the spatial distribution of the induced EM fields across the entire hybrid skin model is determined. The coherent representation of the epidermis, including both macroscopic and microscopic scales, makes it possible to evaluate the energy absorbed by microvolumes corresponding to the size of single keratinocytes in each individual epidermal cell layer. In a second step, this absorbed energy is then projected onto the microscopic scale, allowing a comprehensive study of the effects of EM exposure using fully resolved parametric models of the underlying keratinocytes. Therefore, this methodological framework is introduced as "scale-back projection" due to its ability to project and analyze EM energy absorption across multiple scales. It embodies the approach of starting with a top-down perspective, encompassing the entire hybrid skin model, and subsequently scaling back to the microscopic scale to focus on the individual keratinocytes and their response to EM exposure. This makes it possible to assess how the morphology (size, shape and internal organization) and histochemical composition of the cells influence the field variations in the microstructure and, based on this assessment, to introduce a micro-SAR (Specific Absorption Rate) derived from the statistical analysis of these field variations. In a microdosimetric analysis of the epidermis, the micro-SAR is compared with the classical SAR derived from the bulk representation of cellular microvolumes across the epidermis at the macroscopic scale. Based on this comparison, the suitability of micro-SAR as a potential metric for setting exposure limits within the ICNIRP guidelines is discussed.

## 1.1 Outline

Following this introduction, Chap. 2 offers a general introduction to the dielectric behavior of both homogeneous and heterogeneous media, encompassing dielectric functions, polarization mechanisms, and fundamental methodological concepts within effective material theory.

This is followed by a brief introduction to skin anatomy in Chap. 3, which describes the complexity of the skin as a symbiotic biological system. Physiological adaptations, evident in aspects such as cellular composition and histological organization that occur within the skin and its sublayers to maintain normal function are detailed and quantified. Since the focus of this work is the microdosimetric study of the epidermis, special attention is given to keratinization, the process of programmed cell death characterized by fundamental structural and histochemical changes in epidermal cells that serves to maintain the barrier function of the skin. The focus of this introduction is to build a descriptive foundation, anchored in the standardized nomenclature of histoanatomy and

cytoanatomy, which allows physiological changes to be integrated into computational tissue models.

On this basis, Chap. 4 discusses the complex challenges involved in developing multiscale skin models and addresses these challenges by proposing a novel classification scheme that serves as a conceptual template for developing appropriate computational models. This innovative scheme provides a meaningful categorization and organization of skin structures into hierarchical classes based on their size. Furthermore, it recognizes the symbiotic relationship between macroanatomical and microanatomical structures, ensuring consistent numerical linkage between computational models across these intertwined hierarchical scales. By dividing the skin system into organ, tissue, and cellular scales, the classification scheme offers an approach that allows microdosimetric studies to consider structural and histochemical changes within individual tissues at multiple hierarchical scales simultaneously.

This is followed by a comprehensive review of the state of the art in Chap. 5, covering three relevant topic areas: skin modeling in dosimetric research, muliscale modeling of skin, and modeling of eukaryotic cells. This review outlines the paradigms and methods that have been established in the modeling of skin tissues at the macroscopic and microscopic scales, and highlights the current methodological limitations in linking these scales into comprehensive skin models that are suitable for comprehensive microdosimetric investigations.

In the context of these limitations, Chap. 6 presents scale-back projection as a concept that integrates both bottom-up and top-down multiscale approaches in a simulation cycle. This chapter provides a comprehensive overview that outlines the implementation of scale-back projection into computer models within a simulation environment that enables microdosimetric investigations to be performed at any hierarchical scale in an integrated manner. In addition, the relationship between scale-back projection and conventional multiphysics simulation approaches is elucidated, establishing the foundation for a detailed discussion on how scale-back projection could complement the repertoire of methods currently accepted as standard by ICNIRP for the assessment of exposure limits.

Chap. 7 offers a summary of the ICNIRP guidelines for limiting exposure to electromagnetic fields. In this chapter, the prevalent terminology, metrics, and limits concerning EM exposure in human tissue are introduced. Furthermore, it provides a foundation to ensure that the research presented in this thesis is in alignment with the guidelines established.

After these semi-introductory chapters detailing specific research aspects, Chap. 8 delves into the complexities of modeling eukaryotic cells for accurate EM exposure risk assessment. This chapter examines the importance of an accurate volumetric representation of subcellular structures, especially organelles enclosed by membranes of low conductivity. Using a systematic review and comparison of generic eukaryotic cell models of increasing

complexity, the effect of the volumetric extent of these organelles on the internal distribution of EM fields and the resulting loss distribution is identified.

In Chap. 9, drawing upon the findings of Chap. 8, the detailed development of a high-resolution bottom-up model of the epidermis is presented. Initially, the epidermis is delineated into 24 anatomically accurate layers, encompassing both the viable epidermis and the stratum corneum. On a conceptual level, each layer is defined by a distinct concentration profile, capturing its histochemical composition while considering variations introduced by different stages of keratinization and hydration. To allow these layers to be integrated into a comprehensive model of the skin, parametric cell models of keratinocytes and corneocytes are developed, tailored to represent the unique characteristics of each specific layer. These models capture specific details in terms of cell shape, internal cellular structures, and histochemical composition, highlighting the nuanced differences in the histochemical constituents of various cellular compartments. Using these parametric cell models, the macroscopic effective material properties of each layer are derived. This results in a comprehensive bottom-up model of the epidermis that includes physiological variations across the layers, ensuring representation at both the macroscopic and microscopic scales.

In Chap. 10, the bottom-up model of the epidermis is integrated into a comprehensive skin model based on the modular modeling approach presented by Sasaki et al. in [4]. For verification, this model is compared with measurements of epidermal material properties from the same study. As a result, the model presented by Sasaki serves as a consistent reference throughout this thesis. Subsequent extensive dosimetric studies elucidate the effects of physiological variations on the transmission and absorption of EM energy across individual cell layers, with particular emphasis on absorption in the proliferative pool.

In Chap. 11, the consistent representation of the epidermis at both the macroscopic and microscopic scale allows the introduction of scale-back projection as a top-down multiscale approach. This approach allows the projection of macroscopically determined EM field distributions onto the detailed microstructure of epidermal cell models. Following consideration of the microscopic scale, a parameter referred to as the micro-SAR is defined, which quantifies absorption across the epidermal cell models using statistical measures, i.e. arithmetic means and standard deviations. This offers a more nuanced insight into absorption by factoring in the influence of cell morphology on the distribution of losses within the cell interior. Using this micro-SAR, microdosimetric studies are performed to quantify field variations across all of the 24 cell layers of the epidermis. In addition, the chapter contrasts conventional SAR, as defined by ICNIRP, with the newly introduced statistical micro-SAR at the microscopic scale. Based on these investigations, the chapter evaluates the potential integration of the scale-back projection into the conventional multiphysics simulation framework for focused microdosimetric studies.

Finally, in Chap. 12, the paradigms, approaches, and findings presented in Chap. 3 through Chap. 11 are summarized and comprehensively concluded.

# 2 Technical Description of Dielectric Media

## 2.1 Dielectric Functions and Polarization Mechanisms

The macroscopic properties of an isotropic dielectric material system can be described by a complex relative permittivity:

$$\underline{\varepsilon}_\mathrm{r} = \varepsilon_\mathrm{r}' - \mathrm{j}\varepsilon_\mathrm{r}'' \tag{2.1}$$

where $\varepsilon_\mathrm{r}'$ and $\varepsilon_\mathrm{r}''$ denote its real and imaginary part respectively.

To describe the spectral response of a material system, the relative permittivity must naturally be considered as a function of angular frequency, i.e. $\underline{\varepsilon}_\mathrm{r}(\omega)$. The dielectric function can either be described as a relaxation or a resonance process, both of which are illustrated in Fig. 2.1 as Debye relaxation and Lorentz resonance respectively. When the angular frequency of the applied electric field approaches the characteristic frequency of the physical process described, $\omega_0$, the real part of each dielectric function shows a roll-off from $\varepsilon_{\mathrm{r,s}}$ towards $\varepsilon_{\mathrm{r},\infty}$. In the case of Lorentz resonance, this is accompanied by overshoots and undershoots either side of the characteristic frequency. The roll-off of the dielectric constant, $\varepsilon_\mathrm{r}'$, corresponds to a bell-shaped distribution of the dielectric loss term, $\varepsilon_\mathrm{r}''$, which reaches its maximum value at the characteristic frequency. While relaxation processes are broadband phenomena, resonance processes are narrowband in comparison.

Dielectric relaxation can be described mathematically by a variety of formulas to model the decay of an excited (polarized) state of a material to its ground state. If a material system is sufficiently described by a single relaxation time (or frequency), a simple Debye type relaxation formula can be applied:

$$\underline{\varepsilon}_\mathrm{r} = \varepsilon_{\mathrm{r},\infty} + \frac{\varepsilon_{\mathrm{r,s}} - \varepsilon_{\mathrm{r},\infty}}{1 + \mathrm{j}\omega\tau} \tag{2.2}$$

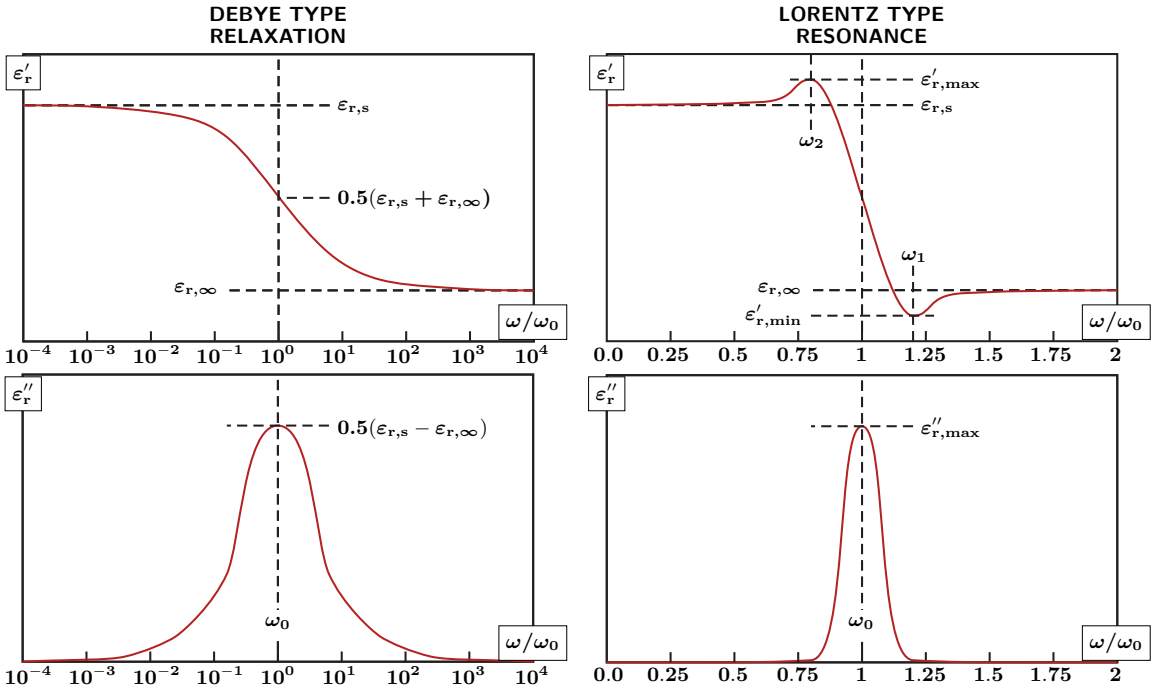


**Figure 2.1:** Spectral response of a Debye type relaxation and Lorentz type resonance. $\varepsilon_{r,s}$ and $\varepsilon_{r,\infty}$ denote the permittivity in the polarized and non-polarized state of the mechanisms described and $\omega_0$ is the characteristic frequency in each case. $\varepsilon'_{r,max}$ and $\varepsilon'_{r,min}$ denote the maximum and minimum values of the real part of the resonant spectral response, while $\omega_1$ and $\omega_2$ give the frequencies at which these occur. $\varepsilon''_{r,max}$ denotes the maximum of the imaginary part of the spectral response.

with its real and imaginary parts

$$\varepsilon'_r = \varepsilon_{r,\infty} + \frac{\varepsilon_{r,s} - \varepsilon_{r,\infty}}{1 + (\omega\tau)^2} \tag{2.3}$$

$$\varepsilon''_r = \frac{(\varepsilon_{r,s} - \varepsilon_{r,\infty})\omega\tau}{1 + (\omega\tau)^2} \tag{2.4}$$

In these equations, $\varepsilon_{r,s}$ and $\varepsilon_{r,\infty}$ denote the permittivity in the polarized and unpolarized states respectively. $\tau$ is the relaxation time of the system and is related to the characteristic frequency, $f_0$, using $f_0 = (2\pi\tau)^{-1}$.

For a more complex material to be described, further parameterizable modifications of the Debye formula can be applied. These include the Cole-Cole [20], Davidson-Cole [21] or Havriliak-Negami [22] relaxation. Dielectric relaxation describes relatively slow electromagnetic processes such as interfacial or orientational polarization. Interfacial polarization, also called Maxwell-Wagner polarization, describes the diffusion of free charge carriers towards material interfaces and thus the accumulation of surface charges at such an interface. Orientational polarization describes the alignment of the positive and negative charge centres of molecules to an applied electric field (i.e. dipole orientation).

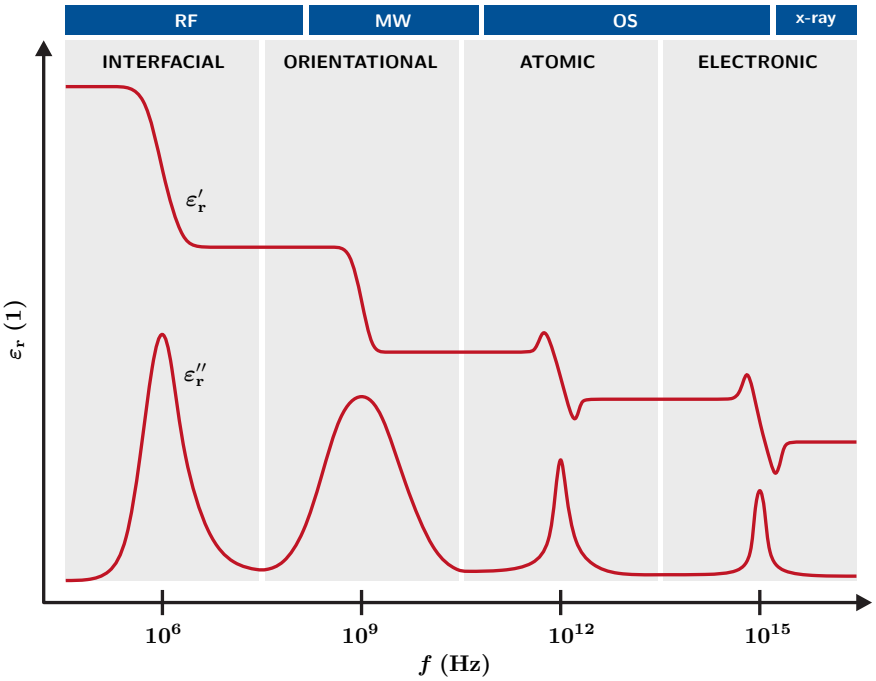


**Figure 2.2:** The real and imaginary parts of a generic dielectric function. The characteristic frequencies of interfacial polarization and orientational polarization are typically found at radio frequencies (RF) or millimeter-wave frequencies (MW) respectively. The characteristic frequencies of atomic and electronic polarization typically occur in the optical spectrum (OS) or at even higher frequencies in the x-ray range.

Dielectric resonances, in contrast, describe relatively fast electromagnetic processes at molecular or atomic scales occurring in the THz and optical range. Resonances caused by vibrational modes of inner molecular bonds can be considered as molecular or atomic polarization whereas resonances caused by vibrational states between the nucleus and bonding electrons are caused by electronic polarization. In analogy to a mechanical harmonic oscillator, dielectric resonances can be described by a dielectric Lorentz function:

$$\underline{\varepsilon}_\mathrm{r} = \varepsilon_{\mathrm{r},\infty} + \frac{\omega_0^2(\varepsilon_{r,\mathrm{s}} - \varepsilon_{\mathrm{r},\infty})}{\omega_0^2 - \omega^2 + \mathrm{j}\omega\gamma} \tag{2.5}$$

with its real and imaginary parts

$$\varepsilon_\mathrm{r}' = 1 + \frac{\omega_0^2(\varepsilon_{\mathrm{r,s}} - \varepsilon_{\mathrm{r},\infty})(\omega_0^2 - \omega^2)}{(\omega_0^2 - \omega^2)^2 + (\omega\gamma)^2} \tag{2.6}$$

$$\varepsilon_\mathrm{r}'' = \frac{\omega_0^2(\varepsilon_{\mathrm{r,s}} - \varepsilon_{\mathrm{r},\infty})\omega\gamma}{(\omega_0^2 - \omega^2)^2 + (\omega\gamma)^2} \tag{2.7}$$

where $\gamma$ is a damping constant.

To model the dielectric function of a material over a wide frequency range, the sum of the relaxation and resonance terms can be used to approximate its spectral material response. As shown in Fig. 2.2, the four polarization mechanisms mentioned are allocated to their respective frequency ranges. Since the investigations presented here are primarily performed at radio frequencies (RF) and millimeter-wave frequencies (MW), only interfacial and orientational polarization are of immediate importance with respect to the investigations. The other two polarization mechanisms (i.e. atomic and electronic polarization) occur in the optical spectrum (OS) or at even higher frequencies in the x-ray range.

## 2.2 Heterogeneous Materials and Effective Material Theory

Effective material theory (EMT) is concerned with the question of whether and how the macroscopic material of a composite can be represented by an equivalent homogeneous bulk material. A comprehensive standard work on the subject of EMT in the context of electromagnetic field problems is [23]. The basic idea of homogenization is illustrated in Fig. 2.3 and is explained using a generic composite placed in an ideal capacitor. The composite is a heterogeneous material structure in which spherical inclusions of a material with permittivity, $\underline{\varepsilon}_{\mathrm{r,i}}$, are embedded in a host medium with permittivity, $\underline{\varepsilon}_{\mathrm{r,h}}$. In the considered case, the inclusions and the host medium have isotropic material properties and the external electric field field applied, $\vec{E}_{\mathrm{e}}$, can be considered quasi-static. As depicted in Fig. 2.3(a), the electric field within the host medium is a function of space, $\vec{E}_{\mathrm{h}}(\vec{r})$. The spatial variations of $\vec{E}_{\mathrm{h}}$ can be explained by depolarization fields around the inclusions. The electric field within an inclusion, $\vec{E}_{\mathrm{i}}$, and the depolarization field around it, $\vec{E}_{\mathrm{d}}$, are depicted in Fig. 2.3(c). The strength of the depolarization field is caused by charge carrier diffusion towards the interface between the host medium and the inclusions and thus strongly depends on the contrast between the material properties of these two media as well as on the frequency applied (see interfacial polarization in Sec. 2.1). By applying numerical or analytical mixing rules, an effective permittivity, $\underline{\tilde{\varepsilon}}_{\mathrm{r}}$, can be found that generates a field within the surrogate medium that corresponds to the spatial average of the field within the composite.

Following this idea, $\underline{\tilde{\varepsilon}}_{\mathrm{r}}$ can be derived as the scaling factor between the (volume-)averaged electric field $\langle\vec{E}(\vec{r})\rangle$ and flux density $\langle\vec{D}(\vec{r})\rangle$ in the composite:

$$\langle\vec{D}(\vec{r})\rangle = \underline{\tilde{\varepsilon}}_{\mathrm{r}}\varepsilon_0\langle\vec{E}(\vec{r})\rangle. \tag{2.8}$$

The averaged electric field and flux density can be formulated as:

$$\langle\vec{D}(\vec{r})\rangle = c_{\mathrm{v}}\,\underline{\varepsilon}_{\mathrm{r,i}}\,\varepsilon_0\,\vec{E}_{\mathrm{i}} + (1-c_{\mathrm{v}})\,\underline{\varepsilon}_{\mathrm{r,h}}\,\varepsilon_0\,\vec{E}_{\mathrm{e}} \tag{2.9}$$

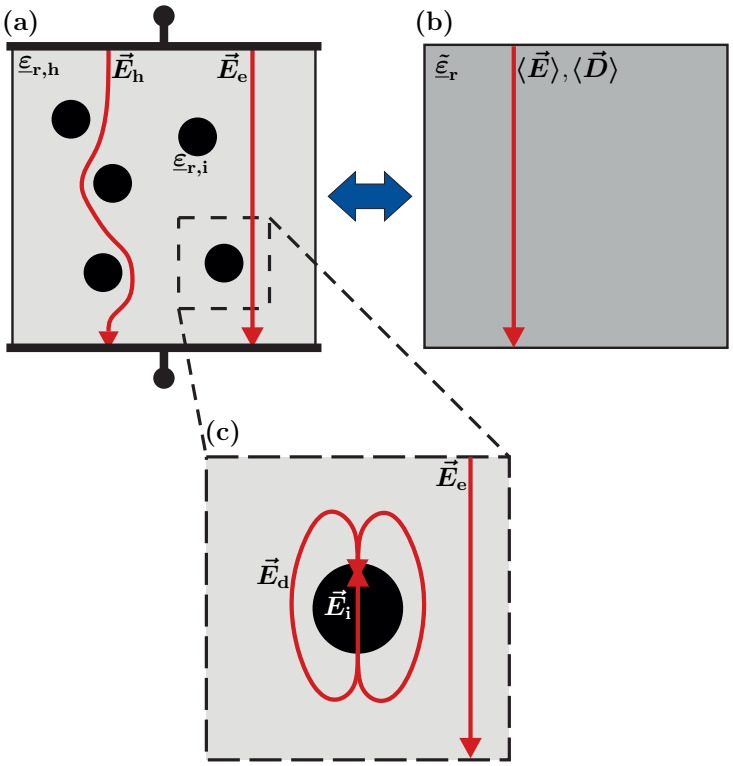


**Figure 2.3:** Principle of homogenization illustrated using an arbitrary composite with spherical inclusions as an example: (a) Heterogeneous material structure with spherical inclusions of permittivity $\underline{\varepsilon}_{r,i}$ embedded in a host medium of permittivity $\underline{\varepsilon}_{r,h}$. The external electric field field applied, $\vec{E}_e$, can be considered quasi-static. The electric field within the host medium is $\vec{E}_h(\vec{r})$. (b) Using numerical or analytical mixing rules, the heterogeneous material is converted into a homogenized surrogate representing equivalent macroscopic material properties, $\tilde{\underline{\varepsilon}}_r$, corresponding to the (volume-)averaged flux density, $\langle\vec{D}\rangle$, and electric field strength, $\langle\vec{E}\rangle$, defined in Eqs. 2.9 and 2.10 respectively. (c) Detailed enlargement of an inclusion. $\vec{E}_i$ and $\vec{E}_d$ denote the electric field within the inclusion and the depolarization field in its surrounding, respectively.

and

$$\langle\vec{E}(\vec{r})\rangle = c_v\,\vec{E}_i + (1-c_v)\,\vec{E}_e \tag{2.10}$$

where $c_v$ denotes the volume fraction of the inclusions.

Dividing Eq. 2.9 by Eq. 2.10, the effective permittivity can be determined to be

$$\tilde{\underline{\varepsilon}}_r = \frac{c_v\,\underline{\varepsilon}_{r,i}\,A + (1-c_v)\,\underline{\varepsilon}_{r,h}}{c_v\,A + (1-c_v)}, \tag{2.11}$$

where $A$ denotes the ratio between the electric field internal and external to the inclusions. In the case being discussed, both fields can be regarded as spatially independent

constants and can therefore be written as

$$A = \frac{|\vec{E}_\mathrm{i}|}{|\vec{E}_\mathrm{e}|}. \tag{2.12}$$

The relation between $\vec{E}_\mathrm{i}$ and $\vec{E}_\mathrm{e}$ can also be derived from the permittivities inside and outside the inclusions by considering these as polarized dielectric spheres in a quasi-static electric field. Thus, $A$ can be rewritten as

$$A = \frac{3\,\underline{\varepsilon}_\mathrm{r,h}}{\underline{\varepsilon}_\mathrm{r,i} - \underline{\varepsilon}_\mathrm{r,h}}. \tag{2.13}$$

Replacing $A$ in Eq. 2.11 by Eq. 2.13, the Maxwell-Garnett mixing rule for spherical inclusions can be derived:

$$\underline{\tilde{\varepsilon}}_\mathrm{r} = \underline{\varepsilon}_\mathrm{r,h} + 3\,c_\mathrm{v}\,\underline{\varepsilon}_\mathrm{r,h}\frac{\underline{\varepsilon}_\mathrm{r,i} - \underline{\varepsilon}_\mathrm{r,h}}{\underline{\varepsilon}_\mathrm{r,i} + 2\,\underline{\varepsilon}_\mathrm{r,h} - c_\mathrm{v}(\underline{\varepsilon}_\mathrm{r,i} - \underline{\varepsilon}_\mathrm{r,h})}. \tag{2.14}$$

Due to the simplifying assumptions mentioned above, the application of the Maxwell-Garnett mixing rule is subject to some limitations:

(a) The Maxwell-Garnett mixing rule can only be applied to diluted mixtures since coupling between the depolarization fields of adjacent inclusions is not considered.

(b) In the given form, the Maxwell-Garnett mixing rule can only be applied to spheres. However, modifications of this formula can be applied to other highly symmetrical types of inclusions, such as ellipsoids, to guarantee an analytical solvability for the polarization of an inclusion.

(c) In general, mixing rules are applicable only under quasi-static conditions. Thus, the operating frequency of the applied electric field, $\vec{E}_\mathrm{e}$, must satisfy $d_\mathrm{i} \lessapprox \frac{\lambda}{2\pi}$, where $d_\mathrm{i}$ and $\lambda$ denote the diameter of the inclusions and the wavelength of the field in the material.

By applying various assumptions that take into account interactions between the depolarization fields of adjacent inclusions, mixing rules can be derived that apply to volume densities up to 80 %, leading to the Hanai-Bruggeman mixing rule:

$$1 - c_\mathrm{v} = \left(\frac{\underline{\tilde{\varepsilon}}_\mathrm{r} - \varepsilon_\mathrm{r,i}}{\varepsilon_\mathrm{r,h} - \varepsilon_\mathrm{r,i}}\right)\left(\frac{\varepsilon_\mathrm{r,h}}{\underline{\tilde{\varepsilon}}_\mathrm{r}}\right)^{\frac{1}{3}} \tag{2.15}$$

A detailed overview of mixing rules, their derivation and suggested fields of application can be found in [23], [24], and [25]. The principles outlined in this chapter are used frequently in this thesis from Chap. 4 onwards.

# 3 A Brief Introduction to Skin Anatomy

Skin is the largest, outermost organ (system) of the human body covering a variety of vital functions. It protects the body against physical, chemical and biological agents, contributes to heat and fluid regulation, allows tactile and thermal perception, and serves as an energy storage system. To accommodate this functional diversity, the skin has evolved into a complex system consisting of epithelial, connective and nervous tissue [26]. An illustration providing an overview of the morphological complexity of human skin is provided by Fig. 3.1.

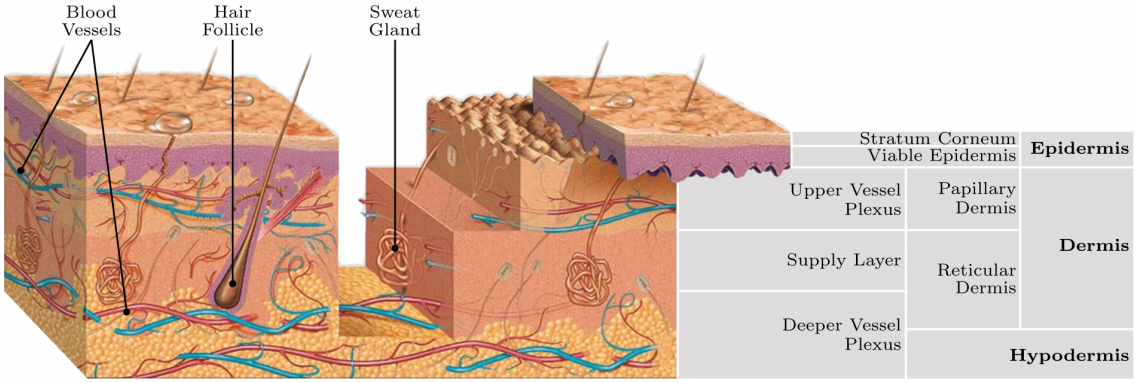


**Figure 3.1:** Illustration showing the layered structure of the skin and its cross-layer features (adapted image from [27]).

Macroscopically, it is characterized by a stratified structure consisting of three layer: the epidermis, dermis and hypodermis. Variation in skin layer thickness and structure can be seen from individual to individual in a population based upon factors such as gender, ethnicity, age and lifestyle. These measures also show distinct variation in different regions of the body [4, 28, 29]. A summary of the mean thicknesses of the individual skin layers and their variations among a population at relevant parts of the body is provided and displayed in Tab. 3.1.

**Table 3.1:** Thickness of the individual skin layers in different parts of the body (adapted from [4]).

| Body Part | Epidermis | Dermis | Hypodermis |
|---|---|---|---|
| **Forearm** | $102 \pm 34\,\mu m$ | $1080 \pm 160\,\mu m$ | $3890 \pm 1400\,\mu m$ |
| **Triceps** | $83.5 \pm 36.2\,\mu m$ | $1030 \pm 330\,\mu m$ | $8650 \pm 4280\,\mu m$ |
| **Quadriceps** | $94.8 \pm 23.6\,\mu m$ | $1220 \pm 320\,\mu m$ | $9350 \pm 4170\,\mu m$ |
| **Abdomen** | $79.4 \pm 33.9\,\mu m$ | $1250 \pm 260\,\mu m$ | $14300 \pm 7500\,\mu m$ |

## 3.1 Detailed Skin Microstructure

The epidermis is the outermost layer of the skin and is itself a multi-layered squamous epithelium predominantly populated by keratinocytes, which account for over 90% of the total cell population [30, 31]. In addition to keratinocytes, melanocytes, Langerhans cells and Merkel cells are also found in the epidermis, which are mentioned for completeness only. The average thickness of the epidermis over the entire body is 0.4 mm with local extrema ranging from 0.02 mm thickness at the eyelids to 1.5 mm thickness at the palms and soles [30]. Going from the outside inwards, the epidermis itself can be further divided into four sublayers: the stratum corneum (SC), the stratum granulosum (SG), the stratum spinosum (SS) and the stratum basale (SB). The latter three sublayers contain viable cells, which means that they have an intact metabolism, while the stratum corneum contains dead, cornified keratinocytes, thus called corneocytes. In a 30 to 50 day period, proliferated keratinocytes move towards the surface and undergo a process of differentiation known as keratinization [32]. During this process, they are subject to functional and morphological changes in which they alter their chemical composition significantly. This process of differentiation is called keratinization because keratin, arranged in tonofilaments, is stored inside the cell and can account for up to 80 % of the protein present in the cells of the stratum granulosum [30]. Due to its importance to provide protection against external agents, this process will be outlined in detail in the following, starting with the stratum basale and then moving upwards.

The stratum basale, also referred to as the stratum germinativum, consists of a single layer of columnar or cuboidal keratinocytes connected to and aligned along the basement membrane. Basal keratinocytes have a comparatively large nucleus, are rich in ribosomes and poor in cytoplasm [32]. The next layer, the stratum spinosum, is, on average, five to ten cell layers thick and composed of polyhedral keratinocytes adhering to each other by desmosomes [32]. It is in the stratum spinosum where the keratinization process begins, because keratohyalin granules are increasingly deposited in the cell with decreasing distance from the skin surface [32]. These deposits have a high electron density and are easily distinguishable from other structures of the cell and the intercellular space as dark areas on electron micrographs. The upper layers of the stratum spinosum increasingly contain cells that possess keratinosomes, also known as Odland corpuscles. These lamellar organelles are formed in the Golgi apparatus, are 80 to 130 nm in size and

contain the glycoproteins, lipids and enzymes needed in the cornification process of the skin [32]. The stratum granulosum is a thin sublayer consisting of three to five cell layers in which the first signs of apoptosis, or programmed cell death, manifest. This occurs primarily by caryopyknosis, a process in which the nucleus shrinks and the chromatin it contains condenses into a uniform mass [33]. The shrinkage of the nucleus results in the cell as a whole flattening and orienting parallel to the skin surface. It is in this layer where granular keratinocytes secrete keratinosomes into the extracellular space resulting in the formation of the hydrophobic lipid envelope of the skin that serves as a diffusion barrier and protects the skin against dehydration. In the upper layer of the stratum granulosum, this apoptosis is terminated resulting in the exocytosis of the remaining metabolic content of the cell (i.e. keratinosomes), which leads to the compaction of the extracellular space into a binding mass that creates the mechanical integrity of the stratum corneum [34, 35, 36]. The corneocytes of the stratum corneum move to the body surface by cell proliferation in the viable epidermis, where they are eventually shed as skin flakes. The life cycle of keratinocytes described here in a histological manner is not only related to chemical and morphological changes of the cells, but also manifests in their size and orientation with respect to the skin surface. Basal and suprabasal keratinocytes of the stratum basale and the directly adjoining layer of the stratum spinosum have cell diameters of approximately 10µm [37] and a nuclear diameter between 6µm and 8µm [38]. These two layers form the proliferation pool of the epidermis and are responsible for 97% of the total miotic activity, with 63% on the basal row and 34% on the suprabasal row [37, 39, 40]. The remaining 3% of miotic activity occurs in higher rows, showing a decrease in the probability of proliferation with increasing distance from the basal layer. In higher layers, keratinocytes lose their proliferative abilities and instead grow by metabolizing substances for cornification. This results in diameters of differentiated cells of approximately 16µm [37] and nuclear diameters of 9µm to 12µm in the stratum spinosum and 12µm to 15µm in the stratum granulosum [38]. An overview of the cellular and nuclear diameters is provided by Tab. 3.2. Independent of their location, the nucleus of a keratinocyte can be regarded as a prolate spheroid. Depending on their location, the ratio between the semi-major axis and the two semi-minor axes, $c_{l/s}$, varies between 1.4 and 1.9 [41]. In addition, the orientation of the semi-major axis rotates from perpendicular to parallel to the skin surface [38, 41].

The epidermis is separated from the dermis by an aggregation of proteins and structures forming the basement membrane. The basement membrane has two functions. The first function is to act as a mechanical barrier that protects the blood and lymphatic systems of the body while allowing the epidermis to be supplied with fluids and nutrients, and allowing metabolic products to be removed. This is necessary since the epidermis itself has no vascular system of its own. The second function is to connect the epidermis and dermis mechanically. To provide this mechanical connection, keratinocytes of the stratum basale are connected to the basement membrane by anchoring filaments of hemidesmosomes and the dermis is connected to the basement membrane by anchoring fibrils consisting of type VII collagen. Due to this connective function of the basement membrane, the interface between the epidermis and dermis is often referred to as the dermoepider-

**Table 3.2:** Overview of the cellular and nuclear diameter of keratinocytes in the individual sublayers of the epidermis as well as the estimated cell density adopted from [37] and [38].

| Layer | Cell Diameter | Nuclear Diameter | Number of Layers | Surface Density (Number/mm$^2$) |
|---|---|---|---|---|
| **Stratum Basale** | 10µm | 6µm - 8µm | 1 | 7000 |
| **Stratum Spinosum (Suprabasal)** | 10µm | 6µm - 8µm | 1 | 7000 |
| **Stratum Spinosum** | 16µm | 9µm - 12µm | 5 - 10 | 4000 |
| **Stratum Granulosum** | 16µm | 12µm - 15µm | 3 - 5 | 1500 |

mal junction. To reinforce the mechanical connection between the two layers, the dermoepidermal junction is characterized by an undulating topology providing more structure by enlarging the surface area of the basement membrane. The resulting downward invaginations of the epidermis and upward interdigitations of the dermis are termed rete ridges and dermal papillae respectively.

The dermis is an irregular connective tissue located between the epidermis and the hypodermis, and is primarily populated by stationary fibrocytes and fibroblasts synthesizing collagen [42] but also by free connective tissue cells such as macrophages, mast and plasma cells. Fibrocytes and fibroblasts have an oval cell body with long irregular cytoplasmic extensions, known as stellae, spreading from them. The diameter of the oval cell body is approximately 5µm to 10µm and that of the complete stellate cell approximately 70µm [43]. These cytoplasmic extensions connect with cytoplasmic extensions of other fibroblasts and form a loose network. In contrast to the epidermis, the cell density in the dermis is low [44]. The main components of the extracellular matrix of the dermis are macromolecules such as elastic fibers and collagen fibers of type I and III, providing mechanical durability to the skin. The proportion of collagen in in vivo dermis is $18-30\,\%$ and accounts for about 75 % of its dry weight [45]. The macromolecules contained in the dermis are hydrophilic yielding a high concentration of bound water (between 60 % and 70 %) [45]. In addition, the dermis contains fine vascular structures such as capillaries of the blood and lymphatic system, and nerve fibers that enable tactile and thermal sensation. Depending on its location, the dermis is 15 to 40 times ticker than the epidermis and can be further divided into the papillary dermis, forming an interface with the epidermis, and the reticular dermis, forming an interface with the subcutaneous tissue of the hypodermis. The two sublayers can be differentiated histologically by structural particularities of the collagen fibers. The papillary dermis consists mostly of type III collagen which is poorly arranged in thin structures while the reticular dermis consisting mostly of type I collagen is well-organized and characterized by thicker structures [30]. Another morphological characteristic that aids in distinguishing the two sublayers of the dermis is the dermal vasculature, the blood vessel system of the skin, which consists of two interconnected vascular networks, the superficial vascular plexus and the deep vascular plexus. The vessels of the deep vascular plexus show larger diameters than those of the

superficial vascular plexus and are located at the bottom of the reticular dermis. The superficial plexus is located in the papillary dermis and is characterized by fine capillary loops extending into each dermal papilla.

The hypodermis consists of connective tissue containing lobules of white adipocytes separated by fibrous septa. It provides mechanical support, thermal insulation, and serves as an energy store. Adipocytes are basically differentiated fibrocytes in which glycerol is stored as an energy carrier within a vacuole [46]. A single adipocyte consists of a lipid vacuole, which occupies about 95 % of the cell volume, and the peripheral cytoplasm with cell organelles. Adipocytes are approximately spherical with a diameter of about 100 µm (depending on the size of the lipid vacuole) [32, 47]. Even a brief overview of skin anatomy, such as the one presented in this chapter, makes clear the challenges presented by the task of modeling the skin and its constituent structures.

# 4 Multiscale Modeling of the Skin - The Categorization of Hierarchical Scales According to Anatomical Attributes

The previous chapter provided an overview of skin anatomy, illustrating its complexity and highlighting the symbiotic relationship between numerous macroanatomical and microanatomical structures that pose significant challenges when attempting to model skin using computational approaches. As mentioned in the introduction, this challenge can only be effectively addressed by decomposing the whole system into definable subsystems using a multiscale modeling approach. However, as discussed earlier, the decomposition of biological systems into macroscopic and microscopic scales does not always provide a straightforward framework that can be readily applied to specific applications. Therefore, it becomes necessary to subdivide the system to be modeled into even finer categories in order to capture the intricacies associated with skin modeling accurately. Although the development of tissue models in the context of this thesis focuses only on the epidermis, the conceptual division into length scales and the assignment of macrostructural and microstructural features to these scales will be discussed in the context of the entire skin system using Fig. 4.1. Based on the comprehensive overview of the human skin and its intricate structures on both macroscopic and microscopic length scales depicted in this figure, a suitable partitioning scheme is proposed to classify the skin into three hierarchical scales, based on shared morphological attributes: (1) an “organ scale" comprising the layered structure of the skin and its cross-layer features as a whole (see Fig. 4.1(a)), (2) a “tissue scale" comprising many cells in a network (see Fig. 4.1(b)), and (3) a “cell scale" comprising a single cell and its subcellular structures (see Figs. 4.1(c)-(k)).

In this way, all of the morphological attributes that give the skin its overall structure can be captured at the organ scale. This includes attributes such as the thickness and density of hairs and sweat glands [48, 49, 50], wrinkles , the capillary network of the upper and lower vascular plexus [14], topological features such as the undulating epidermis/dermis interface [51] and the thickness of individual skin layers [4, 19]. These are all attributes that are highly dependent on the body part being analyzed, as well as attributes depending on the age, gender, and ethnic origin of the skin being modeled. This already opens

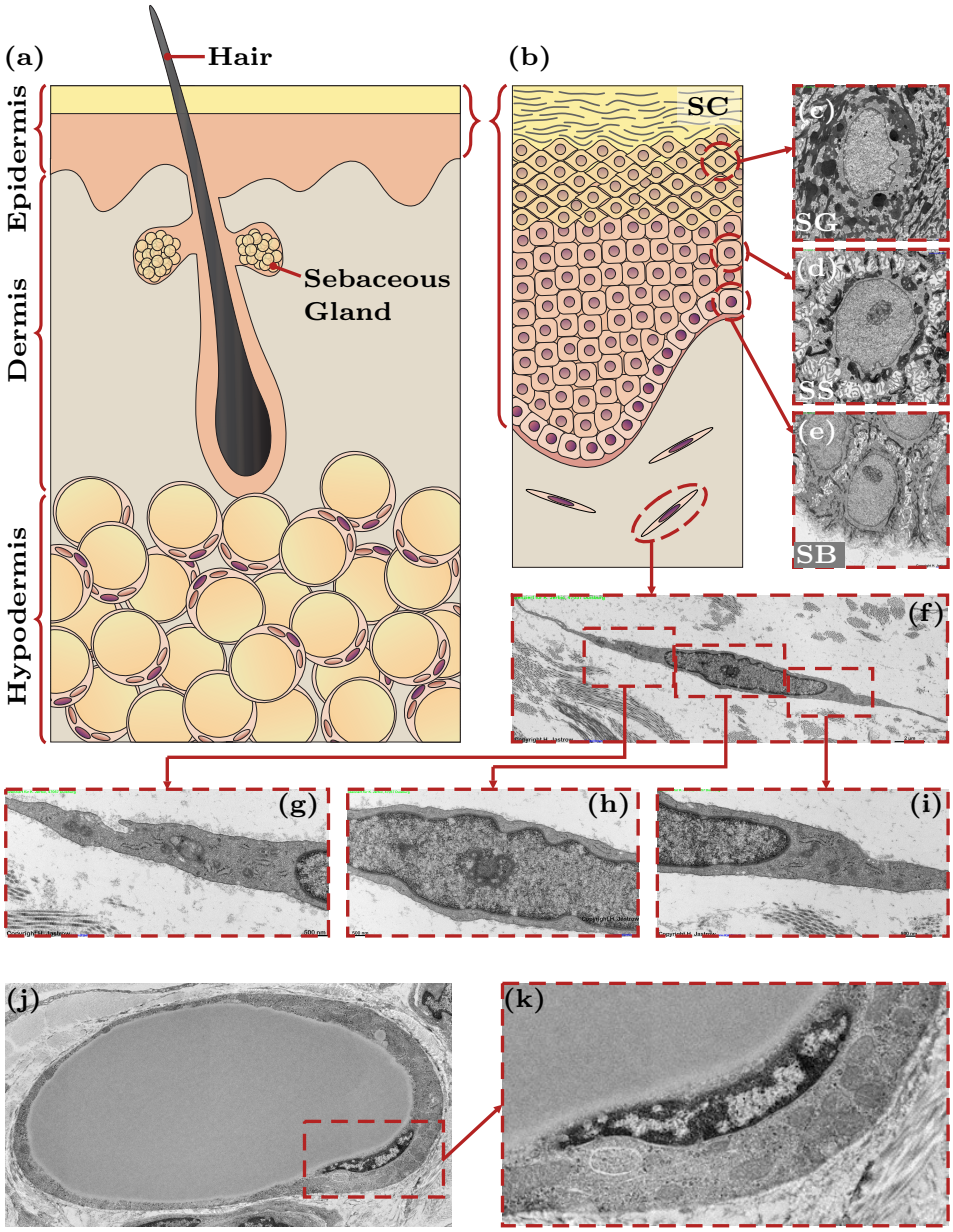


**Figure 4.1:** Overview of human skin and its fine structures on macroscopic and microscopic length scales: (a) Schematic of the layered topology of the skin showing several macroscopic features such as a hair with its sebaceous glands. (b) Detailed magnification of the epidermis showing, from top to bottom, the stratum corneum (SC), stratum granulosum (SG), stratum spinosum (SS) and stratum basale (SB), illustrating the transformation of keratinocytes to corneocytes across these epidermal sublayers with different cell shapes and colors. (c)-(e) Micrographs showing the degree of keratinization of keratinocytes in the SG, SS, and SB respectively [32]. (f) Micrograph of a fibrocyte [32]. (g)-(i) Detailed magnifications of the fibrocyte shown in (f). Figures (g) and (h) show subcellular structures in the cytoplasm such as the endoplasmic reticulum (ER) or mitochondria (M) [32]. Figure (h) shows the nucleus (N). The different shades of gray indicate regions of higher and lower electron density and thus material heterogeneity within the nucleus. (j) Micrograph of an adipocyte showing a large lipid vacuole displacing the remaining cytoplasm to the edge of the cell [32]. (k) Detailed magnification of the cytoplasm [32].

up a large potential parameter space for skin modeling at this conceptual scale. As for the skin modeling on an organic scale, the research conducted in this study adopts the modeling approach outlined by Sasaki in [4], only considering the stratified topology of the skin on a macroscopic scale.

At the tissue scale, all of the histoanatomical attributes that describe the morphology of a specific tissue must be captured. These include attributes such as the cellular composition which focuses on the specific types of cells present in a tissue and the histological organization which describes the arrangement and spatial relationships of these cells. The cellular composition is well illustrated by comparing the hypodermis depicted in Fig. 4.1(a) and the epidermis depicted in Fig. 4.1(b). The epidermis shows a very regular and dense cell arrangement of keratinocytes typical of epithelial tissue, especially in its lower layers, while the hypodermis shows a more amorphous arrangement of adipocytes. The translation of such morphological attributes into performant computer models is challenging and highly context dependent. For instance, the amorphous arrangement of cells in the hypodermis suggests modeling the tissue at the tissue scale by a randomized arrangement of many adipocytes. However, this reduces the level of detail at which the interior of the cell can be represented at this scale due to the need to limit the numerical complexity of the model. As such, it becomes necessary to shift the representation of the cell interior to the cellular scale. The conceptual implementation of such an approach is demonstrated in Appendix E by means of a generic representation of the hypodermis, which serves as an illustrative example. There, the histological organization of tissues is discussed as a factor that significantly influences the limits of analytical and numerical homogenization approaches. However, the regular arrangement of cells in the epidermis allows a modeling approach in which the histological organization of the tissue is approximated by a general cell arrangement adhering to a primitive orthorombic unit cell. This assumption allows an efficient numerical treatment of the tissue using a single cell model with a high level of detail and numerical boundary conditions that take into account the periodicity of the cell model regarding the regular arrangement of entire epidermal cell clusters. This will be elaborated in detail in Chap. 9. The comparison of the hypodermis and the epidermis reveals the prominent context dependency in the choice of an adequate approach. This leads to the understanding that, in the case of the epidermis, the tissue scale and the cellular scale merge as the histological organization of the tissue is implicitly incorporated using appropriate boundary conditions. Given the original division of multiscale approaches into macroscopic and microscopic scales, the tissue scale can be considered a mesoscopic scale whose implementation requires a highly tissue-specific approach.

At the cellular scale, all of the cytoanatomical attributes describing the morphology of a cell and its interior must be captured. These attributes cover a wide range of aspects, including the overall geometry, such as the size and shape of the cell, but also attributes related to the interior of the cell, such as the appearance and arrangement of subcellular structures, or the position and shape of the nucleus. While the internal structure of cells markedly varies depending on the specific tissue, common features are shared among all eukaryotic cells. The cell body is delimited by a plasma membrane, comprising a phos-

pholipid bilayer with incorporated and attached membrane proteins. Organelles within the cell, also surrounded by membranes, serve various functions in cell metabolism, with the nucleus and endoplasmic reticulum occupying the largest portion of the cell volume. Unlike the nucleus, the endoplasmic reticulum is not a continuous structure, but a system of channels distributed throughout the cell. Additionally, other organelles like mitochondria, Golgi bodies, and lysosomes contribute to cellular functionality, located in a gelatinous fluid called the cytosol. All subcellular structures, excluding the nucleus, collectively constitute the cytoplasm, while the material within the nucleus is referred to as the nucleoplasm.

A more detailed discussion on how the overall shape and internal structure of cells differ depending on the tissue under consideration will be discussed in more detail using micrographs showing the predominant cell types of each skin layer. Micrographs of keratinocytes in the stratum basale, stratum spinosum and stratum granulosum are shown in Figs. 4.1(c)-(e) to illustrate keratinization. The differentiation of basal keratinocytes is illustrated by changes in cell shape and deposition of keratohyalin granules, observed as dark regions in the micrographs. The contrast in these micrographs results from local differences in electron density, documenting biochemical distinctions within the nucleus and cytoplasm. This potentially allows conclusions about the biochemical composition on a “molecular scale" to be drawn. Fig. 4.1(f) presents an example of a fibroblast embedded in the dermal collagen matrix, featuring its elongated cell body with a narrow nucleus and branched extensions connecting fibroblasts throughout the dermis. An examination of the detailed enlargements of the fibrocyte in Figs. 4.1(g)-(i) shows that the interior of the cells also has a complex structure consisting of various organelles. An example of how the structure of a cell depends on its function can be seen by comparing the structure of the fibrocyte with that of an adipocyte given in Fig. 4.1(h). In principle, the adipocyte is a differentiated fibrocyte that becomes a univacuolar fat cell due to the incorporation of triglycerol [46]. As a result, the volume of the cells increases and the organelles are pushed to the edge of the cell (see. Fig. 4.1(i)). This serves as an illustration of the complexity of the skin which must be addressed in modelling that will be dealt with in the following chapters.

# 5 State of the Art in Modeling Biological Systems

After discussing the challenges of conceptualizing suitable multiscale models, the following chapter provides an overview of the state of the art in modeling biological systems. The field is divided into three relevant topic areas: (1) skin modeling in dosimetric studies, (2) multiscale modeling of skin, and (3) modeling of eukaryotic cells. The paradigms and methods that have been established for modeling biological systems within these three largely independent areas will be examined. Special emphasis will be placed on identifying the current methodological limitations that arise when attempting to integrate these established methodologies into comprehensive multiscale skin models.

## 5.1 Skin Modeling in Dosimetric Studies

The configuration of a suitable skin model on a macroscopic scale (i.e. organ scale) involves two aspects: (a) the level of detail with which morphological attributes of the skin are considered in the geometric setup of the model, and (b) the material properties associated with these.

Regarding aspect (a), two general approaches in skin modeling emerge concerning the consideration of morphological attributes in a macroscopic representation of the skin when reviewing the scientific literature. In the first approach, the skin is modeled as a one-dimensional, layered material structure, with each sublayer represented as a homogeneous material. This approach is commonly employed to investigate the influence of EM exposure on the volumetric power densities induced in the skin tissue and the resulting temperature distribution in a generalized manner. Studies conceptualized in this way serve as the scientific basis for the definition of appropriate metrics [4, 6, 7, 8, 11, 12] and exposure limits [19, 52, 53, 54], as adopted by ICNIRP. In order to establish a direct reference, and thus ensure comparability with current exposure guidelines, the research presented in this thesis follows this one-dimensional modeling approach, which describes the skin as a layered material, which describes the skin as a layered 1D material at the macroscopic (i.e. organ) scale. However, as the frequency of EM fields increases, their wavelengths shorten to orders of magnitude corresponding to the dimensions of cross-layer skin appendages. To study the specific effects of this phenomenon, the second approach involves modeling the skin as a three-dimensional material structure, accounting

for the undulating topology of the skin and the presence of these appendages. Studies such as [48,50,51] show that certain appendages of the skin, such as hair or sweat glands, can be considered as antennas that significantly influence the EM absorption behavior of the skin. Three-dimensional modeling of these appendages proves valuable in identifying morphological arrangements that lead to "extreme" values in the distribution of EM fields induced in the tissues, thus generating considerable interest and discussion in the scientific community. However, it is important to note that the exposure limits currently accepted by ICNIRP do not take into account studies involving three-dimensional modeling of skin appendages and are mentioned here for the sake of completeness.

Regarding aspect (b), two possible approaches to access the dielectric material properties of tissues can be identified: (1) analytical or numerical derivations based on effective material theory, and (2) measurements. Both approaches have their individual advantages and cases of application closely corresponding to aspect (a), i.e. the geometrical setup on a macroscopic scale. For example, the derivation of material properties using effective material theory is most commonly applied to three-dimensional models of skin because there are no measurements of the material properties of hair or sweat. The fundamental assumption of this theory in the context of tissue modeling is that the macroscopic effective material properties of each skin feature are primarily governed by three constituents: the amount of free water, the amount of bound water, and the amount of dry biological material contained in a tissue [48, 50, 51]. In contrast, measurements offer an approach to derive the dielectric material properties of a biological system with high reliability over a wide frequency range [55, 56, 57] from the generalized EM response of the entire organ system such as the liver, the brain (i.e. grey and white matter), or the skin. However, the decision whether these metrologically obtained material properties can be used in the modeling of a biological system must be made entirely in the context of three factors. The first two factors relate to the measurement system (i.e. equipment) and measurement method (i.e. transmission / reflection) used to acquire material properties. Depending on these two factors, average properties are thus determined over the area and depth of penetration into the tissue covered by the measurement. This averaging includes all morphological attributes at the measurement location. Therefore, the separation of the influence of specific skin appendages, such as sweat glands, on the absorption of EM energy in the tissue is not possible with current measurement technology. The third factor, the most important and subtle one, concerns the material model used in the postprocessing of the measured signal, i.e. the underlying model used to reconstruct the acquired measurement data and translate them into material properties. The importance of this is evident when comparing the pioneering work of Alekseev et al. [58] and Sasaki et al. [4, 5]. In [58], Alekseev conducted in vitro skin measurements using two rectangular waveguides, one with dimensions of $5.2 \times 2.6\,\mathrm{mm}$ and the other $3.6 \times 1.8\,\mathrm{mm}$, operating in the frequency ranges of 37 to 53 GHz and 53 to 78 GHz, respectively. The objective of the study was to deduce a heuristic representation of the topology of the skin as a multilayer structure consisting of four homogenized dispersive layers. However, reconstructing the thickness and dielectric properties of the multilayer skin model presented an ill-posed problem, relying solely on measured reflection data. Consequently,

the layered skin model and calculated dielectric material properties were derived using educated guesses for numerous unknowns, rather than verified knowledge. As a result, the skin model encountered significant measurement uncertainty that is challenging to quantify. In contrast to Alekseev, Sasaki [4,5] addressed the ill-posed problem by separating the skin according to the individual skin layers and measuring them separately. This was performed using both a coaxial sensor operating between 1 and 100 GHz and a THz-time-domain-spectroscopy system operating in reflection mode in the frequency range between 100 GHz and 1 THz [4]. The accuracy of the resulting dielectric description of the individual material layers thus only depended on the precision of the measurement system and the possibility to divide the skin tissue into individual sublayers. This allowed a modular representation of the skin as a stratified material structure composed of arbitrarily thick layers. As the comparison of the two studies shows, both Alekseev and Sasaki rely on a layered skin model to derive dispersive material properties from measured data. Thus, the use of these material properties is limited to simulations with a similar layered approach. A layered skin model thus represents a generalized view of the skin, which, by adapting the material properties of the individual sublayers as published in [4, 5], provides both a metrologically based foundation for and a direct reference to the latest exposure limits provided by ICNIRP. For this reason, Sasaki's material models were used to represent the dielectric properties of the distinct skin layers on a macroscopic scale.

## 5.2 Multiscale Modeling of the Skin

The use of mixing formulas in the context of EMT to determine the macroscopic properties of a composite material dates back to the middle of the 19th century [59, 60] and can be regarded as the most primitive form of a bottom-up multiscale approach in the context of this work. It is primitive because the mixing formulas used considered the morphology of the composite only as largely formless carrier substance, in which two-phase or multiphase composites were considered as spheroidal inclusions. These simplified assumption only allowed the approximate consideration of the morphology of a composite with respect to the relative orientation of the inclusions. Despite this highly simplified representation of a composite material, mixing formulas have proven to be an effective means of predicting the dielectric properties of chemical compounds or more complex mixtures such as ice, snow, rain, or even rocks with sufficient accuracy, in applications such as remote sensing. A more comprehensive overview of effective material theory and its applications is given in the standard work by Sihvola [23]. By clever nesting of several mixed formulas, in which cells are described as layered spheres or ellipsoids, it is even possible to represent cells in dilute suspensions and to perform diagnostic analyses by measuring such suspensions [25, 61].

The first attempts to derive a comprehensive bottom-up model of the skin for noninvasive skin monitoring using dielectric spectroscopy were made by Huclova et al. in [45]. The

main methodological contribution of this work was the development of hierarchically organized mixing schemes in which the dielectric material properties of individual skin layers were described at the macroscopic level by their subcellular composition. These mixing schemes were derived taking into account tissue-specific anatomical features within these sublayers, making it possible, for the first time, to take into account cellular composition, histological organization, and cell size and shape when modeling skin. The innovation in the development of these mixing schemes lay in the involvement of a numerical homogenization procedure that allowed cell shape to be taken into account at the cellular level, and thus the inclusion of interfacial polarization as the dominant polarization mechanism in the frequency range between 1 and 100 MHz.

Building on this bottom-up approach, Saviz et al. [17] performed in a numerical study of corneal tissue exposure in the frequency range between 100 GHz and 10 THz and attempted a new method to extend dosimetric studies to a top-down multiscale approach. In this approach, called de-averaging in [17], three hierarchical scales were defined: (1) a macroscopic scale, where the eye is considered as a layered material system with homogeneous layers, (2) a tissue scale, where individual cells are considered as homogeneous entities embedded in a homogeneous extracellular matrix, and (3) a subcellular scale, where the whole cell space is considered as a heterogeneous composition of multiphase inclusions. The main methodological innovation of [17] was the idea of macroscopically determining the local electric field strength in the tissue and then using numerical simulations to project it first to the tissue scale and then to the subcellular scale to allow a microdosimetric assessment of the field distribution within the subcellular structures. However, the insight gained by this method was severely limited by the inadequate representation of cells at the tissue and subcellular scales. For example, at the tissue scale, cells were assumed to be homogeneous, so that even the coarsest possible subdivision of the cell into two compartments, the cytoplasm and a separate nucleus, was not taken into account. This lack of detail at the tissue scale had direct implications at the subcellular level, where attempts were made to represent the composition of the cell interior by an arbitrary arrangement of spheres intended to represent organelles such as mitochondria, lipid droplets, and lysosomes. However, at both the tissue and subcellular levels, this type of cell modeling neglected the fact that a cell is a highly complex symbiotic system in which the specific function of the cell within the tissue under investigation determines its internal structure. As vividly illustrated in Chap. 4, a cell is not composed of small spherical inclusions; instead, it consists of numerous structural units, including organelles like the endoplasmic reticulum, which forms large interconnected systems represented as cisternae connected by fine channels occupying a substantial volume within the cell. The current approach to modeling the tissue scale and subcellular scale therefore tends to follow the paradigm of squeezing the cell into the framework of effective material theory, rather than fully exploiting the design freedom that computational models allow in modeling complex geometries to authentically represent eukaryotic cells.

## 5.3 Modeling of Eukaryotic Cells

The example of the study conducted in [17] shows the importance of modeling eukaryotic cells within a top-down multiscale approach. It is therefore important to know the state of the art in this field and, based on this, to develop suitable multiscale models that realistically represent the internal structure of cells.

In its simplest representation, a eukaryotic cell is assumed to be a concentric-shelled sphere or ellipsoid. In this representation, the interior of the cell is divided into two distinct compartments: the cytoplasm (CP) and the nucleus. These are separated from each other and from the exterior by thin membranes. Although this assumption (over)simplifies reality, analytical studies using such cell models have been successfully employed to investigate the distribution of EM fields in the cell interior, allowing the approximate determination of induced membrane voltages and losses [16, 62, 63, 64]. This simple representation of a cell has also proven useful in approximating the EM material properties of the two compartments and the membranes under consideration. This has been performed in two phases across a variety of studies. First, dielectric spectroscopy was used to determine the frequency-dependent macroscopic dielectric properties of cell suspensions [65, 66, 67, 68]. Then, in a second step, by inversely applying mixing rules to these properties assuming the same model as used above, a representation of the cell and its compartments was created that corresponded to the statistical average of all cells contained in the suspension allowing their material properties to be derived [23, 25, 61, 69, 70, 71].

Recent developments in cell modeling have been influenced by improvements in computer hardware and software. Using numerical methods, such as the finite element method (FEM), it is possible to calculate the field distribution within cell models that have a much higher morphological complexity, which is expressed in both their shape and internal organization. This allows for a variety of numerical studies that consider the interaction of EM fields with eukaryotic cells in different contexts and fields of application. Focusing on the effects of cell shape on both the EM field distribution and effective macroscopic material properties, studies have conducted numerical investigations using Gielis' super-formula [72], simulating a variety of human cells in vitro [73] and in vivo [15, 74]. Another trend in cell modeling has been initiated by the advent of biosensors that allow dielectric spectroscopy on single cells. In combination with the numerical methods mentioned above (i.e. FEM), not only is it possible to consider the interaction of EM fields with cells in a generic setting but also to create digital twins of underlying experiments, thus allowing phenomenological interpretation of the measured spectral responses [75, 76, 77, 78, 79]. Due to the high degree of correlation required between such simulations and the corresponding experiments, fluorescence microscopy is used together with edge detection and extraction algorithms to incorporate the individual shape of the plasma membrane (PM) as well as that of the internal organelles of the studied cells based on two-dimensional sectional images, [80, 81, 82, 83, 84, 85, 86].

However, cellular models used for risk assessment require a volumetric representation of eukaryotic cells and their organelles. In order to develop such models, basic knowledge of the dispersion properties of cellular components and principles of cellular modeling are used in this thesis as a starting point to develop parametric cellular models that allow for physiological changes across the epidermis in terms of histochemical composition, cell size and shape, and internal organization. While addressing these aspects, the significance of subcellular structures in the modeling of eukaryotic cells was investigated in [18]. This investigation accurately predicted cellular losses in dosimetric studies and is detailed in Chapter 8. The insights gained from this research are subsequently tailored to the unique anatomical structure of the epidermis to model keratinocytes within a symbiotic biological system, as described in Chapter 9.

# 6 The Conceptualization of Scale-Back Projection

The challenges of developing suitable multiscale tissue models and a comprehensive review of the state of the art in skin modeling have been presented in the previous chapters. In this chapter, the application of scale-back projection as a method to perform microdosimetric investigations at the cellular level is described in detail. The relationship between scale-back projection and multiphysics simulation, the latter of which is conventionally used to assess the thermal effects of EM waves on the skin, is also clarified. This serves to instigate a detailed discussion of how scale-back projection could (potentially) be used to complement the repertoire of methods currently accepted as standard by ICNIRP. However, it is important to note that thermal simulations were beyond the scope of this work.

As illustrated in Fig. 6.1(a), this multiphysics approach can be considered as a nested procedure in which both thermal and EM simulations are performed. The scale-back projection, as proposed and discussed in this work, is designed to extend only the EM simulations of this multiphysics approach, as shown on the left in Fig. 6.1(a). This allows the consideration of EM absorption by investigating the effects of induced EM fields at the cellular level, as shown in Fig. 6.1(b). As already explained in the introduction, the scale-back projection is essentially a top-down multiscale approach, which must, as outlined in Chap. 4, assume coherence between the length scales under consideration and requires bottom-up modeling of the tissue under investigation based on appropriate cell models. Applied to the epidermis, the procedure shown in Fig. 6.1(b) can be interpreted as a simulation cycle that can be divided into three steps. In the first step, virtual impedance spectroscopy is performed on the cell models of the epidermis using quasi-static EM simulations, which allows the dispersive effective macroscopic permittivity, $\underline{\tilde{\varepsilon}}_{\mathrm{r}}$, to be determined. The exact implementation of this numerical homogenization approach will be detailed later in this thesis, and can be interpreted phenomenologically as a virtual capacitor experiment by exposing the cell models to an arbitrary voltage, $U_0$. This procedure is based on parametric cell models that account for changes in overall cell size and shape, internal organization, and histochemical composition during the keratinization process in the epidermis. Therefore, it can be used to derive a macroscopic model of the epidermis that represents the life cycle of keratinocytes, with each stage represented by a homogeneous cell layer. As shown in the middle of Fig. 6.1(b), the epidermis in this model is represented by 10 such cell layers within the viable epidermis ($\underline{\tilde{\varepsilon}}_{\mathrm{r,K_1}}$ to

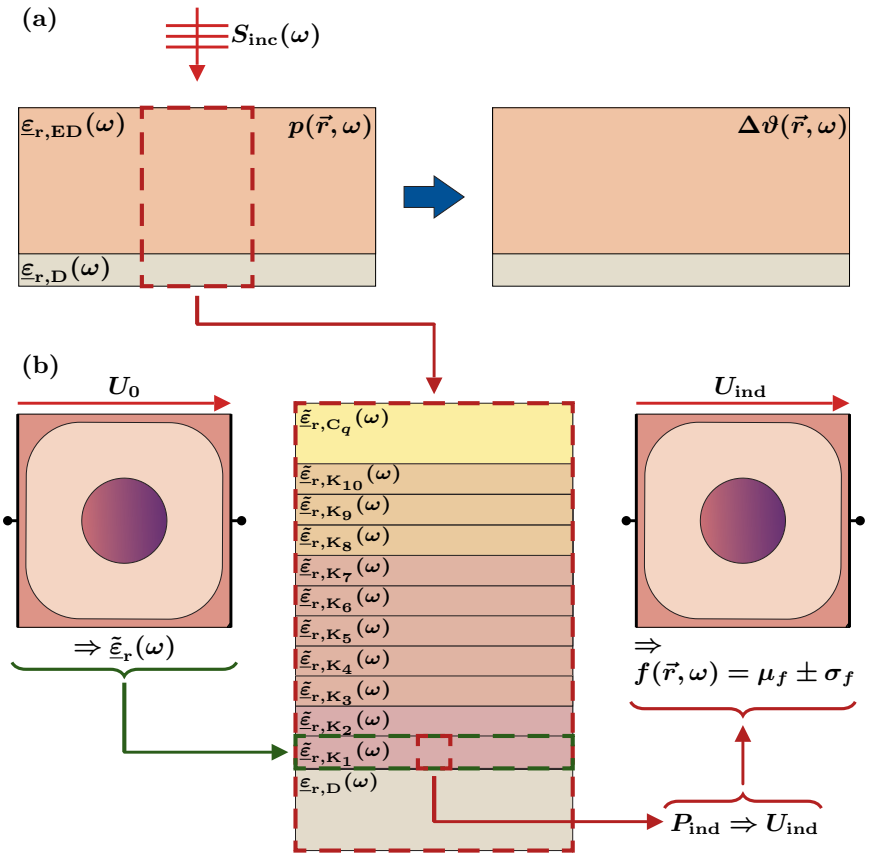


**Figure 6.1:** Overview of scale-back projection as an extension of conventional EM simulation models embedded in a multiphysics simulation environment: (a) Multiphysics simulation approach applied to dosimetric studies on the skin. This establishes a causal relationship between the incident power $S_{\mathrm{inc}}(\vec{r},\omega)$, representing the anthropogenic EM exposure, and the volumetric loss density $p(\vec{r},\omega)$, representing the absorbed EM energy. Temperature increases, $\Delta\vartheta(\vec{r},\omega)$, are then determined based on these data. It is important to note that thermal simulations were beyond the scope of this work. (b) The proposed scale-back projection, described as a top-down multiscale approach that requires bottom-up multiscale modeling based on appropriate cell models to ensure coherence between the macroscopic and microscopic scales. For the epidermis, this procedure can be implemented as a three-step simulation cycle: (1) Impedance spectroscopy on cell models of the epidermis using quasi-static EM simulations to determine the dispersive effective macroscopic permittivity, $\underline{\tilde{\varepsilon}}_{\mathrm{r}}$. (2) Derivation of a macroscopic tissue model of the epidermis, representing the life cycle of keratinocytes across several homogeneous cell layers illustrated in this figure by color gradation. (3) Determination of losses ($P_{\mathrm{ind}}$) across epidermal cell layers within microvolumes corresponding in size to those of the underlying cells being simulated. This allows back projection of microexposure at the cellular level ($U_{\mathrm{ind}}$) and performance of microdosimetric studies based on the variability of the fields projected into the microstructure ($f(\vec{r},\omega) = \mu_f \pm \sigma_f$).

$\underline{\tilde{\varepsilon}}_{\mathrm{r,K}_{10}}$), where the color gradation between cell layers indicates association with the stratum basale, stratum spinosum, and stratum granulosum, as well as $q$ cell layers within

the stratum corneum ($\underline{\tilde{\varepsilon}}_{\mathrm{r,C}_q}$). In the context of an overall skin model, it is now possible to determine losses, $P_{\mathrm{ind}}$, across the epidermal cell layers within microvolumes corresponding in size to those of the underlying cell models. Based on these losses, it is possible to determine voltages, $U_{\mathrm{ind}}$, that allow the definition of a microexposure at the cellular level of an equivalent power for use in parametric cell models of the underlying keratinocytes. Using this procedure, it is now possible to perform microdosimetric investigations based on the variability of the fields projected into the microstructure in terms of spatial means and standard deviations (i.e., $f(\vec{r},\omega) = \mu_f \pm \sigma_f$).

In the course of this thesis, the methodological framework described above will be implemented in a simulation environment that allows modeling of the epidermis and efficient simulation of EM field exposure of the skin in order to predict the effects of this on the epidermal microstructure. This simulation environment is divided into three hierarchical scales: An environmental scale at which the exposure set up is defined; A macroscopic scale at which the skin is considered as a stratified material structure comprising the epidermis, dermis, hypodermis and underlying muscle tissue; A microscopic scale which comprises parametric cell models representing the microstructure of the individual epidermal cell layers. To show the high level of interaction between these functional blocks across all hierarchical levels, a conceptual block diagram is presented in Fig. 6.2. The flow

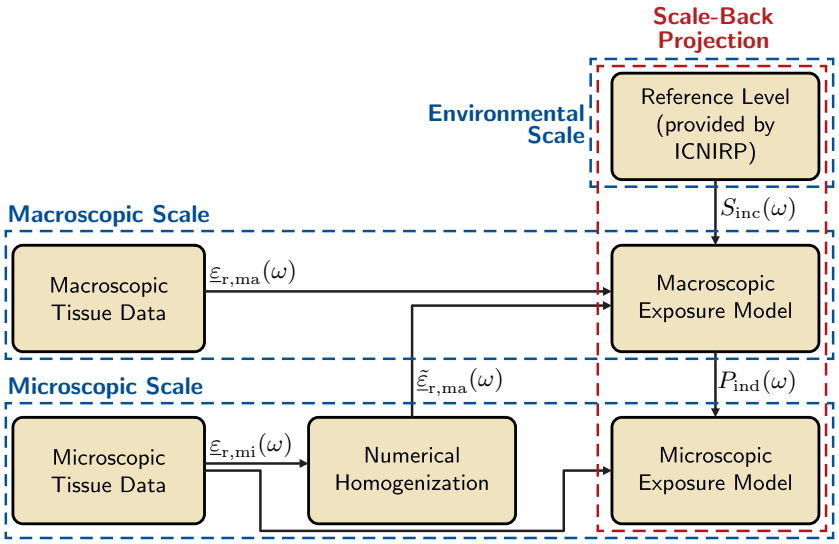


**Figure 6.2:** Conceptual block diagram illustrating the hierarchical organization of the simulation environment implemented to perform scale-back projection in epidermal tissue. The simulation environment encompasses three hierarchical scales: An environmental scale defining the exposure scenario, a macroscopic scale representing the stratified structure of the skin consisting of the epidermis, dermis, hypodermis, and underlying muscle tissue, and a microscopic scale consisting of parametric cell models representing the microstructure of individual epidermal cell layers.

of information in the block diagram is from the left to the right and starts with the identification of appropriate material parameters that describe the tissue at the microscopic and

macroscopic levels. As derived in the state of the art (see Chap. 5), the macroscopic tissue data, $\underline{\varepsilon}_{\mathrm{r,ma}}(\omega)$, include the dispersive permittivities of the individual skin layers measured by Sasaki et al. [4,5]. The adaptation of this data allows the development of a modular skin model and also serves as a metrological reference to validate the bottom-up model of the epidermis. The microscopic tissue data, $\underline{\varepsilon}_{\mathrm{r,mi}}(\omega)$, provides essential information about the dispersive material properties of subcellular structures and fundamental biochemical components, enabling the accurate modeling of the histochemical composition of the parametric cell models for the epidermal cell layers. Using these parametric cell models, numerical homogenization is employed to calculate the effective macroscopic material properties, $\underline{\tilde{\varepsilon}}_{\mathrm{r,ma}}(\omega)$, of the individual skin layers at the macroscopic scale. This is achieved by utilizing $\underline{\varepsilon}_{\mathrm{r,mi}}(\omega)$ as input for bottom-up multiscale simulations, wherein the size, shape, and internal organization of the modeled keratinocytes are resolved in great detail. In the scale-back projection, environmental exposure is simulated using a plane EM wave, adhering to ICNIRP regulations [1] briefly summarized in the following chapter, which limit the incident power density, $S_{\mathrm{inc}}(\omega)$, to the latest reference levels. The skin is modeled as a layered material, incorporating the bottom-up model of the epidermis, while other sublayers (dermis, hypodermis, and underlying muscle tissue) adopt measured dispersive permittivities from Sasaki. By implementing this exposure scenario in an FEM-based simulation environment, the macroscopic exposure model enables the determination of induced losses, $P_{\mathrm{ind}}(\omega)$, in microvolumes corresponding to the size of epidermal cell models. Using $P_{\mathrm{ind}}(\omega,\vec{r})$, local tissue exposure is finally back-projected onto the high-resolution models of the keratinocytes.

# 7 On Electromagnetic Field Restrictions in Human Tissue Exposure

In order to specify the scope of the conducted investigations, a brief recap of the document Guidelines for Limiting Exposure to Electromagnetic Fields (100 kHz to 300 GHz) provided by the International Commission on Non-Ionizing Radiation Protection (ICNIRP) [1, 2] is given here. This summary briefly outlines the terminology, physical quantities, and exposure limits defined in these guidelines and their relationship to the microdosimetric studies presented later. After this recap, the current exposure scenario is specified introducing the skin and cell models which have been developed.

## 7.1 Electromagnetic Exposure of Skin Tissue

The exposure limits adopted by the commission to limit electromagnetic (EM) fields are designed to protect human health and to ensure the highest possible level of safety in contact with EM fields. To maintain their validity, the established guidelines are subject to a continuous (re-)evaluation that takes into account the current state of scientific knowledge as a basis for assessment. Harmful and potentially harmful effects to human health are identified in a review of the scientific literature concerning the effects of EM field exposure on biological systems. Provided that the available literature is of sufficient scientific quality, independently verifiable, and consistent with current scientific understanding, it is classified as evidence and the findings documented therein are considered as a substantiated effect in the evaluation process. Regarding such substantiated effects, three main mechanisms of interaction can be distinguished: (a) thermal exposure, (b) nerve stimulation and (c) electroporation. To establish exposure levels based on such documented findings, the lowest exposure level known to cause an adverse interaction is determined and is referred to as the adverse health effect threshold. Basic restrictions are determined using this threshold along with a reduction factor which accounts for biological and environmental variability, as well as metrological uncertainties associated with the underlying evidence. These basic restrictions are quantified by physical measures occurring within an exposed body closely related to the adverse health effects induced by EM fields. This, however, implies a practical issue using the basic restrictions in operational scenarios, as the exposure within a living person is difficult to measure. Therefore,

reference levels expressed by physical quantities measurable outside the body are derived from the basic restrictions such that an equivalent level of protection is ensured even under worst-case exposure conditions. The restriction values defined in both the basic restrictions and the reference levels differentiate between individuals of the general public and those exposed under controlled conditions associated with their occupational duties restricting, general exposure to lower values but allowing much higher occupational exposure.

## 7.2 Electromagnetic Exposure Limits

As outlined above, the guidelines are designed to limit EM field exposure to levels below the *thresholds for adverse health effects* of the respective *mechanisms of interaction*. However, the present study focuses exclusively on the *adverse health effects* of thermal exposure. These are related to absolute temperature rises above the normothermic temperature of the body part under investigation [87, 88, 89]. However, limitation to absolute temperatures is not possible, since many important factors such as clothing, environmental conditions and metabolic heat generation cannot be considered to be influenced by a guideline. Instead, the guidelines are designed to limit any temperature increase. In the following, physical measures to quantify EM field restrictions preventing such an increase in temperature are introduced.

An important quantity to restrict temperature increases is the specific absorption rate (SAR) defined as

$$SAR(\vec{r}) = \frac{\sigma(\vec{r})|\underline{\vec{E}}(\vec{r})|^2}{\rho(\vec{r})} = \frac{p(\vec{r})}{\rho(\vec{r})}. \tag{7.1}$$

where $\sigma$, $|\underline{\vec{E}}|$, $\rho$ and $p$ denote the electric conductivity, the rms-magnitude of the electric field strength, the density and the power density respectively, all as a function of $\vec{r}$ which denotes the position within the tissue. In this formulation, the SAR is considered to be a function of location expressed in W/kg. In practice, however, it is more applicable to consider the SAR as a quantity which is averaged over a certain volume [1]:

$$SAR_i = \frac{\iiint_{V_i} p(\vec{r})\, dV}{\iiint_{V_i} \rho(\vec{r})\, dV} = \frac{P_i}{m_i} \tag{7.2}$$

In this volume-averaged definition of the $SAR_i$, the index $i \in \{\text{wb,10g}\}$ denotes two types of volume: (a) the whole physical body of a person and (b) a standardized cubic volume at an arbitrary position within the body with a side length of 2.15 cm representing 10 g of mass assuming that the underlying tissue has the same density as water ($\rho_{\text{water}} = 1000\,\text{kg/m}^3$). This generic volume is considered sufficient to adequately account for thermal heat diffusion processes resulting from heterogeneous EM field-induced energy inputs into heterogeneous tissue microstructure in realistic exposure scenarios.

In addition to the volume-averaged definition of the SAR, it is also possible to describe the SAR by the temperature increase within this volume over time:

$$SAR_i = C\frac{\Delta T_i}{\Delta t} \tag{7.3}$$

where $\Delta T_i$, $\Delta t$ and $C$ respectively denote the spatial average of the temperature increase within the investigated volume, a time interval in which this occurs and the specific heat capacity of the tissue under investigation. These two definitions together provide a physical foundation to determine the approximate relationship between the power absorbed by the tissue and its subsequent increase in temperature:

$$SAR_i = \frac{P_i}{m_i} = C\frac{\Delta T_i}{\Delta t} \tag{7.4}$$

The relationship is only labeled as approximate, because the specific heat capacity, $C$, is a non-linear function of time, temperature and a variety of physiological and environmental influences rather than a constant. This is because of the symbiotic nature of the whole organism and its tissues on different hierarchical levels (see Fig. 4.1). Thus, ICNIRP has to rely on scarce numerical and experimental research to establish appropriate *adverse health effect thresholds* [9, 10]. Applying a threshold for adverse health effects was set conservatively at a 1 °C increase in core body temperature within a 30-minute interval, corresponding to a $SAR_{\mathrm{wb}}$ value of 4 W/kg. For occupational and general exposure respectively, a reduction factor of 10 and 50 has been applied to this *operational adverse health effect threshold*. This results in *basic restrictions* for the whole body SAR values of 0.4 W/kg and 0.08 W/kg averaged over a 30-minute interval. However, to prevent local temperature increase, a more differentiated regulatory approach is required. This approach distinguishes between different normothermic temperatures in different parts of the body, leading to a classification into type 1 and type 2 tissues. Type 1 and type 2 tissues are classified as tissues with normothermic temperatures greater than 33-36 °C and 38.5 °C, respectively. Exposure leading to local temperatures higher than 41 °C are considered to be potentially harmful. Therefore, a threshold for adverse health effects was set at a 5 °C increase in type 1 tissues and a 2 °C increase in type 2 tissues within a 6-minute interval. These correspond to a $SAR_{10\mathrm{g}}$ value of 40 W/kg and 20 W/kg for type 1 and type 2 tissues, respectively. For occupational and general exposure reduction factors of 2 and 10 have been applied to this *operational adverse health effect threshold*. This results in basic restrictions for type 1 tissues of 20 W/kg and 4 W/kg, and for type 2 tissues of 10 W/kg and 2 W/kg.

Another factor increasing the complexity of the determination of *adverse health effect thresholds* and the subsequent derivation of appropriate *basic restrictions* is the broad frequency range covered by the guidelines. With increasing frequency, the penetration depth of EM fields in the tissue strongly decreases, leading to high absorption predominantly by the surface tissues of the body, such as skin [4] and the cornea [17]. For that reason, additional measures are needed to quantify local exposure restrictions at frequen-

cies greater than 6 GHz. A measure quantifying transmission into the outermost millimeters of the body is the absorbed power density $S_{\mathrm{ab}}$:

$$S_{\mathrm{ab}} = \frac{\iint_A Re\{\underline{\vec{S}}\} \cdot \vec{\mathrm{n}}\, dA}{A} \tag{7.5}$$

$\mathrm{Re}\{\underline{\vec{S}}\}$ denotes the real part of the Poynting vector and $\vec{\mathrm{n}}$ denotes the normal vector to the surface area $A$ over which it is integrated. Due to the low penetration depth at such high frequencies, a threshold of adverse health effects was set to a temperature increase of 5 °C (type 1 tissue). Adopting the findings from [4], an absorbed power density of 200 W/m$^2$ was set as an *operational adverse health effect threshold* averaged over an 6-minute interval and a square surface area of 4 cm$^2$. For frequencies greater than 30 GHz, however, an absorbed power density of 400 W/m$^2$ was set as for the same interval but for a square surface area of only 1 cm$^2$. For occupational and general exposure respectively, a reduction factor of 2 and 10 has been applied to this *operational adverse health effect threshold*. This results in *basic restrictions* for the $S_{\mathrm{ab}}$ of 100 W/m$^2$ and 2 W/m$^2$ averaged over a 6-minute interval.

To provide a comprehensive overview, Tab. 7.1 summarizes the basic restrictions limiting exposure from 100 kHz to 300 GHz outlined above.

**Table 7.1:** Basic restrictions limiting exposure from 100 kHz to 300 GHz, for averaging intervals ≥ 6 min [1].

| Exposure Scenario | Frequency Range | $SAR_{\mathrm{wb}}$ (W/kg) | Type 2 Tissue $SAR_{10\mathrm{g}}$ (W/kg) | Type 1 Tissue $SAR_{10\mathrm{g}}$ (W/kg) | $S_{\mathrm{ab}}$ (W/m$^2$) |
|---|---|---|---|---|---|
| **Occup.** | 100 kHz - 6 GHz | 0.4 | 20 | 10 | NA |
| | > 6 GHz - 30 GHz | 0.4 | NA | NA | 100 |
| | > 30 GHz - 300 GHz | 0.4 | NA | NA | 200 |
| **Gen. Public** | 100 kHz - 6 GHz | 0.08 | 4 | 2 | NA |
| | > 6 GHz - 30 GHz | 0.08 | NA | NA | 20 |
| | > 30 GHz - 300 GHz | 0.08 | NA | NA | 40 |

As mentioned above, basic restrictions are difficult to apply in practice. Therefore, reference levels are derived to create more applicable measures that provide a similar level of protection. In the frequency range investigated here (i.e. 2 GHz to 300 GHz), the incident power density, $S_{\mathrm{inc}}$, is the measure being restricted. Corresponding to the basic restrictions, the value of $S_{\mathrm{inc}}$ varies with both the exposure scenario (i.e. occupational or general public) and the extent of the exposure to the human body (i.e. whole body or local exposure). An overview of the reference levels in the frequency under investigation is provided by Tab. 7.2. These values only apply for EM fields under far-field conditions.

**Table 7.2:** Reference levels corresponding to the basic restrictions summarized in Tab. 7.1 adopted form [1].

| **Exposure Scenario** | **Frequency Range** | **Whole Body** $S_{\text{inc}}$ **(W/m$^2$)** | **Local** $S_{\text{inc}}$ **(W/m$^2$)** |
|---|---|---|---|
| **Occup.** | 2 GHz - 6 GHz | 50 | 200 |
| | > 6 GHz - 30 GHz | 50 | $275/f_{\text{G}}^{0.177}$ |
| | > 30 GHz - 300 GHz | 50 | $550/f_{\text{G}}^{0.177}$ |
| **Gen. Public** | 2 GHz - 6 GHz | 10 | 40 |
| | > 6 GHz - 30 GHz | 10 | $55/f_{\text{G}}^{0.177}$ |
| | > 30 GHz - 300 GHz | 10 | $110/f_{\text{G}}^{0.177}$ |

# 8 The Importance of Subcellular Structures for the Modeling of Eukaryotic Cells[1]

Cell models used for risk assessment [1, 2] require a volumetric representation of eukaryotic cells and their organelles. In order to determine which are the relevant details that need to be modeled, this chapter systematically reviews and compares different cell models with increasing levels of detail. The cell models under consideration start from the simple spherical cell model, containing only a nucleus, and increase in complexity to an ellipsoidal cell comprising a fully resolved endoplasmic reticulum (ER) surrounded by a membrane of low conductivity. Special attention has been paid to the volumetric representation of organelles within the cell. The ER in the most complex cell model, for instance, is conceptualized as a distributed membrane system, and its volumetric extent is approximated by cisternae concentrically surrounding the nucleus. Two methods are therefore presented here to determine the effect of gradually increasing complexity on the resulting field distribution. One of these methods allows the qualitative separation of and distinction between the influence of dispersive material properties and changes in the geometric structure of the cell. The other allows the quantification and graphical illustration of the effect of an ER on the heterogeneity of the EM field distribution in the interior of the cell. Considering all of these details, the following questions will be answered:

(1) How is the current and volumetric loss density distributed in the cell interior?

(2) Where is EM energy absorbed?

(3) What are the effects of different levels of detail in the underlying cell models on the resulting macroscopic material properties?

At all levels of complexity, the EM field distribution within these models is numerically determined using the finite element method in the context of a virtual capacitor experiment in the frequency range between 10 Hz and 100 GHz.

To address all of the above, the modeling of eukaryotic cells in the context of computational bioelectromagnetic simulations is presented in Sec. 8.1. This includes a detailed

[1] This chapter is an adapted version of the journal article published in [18].

description of the eukaryotic cell models of different complexity, their dispersive material properties, and the computational setup in which they are placed. Following this, in Secs. 8.2 and 8.3, the cell models are investigated in terms of their internal field distributions and effective macroscopic material properties, with special emphasis being placed on introducing the two methods described in the preceding paragraph. Finally, the results of these investigations and their consequences regarding future research are summarized in Sec. 8.4.

## 8.1 Modeling Eukaryotic Cells in the Context of Computational Bioelectromagnetics Simulations

This section provides a general overview of the modeling of eukaryotic cells in the context of computational bioelectromagnetic simulations and is divided into four subsections. In the first of these, the eukaryotic cell models under investigation are introduced alongside a method used to spatially resolve and decompose the cell interior for microdosimetric investigations focusing on current and loss distributions within the cell models. Following on from that, the dispersive material properties of the individual cell compartments are derived based on published data. In the third subsection, a simulation setup is presented to perform a FEM-based capacitor experiment to predict the distribution of EM fields within the cell.

### 8.1.1 Generic Eukaryotic Cell Models and Spatial Segmentation

The three generic cell models under investigation are depicted in Fig. 8.1(a)-(c): (a) a simple spherical cell containing a spherical nucleus, (b) an ellipsoidal cell containing a spherical nucleus and (c) an ellipsoidal cell containing both a spherical nucleus and a distributed ER. The so-called rough ER is approximated by cisternae which surround the nucleus concentrically.

Taking these structures into account, the cell interior can be divided into two or three compartments: the cytoplasm (CP), the nucleoplasm (NP), and the endoplasmic reticulum (ER), each separated from the other and from the exterior surrounding, i.e. extracellular medium (EC), by a lipid membrane of low conductivity. The subdivision of the cell interior into separate (computational) (sub)domains allows field distributions to be determined with a spatial resolution that allows current and volumetric loss densities to be integrated in each of these (sub)domains. The volumetric segmentation is shown as an illustrative example for the most complex cell model in Fig. 8.1(d)-(f). In addition, the (cross-)sectional segmentation of the cells is shown in Fig. 8.1(g)-(i) allowing the determination of EM fields in the XY, YZ, and XZ planes. Using these sectional planes in combination with the volumetric segmentation of the cell into its compartments, it is possible to determine the currents flowing through each of them, as shown in Fig. 8.1(j)-(l).

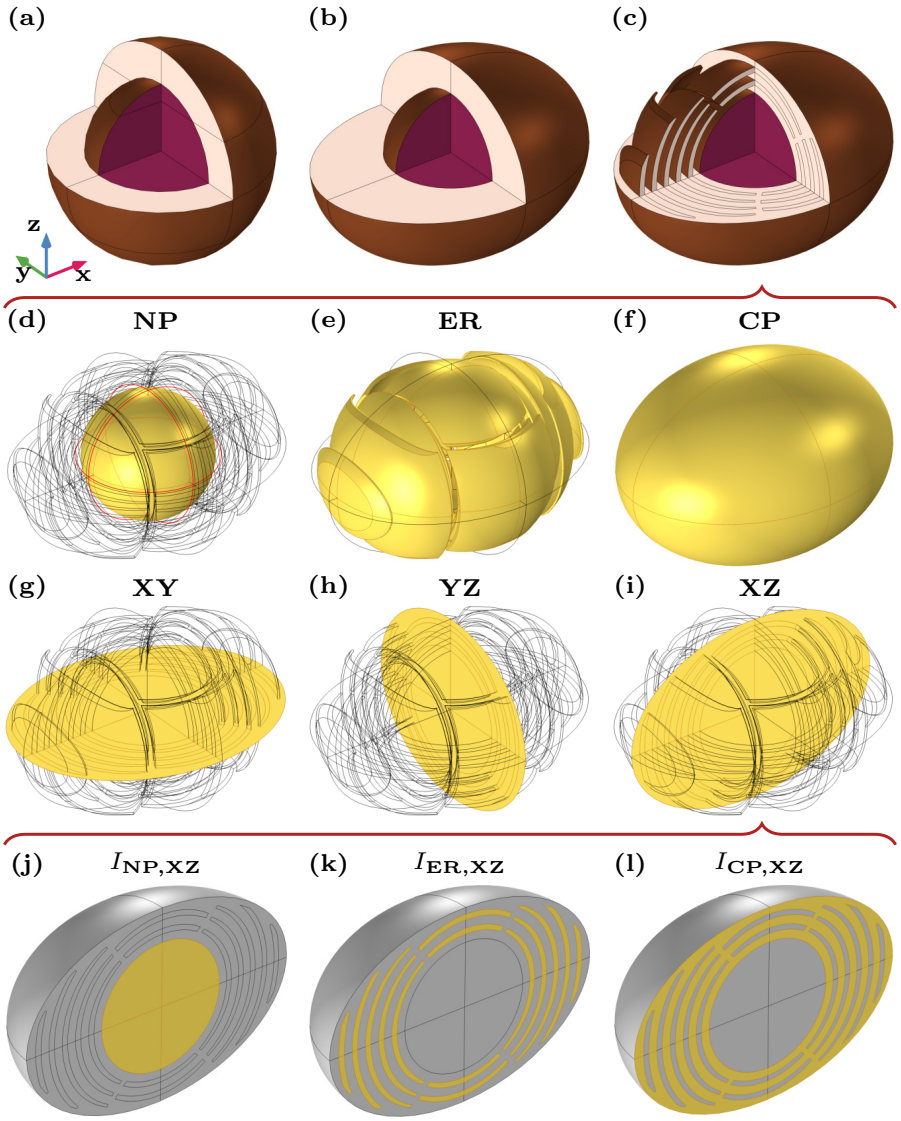


**Figure 8.1:** Overview of the cell models studied and the segmentation used for post-processing: (a)-(c) Generic eukaryotic cells of different shapes and internal complexity. Starting with a simple spherical cell model containing only a nucleus (N) in (a), the level of complexity increases to an ellipsoidal cell model comprising a fully resolved endoplasmic reticulum (ER) in (c). (d)-(f) Segmentation of the cell interior into (computational) domains to capture integral quantities such as the corresponding compartment losses. In the given example, the domains highlighted correspond to the nucleoplasm (NP), the endoplasmic reticulum (ER) and the cytoplasm (CP). (g)-(i) Sectional planes for the evaluation and integration of internal fields showing the XY, YZ and XZ planes respectively. (j)-(l) Segmentation of the sectional planes to capture integral quantities such as the corresponding compartment currents. In the given example, the areas correspond to the currents in the nucleoplasm, the endoplasmic reticulum and the cytoplasm in the XZ plane. The areas of the sectional planes corresponding to the integration are highlighted.

The simple spherical model shown in Fig. 8.1(a) is based on lymphocytes. Lymphocytes were chosen as a template for an initial cell model for two reasons: (1) Their dielectric properties have been extensively studied by the dielectric spectroscopy community [61,69]. (2) They have a very uniform round shape and their internal structure is very well documented, allowing the study of membrane properties on a cell geometry of low complexity. According to [66], their nucleus occupies about 40 % to 70 % of the cell volume and the cytoplasm surrounding the nucleus is poor in organelles. Due to these physiological properties, this first model is well suited for the verification of bottom-up multiscale modeling using mixing rules [69]. In Sec. 8.2, however, the spherical cell model is investigated with respect to the size of the nucleus using numerical simulations. The ratio of the volume of the nucleus to that of the whole cell $c_\mathrm{N}$ normally ranges from 0.4 to 0.7, but here has been extended to cover 0.3 to 0.9 in order to investigate more extreme cases. Following [69], the cell radius was chosen to be $r_\mathrm{cell} = 7\,\mu\mathrm{m}$ , resulting in minimum and maximum radii of $r_\mathrm{N,min} = 4.69\,\mu\mathrm{m}$ and $r_\mathrm{N,max} = 6.76\,\mu\mathrm{m}$ derived from the range given above using $r_\mathrm{N} = \sqrt[3]{c_\mathrm{N}} \cdot r_\mathrm{cell}$. In addition, the reference nuclear radius is $r_\mathrm{N,ref} = 5.9\,\mu\mathrm{m}$ corresponding to $c_\mathrm{N} = 0.6$.

**Table 8.1:** Geometric specifications of the cell models under investigation. SC, EC and ER denote "spherical cell", "ellipsoidal cell" and "endoplasmic reticulum".

| Parameter | SC | EC | ER | Description |
|---|---|---|---|---|
| $r_\mathrm{cell}$ | 7 µm | - | - | Radius of the sph. cell model |
| $r_\mathrm{cell,x}$ | - | 13 µm | 13 µm | Semi-axis in x-direction |
| $r_\mathrm{cell,y}$ | - | 10.5 µm | 10.5 µm | Semi-axis in y-direction |
| $r_\mathrm{cell,z}$ | - | 9 µm | 9 µm | Semi-axis in z-direction |
| $r_\mathrm{N,(ref)}$ | (5.9 µm) | 5.9 µm | 5.9 µm | Radius of the nucleus |
| $t_\mathrm{M}$ | (7 nm) | 7 nm | 7 nm | Thickness of the membrane |
| $t_\mathrm{NE}$ | (40 nm) | 40 nm | 40 nm | Thickness of the nuc. envelope |
| $c_\mathrm{N,(ref)}$ | (0.6) | 0.17 | 0.17 | Volume fraction of the nucleus |
| $c_\mathrm{ER}$ | - | - | 0.2 | Volume fraction of the ER |
| $c_\mathrm{CP}$ | 0.4 | 0.83 | 0.63 | Volume fraction of the nucleus |

In order to investigate the influence of compartmentalization within the cell, the simple spherical cell model is now extended to a more realistic approximation of a cell in the following two steps. Keeping the nuclear radius at a value of $r_\mathrm{N,ref} = 5.9\,\mu\mathrm{m}$, which was previously considered as the reference radius, the plasma membrane is first transformed into an ellipsoidal one with semi-axes $r_\mathrm{cell,x} = 13\,\mu\mathrm{m}$, $r_\mathrm{cell,y} = 10.5\,\mu\mathrm{m}$, and $r_\mathrm{cell,z} = 9\,\mu\mathrm{m}$ (see Fig. 8.1(b)). The influence of this change of shape on the macroscopic material properties and the microdosimetric measures is investigated with respect to the resulting anisotropy. To capture the current density and volumetric loss density distribution within the cell in the context of more complex compartmentalization, a distinct ER was added to the cell in a second step (see. Fig. 8.1(c)), allowing the cell to be studied as a distributed membrane system in Sec. 8.3. The ratio of the volume of the ER to the total cell volume is

$c_{ER} = 0.2$, that of the cytoplasm is $c_{CP} = 0.63$ and that of the nucleus, $c_N = 0.17$. The thickness of the cell membrane and that of the elements of the ER is $t_M = 7\,\text{nm}$ and that of the nuclear envelope is $t_{NE} = 40\,\text{nm}$. To provide a better overview, the geometrical properties are summarized in Tab. 8.1.

### 8.1.2 Derivation of the Dispersive Material Properties Based on Published Data

All cell components have dispersive material properties which are modeled using a lossy Debye-type frequency dependence:

$$\underline{\varepsilon}_r(\omega) = \varepsilon_{r,\infty} + \frac{\varepsilon_{r,s} - \varepsilon_{r,\infty}}{1 + j\frac{\omega}{\omega_0}} - j\frac{\sigma_s}{\varepsilon_0 \omega} \tag{8.1}$$

were $\varepsilon_{r,\infty}$ and $\varepsilon_{r,s}$ denote the permittivity at the high frequency and the low frequency limit of the underlying polarization mechanism respectively. $\sigma_s$ stands for the DC conductivity of the material. As suggested by [16, 71, 90], the dispersive properties of the extracellular medium, the cytoplasm and the nucleoplasm were approximated using the dielectric functions of physiological salt solutions. To be more precise, they were based on measurements of a phosphate-buffered saline solution (PBS) at 27 °C between 100 MHz and 2 GHz performed by [71]. Based on an experimental assessment of the cytoplasmic conductivity in [91], the conductivity of both the cytoplasm and nucleoplasm was set to 0.32 S/m. Although the membranes of cells and organelles are complex (sub-)structures bound by proteins and filaments of the cytoskeleton, and thus are not a simple phospholipid bilayer (see [92, 93, 94]), the material parameters of the membrane were assigned values based approximately on measurements of unilaminar liposome vesicles. These measurements were also performed in [71]. The material coefficients corresponding to the compartments are summarized in Tab. 8.2 and are in accordance with measurements documented in scientific literature (see [69]).

**Table 8.2:** Debye coefficients of the underlying materials related to the specific cell components.

| Compartment | $\varepsilon_{r,s}$ | $\varepsilon_{r,\infty}$ | $f_0$ (GHz) | $\sigma_s$ (S/m) |
|---|---|---|---|---|
| **Cytoplasm (CP)** | 67 | 5 | 17.9 | 0.32 |
| **Plasma membrane (PM)** | 11.7 | 4 | 0.18 | $0.11 \cdot 10^{-6}$ |
| **Nucleoplasm (NP)** | 67 | 5 | 17.9 | 0.32 |
| **Nuclear Envelope (NE)** | 11.7 | 4 | 0.18 | $0.11 \cdot 10^{-6}$ |
| **Extracellular medium (EC)** | 67 | 5 | 17.9 | 0.55 |

The relative permittivity and the conductivity of these compartments are displayed in Figs. 8.2(a) and (b) respectively. The dispersive permittivities of the extracellular medium (EC), the cytoplasm (CP) and nucleoplasm (NP) are identical, as are those of the plasma

membrane (PM) and the nuclear envelope (NE). These spectral responses for the permittivities can be divided into three frequency intervals corresponding to the changes in the dielectric function of the material properties with frequency, i.e. the start and end of the roll-off of the two particular characteristic responses within the investigated range. These intervals are highlighted in shades of blue in Fig. 8.2(a). The conductivity of the compartments can also be divided into three intervals, partially overlapping those of the permittivity, highlighted in shades of red at the top of Fig. 8.2(b). The overlapping ranges of these intervals lead to further segmentation of the investigated spectrum into five frequency ranges highlighted in shades of beige which are enumerated by circled numbers in Fig. 8.2(a).

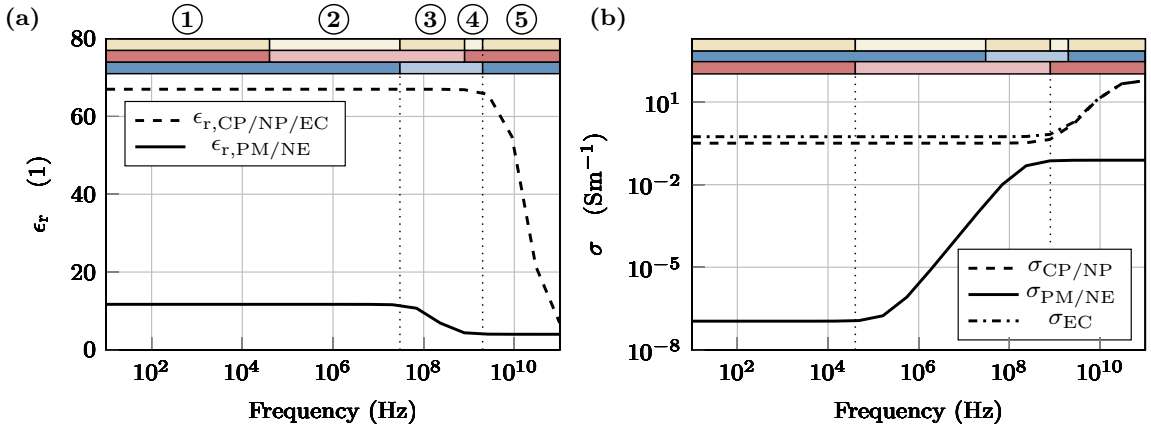


**Figure 8.2:** Overview of the dispersive material parameters: In (a), the relative permittivity of the cytoplasm (CP), nucleoplasm (NP) and the extracellular medium (EC) is represented as a dashed line, and that of the plasma membrane (PM) and the nuclear envelope (NE) as a solid line. In (b), the conductivity of the cytoplasm (CP) and nucleoplasm (NP) is represented as a dashed line, that of the plasma membrane (PM) and the nuclear envelope (NE) as a solid line, and that of the extracellular medium (EC) as a dash-dotted line. The bar displayed in shades of blue corresponds to changes in the spectral response of the relative permittivity while the bar displayed in shades of red corresponds to changes in the conductivity. The overlapping ranges of these intervals lead to further segmentation of the investigated spectrum into five frequency ranges highlighted in shades of beige which are enumerated by circled numbers.

To provide a better overview, these ranges are summarized in Tab. 8.3. As outlined above, the frequency ranges defined by changes in the dispersive material properties of the cell compartments and the extracellular medium will also be plotted in shades of beige above any further graph given in Sec. 8.2 and Sec. 8.3 to show any correspondence to changes in the effective material properties and microdosimetric measures under investigation. These ranges will be referred to as material ranges (MR) 1-5.

**Table 8.3:** Frequency sub-intervals (i.e. material ranges (MR)) corresponding to changes in the dispersive material parameters of the cell compartments and the extracellular medium displayed in Fig. 8.2 highlighted in shades of beige at the top of the graphs.

| | **MR 1** | **MR 2** | **MR 3** | **MR 4** | **MR 5** |
|---|---|---|---|---|---|
| $f$ | 10 Hz to 40 kHz | 40 kHz to 30 MHz | 30 – 800 MHz | 800 MHz to 2 GHz | 2 – 100 GHz |

### 8.1.3 Simulation Setup to Conduct Quasi-Static Electromagnetic Field Analysis

The three cell models displayed in Fig. 8.1(a)-(c) were placed in a virtual parallel plate capacitor setup to conduct a quasi-static EM analysis between 10 Hz and 100 GHz. This capacitor setup was implemented in the FEM-based software package COMSOL Multiphysics [95]. The computational domain containing the centered spherical cell is shown as an illustrative example in Fig. 8.3(a). This figure also shows the assignment of the dispersive material properties to the individual cell compartments. The edge length of the cube-shaped computational domain was 50 µm and was chosen to be large enough to minimize the influence of the depolarization fields around the cells on the neighboring cells. The resulting volume fraction of a cell in the computational domain was 1.15 % for the spherical cell and 4.12 % for the ellipsoidal ones. In the cross-section through the computational domain as shown in Fig. 8.3(b), a time-harmonic voltage with constant amplitude, $U_0 = \varphi_1 - \varphi_0$, was applied between two opposing outer boundaries of the domain that were designed to function as electrodes (i.e Dirichlet boundary conditions). $U_0$ was arbitrarily set to 1 V. The four remaining boundaries were defined with periodic boundary conditions (PBC) in order to suppress fringing fields and to reduce the memory resources of the subsequent quasi-static EM simulation. Due to this setup, the (computational) unit cell is effectively periodically extended in each direction indicated by the PBC. This approach was used in the past to investigate the effective material parameters of randomized (bio-)composites [96, 97], and single cells [15, 98]. A description of how these simulations are verified by mixing rules is given in Appendix A. In order to cope with the anisotropy of the (ellipsoidal) cells under investigation, the voltage $U_0$ is then applied in the other (orthogonal) directions by swapping the electrodes with the PBCs (and vice versa). The low volume fraction in combination with this setup (i.e., the electrodes and PBCs) allows the interpretation of the cell under investigation either as a representative of a cell suspension corresponding to the static mean [69], or as a specific single cell [79, 99].

In order to avoid high aspect ratios in the modeling mesh, the plasma membrane and the membranes of the cell organelles are modeled by a set of equations taking into account

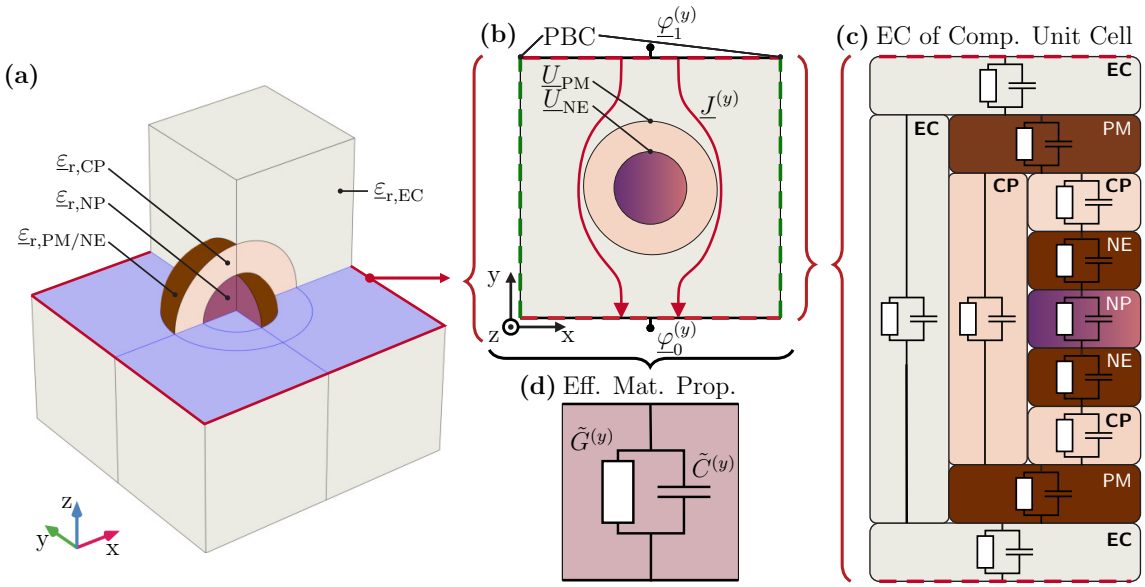


**Figure 8.3:** Overview of the virtual capacitor experiment used for the quasi-static EM analysis of the computational domain: (a) Computational domain containing the spherical cell model as an illustrative example showing the assignment of the dispersive material properties introduced in Sec. 8.1.2 to the individual cell compartments. (b) Cross-section through the computational domain. The voltage, $U_0 = \varphi_1 - \varphi_0$, was applied to two opposing sides of the virtual capacitor set up which were designed to function as electrodes. Periodic boundary conditions (PBC) were applied to the remaining sides of the computational domain. This set up can be interpreted as a spatially periodic (computational) unit cell. To determine the voltages induced across both the plasma membrane, $\underline{U}_{PM}$, and the nuclear envelope, $\underline{U}_{NE}$, their values were monitored at the closest points of the membranes facing the electrodes. (c) Equivalent circuit representation of the computational domain illustrating all the possible circuit paths summarized by RC shunt impedances. Using this equivalent circuit model, it is possible to make qualitative statements about how changes in the geometry of the cell affect the shunt elements in the individual current paths. In combination with the material ranges introduced in Sec. 8.1.2, the conceptual perception of the computational domain as an electrical network allows the qualitative separation and distinction of the influence of dispersive material properties and changes in the geometric structure of the cell. A detailed description of this concept is given in Sec. 8.2.1. The capitals in each circuit path correspond to the individual compartments of the unit cell which are the extracellular medium (EC), and those within the cell, namely, the plasma membrane (PM), the cytoplasm (CP), the nuclear envelope (NE) and the nucleoplasm (NP). (d) Numerical homogenization summarizing the computational domain as an overall shunt impedance allowing the calculation of its effective macroscopic material parameters as outlined in Sec. 8.2.1.

the conduction and the displacement current

$$\vec{n} \cdot \underline{\vec{J}}_{up} = \frac{1}{t_M}(\sigma_M + j\omega\varepsilon_0\varepsilon_{r,M})(\underline{\varphi}_{up} - \underline{\varphi}_{down}) \tag{8.2}$$

$$\vec{n} \cdot \underline{\vec{J}}_{down} = \frac{1}{t_M}(\sigma_M + j\omega\varepsilon_0\varepsilon_{r,M})(\underline{\varphi}_{down} - \underline{\varphi}_{up}) \tag{8.3}$$

where $\underline{\varphi}_{\text{up/down}}$ and $\vec{n} \cdot \underline{\vec{J}}_{\text{up/down}}$ denote the membrane potentials and current densities normal to the upper and lower surfaces of the membrane. $t_{\text{M}}$ represents the thickness of the membrane while $\sigma_{\text{M}}$ and $\varepsilon_{\text{r,M}}$ represent the conductivity and the relative permittivity of the membrane respectively. $\varepsilon_0$ denotes the vacuum permittivity. Referring to Eqs. 8.2 and 8.3, thin membranes can now be represented by these tailored boundary conditions yielding a highly economic treatment as already proposed in [45].

The simulation was performed on a PC equipped with two Intel Xeon E5-2697 V4 processors (36 cores) and 512 GB of memory. In the conducted investigations, a frequency range between 10 Hz and 100 GHz was investigated and sampled with 50 frequency points distributed logarithmically. The data points in between these sampled points were interpolated using piecewise cubic Hermite splines in post-processing. The simulation for each frequency point lasted approximately 30 min using a MUMPS solver. The post-processing of the data was performed within the MATLAB programming environment (version R2020a) [100].

## 8.2 The Necessity to Consider Membranes in Cell Modeling using the Simple Spherical Cell Model

The field distribution within the spherical cell model (see Fig. 8.3(a)) is studied in order to investigate whether cell membranes must be considered over the entire investigated frequency range (i.e. 10 Hz to 100 GHz) or whether they may be neglected since their capacitive nature causes them to be bypassed at high frequencies. In these investigations, two aspects are of primary interest: (1) The electric potential and the resulting losses occurring at both the plasma membrane and the nuclear envelope under the application of an electric field and (2) the effect of these membranes on the effective material properties of the simulated cell (suspension). In the following, the methodology of this numerical study and the variables involved are explained (Sec. 8.2.1). The results are then presented (Sec. 8.2.2).

### 8.2.1 Methodology

The first aspect is addressed by adopting the methodological approaches presented in [16, 62], where the induced potential difference across the plasma membrane, $\underline{U}_{\text{PM}}$, and that across the nuclear envelope, $\underline{U}_{\text{NE}}$, were monitored as shown in Fig. 8.3(b). The volumetric loss densities corresponding to the induced membrane voltages can be calculated using $p_i = \sigma_i \cdot (U_i / t_i)^2$, expressed in W/m$^3$, where $t_i$ and $\sigma_i$ represents the thickness and conductivity of the membrane, respectively, and the index $i \in \{\text{PM}, \text{NE}\}$ denotes either the plasma membrane or the nuclear envelope. However, the arbitrary choice of the voltage applied to the computational domain, $U_0$, means that it is relative rather than absolute values that are significant. The relative values are calculated for the membrane voltages,

$U_i$, by normalizing to $U_0$ and for the loss densities, $p_i$, by normalizing to the maximum observed loss density, $p_{\max}$. $p_{\max} = \max\big(\max_f p_{PM}(f), \max_f p_{NE}(f)\big)$ and is defined as the maximum loss density detected over the investigated frequency interval at either the plasma membrane or the nuclear envelope.

Moving on to the second aspect requiring consideration, the effective material parameters of the cell (suspension) were determined using the virtual capacitor experiment as depicted in Fig. 8.3(d). The time-harmonic quasi-static EM analysis in the form of the capacitor setup presented in Sec. 8.1.3 leads to an effective admittance that is represented by an equivalent electrical parallel circuit consisting of the elements $\tilde{G}(\omega)$ and $\tilde{C}(\omega)$. This is given by

$$\underline{\tilde{Y}}(\omega) = \frac{\underline{I}(\omega)}{\underline{U}_0} = \tilde{G}(\omega) + \mathrm{j}\omega\tilde{C}(\omega) \tag{8.4}$$

where the applied voltage, $\underline{U}_0$, and the resulting current, $\underline{I}(\omega)$, are directly accessible via COMSOL Multiphysics for an angular frequency $\omega = 2\pi f$. The dispersive effective material properties, $\tilde{\varepsilon}_\mathrm{r}(\omega)$ and $\tilde{\sigma}(\omega)$, are thus easily deduced according to

$$\underline{\tilde{Y}}(\omega) \cdot \frac{d}{A} = \frac{\underline{I}(\omega)}{\underline{U}_0} \cdot \frac{d}{A} = \underbrace{\tilde{\sigma}(\omega) + \mathrm{j}\omega\varepsilon_0\tilde{\varepsilon}_\mathrm{r}(\omega)}_{\underline{\tilde{\sigma}}(\omega)} \tag{8.5}$$

where $d$ is the parallel plate distance and $A$ is the area of the electrode. In Eq. 8.5, the right-hand term can be interpreted as the complex effective conductivity of the homogenized effective material, $\underline{\tilde{\sigma}}(\omega)$, from which the required material parameters directly follow:

$$\tilde{\sigma}(\omega) = \mathrm{Re}\{\underline{\tilde{\sigma}}(\omega)\} \tag{8.6}$$

$$\tilde{\varepsilon}_\mathrm{r}(\omega) = \frac{\mathrm{Im}\{\underline{\tilde{\sigma}}(\omega)\}}{\omega\varepsilon_0} \tag{8.7}$$

In order to consider anisotropies in the effective material, the quasi-static capacitor analysis is performed with excitation in the x, y and z directions yielding corresponding frequency-dependent second-rank tensors for the effective conductivity,

$$\overleftrightarrow{\tilde{\sigma}}(\omega) = \begin{pmatrix} \tilde{\sigma}_\mathrm{x}(\omega) & 0 & 0 \\ 0 & \tilde{\sigma}_\mathrm{y}(\omega) & 0 \\ 0 & 0 & \tilde{\sigma}_\mathrm{z}(\omega) \end{pmatrix} \tag{8.8}$$

and

$$\overleftrightarrow{\tilde{\varepsilon}}_\mathrm{r}(\omega) = \begin{pmatrix} \tilde{\varepsilon}_{\mathrm{r,x}}(\omega) & 0 & 0 \\ 0 & \tilde{\varepsilon}_{\mathrm{r,y}}(\omega) & 0 \\ 0 & 0 & \tilde{\varepsilon}_{\mathrm{r,z}}(\omega) \end{pmatrix}. \tag{8.9}$$

As originally discussed in Sec. 8.1.1, the numerical quantities addressing both aspect one and aspect two will be investigated in the context of a parameter analysis that varies the diameter of the nucleus so that the share of the cell volume, $c_N$, covers 0.3 to 0.9. The simple geometry of the spherical cell model allows the results of the numerical investigations carried out here to be compared with those published in [16, 61, 62, 69]. In this way, the comparison with the analytical results of the above-mentioned references provides a verification of the computational model that has been implemented.

The addition of variable geometry, represented by $c_N$, along with the dispersive material properties of the individual cell compartments, requires more comprehensive analysis compared to the previously cited studies, which only considered constant material parameters. This analysis is needed to identify variations in cell geometry (i.e. in $c_N$), rather than the dispersive material properties of the individual cell components, as being the cause of dispersive characteristics in the spectral analysis of the effects under investigation. Given this requirement, the methodologies adopted from the cited studies need to be conceptually extended by considering the computational domain as an electrical network. An example of this is shown in Fig. 8.3(c) where an equivalent circuit model of the simple spherical cell is given in which all the possible current paths are summarized by RC shunt impedances. The abbreviations EC, PM, CP, NE and NP denote the extracellular medium, the plasma membrane, the cytoplasm, the nuclear envelope, and the nucleoplasm respectively. Using this equivalent circuit model in Subsec. 8.2.2.1, it is possible to make qualitative statements about how changes in the geometry of the cell effect the shunt elements in the individual current paths. Increasing the nuclear radius, for example, results in a lower shunt conductance in the cytoplasmic pathway. These considerations, in combination with the material ranges (MR) defined in the previous subsection, provide a framework to qualitatively separate and distinguish the influence of dispersive material properties and changes in the geometric structure of the cell. In practice, this is performed by plotting the material ranges above the spectral responses of each quantity under investigation. The ranges then allow the changes in the underlying material properties to be related to changes in the dispersive characteristics being observed. The implementation of this concept can be seen in all of the illustrations shown in the following results section.

## 8.2.2 Results

The investigations to determine the need for membrane modeling are presented below. As described in the previous section, this is done in two steps: In a first step, discussed in Sec. 8.2.2.1, the induced membrane voltages and the resulting losses occurring at both the plasma membrane and the nuclear envelope are studied in the context of a parameter analysis varying the diameter of the nucleus ($c_N \in [0.3, 0.9]$) along with a broadband frequency analysis taking into account the dispersive material properties. In a second step, the effect of cell membranes on the effective macroscopic permittivities of the capacitor setup is discussed in Sec. 8.2.2.2, also in the context of the same parameter analysis. The

frequency ranges corresponding to changes in the underlying material properties (i.e., material ranges) are plotted above the spectral responses of each quantity under investigation and help to attribute observed effects either to changes in the material parameters or to effects caused by the geometric composition of the cell model.

#### 8.2.2.1 Induced Membrane Voltage and the Resulting Losses Occurring at both the Plasma Membrane and the Nuclear Envelope

In Fig. 8.4(a), the induced membrane voltages normalized to the voltage applied to the computational domain, $U_0$, can be observed. The blue curves correspond to the voltage monitored at the plasma membrane, $U_{\mathrm{PM}}$, and the red curves correspond to the voltage monitored at the nuclear envelope, $U_{\mathrm{NE}}$, (see. Fig. 8.3(b)). The dashed, solid, and dashed-dotted lines show the results of cell models with a volume fraction of the nucleus in the cell of $c_{\mathrm{N}} = 0.3$, $c_{\mathrm{N}} = 0.6$, and $c_{\mathrm{N}} = 0.9$, respectively.

In general, $U_{\mathrm{PM}}$ shows low-pass behavior and $U_{\mathrm{NE}}$ shows bandpass behavior. The parameter analysis leads to the identification of two effects on the induced membrane voltage: (1) The larger the nuclear radius, the lower the frequency at which the transitions to low-pass behavior across the plasma membrane can be observed. (2) Correspondingly, bandpass behavior also shifts to lower frequencies while also demonstrating higher induced voltages at the nuclear envelope. The range of observed membrane voltages corresponding to the $c_{\mathrm{N}}$ values under investigation is confined by the dotted (i.e., $c_{\mathrm{cell}} = 0.3$) and dashed-dotted (i.e., $c_{\mathrm{cell}} = 0.9$) lines and highlighted by the gray-shaded areas in between.

To separate the influence of dispersive material properties from that of changes in cell geometry, the observed effects on membrane voltages are evaluated with respect to the material ranges (MR) represented by the beige bars above Fig. 8.4(a). The initial changes in the response of the membrane voltages induced at both the nuclear envelope and the plasma membrane occur in MR 1 and thus, are not caused by any change in the underlying material parameters. Consequently, the shift of the onset of the observed effects can be explained by the geometrical composition of the cell model. Considering the equivalent circuit model of the computational domain in Fig. 8.3(c), two parallel paths exist within the cell, one leading through the nucleus and one bypassing it. In the case of a larger nucleus, the cross-sectional area of the bypassing cytoplasm path is reduced resulting in lower conductance. This, in turn, leads to a higher impedance of the whole cell interior (i.e. cytoplasm and nucleus path) causing an significant increase of the induced membrane voltage at the nuclear envelope at lower frequencies. At frequencies larger than 5 MHz in MR 2, the conductivity of the membrane increases and reduces the difference between the impedances of the circuit passing through the nucleus and the one bypassing it. As a result, the voltages $U_{\mathrm{PM}}$ and $U_{\mathrm{NE}}$ of the different model variants, indexed by the individual volume fractions, $c_{\mathrm{N}}$, begin to align and seem to converge to a single curve again.

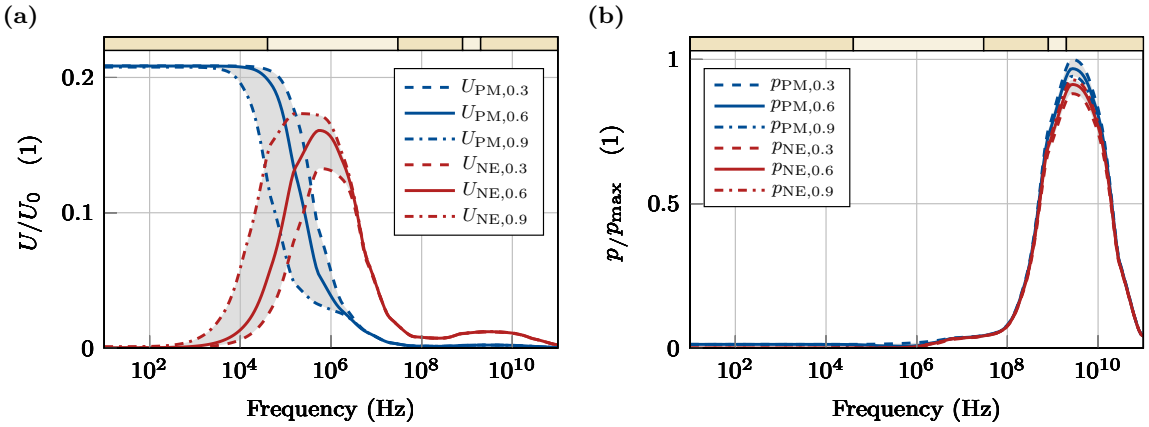


**Figure 8.4:** (a) Overview of the induced membrane voltages normalized to the voltage applied to the computational domain, $U_0$, and (b) the volumetric loss density normalized to the maximum observed volumetric density, $p_{max}$. The blue curves show these measures at the plasma membrane (PM), the red ones at the nuclear envelope (NE). The dashed, solid, and dashed-dotted lines show the results of cell models with a volume fraction of the nucleus in the cell of $c_N = 0.3$, $c_N = 0.6$, and $c_N = 0.9$, respectively.

The volumetric loss density normalized to $p_{max}$ is displayed in Fig. 8.4(b). The blue curves correspond to the loss densities at the plasma membrane, $p_{PM}$, and the red curves correspond to the corresponding position on the nuclear envelope, $p_{NE}$,. The dashed, solid, and dashed-dotted lines show the results of cell models with a volume fraction of the nucleus in the cell of $c_N = 0.3$, $c_N = 0.6$, and $c_N = 0.9$, respectively.

Here it can be observed that for frequencies lower than 1 MHz, the volumetric loss density is relatively low compared to that at larger frequencies. This can be explained by the low conductivity of the membrane resulting in a barrier for every current penetrating it. For larger frequencies, the loss densities in both the plasma membrane and the nuclear envelope increase strongly, reaching a global maximum between 1 GHz and 10 GHz. This increase is initiated due to the decreasing relative permittivity of the membranes in MR 3. The rapid decrease of the volumetric loss density after reaching the maximum is initiated by the decrease of the permittivity of the cytoplasm and the nucleoplasm in MR 5. In contrast to the observed effects on the induced membrane voltages, the size of the nucleus has only little influence on the volumetric loss density. This is illustrated by the range of observed values confined by the dotted (i.e., $c_{cell} = 0.3$) and dashed (i.e., $c_{cell} = 0.9$) lines and highlighted by the gray-shaded areas in between.

#### 8.2.2.2 The Effect of Cell Membranes on the Effective Material Parameters of the Spherical Cell Model

The effective material parameters of the simulated cell (suspension) are illustrated in Figs. 8.5(a) and (b), showing the relative permittivity and the conductivity respectively.

The dashed, solid, and dashed-dotted lines show the results of cell models with a volume fraction of the nucleus in the cell of $c_N = 0.3$, $c_N = 0.6$, and $c_N = 0.9$, respectively.

The effective permittivity depicted in Fig. 8.5(a) clearly displays a range of values between 10 kHz and 1 MHz for the various models under investigation. It can be seen that the cell model with the larger nucleus leads to a reduced ability to accumulate charges, due to the previously discussed shift of the induced membrane voltages within the cell, especially at the plasma membrane. The size of the nucleus thus leads to a lowering of the characteristic frequency of the interfacial polarization. Due to the high conductivity of the extracellular medium, no variations within the effective conductivity of the suspension can be observed.

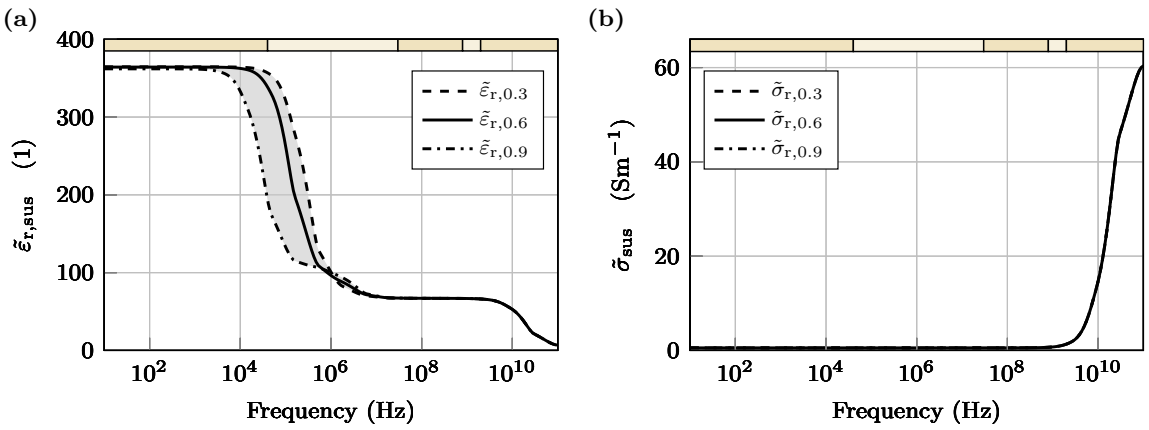


**Figure 8.5:** Overview of the effective macroscopic material properties: (a) Effective relative permittivity and (b) effective conductivity for volume fractions of the nucleus in the cell of $c_N = 0.3$, $c_N = 0.6$, and $c_N = 0.9$, respectively.

The cell models investigated were compared to analytical models based on mixing rules. The comparison showed maximum relative errors of < 0.5 % for both conductivity and permittivity over the entire interval. The calculation rules for verification can be found in Appendix A.

## 8.3 The Influence of Organelles on the Field Distribution in the Interior of Eukaryotic Cells

In the following, the implications of considering membrane-enclosed organelles in cell modeling will be discussed in terms of two aspects: (1) the influence of internal organelles on the field distribution within a cell (i.e., microdosimetry), and (2) the effect of this influence on the effective material properties of the simulated cell (suspension). The methodology for performing these effects is first outlined in Sec. 8.3.1. The results of the outlined investigations are then presented in Sec. 8.3.2.

### 8.3.1 Methodology

In order to investigate the influence of organelles enclosed by a membrane, the field distribution within the cell in both ellipsoidal models is studied. In these investigations, two aspects are of primary interest: (1) The absolute field distribution within the cell model with an ER and (2) the differences in the field distribution comparing the models with and without an ER. Both aspects will be addressed in a threefold analysis. First, the field distribution of current and volumetric loss density within the ellipsoidal cell models will be graphically analyzed in the symmetry plane which is parallel to the electrodes. After that, spatial minima and maxima will be determined and analyzed in the investigated frequency range (10 Hz to 100 GHz). Finally, the fields will be integrated using the spatial segmentation introduced earlier providing an overview of the currents flowing through and losses occurring within the cell models.

In order to introduce this field analysis in detail, the distribution of the absolute magnitude of the current density, $|\underline{\vec{J}}|$, in A/m$^2$ and the volumetric loss density, $p$, in W/m$^3$ are plotted in Fig. 8.6(b) for the cell models with and without and an ER. As illustrated in Fig. 8.6(a), the field distributions of both quantities are displayed in the XZ plane under application of the voltage $U_0$ in the y-direction at 10 Hz. According to the color scale on the right of Fig. 8.6(b), red areas indicate maximum values and light areas indicate minimum values.

Considering $|\underline{\vec{J}}|$ and $p$ as a function of space, $\vec{r}$, and frequency, $f$, the comparison of the field distributions of both ellipsoidal models yields the relative spatial differences of the current density, $\Delta J$, and the volumetric loss density, $\Delta p$, which are shown in Fig. 8.6(c) and defined as follows:

$$\Delta J(\vec{r},f) = \frac{|\underline{\vec{J}}(\vec{r},f)|_{\mathrm{ER}} - |\underline{\vec{J}}(\vec{r},f)|_{\mathrm{EC}}}{\left\langle |\underline{\vec{J}}(\vec{r},f)| \right\rangle_{\mathrm{ER}}} \tag{8.10}$$

$$\Delta p(\vec{r},f) = \frac{|p(\vec{r},f)|_{\mathrm{ER}} - |p(\vec{r},f)|_{\mathrm{EC}}}{\left\langle |p(\vec{r},f)| \right\rangle_{\mathrm{ER}}} \tag{8.11}$$

The indices ER and EC denote the endoplasmic reticulum and the ellipsoidal cell without endoplasmic reticulum respectively, and $\left\langle |\underline{\vec{J}}(\vec{r},f)| \right\rangle_{\mathrm{ER}}$ and $\left\langle |p(\vec{r},f)| \right\rangle_{\mathrm{ER}}$ are the spatial averages within the whole cell with an ER. Thus, $\Delta J$ and $\Delta p$ represent the spatial differences within the cell models normalized to the spatial average as a function of frequency and position. This is graphically illustrated by the red boxes around the column headers and the signs between them in Fig. 8.6. From the field plots shown in Fig. 8.6(b), it can be seen that some regions within the cell model with an ER have higher current and volumetric loss densities than the same regions in the cell model without an ER, and vice versa. Therefore, the visualization of these differences is adjusted by using a symmetrized color scale in Fig. 8.6(c). According to the numerator terms in Eqs. 8.10 and 8.11, the red (positive) and blue (negative) areas in Fig. 8.6(c) can be interpreted as follows. In the red areas, the model with an ER has field strengths that are higher than those of the model

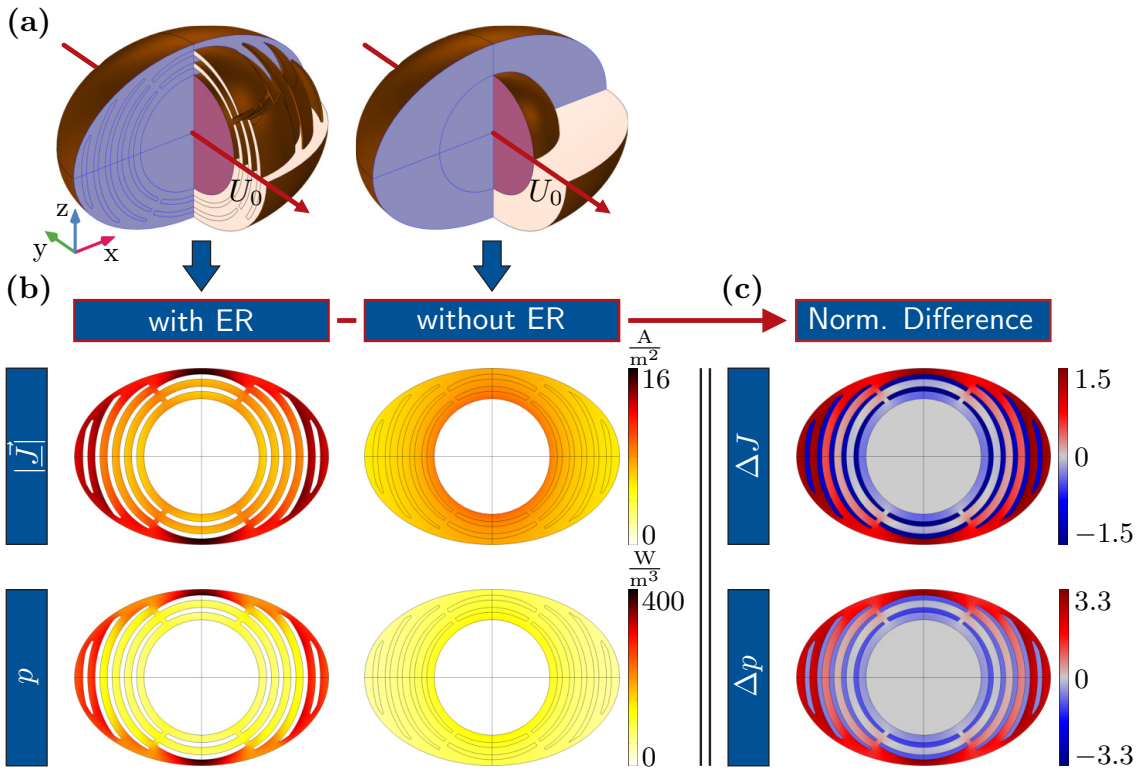


**Figure 8.6:** Illustrative example of the stages of the field analysis using the ellipsoidal models at 10 Hz: (a) Ellipsoidal cell models highlighting the plane of investigation (XZ plane) in blue. The red arrows passing through both ellipsoidal cell models indicate an applied voltage $U_0$ in the y-direction. (b) The current density, $|\vec{J}|$, and the volumetric loss density distribution, $p$, are displayed in the XZ plane at 10 Hz. Maximum values are indicated by red areas and minimum values by light areas. The field plots can be observed while applying a voltage in the y-direction. (c) The distribution of the differences in current density, $\Delta J$, and the volumetric loss density, $\Delta p$, displayed in the XZ plane at 10 Hz. $\Delta J$ and $\Delta p$ are defined as formulated in Eqs. 8.10 and 8.11. Maximum values are indicated by red areas and minimum values by blue areas. The field plots can be observed while applying a voltage in the y-direction.

without an ER, and in the blue areas, the model with an ER has field strengths that are lower than those of the model without an ER. This graphical evaluation shows in which areas the field magnitudes are overestimated or underestimated in a model without organelles. Grey regions indicate areas where there are no, or only very small, differences between the models with and without an ER.

Moving away from this illustrative example investigating a single frequency towards the general broadband investigation conducted in this study, it is necessary to interrelate and quantitatively compare the spatial minimum and maximum field values over the entire spectrum. For the current density, $|\vec{J}|$, and the volumetric loss density, $p$, this is done by determining the spatial minimum and maximum values of $J_{\mathrm{min/max}}$ and $p_{\mathrm{min/max}}$ over

the entire frequency range investigated:

$$J_{\min/\max}(f) = \begin{cases} \min\limits_{\vec{r}} |\underline{\vec{J}}(f,\vec{r})| \\ \max\limits_{\vec{r}} |\underline{\vec{J}}(f,\vec{r})| \end{cases} \tag{8.12}$$

$$p_{\min/\max}(f) = \begin{cases} \min\limits_{\vec{r}} p(f,\vec{r}) \\ \max\limits_{\vec{r}} p(f,\vec{r}) \end{cases} \tag{8.13}$$

However, due to the arbitrary choice of the voltage $U_0$, only relative values are of significance, and thus, $J_{\min/\max}$ and $p_{\min/\max}$ need to be normalized to the global maxima observed in the entire frequency range. Defining $J_{\text{abs,max}}$ and $p_{\text{abs,max}}$ as

$$J_{\text{abs,max}} = \max_{f} J_{\max}(f) \tag{8.14}$$

and

$$p_{\text{abs,max}} = \max_{f} p_{\max}(f) \tag{8.15}$$

the normalized logarithmic amplitude ratios

$$J_{\text{n}} = 20\ \log_{10}\left(\frac{J_{\min/\max}(f)}{J_{\text{abs,max}}(f)}\right) \tag{8.16}$$

and

$$p_{\text{n}} = 10\ \log_{10}\left(\frac{p_{\min/\max}(f)}{p_{\text{abs,max}}(f)}\right) \tag{8.17}$$

can be calculated and used for spectral analysis. In contrast, for the spatial differences of the current density, $\Delta J$, and the loss density, $\Delta p$, a spectral analysis can be easily performed by determining the respective minima and maxima over the frequency range:

$$\Delta J_{\min/\max}(f) = \begin{cases} \min\limits_{\vec{r}} \Delta J(f,\vec{r}) \\ \max\limits_{\vec{r}} \Delta J(f,\vec{r}) \end{cases} \tag{8.18}$$

$$\Delta p_{\min/\max}(f) = \begin{cases} \min\limits_{\vec{r}} \Delta p(f,\vec{r}) \\ \max\limits_{\vec{r}} \Delta p(f,\vec{r}) \end{cases}. \tag{8.19}$$

This is possible since $\Delta J$ and $\Delta p$ represent comparative quantities between two models which are already normalized to the spatial average of the respective quantities occurring in the ellipsoidal cell model with an ER. To complete the threefold analysis, the focus

now turns to the relative current and loss distributions within the cell rather than the spatial distributions of current and volumetric loss densities. These relative quantities are defined as

$$\frac{I_i}{I_{\text{cell}}} \tag{8.20}$$

and

$$\frac{P_i}{P_{\text{cell}}} \tag{8.21}$$

where $i \in \{\text{CP};\text{NP};\text{ER}\}$ denotes the cytoplasm, nucleoplasm or endoplasmic reticulum. The currents in each compartment,

$$I_i(f) = \iint_{A_i} \underline{\vec{J}}(f,\vec{r}) \cdot \vec{n}\, dA_i \tag{8.22}$$

are obtained by integrating the current densities in the sectional planes of the cell under investigation (see. Fig. 8.1(g)-(i)) over the surface area of each compartment (see. Fig. 8.1(j)-(k)) with $\vec{n} \in \{\vec{e}_x, \vec{e}_y, \vec{e}_z\}$. Correspondingly, the losses in each compartment,

$$P_i(f) = \iiint_{V_i} \vec{p}(f,\vec{r}) \cdot \vec{n}\, dV_i \tag{8.23}$$

are obtained by integrating the loss densities over the volume of the individual compartments (see Fig. 8.1(d)-(f)). The cell currents and cell losses are defined as

$$I_{\text{cell}}(f) = I_{\text{CP}}(f) + I_{\text{NP}}(f) + I_{\text{ER}}(f) \tag{8.24}$$

$$P_{\text{cell}}(f) = P_{\text{CP}}(f) + P_{\text{NP}}(f) + P_{\text{ER}}(f) \tag{8.25}$$

In addition to the microdosimetric analysis presented above, the effect of a modeled ER on the effective macroscopic material properties will be assessed by applying the approach outlined in Sec. 8.2.1.

### 8.3.2 Results

As introduced in the previous subsection (i.e., Sec. 8.3.1), the influence of organelles enclosed by a membrane on the field distribution inside the cell is investigated by applying the the threefold analysis given above, which covers the graphical evaluation of field distributions, the quantification of spatial minima and maxima in the observed field values, and the determination of integral EM measures within the individual cell compartments using spatial segmentation. The investigation begins with an analysis of the absolute magnitude of the current density, $|\underline{\vec{J}}|$, and volumetric loss density, $p$, throughout the interior of the ellipsoidal cell model with an ER in Sec. 8.3.2.1. Subsequently, the field distribution within the model with an ER is compared with that of the ellipsoidal cell model without an ER, focusing on the resulting differences that would arise in the modeling process if the cell interior were (over)simplified in Sec. 8.3.2.2. Finally, the effect of

an internal distributed membrane system on the effective macroscopic permittivities of the cell is evaluated in Sec. 8.3.2.3.

### 8.3.2.1 Field Analysis of the Ellipsoidal Cell Model with an Endoplasmic Reticulum

An overview of the field analysis investigating the influence of organelles enclosed by a membrane to the field distribution of the cell interior is provided by Fig. 8.7. In Fig. 8.7(a), the current density, $|\vec{J}|$, and the volumetric loss distribution, $p$, are displayed in the XZ plane at different frequencies. Maximum values in each plot are indicated by red areas and minimum values by light areas. The field plots show data under the application of a voltage in the y-direction. To interrelate and quantitatively assess the minimum and maximum values of the color scale in the field plots in Fig. 8.7(a), $J_{\mathrm{n,min/max}}$ and $p_{\mathrm{n,min/max}}$ are displayed in Figs. 8.7(b) and (c) respectively.

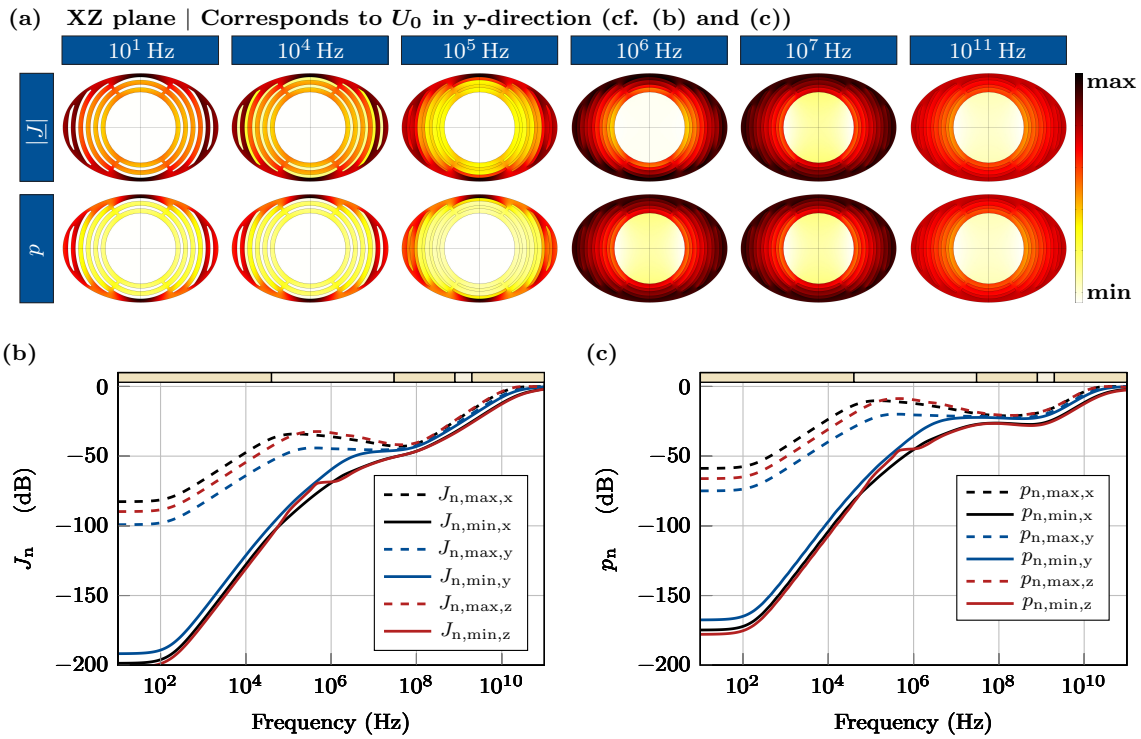


**Figure 8.7:** Overview of the field analysis investigating the influence of organelles enclosed by a membrane on the field distribution of the cell interior: (a) The current density, $|\vec{J}|$, and the loss distribution, $p$, are displayed in the XZ plane at different frequencies. Maximum values are indicated by red areas and minimum values by light areas. The field plots can be observed while applying a voltage in the y-direction. (b)-(c). Quantitative assessment of the minimum and maximum values of both $J_{\mathrm{n}}$ (see. Eq. 8.16) and the $p_{\mathrm{n}}$ (see. Eq. 8.17) plotted on a logarithmic scale. The indices in the legend, x, y and z, denote the direction of the voltage applied in the capacitor experiment.

In Fig. 8.7(a), it can be seen that the cisternal organelle structures, which are concentrated around the nucleus, cause a heterogeneous field distribution in the cytoplasm. The layered structure of the membranes of the ER around the nucleus throughout the CP means that the current entering the cell is primarily conducted via the outer cell edge and the current and volumetric loss densities around and in the nucleus are comparatively low, especially at low frequencies. At a frequency of 10 Hz for example, it can be seen that almost no current flows or losses occur in the ER or the nucleus. However, these compartments become increasingly penetrable as the frequency increases. At frequencies of 10 MHz and above, a current distribution is established within the cell that corresponds approximately to the area of the respective compartments on the (cross-)sectional plane of the cell. In Fig. 8.7(b), it can be observed that the maximum current density at 10 Hz is about 10 dB smaller than at 100 GHz. The reason for this is the high conductivity of the extracellular medium and the low conductivity of the plasma membrane. Roughly speaking, the current density within the cell increases strongly between 100 Hz and 1 MHz. Furthermore, the difference between the minimum and maximum current density decreases from about 90 dB to < 1.5 dB. For frequencies larger than 1 MHz, the current density increases further and reaches a plateau around 100 GHz. To summarize, it can be noted that low cell currents with high relative current density differences occur at frequencies < 1 MHz while high currents with lower differences are observed at frequencies > 1 MHz. These statements can also be made for the volumetric loss density shown in Fig. 8.7(c).

**Table 8.4:** Overview of the normalized minimum and maximum current and loss densities in the frequency interval between 1 GHz and 100 GHz.

| **Current Density** | | | | |
|---|---|---|---|---|
| **Frequency (GHz)** | $J_{\mathrm{n,min,y}}$ | $J_{\mathrm{n,max,y}}$ | $J_{\mathrm{n,min,y}} - J_{\mathrm{n,max,y}}$ | $J_{\mathrm{max,y}}/J_{\mathrm{min,y}}$ |
| 100 | -0.182 | -0 | -0.182 | 1.016 |
| 50 | -1.012 | -0.87 | -0.142 | 1.021 |
| 10 | -7.908 | -6.74 | -1.168 | 1.144 |
| 1 | -26.9 | -25.63 | -1.27 | 1.157 |
| **Volumetric Loss Density** | | | | |
| **Frequency (GHz)** | $p_{\mathrm{n,min,y}}$ | $p_{\mathrm{n,max,y}}$ | $p_{\mathrm{n,min,y}} - p_{\mathrm{n,max,y}}$ | $p_{\mathrm{max,y}}/p_{\mathrm{min,y}}$ |
| 100 | -0.182 | -0 | -0.182 | 1.043 |
| 50 | -0.679 | -0.364 | -0.313 | 1.075 |
| 10 | -7.15 | -5.987 | -1.163 | 1.303 |
| 1 | -21.897 | -20.618 | -1.279 | 1.342 |

Tab. 8.4 provides an overview of the normalized minimum and maximum current and volumetric loss densities in the frequency interval between 1 GHz and 100 GHz. It is worth noting that the ratio between the maximum and minimum current density is between 1.016 and 1.157 and that of the volumetric loss density between 1.043 and 1.342, and thus, a non-negligible difference between currents and losses in the outer edge of the cell interior and the nucleus exists, even at such high frequencies.

To be concise, a comprehensive field analysis of the cell model without an ER is omitted, since this information is inherently contained within the comparative field analysis between the two ellipsoidal models presented in the following subsection.

#### 8.3.2.2 Comparative Field Analysis of the Ellipsoidal Cell Models with and without an Endoplasmic Reticulum

An overview of the comparative field analysis investigating the influence of organelles enclosed by a membrane to the field distribution of the cell interior is provided by Fig. 8.8. Here, the emphasis is to contrast the differences in the field distribution when modeling the cell with and without an ER. In Fig. 8.8(a), the distribution of the differences in the current density, $\Delta J$, and the volumetric loss density, $\Delta p$, is displayed in the XZ plane at different frequencies. $\Delta J$ and $\Delta p$ are defined as formulated in Eqs. 8.10 and 8.11 in Sec. 8.3.1. Maximum values in each plot are indicated by red areas and minimum values by blue areas. The field plots show data under the application of a voltage in the y-direction. To interrelate and quantitatively assess the minimum and maximum values of the color scale in the field plots in Fig. 8.8(a), $\Delta J_{\mathrm{min/max}}$ and $\Delta p_{\mathrm{min/max}}$ are displayed in Figs. 8.8(b) and (c) respectively.

Observing the field distribution of $\Delta J$ and $\Delta p$ at low frequencies ($\leq 10\,\mathrm{kHz}$) in Fig. 8.8(a), it can be seen that an ER enclosed by a membrane has a large influence on the current and volumetric loss density, as these regions are electrically shielded. At frequencies larger than 10 kHz and less than 10 MHz, it becomes very clear that although shielding provided by the ER is not absolute, the current distribution is changed in such a way that currents are mainly conducted at the outer edge of the cell compared to the model without ER. In particular, the field images at 1 MHz show that the cascade-like concentric layering of the ER around the nucleus leads to its electrical shielding, thus, the ellipsoidal cell model without an ER overestimates the current flowing through or around the nucleus. Looking at the spectral responses of the minimum and maximum values of $\Delta J_{\mathrm{min/max}}$ and $\Delta p_{\mathrm{min/max}}$ illustrated in Figs. 8.8(b) and (c) respectively, it can be seen that the differences between the current and loss densities in both models are relatively low for frequencies $> 10\,\mathrm{MHz}$ in the entire cell space.

Shifting attention from the analysis of the current and volumetric loss density distribution performed previously, the relative current and loss distribution within both cell models will now be analyzed using the integral quantities defined in Sec. 8.3.1 (see Eqs. 8.20 to 8.25). In Fig. 8.9, the differences between the relative currents and losses in the individual cell compartments are contrasted in both ellipsoidal cell models. The currents and losses in the model with an ER are displayed in Fig. 8.9(a) and (c) respectively, while Fig. 8.9(b) and (d) display these quantities in the model without an ER. In the legends, the indices CP, NP and ER denote the cytoplasm, nucleoplasm and endoplasmic reticulum and x, y and z, denote the direction of the voltage applied in the capacitor experiment.

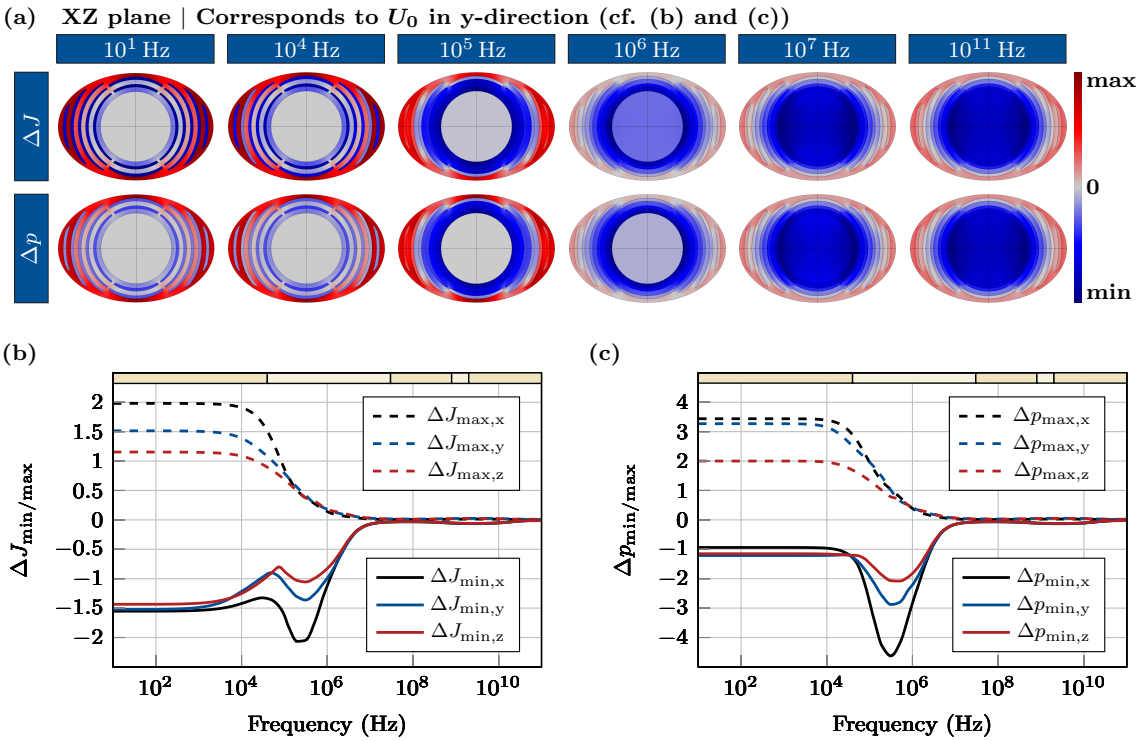


**Figure 8.8:** Overview of the comparative field analysis investigating the influence of organelles enclosed by a membrane to the field distribution of the cell interior contrasting the differences occurring when modeling the cell with or without an ER: (a) The distribution of the differences in the current density, $\Delta J$, and the volumetric loss density, $\Delta p$, displayed in the XZ plane at different frequencies. $\Delta J$ and $\Delta p$ are defined as formulated in Eqs. 8.10 and 8.11. Maximum values are indicated by red areas and minimum values by blue areas. The field plots can be observed while applying a voltage in the y-direction. (b)-(c) Quantitative assessment of the minimum and maximum values of both $\Delta J$ (see Eq. 8.18) and $\Delta p$ (see Eq. 8.19) are plotted. The indices in the legend, x, y and z, denote the direction of the voltage applied in the capacitor experiment.

In Fig. 8.9(a) for instance, it can be clearly seen that cell currents at frequencies < 1 kHz are almost exclusively conducted in the cytoplasm, with little or no current in the ER and the nucleus. At frequencies > 1 kHz, the cell current also flows through the cisternae of the ER. Furthermore, it can be seen that the nucleus only conducts a part of the cell current from a frequency > 100 kHz upwards. At frequencies of 10 MHz and higher, a current distribution is established within the cell that corresponds approximately to the area of the respective compartments on the (cross-)sectional plane of the cell. Due to the different dimensions of the individual compartments in the (cross-)sectional plane, a slightly anisotropic current distribution can be observed. These observations can also be transferred to the relative cell losses displayed in Fig. 8.9(c). Another finding is that the nucleus conducts current at higher frequencies than the rest of the organelles, because of the thicker membrane assumed in the model ($t_{\mathrm{M}} = 7\,\mathrm{nm}$ and $t_{\mathrm{NE}} = 40\,\mathrm{nm}$). In addition, Fig. 8.9(b) and (d) display the relative current and loss distributions for the model without an ER to better relate them to those of the model with an ER.

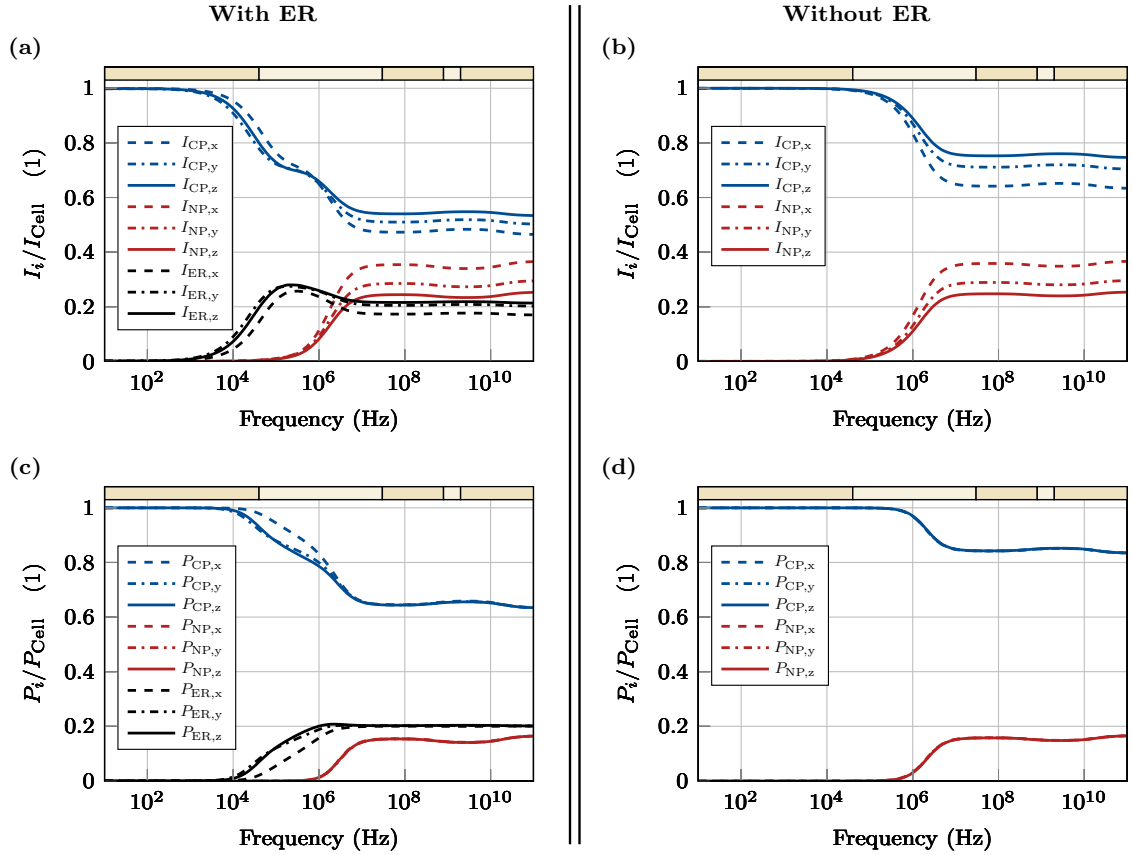


**Figure 8.9:** Comparison of the spectral response of the relative current and loss distribution within the individual cell compartments between the cell model with an endoplasmic reticulum (ER) and the one without. (a) and (c) display the relative currents and losses in the individual cell compartments in the ellipsoidal cell model with an ER, while (b) and (d) display these quantities in the model without an ER. The indices, CP, NP and ER, denote the cytoplasm, nucleoplasm and endoplasmic reticulum. The indices in the legend, x, y and z, denote the direction of the voltage applied in the capacitor experiment.

#### 8.3.2.3 The Effect of an Endoplasmic Reticulum on the Effective Material Parameters of the Ellipsoidal Cell Models

The effective material parameters of the simulated suspension are displayed in Figs. 8.10(a) and (c) for the cell model with an endoplasmic reticulum and in Figs. 8.10(b) and (d) for the model without an ER. The indices, x, y and z, denote the direction of the voltage applied in the capacitor experiment, based on the semi-axes of the cell defined in these directions.

Comparing the effective macroscopic permittivity of both models, $\tilde{\varepsilon}_{\text{r,sus}}$, it can be observed that there is no difference in the static permittivity for frequencies < 10 kHz. The direction of the applied voltage, however, leads to different values for the permittivity while the pattern of this anisotropy remains the same between the two models. In the fre-

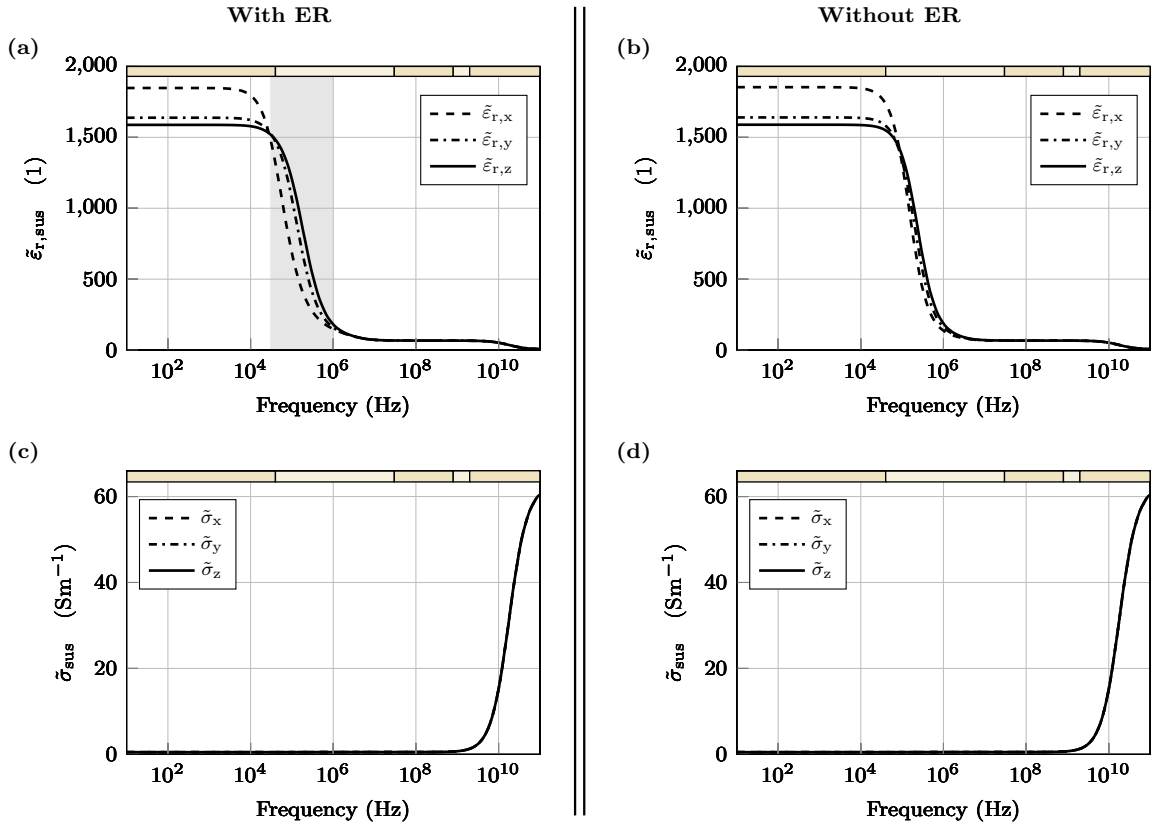


**Figure 8.10:** Overview of the effective material properties of the ellipsoidal cell models: (a) and (c) display the effective permittivity, $\tilde{\varepsilon}_{r,sus}$, and conductivity, $\tilde{\sigma}_{sus}$, of the cell suspension with cells including an endoplasmic reticulum (ER), and (b) and (d) display the values of a suspension without an ER. The indices in the legend, x, y and z, denote the direction of the voltage applied in the capacitor experiment.

quency range highlighted in grey (i.e. between 10 kHz and 1 MHz), differences between the models can be observed. In the model with an ER, the characteristic frequency of the interfacial polarization process shifts towards lower frequencies, so that the observed Maxwell-Wagner roll-off starts at low frequencies. This is especially true when the voltage is applied in the x-direction, since in this case, the largest number of cisternae lies between the plasma membrane and the nuclear envelope (see Fig. 8.1(c)). This can be attributed to the changes in the transmembrane potential as discussed earlier (see Sec. 8.2.2.1). At frequencies where the impedance of the plasma membrane loses its overriding dominance, the concentric arrangement of many cisternal membranes leads to a series of internal voltage drops and a potential distribution that is oriented toward the interior of the cell. For frequencies > 1 MHz, all curves converge to the same value and show the same trends in both models. Due to the high conductivity of the extracellular medium, the ER has no impact on the effective conductivity of the suspension. As already observed for the spherical cell model, the effective conductivity of the ellipsoidal model is primarily governed by the material properties of the extracellular space.

## 8.4 Summary and Conclusions

As part of a comparative study investigating the impact of increasing levels of detail in modeling eukaryotic cells, new methods for the graphical and quantitative analysis of resulting field distributions within cell bodies have been presented. In addition, the qualitative separation of and distinction between the influence of dispersive material properties and changes in the geometric structure of the cell have been demonstrated.

Using a simple spherical cell model, it has been shown that the cell membrane has to be considered at low frequencies (< 1 MHz) as well as at high frequencies (> 1 MHz) for the following reasons. At low frequencies, the modeling of the membrane is necessary because, in the absence of induced physiological changes such as electroporation, the membrane electrically shields the interior of the cell and has a high impact on the effective relative permittivity of the cell system. At high frequencies, modeling of the membrane is necessary because the different characteristic frequencies of the dispersive material functions lead to peaks in the volumetric loss density in the membrane, which must be considered in the context of microdosimetric investigations. This conclusion is in agreement with analytical and numerical studies published in [16] and [17].

Using an ellipsoidal cell model involving an ER, microdosimetric investigations have shown that a system of organelles enclosed by membranes has a large influence on the field distribution within the cell. At frequencies below 10 kHz, it has been demonstrated that organelle structures may act like barriers due to their material properties. As a result, cell currents tend to be conducted across the outer edge of the cell. In general, the maximum relative difference between the largest and smallest local current and loss densities occurs at such low frequencies, with the high resistance of the cell membrane allowing only small currents to enter the cell. At frequencies between 10 kHz and 10 MHz, the membranes become increasingly penetrable, causing the cell current to increase and the relative differences between minimum and maximum field strengths to decrease, resulting in the field distribution becoming increasingly homogeneous. Despite this trend toward a more homogeneous current and loss distribution, it has been demonstrated that the ratio between the maximum and the minimum current density is still 1.157 and the corresponding value for the volumetric loss density is still 1.342 at frequencies as high as 1 GHz and so, the variation should not be considered negligible.

Comparing ellipsoidal cell models with and without an ER, it has been shown that neglecting the cisternae of organelles in the model without an ER leads to a strong underestimation of both the current and volumetric loss density distribution at the outer edge of the cell, while at the nucleus, both values are overestimated. This observation has been consistently made over the entire frequency range studied, despite the better conductivity of the membrane at higher frequencies. Thus, although the cisternae of the ER no longer act as rigid barriers, their membranes increase the resistance of the current paths that lead across the nucleus by layering many membranes on top of each other, as a result of which the current density in the nucleus is significantly higher in the model without an ER. In conclusion, microdosimetric studies evaluating potential health risks

from EM exposure at the cellular level should therefore include cell organelles in modeling field-tissue interactions, even at frequencies used or being considered for use in 5G telecommunications standards (600 MHz to 2.5 GHz and 24 GHz to 52 GHz).

# 9 Bottom-Up Multiscale Model of the Epidermis

In the following chapter, a hierarchical multiscale model of the epidermis is developed by applying the knowledge of eukaryotic cell modeling presented in Chap. 8 to a bottom-up approach pioneered by Huclova [45]. Using this approach, the physiological features of cell structure within epidermal cell layers in terms of cell shape, structure, and histochemical composition are translated into a computational model of the epidermis. This model will then be used in later chapters of this thesis to perform (micro)dosimetric studies of the epidermis based on full-wave EM simulations.

To conceptualize a comprehensive bottom-up multiscale model of the epidermis (see Fig. 9.1(a)), the system must be considered on both a macroscopic and microscopic scale. On the macroscopic scale, the epidermis is considered to be a stratified material structure consisting of 10 cell layers comprising the viable epidermis (i.e. the SB, the SS and the SG) [32] and 14 cell layers comprising the SC [101]. At the microscopic scale, the layers of the viable epidermis are represented by 10 individual keratinocyte models showing all stages of keratinization, and the layers of the stratum corneum are represented by 14 individual corneocyte models showing different stages of hydration. In order to convert this purely conceptual, histological representation of the epidermis into a bottom-up model (see Fig. 9.1(b)), parametric CAD models of the two cell types must first be created and adapted to the physiological conditions of the individual cell layers. These adapted cell models can then be used in numerical quasi-static EM simulations to determine the effective material parameters of each cell layer. This allows the microstructure of the cells to be represented on a macroscopic scale by frequency-dependent effective permittivities, $\underline{\tilde{\varepsilon}}_{\mathrm{r,K}_p}(\omega)$ and $\underline{\tilde{\varepsilon}}_{\mathrm{r,C}_q}(\omega)$, where the indices $p$ and $q$, with $p \in \{1;2;\ldots;10\}$ and $q \in \{1;2;\ldots;14\}$, correspond to the individual cell layers from the inside outwards.

In order to derive the parameters of the CAD models used to represent the physiological conditions in each of the cell layers mentioned above, the stages of keratinization in the viable epidermis and hydration in the stratum corneum will be discussed in terms of two aspects: (1) geometrical changes of the cell and its organelles, and (2) histochemical changes within the cell compartments and the extracellular space. Following this discussion, the effective material properties of the epidermis at both the microscopic and the macroscopic scale will be derived yielding a dielectric representation of the epidermis that allows (micro)dosimetric investigations.

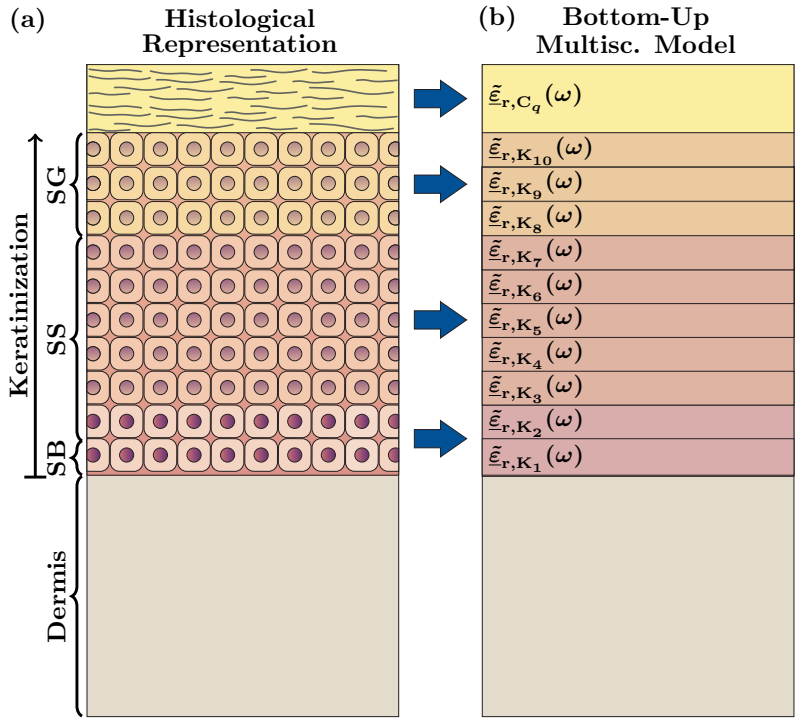


**Figure 9.1:** Bottom-up multiscale model of the epidermis: (a) Simplified histological representation of the epidermis. The epidermis is considered to be a stratified material structure consisting of 10 cell layers forming the viable epidermis and 14 cell layers forming the stratum corneum (SC). The viable epidermis comprises the stratum basale (SB), the stratum spinosum (SS) and the stratum granulosum (SG). The keratinocytes within the viable epidermis show different stages of keratinization and the corneocytes within the SC show different stages of hydration. The epidermis is contiguous with the dermis (D), which is considered homogeneous. (b) Bottom-up multiscale model of the epidermis in which the individual cell layers are represented as homogeneous material layers. The dispersive material properties of these layers, $\underline{\tilde{\varepsilon}}_{\mathrm{r,K}_p}(\omega)$ and $\underline{\tilde{\varepsilon}}_{\mathrm{r,C}_q}(\omega)$, are obtained using numerical homogenization. The indices $p$ and $q$, with $p \in \{1;2;\ldots;10\}$ and $q \in \{1;2;\ldots;14\}$, correspond to the individual cell layers from the inside outwards.

## 9.1 Geometric Parametrization of the Bottom-Up Model of the Epidermis Derived from the Scientific Literature

The following section is divided into three subsections. The first subsection presents the geometric parameters of the keratinocytes and the second subsection presents those of the corneocytes. Both of these subsections follow the same structure: First, the CAD model of the corresponding cell type and its geometric parameters are presented in general, and then the design rules for each cell layer are derived based on skin anatomy. In the third subsection, the geometric dimensions of the epidermal sublayers are summarized and the macroscopic model of the epidermis is derived.

### 9.1.1 Parametric Model of the Keratinocytes

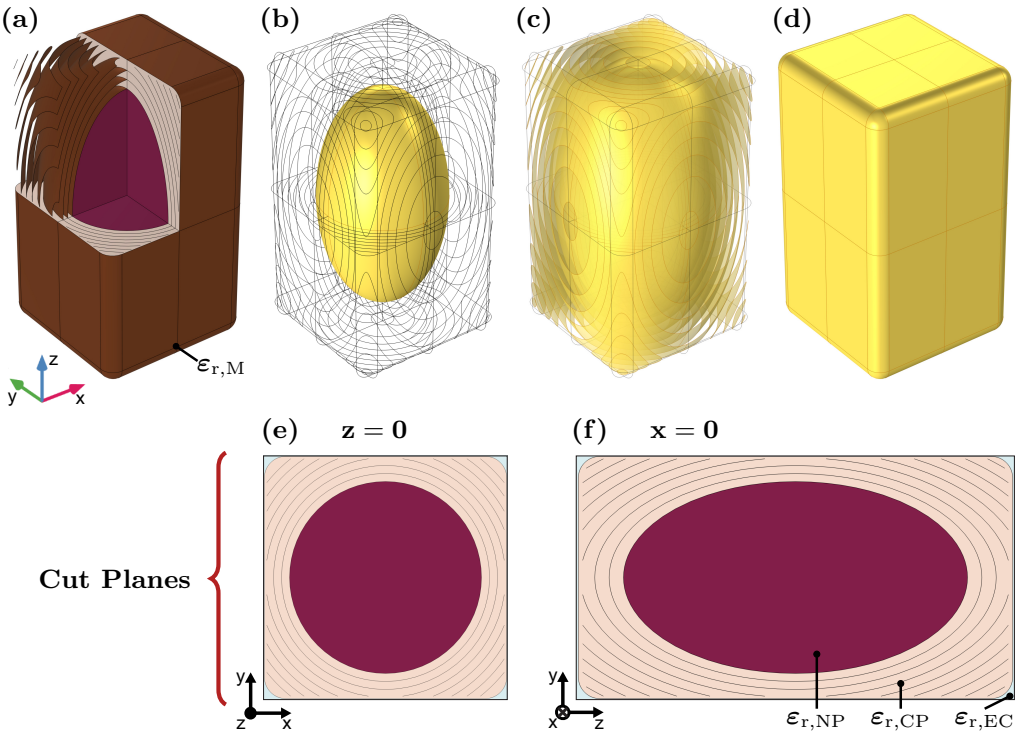


**Figure 9.2:** Parametric CAD model of a keratinocyte in the viable epidermis showing a basal keratinocyte as an illustrative example: (a) Keratinocyte modeled as a square cuboid containing an ellipsoidal nucleus concentrically surrounded by shells emulating organelle membranes. The plasma membrane, the nuclear envelope and the organelle membranes are considered as phospholipid bilayers and are depicted in brown. The keratinocyte can be further subdivided into the cytoplasm colored beige and the nucleoplasm colored purple. The cytoplasm is separated from the cell exterior by the plasma membrane and the nucleoplasm is separated from the cytoplasm by the nuclear envelope. (b)-(d) Transparent wire frames of the cell models highlighting the nucleus, the organelle membranes and the cytoplasm respectively. (e)-(f) Cross-sectional planes through the cell showing the xy plane and the yz plane respectively. The extracellular space is colored light blue. The material properties of the extracellular medium (EC), the cytoplasm (CP), the nucleoplasm (NP) and the membranes (M) are denoted by $\underline{\varepsilon}_{r,EC}$, $\underline{\varepsilon}_{r,CP}$, $\underline{\varepsilon}_{r,NP}$ and $\underline{\varepsilon}_{r,M}$ respectively.

The parametric CAD model of keratinocytes is introduced using Fig. 9.2, which shows a basal keratinocyte as an illustrative example. The plasma membrane, the nuclear envelope and the organelle membranes are considered as phospholipid bilayers depicted in brown in Fig. 9.2(a). The cell interior can be subdivided into two compartments: (1) the cytoplasm (CP) depicted in beige, and (2) the nucleoplasm (NP) depicted in purple. The CAD model of the keratinocytes is embedded in a cuboidal computational unit cell (UC) with a volume approximately 2 % larger than the cell body. The cytoplasm is separated from the cell exterior by the plasma membrane (PM) and the nucleoplasm is separated from the cytoplasm by the nuclear envelope (NE). The organelle membranes (OM) are

contained in the cytoplasm. Figs. 9.2(b)-(d) show the nucleus, organelle membranes and cell body as wireframe representations. Cross-sectional planes through the cell showing the xy plane and the yz plane are illustrated in Fig. 9.2(e)-(f), with the extracellular space (EC) colored light blue.

The cell bodies of the keratinocytes are modeled as square cuboids with rounded edges and corners. The cell is characterized by its dimensions with axes aligned to the spatial dimensions x, y and z. The nucleus is modeled as a spheroid with major and minor axes aligned with those of the cell. The length of the axes of the cell body are expressed by the parameters $l_{\mathrm{Cell,xy}}$ and $l_{\mathrm{Cell,z}}$ and those of the nucleus by $d_{\mathrm{N,xy}}$ and $d_{\mathrm{N,z}}$. Another key parameter here is the ratio between the long and short dimensions of the cell as well as the major and minor axes of the nucleus, $c_{\mathrm{Cell,l/s}}$ and $c_{\mathrm{N,l/s}}$. The organelles contained in the cytoplasm are modeled as shells arranged concentrically around the nucleus. The decision to approximate these organelles by only their membranes is based on results published in [18], which have been discussed in detail in Chap. 8. In this reference, it was shown that although high volumetric loss densities occur within organelle membranes at frequencies above 1 GHz and must therefore be accounted for in microdosimetric studies, the membranes no longer represent rigid barriers. The current flow within the organelle is, therefore, no longer significantly impeded by its membrane, so that a volumetric representation of the organelle bodies can be dispensed with, at least for the estimation of total cell losses. In order to create a generalized representation of organelle structures within the cytoplasm while maintaining a high degree of realism, the surface areas of the organelle membranes, $S_{\mathrm{OM}}$, and that of the nuclear envelope, $S_{\mathrm{NE}}$, are derived from the scientific literature [102]. These parameters are related to each other and included in the model as a single geometrical design parameter, $c_{\mathrm{s,OM/NE}}$, where $c_{\mathrm{s,OM/NE}} = \frac{S_{\mathrm{OM}}}{S_{\mathrm{NE}}}$. All design parameters listed in this paragraph are summarized in Tab. 9.1. In addition to all of the parameters above, the compartmentalization of the cell results in the volume ratios of each compartment to the total volume of the UC, expressed as

$$c_{\mathrm{v},i} = \frac{V_i}{V_{\mathrm{UC}}} \tag{9.1}$$

where $i \in \{\mathrm{EC;CP;NP;Cell}\}$. The index "Cell" denotes the volume of the cell body and includes both the volume of the cytoplasm and the volume of the nucleoplasm. These volume ratios, $c_{\mathrm{v},i}$, are important for the description and derivation of chemical changes between the cell layers during keratinization, which is described in detail in Sec. 9.2.

Having introduced the parametric CAD model, the geometric parameters of the keratinocytes within each cell layer are now derived from published data, allowing physiological conditions to be considered specifically for each of these layers within the viable epidermis. First, the geometric parameters of the cells of the SB and the cells of the subbasal row (i.e. the first cell layer of the SS) are determined. The decision to design these two cell layers according to the same rule is based on the fact that the cells of both layers are very similar in shape, size and function and together form the proliferative pool of the epidermis containing about 97 % of the miotic activity [37,39,40]. The longitudinal axes of

**Table 9.1:** Geometry parameter of the parametric CAD model of the keratinocytes.

| Parameter | Description |
|---|---|
| $l_{\mathbf{Cell,xy}}$ | Axes of the cell oriented in the x-direction and the y-direction |
| $l_{\mathbf{Cell,z}}$ | Axis of the cell oriented in the z-direction |
| $c_{\mathbf{Cell,l/s}}$ | Ratio between the longer and shorter axis of the cell |
| $d_{\mathbf{N,xy}}$ | Axes of the nucleus oriented in the x-direction and the y-direction |
| $d_{\mathbf{N,z}}$ | Minor axis of the nucleus oriented in the z-direction |
| $c_{\mathbf{N,l/s}}$ | Ratio between the longer and shorter axis of the nucleus |
| $c_{\mathbf{s,OM/NE}}$ | Ratio between the surface area of organelles within a cell and the nucleus |

the cell body and nucleus are perpendicular to the skin surface [38, 41], with axis lengths of $l_{\mathrm{Cell,z}} = 10\,\mu\mathrm{m}$ [37] and $d_{\mathrm{N,z}} = 8\,\mu\mathrm{m}$ [38]. The length ratio of the longitudinal axis to the other two axes, $c_{\mathrm{l/s}}$, is 1.8 for both the cell body and the nucleus [41]. According to [102], the ratio of the surface area of organelle membranes to the surface area of the nuclear envelope, $c_{\mathrm{s,OM/NE}}$, is about 10 and the volume ratio of extracellular space to the UC, $c_{\mathrm{v,EC}}$, approximately 0.26 %. However, the latter ratio has been increased to approximately 2 % to avoid small mesh lengths and their associated numerical instabilities in simulation. In higher cell layers, keratinocytes lose their proliferative abilities and instead grow by metabolizing substances for cornification. The cells in the SS therefore have larger cell bodies and nuclei which are still perpendicular to the skin surface. The longitudinal axes, $l_{\mathrm{Cell,z}}$ and $d_{\mathrm{N,z}}$, are documented in the scientific literature as 16 µm and 12 µm, with $c_{\mathrm{l/s}}$ now 1.4. Keratinocytes in the SG show signs of programmed cell death, known as apoptosis, which is primarily manifested by karyopyknosis, a process in which the nucleus shrinks and the chromatin it contains condenses into a homogeneous mass [33]. Shrinkage of the nucleus causes the cell body to flatten, changing its orientation from perpendicular to parallel to the skin surface. The longitudinal axes of the cell body, $l_{\mathrm{Cell,xy}}$, and the nucleus, $d_{\mathrm{N,xy}}$, are now 16 µm and 15 µm respectively, with $c_{\mathrm{l/s}}$ increasing again to 1.8. The geometric changes described above take place over a growth process of 30-50 days [32] and must therefore be accounted for in the geometric setups of the CAD cell models by gradual changes from one cell layer to the next. This is implemented mathematically by geometric compressing and stretching operations applied to the cell body and nucleus.

The geometric parameters of each cell layer, $p$, are summarized in Tab. 9.2. The numerical values in bold type are taken directly from the literature and serve as "boundary values" from which the transition values between the layers, due to compression or stretching, are linearly interpolated. In this way, three transition phases, $P_1$ to $P_3$, can be distinguished, occurring between the source data layers highlighted in gray in the table. In phase $P_1$, the keratinocytes start to grow and metabolizes material for cornification, while the orientation of the cell and nucleus relative to the skin surface remains vertical (compare the values of $l_{\mathrm{Cell,xy}}$ and $l_{\mathrm{Cell,z}}$ in the table). In phase $P_2$, the cell shows the first signs of karyopyknosis resulting in the flattening of the cell body and the nucleus without sig-

**Table 9.2:** Geometrical parameters of the keratinocyte models of the individual cell layers, $p$.

| $p$ | Layer | Phase | $c_{\text{Cell,l/s}}$ | $l_{\text{Cell,xy}}$ | $l_{\text{Cell,z}}$ | $c_{\text{N,l/s}}$ | $d_{\text{N,xy}}$ | $d_{\text{N,z}}$ | $c_{\text{s,OM/N}}$ |
|---|---|---|---|---|---|---|---|---|---|
| **1** | SB | - | **1.8** | 5.56µm | **10 µm** | **1.8** | 4.44µm | **8 µm** | **9.78** |
| **2** | SS | - | **1.8** | 5.56µm | **10 µm** | **1.8** | 4.44µm | **8 µm** | **9.78** |
| 3 | SS | $P_1$ | 1.67 | 7.2µm | 12µm | 1.67 | 5.6µm | 9.33µm | 11.09 |
| 4 | SS | $P_1$ | 1.53 | 9.13µm | 14µm | 1.53 | 6.95µm | 10.67µm | 12.11 |
| **5** | SS | $P_1$ | **1.4** | 11.43µm | **16 µm** | **1.4** | 8.57µm | **12 µm** | 12.91 |
| 6 | SS | $P_2$ | 1.53 | 12.95µm | 13.63µm | 1.53 | 10.71µm | 10.78µm | 9.13 |
| 7 | SS | $P_2$ | 1.67 | 14.48µm | 11.26µm | 1.67 | 12.86µm | 9.56µm | 6.56 |
| **8** | SG | $P_2$ | **1.8** | **16 µm** | 8.89µm | **1.8** | **15 µm** | 8.33µm | 4.46 |
| 9 | SG | $P_3$ | 2.11 | 16.75µm | 7.94µm | 2.34 | 15µm | 6.42µm | 8.19 |
| 10 | SG | $P_3$ | 2.51 | 17.57µm | 7µm | 3.33 | 15µm | 4.5µm | 7.4627 |

nificant variation in cell size. This process coincides with a change in the orientation of the cell from perpendicular to parallel to the skin surface. In phase $P_3$, apoptosis is modeled by further flattening of the nucleus and thus of the cell body, but here also represents the fragmentation of the nucleus and corresponding loss of cell size. The cell dimensions are such that the cell volumes in layers 9 and 10 decrease by 2% and 5%, respectively, compared to layer 8, so that a smooth transition from viable epidermis to SC also occurs at the microscopic level.

### 9.1.2 Parametric Model of the Corneocytes

The basic structure of the parametric model of the corneocytes is derived from that of the keratinocytes, in which the cell body is still a square cuboid with rounded corners embedded in a cuboidal UC. However, the keratinocytes of the SG (see cell model $K_{10}$) undergo profound biochemical changes during the transition to the SC, which have a massive impact on the interior of the cell. As mentioned above, apoptosis is terminated in the uppermost layer of the SG, leading to exocytosis of the remaining metabolites of the cell (i.e. keratinosomes), which compacts the extracellular space into a lipid-containing binding mass that ensures the mechanical integrity of the SC [34, 35, 36]. In addition, the nucleus fragments and the intracellular space hardens into an undifferentiated protein mass with a high keratin content. For this reason, the interior of the cell is no longer divided into individual compartments with organelles, but is represented as a homogeneous cell body. However, the shape of the cell body is still considered to be a square cuboid with rounded corners, embedded in a cuboidal UC. For the CAD model, the only directly accessible geometric design parameter is the axis length of the unit cell in the z direction, $l_{\text{UC,z}}$. The other geometric dimensions of the cell model, i.e. the axis lengths of the UC in the x-direction and the y-direction, $l_{\text{UC,xy}}$, as well as the axis lengths of the

**Table 9.3:** Geometrical parameters of the corneocyte models of the individual cell layers, $q$.

| $q$ | 1 | 2 | 3 | 4 | 5 | 6 | 7 | 8 | 9 | 10 | 11 | 12 | 13 | 14 |
|---|---|---|---|---|---|---|---|---|---|---|---|---|---|---|
| $l_{\mathrm{UC,xy}}$ (µm) | 28.45 | 26.81 | 26.34 | 26.11 | 26.01 | 26.05 | 26.2 | 26.46 | 26.82 | 27.29 | 27.86 | 28.54 | 29.36 | 30.31 |
| $l_{\mathrm{UC,z}}$ (µm) | 2 | 1.92 | 1.84 | 1.77 | 1.69 | 1.62 | 1.54 | 1.46 | 1.38 | 1.31 | 1.23 | 1.15 | 1.08 | 1 |
| $l_{\mathrm{Cell,xy}}$ (µm) | 28.32 | 26.67 | 26.2 | 25.96 | 25.87 | 25.91 | 26.06 | 26.32 | 26.68 | 27.15 | 27.73 | 28.42 | 29.24 | 30.2 |
| $l_{\mathrm{Cell,z}}$ (µm) | 1.88 | 1.78 | 1.70 | 1.62 | 1.55 | 1.47 | 1.39 | 1.32 | 1.25 | 1.17 | 1.1 | 1.03 | 0.96 | 0.89 |

cell body, $l_{\mathrm{Cell,xy}}$ and $l_{\mathrm{Cell,z}}$, result from the histochemical composition of the SC. The reason for this is that the hydration of the individual cell layers of the SC must be taken into account in the cell models of the corneocytes. To account for hydration within these layers, $l_{\mathrm{Cell,xy}}$ and $l_{\mathrm{Cell,z}}$ are determined to match the reduction of cell volume due to water loss from one cell layer to the next. The volume of the UC of the $\mathrm{K}_{10}$ keratinocytes is the reference volume from which the volume of the UC of the corneocytes, $\mathrm{C}_q$, is deduced as a function of the water content within each layer. The histochemical composition of the SC and the exact calculation of $l_{\mathrm{UC,xy}}$, $l_{\mathrm{Cell,xy}}$ and $l_{\mathrm{Cell,z}}$ are discussed in more detail in Sec. 9.2. However, the parameterisation of $l_{\mathrm{UC,z}}$ can be obtained from the scientific literature [45, 101]. Based on these references, the thickness of the top layer $l_{\mathrm{Cell,z,C_{14}}}$ is set to 1µm and, to allow for the gradual water loss of the cell bodies from one layer to the next, the thickness of the bottom layer $l_{\mathrm{UC,z,C_1}}$ is set to 2µm. The thickness of all intermediate layers is determined by linear interpolation between these values. The values for all of these geometric parameters are summarized in Tab. 9.3.

To give an overview of the spatial dimensions of the cell models introduced above, cross-sections through the yz plane of the cell models $\mathrm{K}_{1\&2}$, $\mathrm{K}_5$, $\mathrm{K}_8$, $\mathrm{C}_1$ and $\mathrm{C}_{14}$ are illustrated in Appendix B.

### 9.1.3 The Macroscopic Model of the Epidermis Related to the Microscopic Cell Models

The configuration of the different stages of keratinization and hydration in the parametric cell models is summarized in Fig. 9.3. The upper diagram shows the volumes of the cell compartments, $V_i$, illustrated by stacked bars categorized according to the models of the keratinocytes, $\mathrm{K}_p$, and the corneocytes, $\mathrm{C}_q$, in the different sublayers of the epidermis, along with the transition phases $\mathrm{P}_1$ to $\mathrm{P}_3$. The bottom diagram shows the ratios of the volume of these compartments to that of the UC, $c_{\mathrm{v},i}$, using the same categories.

In order to describe the bottom-up model of the epidermis on a macroscopic scale, the axial lengths of the UC must be added together in the z-direction. The resulting thicknesses of the epidermal sublayers are summarized in Tab. 9.4.

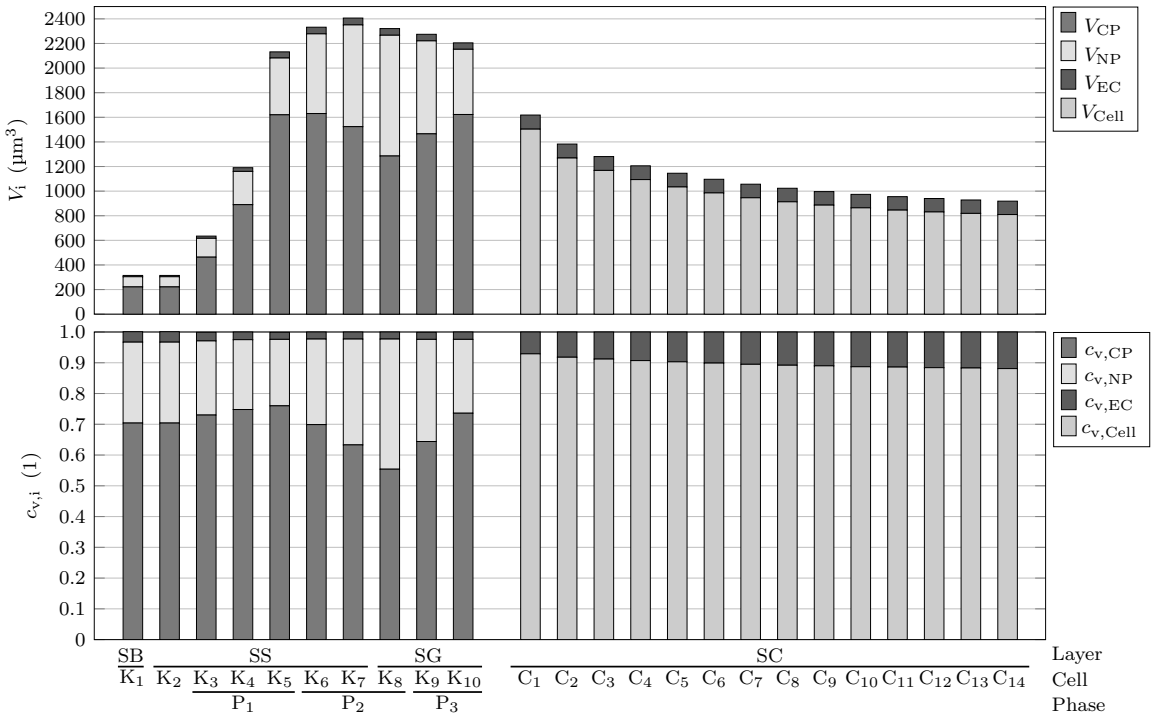


**Figure 9.3:** Geometrical configurations of the cell models under investigation: (top) Volumes of the cell compartments, $V_i$, illustrated by stacked bars categorized according to the models of the keratinocytes, $K_p$, and the corneocytes, $C_q$, in the different sublayers of the epidermis, along with the transition phases $P_1$ to $P_3$. (bottom) Ratios of the volume of the cell compartments to that of computational domain, $c_{v,i}$, using the same categories. The index $i \in \{CP; NP; EC; Cell\}$ denotes the cytoplasm, the nucleoplasm, the extracellular medium and the cell body respectively.

**Table 9.4:** Overview of the thickness and number of cell layers corresponding to all of the epidermal sublayers.

| | **SB** | **SS** | **SG** | **SC** |
|---|---|---|---|---|
| **Thickness** | 10.04µm | 77.31µm | 24.08µm | 21µm |
| **# of Layers** | 1 | 6 | 3 | 14 |

## 9.2 Histochemical Parameterization of the Bottom-Up Model of the Epidermis Derived from the Scientific Literature

Following the introduction of the parametric CAD models of keratinocytes and corneocytes in Sec. 9.1, the histochemical changes within the epidermis are now described. The problem with describing these changes is that there is no histochemical model of the epidermis available in the scientific literature that provides a coherent summary of the biochemical composition of the skin in the form of a concentration profile across all lay-

ers. As such a model is necessary for realistic modelling of the skin, it is derived below on the basis of available scientific data on both (1) a macroscopic scale and (2) a microscopic scale.

### 9.2.1 Histochemical Parameterization of the Epidermis on a Macroscroscopic Scale

A coherent concentration profile describing the biochemical composition of the human epidermis at a microscopic scale is derived below. The starting point for this derivation is the water concentration profile across the human epidermis shown in Fig. 9.4(a). Originally published in [103], this concentration profile has been adapted to the thicknesses of the epidermal sublayers summarized in Tab. 9.4 which are illustrated using a gray-shaded background. At this stage, the epidermis is considered to be a two-phase material represented by the mass fractions of water, $c_{\mathrm{m,w}}$, and dry biological material, $c_{\mathrm{m,dm}}$. The mass fractions, $c_{\mathrm{m},j}$, are defined as

$$c_{\mathrm{m,j}} = \frac{m_j}{m_{\mathrm{tot}}} \tag{9.2}$$

where $m_j$ and $m_{\mathrm{tot}}$ are the mass of each material and the total mass of any given sample. However, to create a more refined material model of the epidermis, $c_{\mathrm{m,dm}}$ is further subdivided into $c_{\mathrm{m,l}}$, $c_{\mathrm{m,k}}$ and $c_{\mathrm{m,p}}$, denoting lipid, keratin and general protein concentrations respectively. For this purpose, Fig. 9.4(b) divides the epidermis into the viable epidermis, which has an active metabolism, and the SC, which consists only of dead cells in various stages of hydration. In a first step, the metabolism of keratin and lipids within the viable epidermis is derived by considering keratinization as a developmental process during the life cycle of the cells, starting from the basement membrane (i.e. $z = 0\,\mu\mathrm{m}$), denoted by ①. At this location, basal keratinocytes are considered to be cells that have the potential to migrate through higher cell layers and differentiate, but have not yet started this process. Therefore, $c_{\mathrm{m,dm}}$ is assumed to consist only of a general protein content, $c_{\mathrm{m,p}}$, which accounts for all macromolecules that form organelles. Considering this as a basic assumption, the concentration of $c_{\mathrm{m,p}}$ remains constant during the migration to higher layers. The diminishing concentration of water illustrated by the blue line, $c_{\mathrm{m,w}}$, is not considered as a loss of water but rather a shift in concentration ratios due to the deposition of keratohyalin granules in the cell. Thus, the difference between the constant concentration of of protein, $c_{\mathrm{m,p}}$, and the decreasing concentration of water, $c_{\mathrm{m,w}}$, represents the concentration of keratin in the cells, $c_{\mathrm{m,k}}$. According to [104], lipid formation in the SG is accounted for by an exponential function approaching a maximum value of 10.3 % normalized to the total ammount of dry biological material at the end of the viable epidermis (i.e., $z = 111.43\,\mu\mathrm{m}$), denoted by ②. The SG/SC interface marks the point at which the epidermis can no longer be considered a living system. It is therefore necessary to make a conceptual distinction in the following derivation of the epidermal material composition, and this is illustrated by the graphical separation of the viable epidermis and the SC in the figure. In analogy to the continuity at an interface within a

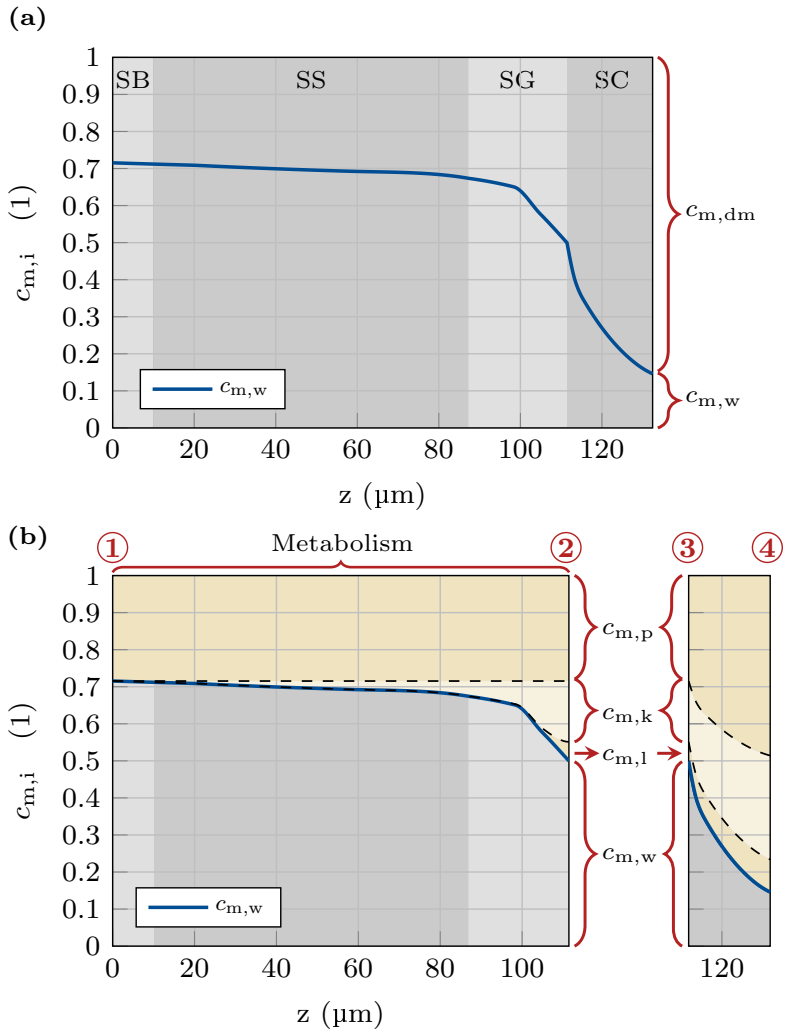


**Figure 9.4:** Overview of the histochemical composition of the human epidermis considered in the bottom-up model on a macroscopic scale: (a) Water concentration profile across the human epidermis, considering its biochemical composition as a two-phase material represented by the mass fractions of water, $c_{m,w}$, and dry biological material, $c_{m,dm}$, where $c_{m,j} = \frac{m_j}{m_{tot}}$, with $m_{tot}$ denoting the total mass of any given sample. Such a water concentration profile was originally published by [103], and here, the thickness of the stratum basale (SB), the stratum spinosum (SS), the stratum granulosum (SG) and the stratum corneum (SC) are adapted to those derived form the parametric CAD models of the keratinocytes and corneocytes summarized in Tab. 9.4. (b) Derivation of a refined concentration profile which further subdivides $c_{m,dm}$ into a lipid, a keratin and a general protein concentration denoted by $c_{m,l}$, $c_{m,k}$ and $c_{m,p}$ respectively. The color gradation within the beige background serves as visual support to better delineate changes in the concentration profile. The epidermis is divided into the viable epidermis having an active metabolism and the SC comprising only dead cells showing different stages of hydration. The boundary layers between the dermis and the SC, ①, the SG and the SC, ② and ③, and the skin surface, ④, form intervals in which this metabolization (①-②) and dehydration (③-④) can be determined.

boundary value problem, the metabolized material composition within the viable epidermis is taken from ② as the starting point for the dehydration process across the SC in ③ (i.e. $z = 111.43\,\mu\text{m}$). Starting from the given initial mass $m_{\text{tot}} = m_{\text{dm}} + m_{\text{w}}$, the material composition within the SC is no longer dominated by the formation of new substances, but by the loss of water, which results in a change in the concentrations towards the skin surface (i.e. $z = 132.43\,\mu\text{m}$), denoted by ④.

However, the above mass fractions must be converted into volume fractions. This is done in order to be able to use the concentration profile across the epidermis to derive the dielectric material properties of the cells and their compartments at the molecular level using mixing formulae, which will be presented in detail in Sec. 9.3. The volume fractions of the biochemical compounds under investigation are defined as

$$c_{\text{v},j} = \frac{V_j}{V_{\text{tot}}} \tag{9.3}$$

with $V_j = \frac{c_{\text{m},j} \cdot m_{\text{tot}}}{\rho_j}$ and $V_{\text{tot}} = \sum_j V_j$. The volumetric mass densities of the individual compounds are represented by $\rho_j$. The densities of water, $\rho_{\text{w}}$, protein, $\rho_{\text{p}}$, keratin, $\rho_{\text{k}}$, and lipids, $\rho_{\text{l}}$, considered in this conversion are summarized in Tab. 9.5, along with the references from which these values are adopted.

**Table 9.5:** Volumetric mass densities, $\rho_j$, of the biochemical compounds of the epidermis. The indices w, p, k and l denote water, protein, keratin and lipids.

| | **w** | **p** | **k** | **l** |
|---|---|---|---|---|
| $\rho_j \left(\frac{\text{kg}}{\text{m}^3}\right)$ | 1000 | 1410 [105] | 1410 [105, 106] | 950 [107] |

Based on the above, Fig. 9.5 shows the histochemical concentration profile across the human epidermis illustrating its composition using the volume fractions of water, $c_{\text{v,w}}$, lipids, $c_{\text{v,l}}$, keratin, $c_{\text{v,k}}$, and protein, $c_{\text{v,p}}$. The vertical red dashed lines in the viable epidermis correspond to the midpoints of the cell layers in the z-direction denoted by $\text{K}_1$ to $\text{K}_{10}$. The concentrations at these midpoint will be used in Sec. 9.2.2 to derive the chemical composition of the individual cell compartments within each cell layer. Although the midpoints of the cell layers in the SC are not shown for clarity, the same procedure is applied to the corneocytes.

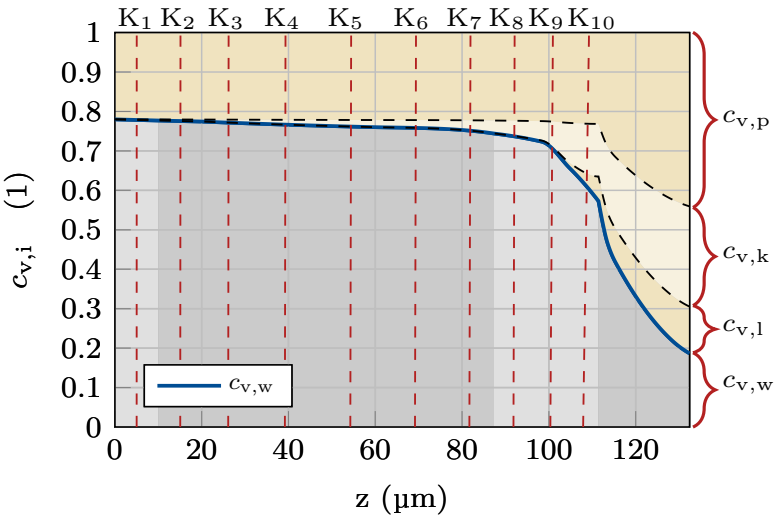


**Figure 9.5:** Histochemical concentration profile across the human epidermis illustrating its composition using the volume fractions of water, $c_{v,w}$, lipids, $c_{v,l}$, keratin, $c_{v,k}$, and protein, $c_{v,p}$. The vertical red dashed lines correspond to the midpoints of the cell layers (i.e. keratinocytes) denoted by $K_1$ to $K_{10}$.

Tab. 9.6 summarizes the concentrations at $z = 0\,\mu m$ (i.e. ①), $z = 111.43\,\mu m$ (i.e. ② & ③) and $z = 132.43\,\mu m$ (i.e. ④) in terms of both mass and volume fractions.

**Table 9.6:** Material composition of the epidermis at $z = 0\,\mu m$ (i.e. ①), $z = 111.43\,\mu m$ (i.e. ② & ③) and $z = 132.43\,\mu m$ (i.e. ④) expressed as mass fractions. The concentration of the water, protein, keratin and lipid content is denoted by $c_{m,w}$, $c_{m,p}$, $c_{m,k}$ and $c_{m,l}$ respectively. The corresponding volume fractions, $c_{v,j}$, are given on the right-hand side.

| | $c_{m,w}$ | $c_{m,p}$ | $c_{m,k}$ | $c_{m,l}$ | $c_{v,w}$ | $c_{v,p}$ | $c_{v,k}$ | $c_{v,l}$ |
|---|---|---|---|---|---|---|---|---|
| ① | 0.715 | 0.285 | 0 | 0 | 0.78 | 0.22 | 0 | 0 |
| ② & ③ | 0.499 | 0.285 | 0.164 | 0.052 | 0.573 | 0.231 | 0.133 | 0.063 |
| ④ | 0.146 | 0.285 | 0.280 | 0.088 | 0.187 | 0.441 | 0.254 | 0.118 |

### 9.2.2 Histochemical Parameterization of the Epidermis on a Microscopic Scale

The biochemical concentrations of the individual cell compartments of each cell layer will be derived below, starting with the keratinocytes. In a first step, the geometrical composition of the CAD models of each cell layer must be considered in terms of the volumes of the individual compartments, $V_{i,\mathrm{K}_p}$:

$$c_{\mathrm{v},i,\mathrm{K}_p} = \frac{V_{i,\mathrm{K}_p}}{V_{\mathrm{UC},\mathrm{K}_p}} \tag{9.4}$$

$$c_{\mathrm{v},i,\mathrm{Cell},\mathrm{K}_p} = \frac{V_{i,\mathrm{K}_p}}{V_{\mathrm{Cell},\mathrm{K}_p}} \tag{9.5}$$

with $V_{\mathrm{UC},\mathrm{K}_p} = V_{\mathrm{EC},\mathrm{K}_p} + V_{\mathrm{CP},\mathrm{K}_p} + V_{\mathrm{NP},\mathrm{K}_p}$, $V_{\mathrm{Cell},\mathrm{K}_p} = V_{\mathrm{CP},\mathrm{K}_p} + V_{\mathrm{NP},\mathrm{K}_p}$ and $i \in \{\mathrm{EC};\, \mathrm{CP};\, \mathrm{NP}\}$. In a second step, the volume of each biochemical component is determined by multiplying the unit cell volume of each CAD model by the biochemical concentrations at the midpoints of each cell layer (see Fig. 9.5):

$$V_{j,\mathrm{K}_p} = V_{\mathrm{UC},\mathrm{K}_p} \cdot c_{\mathrm{v},j,\mathrm{K}_p} \tag{9.6}$$

with $j \in \{\mathrm{w};\, \mathrm{l};\, \mathrm{k};\, \mathrm{p}\}$. In a third step, these volumes are each distributed across the individual cell compartments, beginning with the EC space. This is done by assuming the extracellular medium to be filled with water only

$$V_{\mathrm{w},\mathrm{EC},\mathrm{K}_p} = V_{\mathrm{EC},\mathrm{K}_p}. \tag{9.7}$$

The residual cell water, $V_{\mathrm{w},\mathrm{Cell},\mathrm{K}_p} = V_{\mathrm{w},\mathrm{K}_p} - V_{\mathrm{w},\mathrm{EC},\mathrm{K}_p}$, and the volumes of each remaining substance now needs to be distributed to the CP and the NP. In the cell layers $\mathrm{K}_1$ to $\mathrm{K}_8$, the NP is considered to be a two-phase mixture containing protein and water to an extent proportional to the total amount of water in the cell:

$$V_{\mathrm{w},\mathrm{NP},\mathrm{K}_p} = V_{\mathrm{w},\mathrm{Cell},\mathrm{K}_p} \cdot c_{\mathrm{NP},\mathrm{Cell}} \tag{9.8}$$

$$V_{\mathrm{p},\mathrm{NP},\mathrm{K}_p} = (V_{\mathrm{Cell},\mathrm{K}_p} - V_{\mathrm{w},\mathrm{Cell},\mathrm{K}_p}) \cdot c_{\mathrm{NP},\mathrm{Cell}} \tag{9.9}$$

In cell layers $\mathrm{K}_9$ and $\mathrm{K}_{10}$ the amount of protein remains constant compared to cell layer $\mathrm{K}_8$. However, the water content decreases according to the shrinkage of the nucleus due to karyopyknosis (see Sec. 9.1.1, Fig. 9.3):

$$V_{\mathrm{w},\mathrm{NP},\mathrm{K}_9} = V_{\mathrm{w},\mathrm{NP},\mathrm{K}_8} - (V_{\mathrm{NP},\mathrm{K}_8} - V_{\mathrm{NP},\mathrm{K}_9}) \tag{9.10}$$

$$V_{\mathrm{p},\mathrm{NP},\mathrm{K}_9} = V_{\mathrm{p},\mathrm{NP},\mathrm{K}_8} \tag{9.11}$$

$$V_{\mathrm{w},\mathrm{NP},\mathrm{K}_{10}} = V_{\mathrm{w},\mathrm{NP},\mathrm{K}_8} - (V_{\mathrm{NP},\mathrm{K}_8} - V_{\mathrm{NP},\mathrm{K}_{10}}) \tag{9.12}$$

$$V_{\mathrm{p},\mathrm{NP},\mathrm{K}_{10}} = V_{\mathrm{p},\mathrm{NP},\mathrm{K}_8} \tag{9.13}$$

The remaining cell water and protein are distributed to the CP. The metabolised keratin and lipids are also deposited there:

$$V_{\mathrm{w,CP,K}_p} = V_{\mathrm{w,Cell,K}_p} - V_{\mathrm{w,NP,K}_p} \tag{9.14}$$

$$V_{\mathrm{p,CP,K}_p} = V_{\mathrm{p,K}_p} - V_{\mathrm{p,NP,K}_p} \tag{9.15}$$

$$V_{\mathrm{k,CP,K}} = V_{\mathrm{k,K}_p} \tag{9.16}$$

$$V_{\mathrm{l,CP,K}} = V_{\mathrm{l,K}_p} \tag{9.17}$$

In a final step, the volume fractions of the biochemical compounds in each compartment in any given cell layer, $c_{\mathrm{v},j,i,\mathrm{K}_p}$, can be defined as

$$c_{\mathrm{v},j,i,\mathrm{K}_p} = \frac{V_{j,i,\mathrm{K}_p}}{V_{i,\mathrm{K}_p}} \tag{9.18}$$

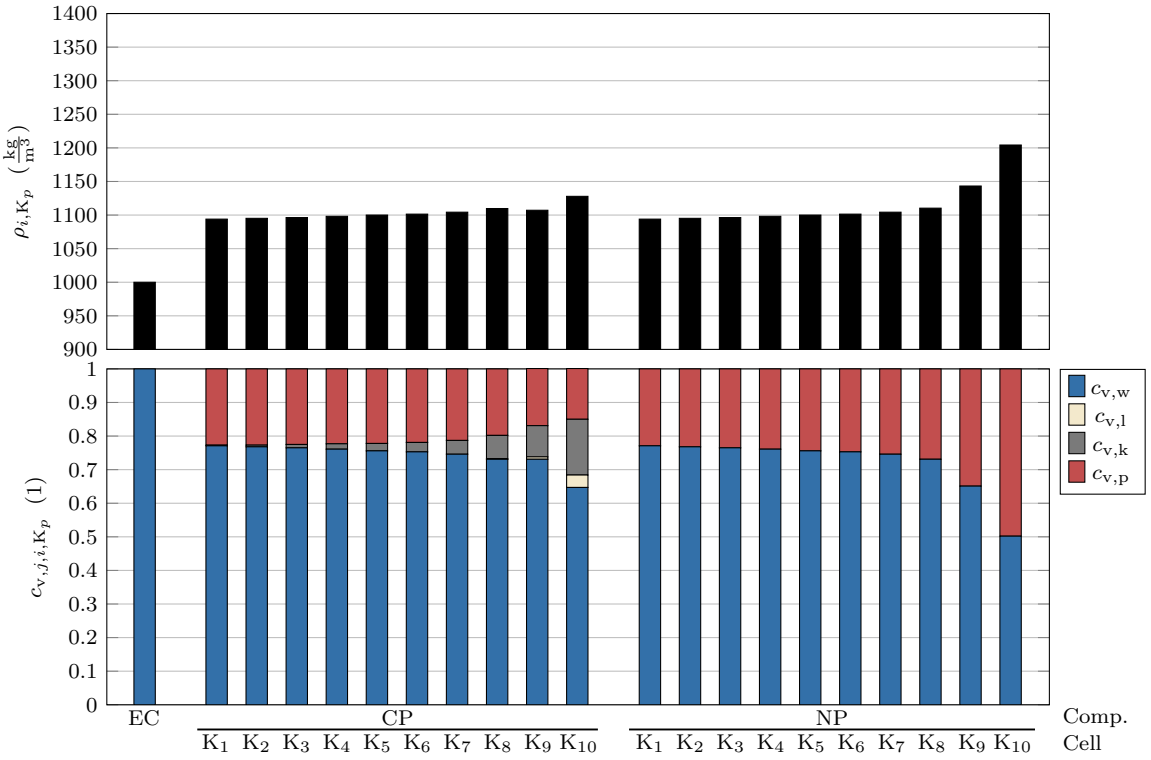


**Figure 9.6:** Histochemical configurations of the keratinocytes under investigation: (top) Volumetric mass densities, $\rho_{i,\mathrm{K}_p}$, illustrated by black bars for each different keratinocyte model, $\mathrm{K}_p$, and categorized according to the cell compartments (i.e. EC, CP, and NP). (bottom) Histochemical composition of the cell compartments expressed as volume fractions, $c_{\mathrm{v},j,i,\mathrm{K}_p}$, relative to the total volume of the individual compartments using the same categories. The index $j \in \{\mathrm{w; l; k; p}\}$ denotes the content of water, lipids, keratin and protein, and the index $i \in \{\mathrm{CP; NP; EC}\}$ denotes the individual cell compartments of the keratinocytes.

Based on $c_{\mathrm{v},j,i,\mathrm{K}_p}$, the volumetric mass density within the cell compartments, $\rho_{i,\mathrm{K}_p}$, can now also be determined qualitatively. These are calculated by

$$\rho_{i,\mathrm{K}_p} = \sum_j \rho_j \cdot c_{\mathrm{v},j,i,\mathrm{K}_p} \tag{9.19}$$

The relationship is only labeled qualitatively, as the simple summation of the products of the individual densities and their volume fractions can only be assumed if the individual substances do not react chemically with each other.

Fig. 9.6 provides an overview of the histochemical configurations of the keratinocytes in each cell layer of the viable epidermis. The top diagram illustrates the volumetric mass densities, $\rho_{i,\mathrm{K}_p}$, by black bars for each different keratinocyte model, $\mathrm{K}_p$, categorized according to the cell compartments (i.e. EC, CP, and NP). The bottom diagram illustrates the volume fractions, $c_{\mathrm{v},,j,i,\mathrm{K}_p}$, relative to the total volume of the individual compartments using the same categories.

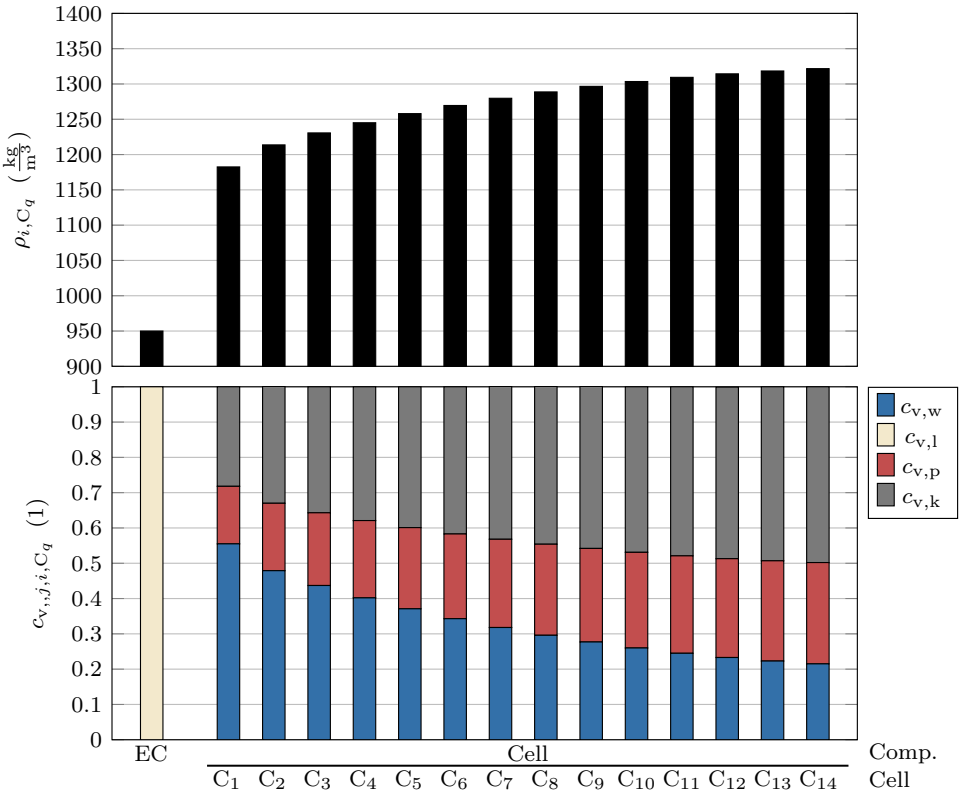


**Figure 9.7:** Histochemical configurations of the corneocytes under investigation: (top) Volumetric mass densities, $\rho_{i,\mathrm{C}_q}$, illustrated by black bars for each different corneocyte model, $\mathrm{C}_q$, and categorized according to the cell compartments (i.e. EC, Cell). (bottom) Histochemical composition of the cell compartments expressed as volume fractions, $c_{\mathrm{v},,j,i,\mathrm{C}_q}$, relative to the total volume of the individual compartments using the same categories. The index $j \in \{\mathrm{w};\mathrm{l};\mathrm{k};\mathrm{p}\}$ denotes the content of water, lipids, keratin and protein, and the index $i \in \{\mathrm{Cell};\mathrm{EC}\}$ denotes the individual cell compartments of the corneocytes.

The biochemical composition of the corneocytes within the SC is analogous to the derivation above. With the difference that the distribution of the respective substances is much simpler. Through exocytosis, the EC fills with lipids, so that the water together with the keratin and the other protein compounds in the SC are only inside the cell body. Fig. 9.7 provides an overview of the histochemical configurations of the corneocytes in each cell layer of the SC. The top diagram illustrates the volumetric mass densities, $\rho_{i,\mathrm{C}_q}$, by black bars for each different corneocyte model, $\mathrm{C}_q$, categorized according to the cell compartments (i.e. EC, Cell). The bottom diagram illustrates the volume fractions, $c_{\mathrm{v},,j,i,\mathrm{C}_q}$, relative to the total volume of the individual compartments using the same categories.

## 9.3 Effective Material Properties of the Bottom-Up Model of the Epidermis

Based on the material composition of the cells at the microscopic scale outlined in the previous section, the effective material properties of the cell compartments are determined using analytical mixing rules in Sec. 9.3.1. Subsequently, these material properties will be used in the parametric CAD models of the keratinocytes and corneocytes to determine the effective material properties of the cell layers using quasi-static numerical simulations in Sec. 9.3.2.

### 9.3.1 Effective Material Properties of the Parametric Cell Models on a Microscopic Scale

Considering the compartments of the cell models as multiphase composites consisting of water, proteins, keratin and lipids, the effective dielectric properties of these compartments in each cell layer can be calculated using analytical mixing rules. However, such calculations require knowledge of both the volume fraction and the dielectric properties of each substance present in each compartment. The volume fractions of each material have already been derived in Sec. 9.2 and can be taken from Figs. 9.6 and 9.7. However, the permittivities of the basic cell substances remain to be derived from the scientific literature, starting with those of the water in the following.

As described in detail in section 8.1.2, the dispersive properties of the extracellular medium, cytoplasm, and nucleoplasm are approximated by the dielectric functions of physiological salt solutions. This approach is adopted for modeling the cellular water within each compartment so that its lossy dispersive permittivities, $\underline{\varepsilon}_{\mathrm{r,w},i}(\omega)$, are modeled by a Debye-type equation:

$$\underline{\varepsilon}_{\mathrm{r,w},i}(\omega) = \varepsilon_{\mathrm{r,w},i,\infty} + \frac{\varepsilon_{\mathrm{r,w},i,\mathrm{s}} - \varepsilon_{\mathrm{r,w},i,\infty}}{1 + \mathrm{j}\frac{\omega}{\omega_0}} - \mathrm{j}\frac{\sigma_{\mathrm{w},i,\mathrm{s}}}{\varepsilon_0 \omega}, \tag{9.20}$$

with $i \in \{\text{CP};\text{NP};\text{EC};\text{Cell}\}$. The Debye coefficients corresponding to the individual compartments are summarized in Tab. 9.7.

**Table 9.7:** Debye coefficients for modeling the dispersive dielectric material properties of the cytoplasm (CP), nucleoplasm (NP) and extracellular medium (EC), representing the dispersive material properties of the water in the corresponding compartment, $\underline{\varepsilon}_{\mathrm{r,w},i}(\omega)$, with $i \in \{\text{CP};\text{NP};\text{EC};\text{Cell}\}$.

| Compartment | $\varepsilon_{\mathrm{r,w},i,\mathrm{s}}$ | $\varepsilon_{\mathrm{r,w},i,\infty}$ | $f_0$ (GHz) | $\sigma_{\mathrm{w},i,\mathrm{s}}$ (S/m) |
|---|---|---|---|---|
| **Cytoplasm (CP)** | 67 | 5 | 17.9 | 0.32 |
| **Nucleoplasm (NP)** | 67 | 5 | 17.9 | 0.32 |
| **Extracellular medium (EC)** | 67 | 5 | 17.9 | 0.55 |
| **Cell body (Cell)** | 67 | 5 | 17.9 | 0.32 |

The dielectric properties of the protein content and those of the keratin are considered to be independent of the frequency with the following values

$$\underline{\varepsilon}_{\mathrm{r,p}} = 2.5 - \mathrm{j}0 \quad \text{and} \quad \underline{\varepsilon}_{\mathrm{r,k}} = 3.548 - \mathrm{j}0.244,$$

where the former value is taken from [50,51] and the latter from [108]. The material properties of the lipids are modeled by a double Debye equation defined as

$$\underline{\varepsilon}_{\mathrm{r,l}}(\omega) = \varepsilon_{\mathrm{r,l},\infty} + \frac{\Delta\varepsilon_{\mathrm{r,l},1}}{1+\mathrm{j}\frac{\omega}{\omega_{0,1}}} + \frac{\Delta\varepsilon_{\mathrm{r,l},2}}{1+\mathrm{j}\frac{\omega}{\omega_{0,2}}} - \mathrm{j}\frac{\sigma_{l,s}}{\varepsilon_0\omega}, \tag{9.21}$$

whose coefficients are adopted from [109] and summarized in Tab. 9.8.

**Table 9.8:** Debye coefficients to model the dispersive permittivity of lipids (adopted from [109]).

| | $\varepsilon_{\mathrm{r,l},\infty}$ | $\Delta\varepsilon_{\mathrm{r,l},1}$ | $\Delta\varepsilon_{\mathrm{r,l},2}$ | $f_{0,1}$ (THz) | $f_{0,2}$ (THz) | $\sigma_{\mathrm{l,s}}$ (S/m) |
|---|---|---|---|---|---|---|
| **Lipids (l)** | 2.15 | 0.2 | 0.1 | 1 | 10 | 0 |

The initial permittivities of water are incrementally combined with the other basic components (i.e. protein, keratin and lipids) using the Hanai-Bruggeman (HB) mixing formula to account for the influence of different keratinization and hydration stages within the epidermis on the effective material parameters of the individual cell compartments:

$$0 = (1-\Phi^s)\cdot\left(\frac{\underline{\varepsilon}^s_{\mathrm{r},i,\mathrm{K}_p,\mathrm{HB}} - \underline{\varepsilon}^s_{\mathrm{r},i,\mathrm{K}_p,\mathrm{I}}}{\underline{\varepsilon}^s_{\mathrm{r},i,\mathrm{K}_p,\mathrm{H}} - \underline{\varepsilon}^s_{\mathrm{r},i,\mathrm{K}_p,\mathrm{I}}}\right)\cdot\left(\frac{\underline{\varepsilon}^s_{\mathrm{r},i,\mathrm{K}_p,\mathrm{H}}}{\underline{\varepsilon}^s_{\mathrm{r},i,\mathrm{K}_p,\mathrm{HB}}}\right)^{\frac{1}{3}}, \tag{9.22}$$

where $s$ denotes the incremental mixing step. The dielectric material properties of the substance considered to be the inclusion are denoted by $\underline{\varepsilon}^s_{\mathrm{r},i,\mathrm{K}_p,\mathrm{I}}$ and those which are considered to be the host medium by $\underline{\varepsilon}^s_{\mathrm{r},i,\mathrm{K}_p,\mathrm{H}}$. $\Phi^s$ denotes the volume fraction of the inclusions relative to the total volume of the two-phase mixture. $\underline{\varepsilon}^s_{\mathrm{r},i,\mathrm{K}_p,\mathrm{HB}}$ denotes the effective

permittivity of each step. In any step where $s \geq 2$, $\underline{\varepsilon}^{s}_{\mathrm{r},i,\mathrm{K}_p,\mathrm{H}} = \underline{\varepsilon}^{s-1}_{\mathrm{r},i,\mathrm{K}_p,\mathrm{HB}}$. Tab. 9.9 provides an overview of the mixing procedure used to determine the effective permittivities of the individual cell compartments, $i \in \{\mathrm{CP};\ \mathrm{NP};\ \mathrm{Cell}\}$, at any given cell layer of the viable epidermis, $\mathrm{K}_p$, and the SC, $\mathrm{C}_q$.

**Table 9.9:** Overview of the mixing procedure used to determine the effective permittivities of the individual cell compartments, $i \in \{\mathrm{CP};\ \mathrm{NP};\ \mathrm{Cell}\}$, in any given cell layer of the viable epidermis, $\mathrm{K}_p$, and the SC, $\mathrm{C}_q$. $s$ denotes the incremental mixing step. The dielectric material properties of the substance considered to be the inclusion are denoted by $\underline{\varepsilon}^{s}_{\mathrm{r},i,\mathrm{K}_p,\mathrm{I}}$ and those which are considered to be the host medium by $\underline{\varepsilon}^{s}_{\mathrm{r},i,\mathrm{K}_p,\mathrm{H}}$. Here, $\underline{\varepsilon}_{\mathrm{r,w}}$, $\underline{\varepsilon}_{\mathrm{r,p}}$, $\underline{\varepsilon}_{\mathrm{r,k}}$ and $\underline{\varepsilon}_{\mathrm{r,l}}$ denote the dielectric values of the water (i.e. physiological salt solution), the protein, the keratin and the lipids respectively.

| | **Keratinocytes** | | | | **Corneocytes** | |
|---|---|---|---|---|---|---|
| $s$ | **CP** | | **NP** | | **Cell** | |
| | $\underline{\varepsilon}^{s}_{\mathrm{r},i,\mathrm{K}_p,\mathrm{H}}$ | $\underline{\varepsilon}^{s}_{\mathrm{r},i,\mathrm{K}_p,\mathrm{I}}$ | $\underline{\varepsilon}^{s}_{\mathrm{r},i,\mathrm{K}_p,\mathrm{H}}$ | $\underline{\varepsilon}^{s}_{\mathrm{r},i,\mathrm{K}_p,\mathrm{I}}$ | $\underline{\varepsilon}^{s}_{\mathrm{r},i,\mathrm{C}_q,\mathrm{H}}$ | $\underline{\varepsilon}^{s}_{\mathrm{r},i,\mathrm{C}_q,\mathrm{I}}$ |
| **1** | $\underline{\varepsilon}_{\mathrm{r,w}}$ | $\underline{\varepsilon}_{\mathrm{r,p}}$ | $\underline{\varepsilon}_{\mathrm{r,w}}$ | $\underline{\varepsilon}_{\mathrm{r,p}}$ | $\underline{\varepsilon}_{\mathrm{r,w}}$ | $\underline{\varepsilon}_{\mathrm{r,p}}$ |
| **2** | $\underline{\varepsilon}_{\mathrm{r,wp}}$ | $\underline{\varepsilon}_{\mathrm{r,k}}$ | | | $\underline{\varepsilon}_{\mathrm{r,wp}}$ | $\underline{\varepsilon}_{\mathrm{r,k}}$ |
| **3** | $\underline{\varepsilon}_{\mathrm{r,wpk}}$ | $\underline{\varepsilon}_{\mathrm{r,l}}$ | | | | |

The resulting effective permittivities of the individual cell compartments in each cell layer of the viable epidermis, $\underline{\varepsilon}_{\mathrm{r},i,\mathrm{K}_p}$, are shown in Fig. 9.8. The real and imaginary parts of the dielectric function of the EC space are shown in Figs. 9.8(a) and (b). These are identical for all cell layers of the viable epidermis, assuming that biochemical changes within each cell layer are expressed only by material accumulation within cell bodies (see Sec. 9.2). In this way, the graphs illustrate the Debye type characteristic of the EC, as described in Tab. 9.8. Figs. 9.8(c) and (d) show the real and imaginary parts of the effective permittivities calculated using the HB mixing rule according to Tab. 9.9. It can be seen that the permittivities of the top layer of the SG, $\mathrm{K}_{10}$, shown as a blue dotted line, have lower values than those of the basal layer, $\mathrm{K}_1$, shown by a red line. The range of values across the cell layers resulting from the different material compositions within the CP is illustrated by a gray area. These differences are caused by increasing keratin and lipid deposition within the CP towards the skin surface. Comparing the permittivities of the CP with those of the NP (see Fig. 9.8(e) and (f)), it can be seen that in both cases, there is also a range of values with lower permittivities for layers closer to the skin surface, and the range of values is significantly broader for than for the CP. This is due to the shrinkage of the nucleus and the condensation of the cromatin contained therein into a uniform mass, which was accounted for in Sec. 9.2 by shifting the water/protein ratio in favor of the protein.

The resulting effective permittivities of the individual cell compartments in each cell layer of the SC, $\underline{\varepsilon}_{\mathrm{r},i,\mathrm{C}_q}$, are shown in Fig. 9.9. Figs. 9.9(a) and (b) show the real and imaginary parts of the EC space. In contrast to the viable epidermis, saline solution is not used to model its dielectric properties. As described in detail in Sec. 9.2, the keratinocytes of the SG secrete lipid deposits from the cell interior in a process known as exocytosis. These

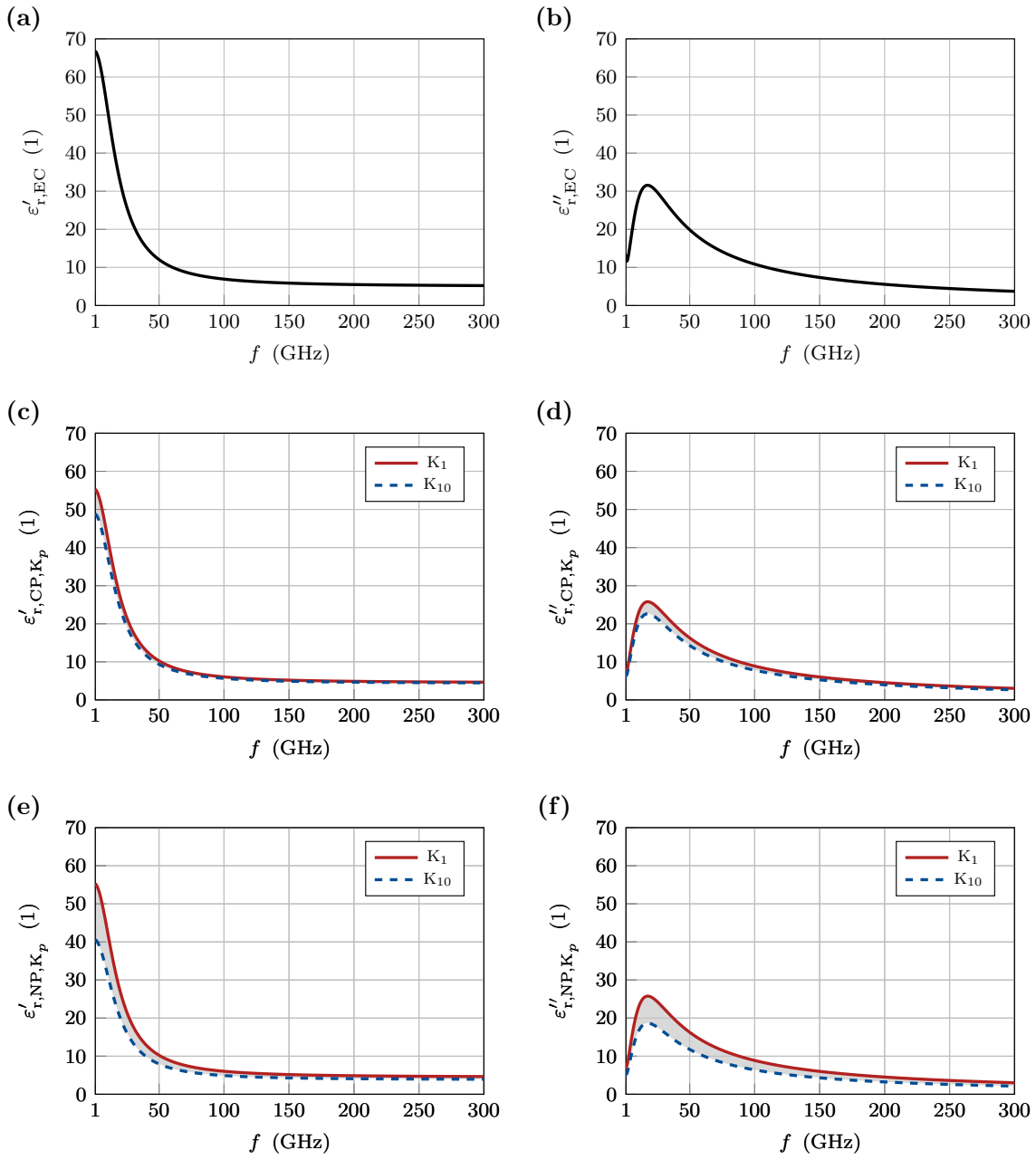


**Figure 9.8:** Overview of the dielectric material properties of the cell compartments in each cell layer of the viable epidermis determined using the mixing procedure summarized in Tab. 9.9. Real and imaginary parts of the dielectric permittivity are shown for the extracellular medium (EC) in (a) and (b), for the cytoplasm (CP) in (c) and (d), and for the nucleoplasm (NP) in (e) and (f). The range of values across the cell layers resulting from different material compositions within the CP and NP is illustrated by a gray-shaded area bound at the top by the dielectric properties of cell layer $K_1$ and at the bottom by cell layer $K_{10}$.

lipid deposits form an extracellular lipid matrix in which the corneocytes are embedded. Therefore, the graphs of the dielectric functions presented here show the Debye char-

acteristic specified in Tab. 9.8 for lipids, which is assumed to be constant for all layers of the SC. Since lipids have significantly lower values for the real and imaginary parts of their dielectric permittivities compared to physiological salt solutions, it was necessary to deviate from the previously uniformly chosen range of values (0 to 70) for the representation and, in the case of Fig. 9.9(b), to resort to a logarithmic representation. Moving on to the effective permittivities of the cell bodies shown in Figs. 9.9(c) and (d), it can be seen that both the real and imaginary parts of the permittivity show a significant range of values between the lowermost and uppermost cell layers. This is represented by a gray area bounded by a red line corresponding to layer $C_1$ and a blue dashed line corresponding to layer $C_{14}$. The decrease in permittivity towards the skin surface is associated with a decrease in the amount of water bound in the cell body (see Fig. 9.7).

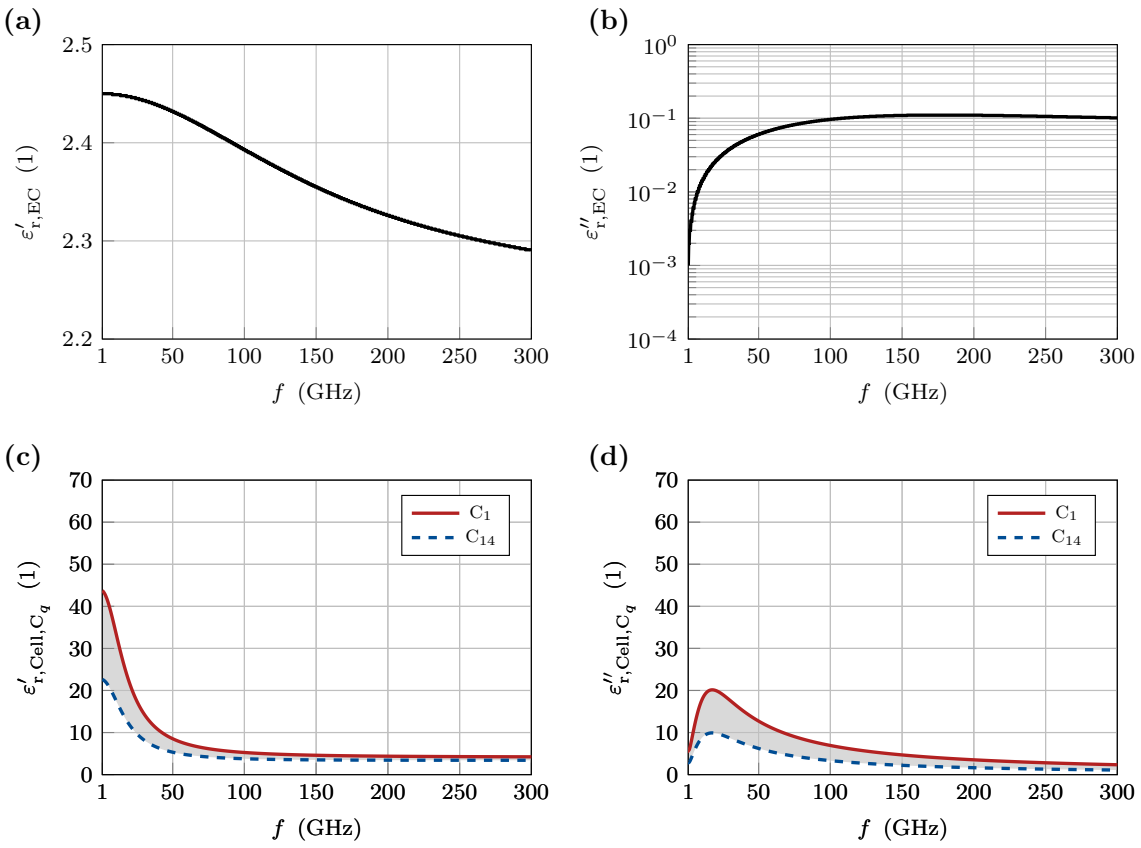


**Figure 9.9:** Overview of the dielectric material properties of the cell compartments in each cell layer of the SC determined using the mixing procedure summarized in Tab. 9.9. Real and imaginary parts of the dielectric permittivity are shown for the extracellular medium (EC) in (a) and (b), for the cell body (Cell) in (c) and (d). The range of values across the cell layers resulting from different material compositions within the cell body is illustrated by a gray-shaded area bound at the top by the dielectric properties of cell layer $C_1$ and at the bottom by cell layer $C_{14}$.

### 9.3.2 Effective Material Properties of the Epidermal Sublayers on a Macroscopic Scale

Having calculated the effective material properties of the cell compartments in the previous section, they can now be implemented into the parametric CAD models of each cell layer. Placing these models in the virtual capacitor setup used for the quasi-static EM analysis introduced in Sec. 8.1.3, numerical homogenization (as described in Sec. 8.2.1) yields the effective material parameters of each cell layer of the viable epidermis, $\underline{\tilde{\varepsilon}}_{\mathrm{r,K}_p}$, and the SC, $\underline{\tilde{\varepsilon}}_{\mathrm{r,C}_q}$.

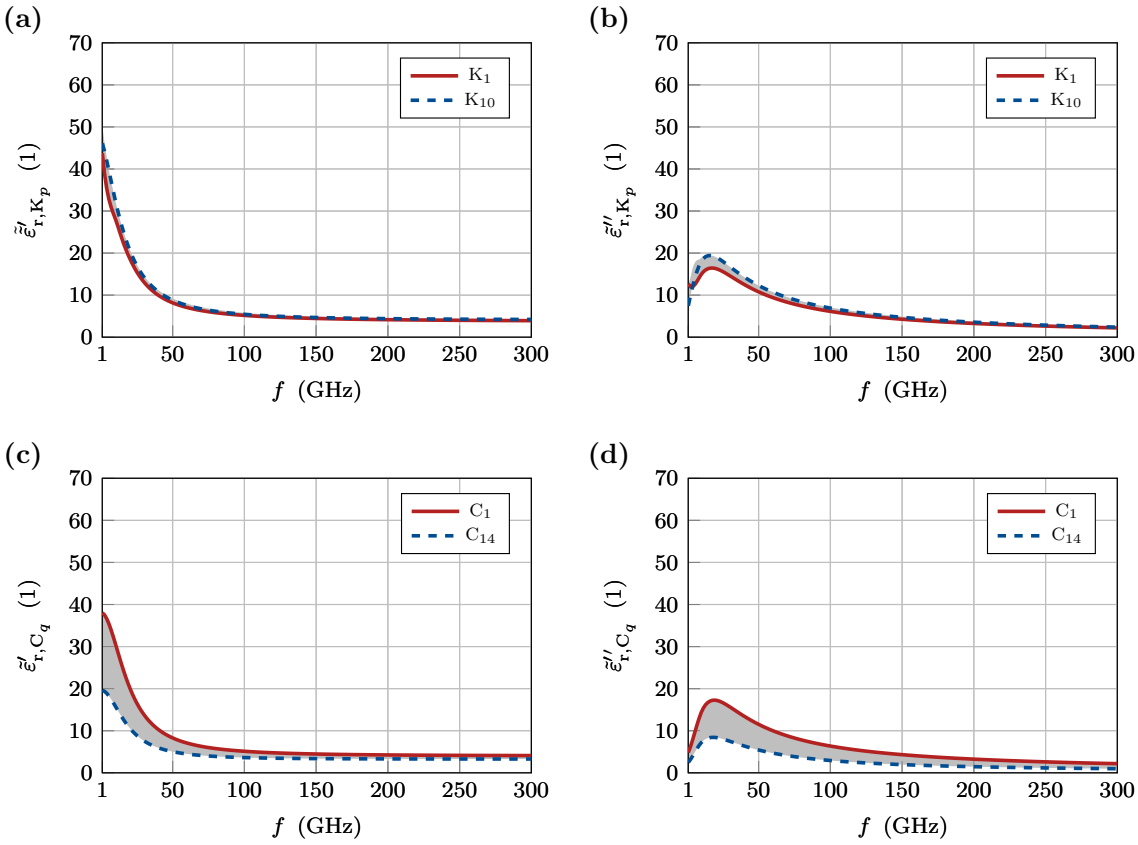


**Figure 9.10:** Overview of the effective macroscopic permittivities of each cell layer of the epidermis determined using numerical homogenisation as described in Sec. 8.2.1 and 8.1.3. In (a) and (b), the real and imaginary parts of the dielectric permittivity are shown for the individual cell layers of the viable epidermis, $\underline{\tilde{\varepsilon}}_{\mathrm{r,K}_p}$. In (c) and (d), the real and imaginary parts of the dielectric permittivity are shown for the individual cell layers of the stratum corneum (SC), $\underline{\tilde{\varepsilon}}_{\mathrm{r,C}_q}$. The range of values across the cell layers resulting from different material compositions within these layers (see Figs. 9.6 and 9.7) is illustrated by a gray-shaded area bounded at the top by the dielectric properties of the bottommost cell layer (i.e. $\mathrm{K}_1$ and $\mathrm{C}_1$) and at the bottom by the uppermost cell layer (i.e. $\mathrm{K}_{10}$ and $\mathrm{C}_{14}$).

$\underline{\tilde{\varepsilon}}_{\mathrm{r,K}_p}$ and $\underline{\tilde{\varepsilon}}_{\mathrm{r,C}_q}$ are illustrated in Figs. 9.10(a) and (b) for the cell layers of the viable epidermis and in Figs. 9.10(c) and (d) for the cell layers of the SC. Comparing Figs. 9.10(a) and (b) with (c) and (d), it can be seen that the loss of water in the SC causes a broader range of values compared to the metabolism of keratin and lipids in the viable epidermis.

The simulation was performed on a PC equipped with two Intel Xeon E5-2697 V4 processors (36 cores) and 512 GB of memory. The frequency range of interest (i.e. 1 GHz to 300 GHz) was examined and sampled with 45 linearly distributed frequency points per cell model. The data points between these sampled points were interpolated using piecewise cubic Hermite splines in post-processing. The simulation for each frequency point took approximately 33 min using a MUMPS solver. Post-processing of the data was performed within the MATLAB programming environment (version R2020a) [100].

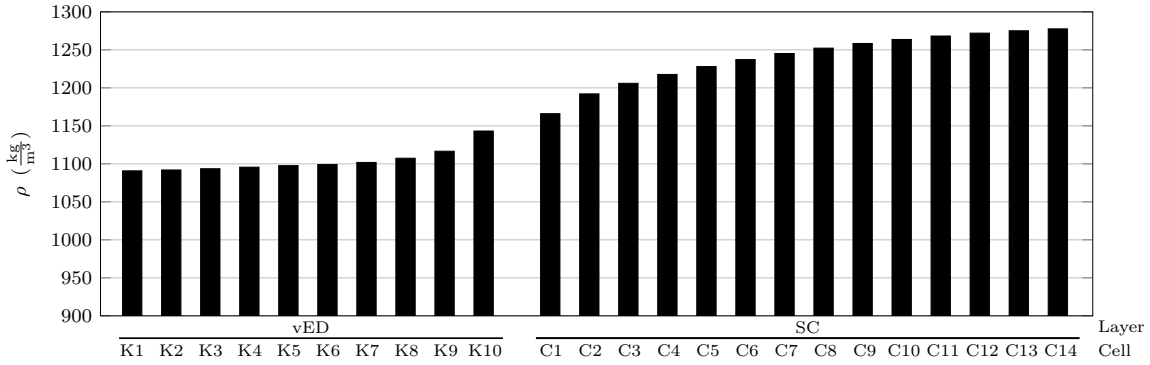


**Figure 9.11:** Volumetric mass densities of each cell layer in viable epidermis and the stratum corneum, $\rho_{\mathrm{K}_p/\mathrm{C}_q}$, illustrated by black bars and categorized according to the individual layers (i.e. $\mathrm{K}_p$ and $\mathrm{C}_q$).

Volumetric mass densities of each cell layer on a macroscopic scale, $\rho_{\mathrm{K}_p/\mathrm{C}_q}$, are determined by:

$$\rho_{\mathrm{K}_p/\mathrm{C}_q} = \sum_i \rho_{i,\mathrm{K}_p/\mathrm{C}_q} \cdot c_{\mathrm{v},i,\mathrm{K}_p/\mathrm{C}_q} \tag{9.23}$$

where, $\rho_{i,\mathrm{K}_p/\mathrm{C}_q}$ denotes volumetric mass densities of the individual cell compartments in each cell layer and $c_{\mathrm{v},i,\mathrm{K}_p/\mathrm{C}_q}$ its corresponding volume fraction (see Eqs. 9.4 and 9.19). In Fig. 9.11, it can be seen that the reduction of the water content within the cell layers towards the skin surface leads to a significant increase in the volumetric mass density.

## 9.4 Summary and Conclusions

In this chapter, a hierarchical, computational bottom-up multiscale model of the epidermis has been developed, which ultimately leads to a coherent description of the EM material properties of the epidermis at both a macroscopic and the microscopic scale (including the (sub-)cellular level). In contrast to previous multiscale approaches [14, 51,

110], which considered the epidermis to be homogenized in its entirety and thus neglected any physiological variation within this skin layer, here the epidermis has been considered as a biological system with morphology determined by the life cycle of its predominant cell type, the keratinocytes (or corneocytes). This consideration of the epidermis as an evolving system has resulted in to a stratified cell model that includes 10 cell layers in the viable epidermis and 14 cell layers in the SC. The differentiation of basal keratinocytes towards the skin surface during the keratinization process has been represented in this layer model by gradual changes from one layer to the next, which have been accounted for by two aspects:

(1) Changes in cell geometry and cell structure, and

(2) changes in the histochemical composition of the cells.

Both aspects have been considered at the microscopic level, i.e. for the models of the individual cells, as well as at the macroscopic level, i.e. for the layer model of the entire epidermis. The complex intertwined relationship between both of these aspects and the two levels on which they have been considered has been used to create a holistic representation of the epidermis. The key elements of this developmental process are recapitulated in the following.

Initially, parametric CAD models were created for both keratinocytes and corneocytes, representing their microstructure. Then, in order to implement cell differentiation, these were adapted to the physiological conditions of each cell layer using geometric parameters derived from the scientific literature. The thicknesses of the epidermal sublayers were then determined from the adapted cell models. Data from [103] and [104] were then used to derive a concentration profile for the epidermis at a macroscopic scale, considering the histochemical composition of the epidermis as a multiphase composite of water, lipids, keratin and a general protein component. From the macroscopic concentration profile, the histochemical composition of each cell layer was determined and projected onto the respective cell compartments at the microscopic scale. Based on the concentration profiles of the individual cell compartments in each cell layer, the effective permittivities of the compartments were calculated using an incremental mixing procedure using the HB mixing formula and assigned to the parameterized cell models as material parameters. The effective material properties of the individual cell layers were determined on a macroscopic scale using quasi-static computer-aided EM homogenization.

# 10 The Importance of Physiological Variations across the Epidermis for Dosimetric Investigations of EM Exposure of the Skin

In the following, extensive dosimetric studies of the skin based on numerical simulations will be performed to identify physiological variations across the epidermis as an important factor significantly affecting both the transmission of EM energy into the body surface and the distribution of this energy across the epidermis. A particular focus of these investigations will be on the proliferative pool of the epidermis (i.e., the basal and subbasal rows), which is of particular importance for skin resurfacing. Therefore, accurate prediction of EM exposure in these layers is essential to assess the risk of adverse health effects on miotic activity. The investigations will be carried out as a comparison between two stratified skin models:

(1) A model derived entirely from the scientific literature based on measured material properties of the individual sublayers of the skin, hereafter referred to as the "reference model". This represents the current state of the art in skin modeling used in virtual EM exposure studies;

(2) A modified version of this model in which the epidermis is replaced by the equivalent layer from the bottom-up model introduced in Chap. 9. This combination of the purely numerical tissue model of the epidermis and the existing measured models of the other skin layers is hereafter referred to as the "hybrid model".

The layered topology and the dielectric properties of the individual skin layers considered in the reference model are based on data reported in [4] and [5]. These studies were chosen as a scientific reference for two reasons: their great influence on the current exposure guidelines [1] (see Sec. 7.2), and the fact that they are the only scientific source providing distinct measurements of all skin sublayers in a frequency range from 1 GHz to 1 THz. The comparison between the reference model and the hybrid model thus allows a dosimetric analysis of the skin with a direct relationship to current exposure guidelines, and links numerically obtained exposure data with corresponding exposure measurements published in the references cited above.

A detailed introduction to these skin models and their implementation within a computational simulation environment is provided in Sec. 10.1. To outline the dosimetric analysis that follows, Sec. 10.2 presents the methodology and measures employed in the analysis. Subsequently, in Sec. 10.3, a thorough evaluation of the skin models is conducted, including an assessment of the permittivities of the individual epidermal cell layers incorporated into the hybrid model. Moving on to Sec. 10.4, the chapter presents the results of the investigations. This section is divided into two subsections: a reflectometric analysis of the skin models is presented first, followed by a dosimetric analysis of the power intake across the epidermis. The subsequent section, Sec. 10.5, delves into a comprehensive discussion of the obtained results. Finally, the key findings and main points discussed throughout this chapter are summarized in Sec. 10.6.

## 10.1 Macrosopic Exposure Setup

In order to study skin exposure in the most general manner, an exposure setup was established to simulate skin irradiation at operating frequencies between 1 GHz and 300 GHz, hereafter referred to as the macroscopic exposure setup. The skin model considered in this setup has a layered topology comprising the epidermis (ED), the dermis (D), the hypodermis (HYP) and underlying muscle tissue (MC) which is illustrated in Fig. 10.1(a). The thickness of the epidermis, $t_{\mathrm{ED}}$, corresponds to that of the bottom-up model derived in Chap. 9 and thus equals 132.43 µm. The thicknesses of the remaining skin layers have been adopted from [4] and correspond to the mean values at the forearm resulting in a thicknesses of $t_{\mathrm{D}} = 1080\,\mu\mathrm{m}$ and $t_{\mathrm{HYP}} = 3890\,\mu\mathrm{m}$. For numerical reasons outlined later in this section, the thickness of the muscle tissue, $t_{\mathrm{MC}}$, is considered to be infinite. For the calculation of the $SAR$ in later chapters, it is necessary to assign volumetric mass densities, $\rho_k$, with $k \in \{\mathrm{ED};\mathrm{D};\mathrm{HYP};\mathrm{MC}\}$, to each skin sublayer. These values are taken from [51] resulting in the volumetric mass densities given in Tab. 10.1. All of the thicknesses and volumetric mass densities mentioned above apply to both the reference model and the hybrid model, with only one exception: $\rho_{\mathrm{ED}}$. The hybrid model applies the specific volumetric mass densities for each epidermal cell layer, $\rho_{\mathrm{ED,K}_p/\mathrm{C}_q}$, shown in Fig. 9.11. The thicknesses of the individual skin layers, $t_k$, and the volumetric mass densities assigned to these layers, $\rho_k$, are summarized in Tab. 10.1.

**Table 10.1:** Overview of the thicknesses of the individual skin layers, $t_k$, and of the volumetric mass densities, $\rho_k$, assigned to these layers.

| | **Epidermis (ED)** | **Dermis (D)** | **Hypodermis (HYP)** | **Muscle (MC)** |
|---|---|---|---|---|
| **Thickness $t_i$ (µm)** | 132.43 | 1080 | 3890 | $\infty$ |
| **Density $\rho_i$ (kg/m$^3$)** | 1190 | 1116 | 971 | 1041 |

In addition to the values above, complex dispersive permittivities need to be applied to the individual skin layers with the real and imaginary values, $\underline{\varepsilon}_{\mathrm{r},k}$, displayed in Figs. 10.1(b)

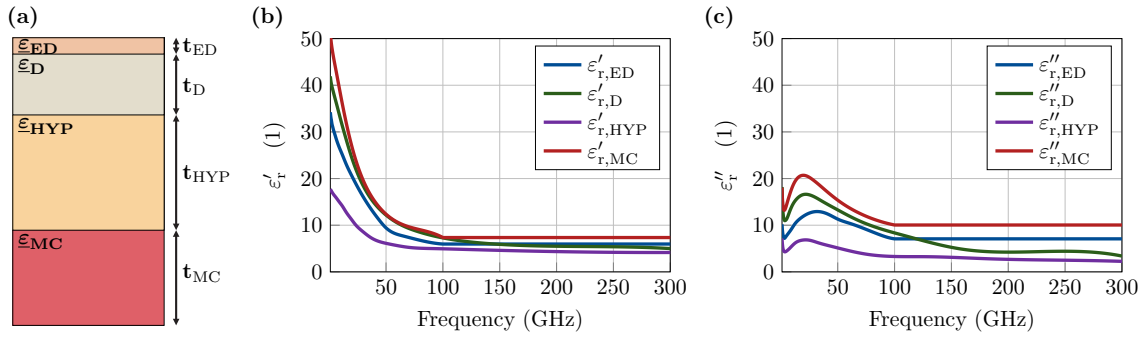


**Figure 10.1:** Overview of the layered topology of the skin model (not to scale) and the complex dielectric material properties, $\underline{\varepsilon}_{r,k}$, assigned to the individual sublayers of the skin: (a) Illustration of the stratified skin model showing the complex permittivities, $\underline{\varepsilon}_{r,k}$ and thicknesses, $t_k$, assigned to the individual tissue layers. (b) Real part of the permittivity, $\varepsilon'_{r,k}$. (c) Imaginary part of the permittivity, $\varepsilon''_{r,k}$. The index $k \in \{\mathrm{ED};\mathrm{D};\mathrm{HYP};\mathrm{MC}\}$ denotes epidermis, dermis, hypodermis and muscle tissue respectively.

and (c) respectively. These material parameters, which were originally published in [4] and [5], are based on measurements on pig skin. However, it should be noted that there is a lack of data contained in this data source. Only the material properties of the dermis and hypodermis, $\underline{\varepsilon}_{r,D}$ and $\underline{\varepsilon}_{r,HYP}$, have been reported over the whole frequency range under investigation. The effective material properties of the remaining sublayers of the skin, $\underline{\varepsilon}_{r,ED}$ and $\underline{\varepsilon}_{r,MC}$, have only been reported between 1 GHz and 100 GHz. To compensate for the lack of data, the values of $\underline{\varepsilon}_{r,ED}$ and $\underline{\varepsilon}_{r,MC}$ for frequencies above 100 GHz are set equal to those at 100 GHz. The extrapolation of the documented values on the basis of a constant is chosen over more refined methods, such as the extrapolation of a Debye function, in order to be able to qualitatively identify possible artefacts resulting from this estimation in the simulation results. The dispersive permittivities of the individual epidermal cell layers, $\underline{\tilde{\varepsilon}}_{r,\mathrm{K}_p\mathrm{C}_q}$, which are considered in the hybrid model, can be taken from Fig 8.5.

After defining the skin model, it needs to be embedded in a generic exposure setup, which is numerically implemented using the COMSOL Multiphysics software environment [95], allowing the determination EM fields penetrating in the individual skin layers. This macroscopic exposure setup is illustrated in Fig. 10.2. A plane wave is emitted from a non-reflective port at an angle of incidence, $\alpha$, (here 0°) having either s or p-polarization with respect to the reflection plane (i.e. xz plane). The amplitude of the incident plane wave corresponds to a constant input power, $P_{inc}(\omega)$, which is derived from the incident power density, $S_{inc}(\omega)$, defined in the basic restrictions (see Tab. 7.1). The reflected power, $P_R$, is detected by the same non-reflective port, and the power transmitted to the skin tissue, $P_T$, is calculated from $P_T = P_{inc} - P_R$. From these values, the power reflection coefficient, $R$, and the power transmission coefficient, $T$, are given by

$$R = \frac{P_R}{P_{inc}} \tag{10.1}$$

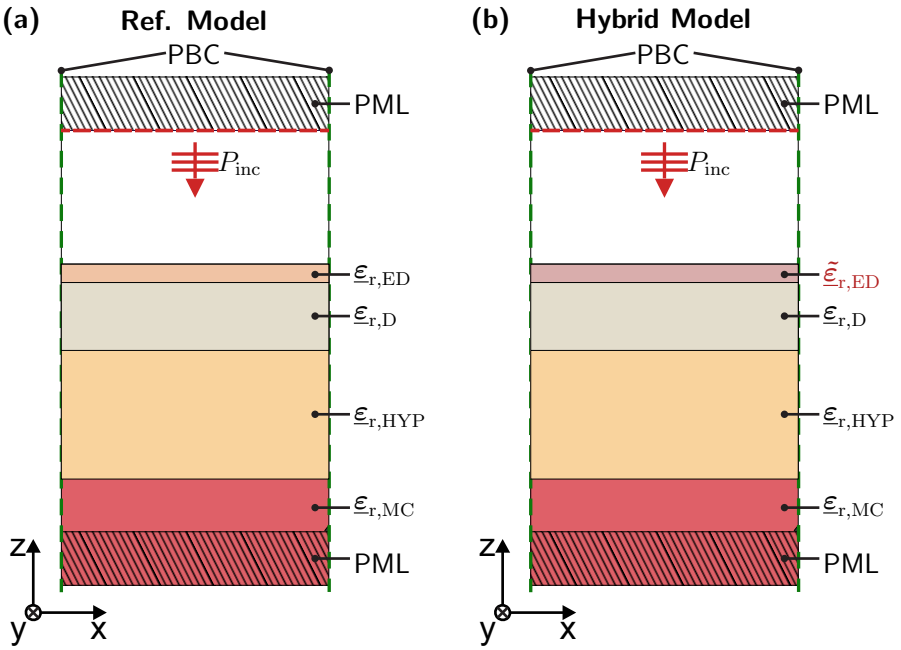


**Figure 10.2:** An overview of the macroscopic exposure setup: The stratified skin model is exposed to a plane EM wave using a non-reflective port. The amplitude of the incident plane wave corresponds to a constant input power, $P_{inc}(\omega)$, which is derived from an incident power density, $S_{inc}(\omega)$, defined in the basic restrictions outlined in Chap. 7. The top and bottom of the computational domain are terminated with perfectly matched layers (PML). Periodic boundary conditions (PBC) are used to prevent fringing fields. The square-shaped surface area under exposure is $1\,\mathrm{mm}^2$. The complex permittivities of the individual skin layers, $\underline{\varepsilon}_{r,k}$, are adopted from [4] and [5]. The index $k \in \{\mathrm{ED};\mathrm{D};\mathrm{HYP};\mathrm{MC}\}$ denotes epidermis, dermis, hypodermis and muscle respectively. The hybrid model deviates from the reference model by assigning material properties calculated using bottom-up multiscale modelling, $\underline{\tilde{\varepsilon}}_{r,ED}$, comprising the effective permittivities of the individual epidermal skin layers, $\underline{\tilde{\varepsilon}}_{r,K_p}$ and $\underline{\tilde{\varepsilon}}_{r,C_q}$, derived in Chap. 9.

and

$$T = \frac{P_T}{P_{inc}} \tag{10.2}$$

To avoid further reflections of waves from the outer top and bottom boundaries, the computational domain is terminated above and below with perfectly matched layers (PML). Similar to the capacitor setup introduced in Chap. 8, periodic boundary conditions (PBCs) are also introduced into the macroscopic exposure setup to prevent fringing fields. Figs. 10.2(a) and (b) illustrate the different material properties assigned to the individual skin layers depending on the choice of either the reference or the hybrid model introduced earlier. Both models have a square-shaped surface under exposure with an area of $1\,\mathrm{mm}^2$.

The simulation was performed on a PC equipped with an Intel i7-6700k processor (4

cores) and 64 GB of memory. In this study, a frequency range between 1 GHz and 300 GHz was investigated and sampled with 227 frequency points distributed linearly. The data points in between these sampled points were interpolated using cubic splines in post-processing. The simulation for each frequency point lasted approximately 10 seconds using a MUMPS solver. The post-processing of the data was performed within the MATLAB programming environment (version R2020a) [100].

## 10.2 Outline of the Dosimetric Analysis of the Epidermis

In order to assess the importance of physical variations across the epidermis, the EM exposure of the skin is investigated in a three-fold analysis. In the first step, the total power transmitted to to the skin is analyzed in a reflectometric analysis. Following on from this, the power transfer to deeper sublayers of the skin is investigated. In the last step, the power distribution across a virtual volume corresponding to the epidermal cell layers, $\mathrm{K}_p$ and $\mathrm{C}_q$, is analyzed.

While the reflectometric analysis of the total power transmitted to the skin tissue is performed using the power reflection and transmission coefficient introduced in Sec. 10.1 (see Eqs. 10.1 and 10.2), the latter two aspects need additional introduction. As shown in Figs. 10.3(a) and (b), the sublayered structure of the epidermis is illustrated in both the reference model and the bottom-up model. As indicated by the different color schemes, the individual cell layers in the reference model are assigned identical dispersive material properties, $\underline{\varepsilon}_{\mathrm{r,ED}}(\omega)$, while those of the hybrid model have individual ones, $\underline{\varepsilon}_{\mathrm{r,K}_p/\mathrm{C}_q}(\omega)$. The implementation of these cell layers in the macroscopic exposure setup as distinct computational domains allows the integration of the volumetric loss density, $p(\vec{r},\omega)$, over each individual layer. This leads to the determination of the power induced within each of these layers, $P_{\mathrm{K}_p/\mathrm{C}_q}(\omega)$.

To enable an accurate comparison between the transfer of power into deeper sublayers of the skin provided by each of the models, the power absorbed by the epidermis,

$$P_{\mathrm{ED}}(\omega) = \sum_{p=1}^{10} P_{\mathrm{K}_p}(\omega) + \sum_{q=1}^{14} P_{\mathrm{C}_q}(\omega) \quad , \tag{10.3}$$

needs to be expressed relative to the total power transmitted to the skin tissue, as this obviously differs between models. This is given by

$$A_{\mathrm{ind,ED}}(\omega) = \frac{P_{\mathrm{ED}}(\omega)}{P_{\mathrm{T}}(\omega)} \tag{10.4}$$

In order to compare the power distribution within the epidermis resulting from the two models, the power absorbed by the viable epidermis (vED) and the SC, $P_{\mathrm{vED}}$ and $P_{\mathrm{SC}}$, are

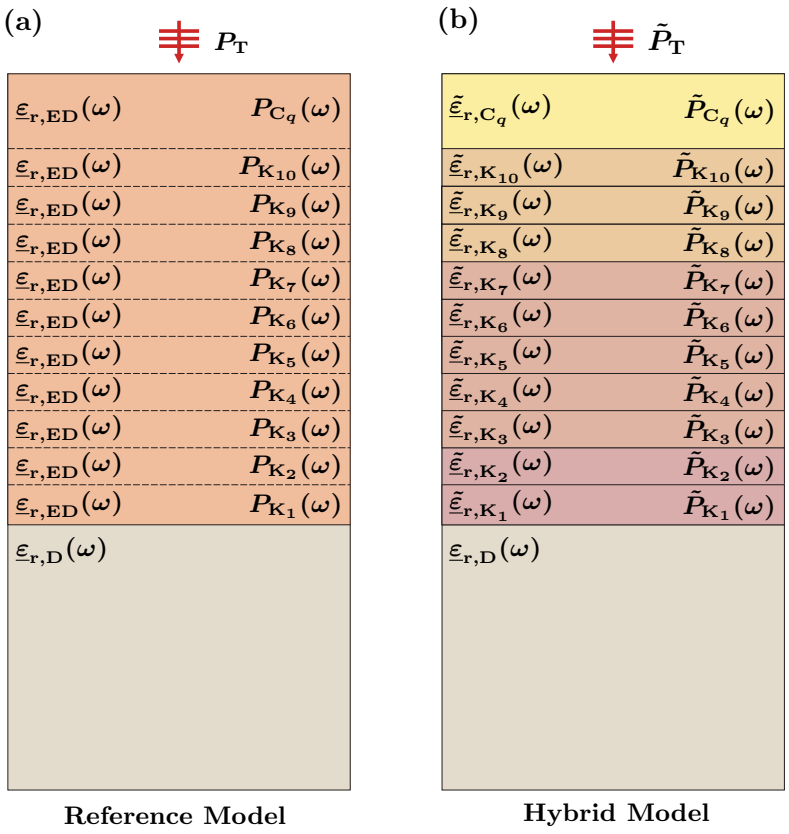


**Figure 10.3:** Conceptual overview of the dosimetric analysis of the epidermis, illustrating its layered structure: All of the individual cell layers in the reference model, $K_p$ and $C_q$, are assigned identical dispersive material properties, $\underline{\varepsilon}_{r,ED}(\omega)$, while those of the hybrid model have individual ones, $\underline{\varepsilon}_{r,K_p/C_q}(\omega)$. This is indicated by the different color schemes given to these layers in Figs. (a) and (b). The implementation of these cell layers in the macroscopic exposure setup as distinct computational domains allows the integration of the volumetric loss density, $p(\vec{r},\omega)$, over each individual layer. This leads to the determination of the power induced within each of these layers, $P_{K_p/C_q}(\omega)$. Considering the power transmitted to the skin tissue, $P_T(\omega)$, which differs between models due to different epidermal permittivities, a comparative analysis of the power transfer to deeper sublayers of the skin and the power distribution across the epidermal cell layers must be expressed relative to $P_T(\omega)$. In all of the above parameters, a tilde will be added to refer to the hybrid model rather than the reference model.

expressed with respect to the total power absorbed by the epidermis, $P_{ED}$, giving

$$A_{ED,vED/SC}(\omega) = \frac{P_{vED/SC}(\omega)}{P_{ED}(\omega)} \tag{10.5}$$

A more detailed overview of the distribution of the power across the individual cell layers

of the epidermis is given by

$$A_{\mathrm{ED,K}_p/\mathrm{C}_q}(\omega) = \frac{P_{\mathrm{K}_p/\mathrm{C}_q}(\omega)}{P_{\mathrm{ED}}(\omega)} \tag{10.6}$$

where $P_{\mathrm{K}_p/\mathrm{C}_q}(\omega)$ denotes the power absorbed by these layers. In all of the above parameters, a tilde will be added to refer to the hybrid model rather than the reference model.

## 10.3 Evaluation of the Skin Models: Revealing Biases and Assessing Epidermal Permittivities

In order to interpret and ultimately draw meaningful conclusions from the simulation results presented in the next section, a detailed comparison of the two skin models is required. This comparison aims to reveal biases in the reference model and assess the permittivities of the individual epidermal cell layers, which are considered only in the hybrid model.

To provide such a comprehensive analysis, it is necessary to delve into the measurements conducted by Sasaki, as documented in [4]. According to the study, the measurements of individual skin layers were performed 48 hours after slaughter. During transport, the sample was kept at a temperature of 4 °C to slow down biological decay. The actual measurements were carried out at a temperature ranging from 34 °C to 37 °C. The reported thickness of the epidermis was 1.1 mm, while the dermis measured 1.5 mm in thickness. However, further studies on pig skin from different sites, as outlined in [111], indicate significantly lower average epidermal thicknesses ranging from 51.6 µm to 59.9 µm. Considering these findings and the undulating topology of the epidermis/dermis interface (see Fig. 3.1), it is likely that the sectioning of the epidermis in [4] was performed incorrectly, potentially including parts of the dermis. Therefore, it must be borne in mind when comparing the hybrid model with the reference model that these measurements may contain a certain bias in the measured epidermal material properties that result from this commonly occurring difficulty.

Additionally, it should be noted that the measurements of $\varepsilon_{\mathrm{r,ED}}$ are limited to frequencies up to 100 GHz, which prevents verification at higher frequencies. Consequently, the verification will be primarily based on $\varepsilon_{\mathrm{r,D}}$, as it closely corresponds to the epidermis in terms of water concentration.

Given these measurement-related challenges, a comparison is performed between the calculated and adopted epidermal permittivities. Fig. 10.4 presents the dispersive permittivities of the epidermis in the hybrid model ($\underline{\tilde{\varepsilon}}_{\mathrm{r,K}_p/\mathrm{C}_q}$), the reference model ($\underline{\varepsilon}_{\mathrm{r,ED}}$), and the dermis ($\underline{\varepsilon}_{\mathrm{r,D}}$). Comparing the real parts of the dispersive permittivities of the individ-

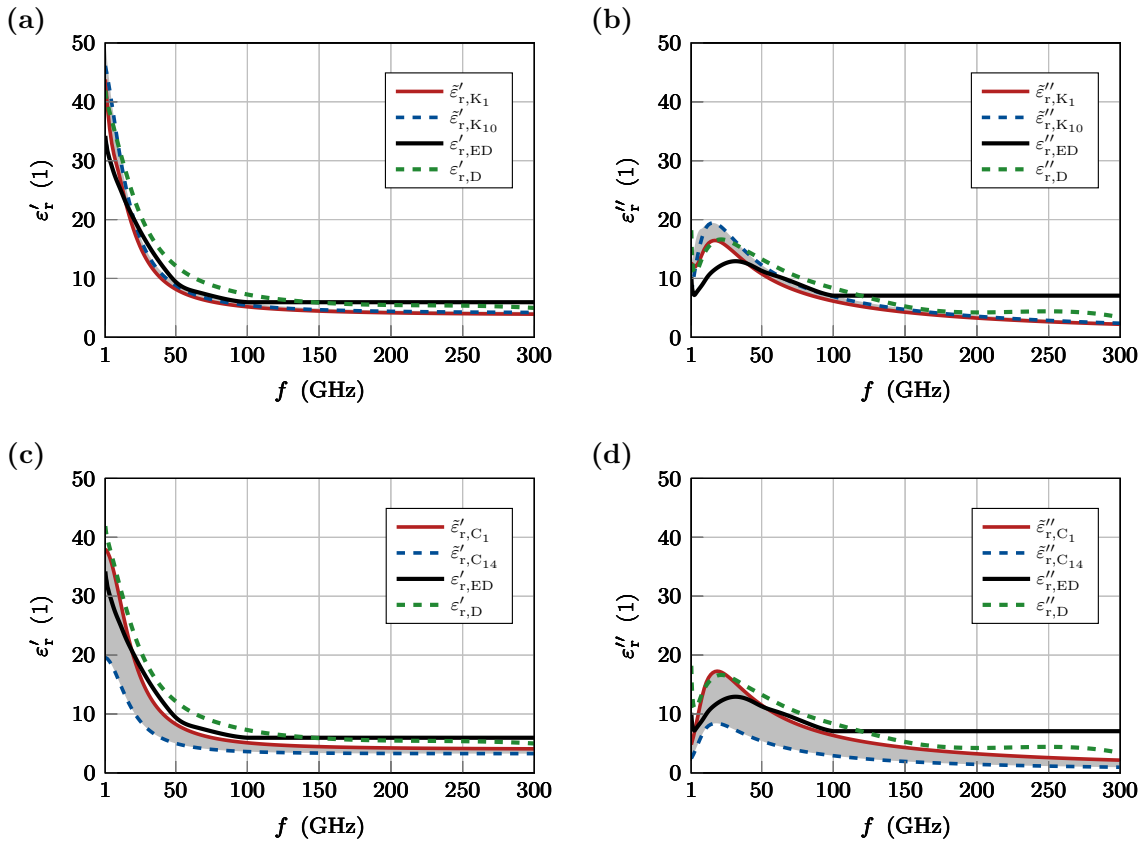


**Figure 10.4:** Comparison of the measured material properties of the epidermis, $\underline{\varepsilon}_{\mathrm{r,ED}}$, and the dermis, $\underline{\varepsilon}_{\mathrm{r,D}}$, taken from [4, 5] with those of the epidermal cell layers, $\tilde{\underline{\varepsilon}}_{\mathrm{r,K}_p/\mathrm{C}_q}$, determined using the bottom-up model. (a) and (b) show the real and imaginary parts of the measured material properties respectively, comparing the data with that for the viable epidermis determined using the bottom-up model (see Chap. 9). (c) and (d) show the equivalent comparison with the SC.

ual epidermal cell layers calculated using the bottom-up model ($\tilde{\varepsilon}'_{\mathrm{r,K}_p/\mathrm{C}_q}$) with the measured permittivities of the epidermis ($\varepsilon'_{\mathrm{r,ED}}$) and dermis ($\varepsilon'_{\mathrm{r,D}}$) from [4, 5], a good agreement is observed, particularly in the viable epidermis as shown in Fig. 10.4(a). Moving attention to the stratum corneum, Fig. 10.4(c) indicates a prominent correlation between the measured material parameters and those of the bottommost cell layer ($\mathrm{C}_1$), with the degree of correspondence decreasing towards the skin surface (cell layer $\mathrm{C}_{14}$). This observation can be attributed to the water concentration profile within the epidermis, as depicted previously in Fig. 9.4(a), which demonstrates a substantial decrease in water content within the stratum corneum (SC) and consequently leads to a lower permittivity. Considering the work of Ziskin and Alekseev [52, 58], which emphasizes the significance of water content in determining tissue material properties, the histochemical assumptions made in the derivation of $\varepsilon_{\mathrm{r,K}_p/\mathrm{C}_q}$ using the bottom-up model of the epidermis can be deemed reliable.

Examining the imaginary parts shown in Figs. 10.4(b) and (d), it becomes evident that ex-

trapolating $\underline{\varepsilon}_{\mathrm{r,ED}}$ beyond 100 GHz by equating it with $\underline{\varepsilon}_{\mathrm{r,ED}}$ at 100 GHz leads to notable deviations from both the effective permittivities predicted by the bottom-up model ($\tilde{\varepsilon}''_{\mathrm{r,K}_p/\mathrm{C}_q}$) and the measured permittivities of the dermis ($\varepsilon''_{\mathrm{r,D}}$). In contrast, a generally strong correlation is observed between $\varepsilon''_{\mathrm{r,D}}$ and $\tilde{\varepsilon}''_{\mathrm{r,K}_p/\mathrm{C}_q}$, with significant deviations from $\varepsilon''_{\mathrm{r,D}}$ are only observed for the upper cell layers of the SC, which can be explained by the lower water content in those layers.

In summary, the evaluation of skin models reveals biases in the reference model due to incorrect sectioning of the epidermis and potential inclusion of dermal parts. In addition, the limited availability of measurements for higher frequencies necessitates the use of the dermal permittivity for correlation analysis. As such, deviations arise when extrapolating beyond 100 GHz. However, a strong correlation persists for the dermal permittivity with significant deviations occurring only in the upper layers of the stratum corneum due to varying water concentration. Comparing the calculated epidermal permittivities with those adopted from Sasaki [4, 5], a significant agreement is observed between the real parts of individual epidermal cell layers and measured values, particularly in the viable epidermis. The above assessment demonstrates that the permittivities derived from the bottom-up model can be considered reliable, enabling more precise investigations in the following.

## 10.4 Results

In the following, the results generated by the macroscopic exposure setup are presented illustrating two aspects: (1) The total power intake of the skin, and (2) the absorption of the individual cell layers of the epidermis.

### 10.4.1 Reflectometric Analysis of the Skin Models

The simulation results of the reflectometric analysis of the reference and hybrid models are displayed in Fig. 10.5. In Fig. 10.5(a), the power of the EM wave to which the skin is exposed, $P_{\mathrm{inc}}$, is shown as a solid black line. In addition, the dashed black and dashed red lines illustrate the power transmitted in the skin tissue of the reference and hybrid model respectively. These are denoted by $P_{\mathrm{T}}$ and $\tilde{P}_{\mathrm{T}}$. Comparing these values, there is a difference between the two skin models starting at about 100 GHz and becoming more significant with increasing frequency. The same result can also be observed in Fig. 10.5(b), where the power reflection and transmission coefficients of the reference model, $R$ and $T$, are plotted alongside those of the hybrid model, $\tilde{R}$ and $\tilde{T}$. Moving on to Fig. 10.5(c), the relative differences in reflection and transmission between the two skin models, defined as $\Delta R = \frac{R-\tilde{R}}{R}$ and $\Delta T = \frac{T-\tilde{T}}{T}$, are analyzed in more detail. Regarding the relative deviations between the two models, the frequency interval studied can be divided into three subintervals: ① an interval between 1 GHz and 50 GHz where only moderate deviations

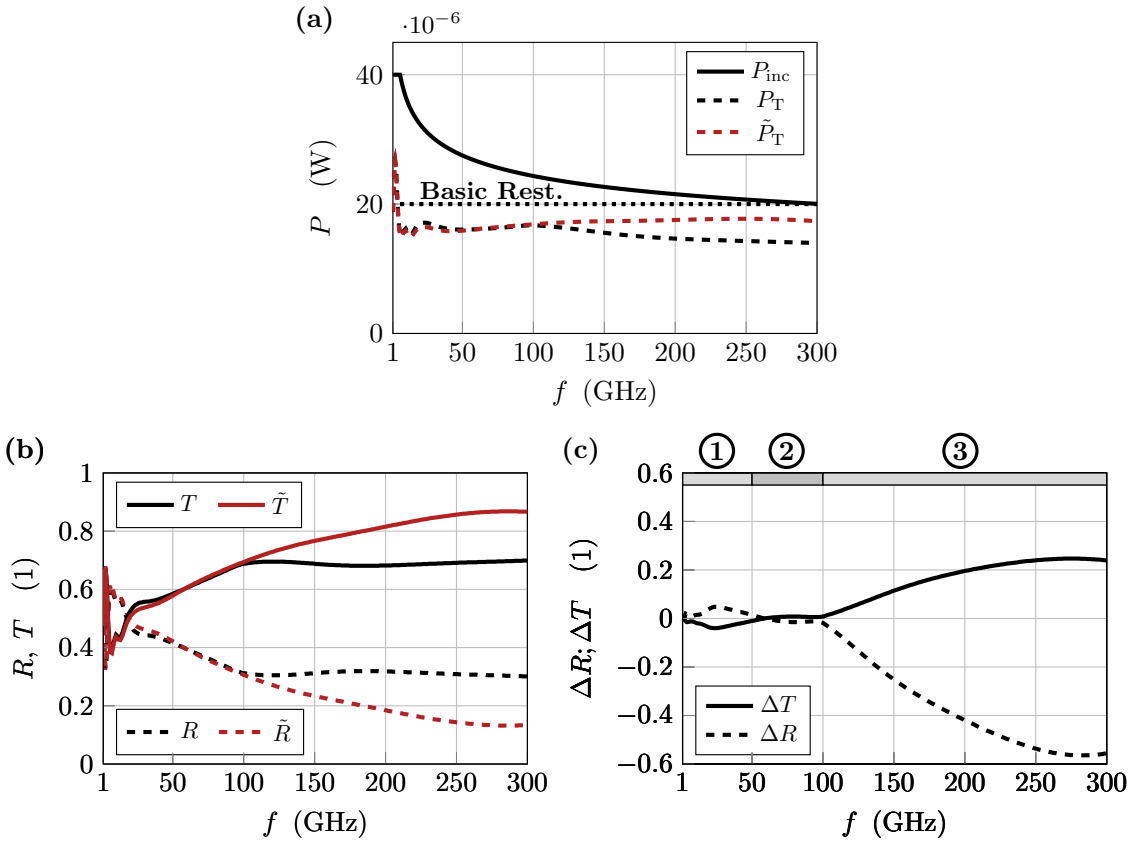


**Figure 10.5:** Overview of the simulation results of the reflectometric analysis of the reference and hybrid models: (a) Incident power, $P_{\mathrm{inc}}(\omega)$, derived from $S_{\mathrm{inc}}(\omega)$ corresponding to a square skin area of 1 mm$^2$. $P_{\mathrm{T}}(\omega)$ and $\tilde{P}_{\mathrm{T}}(\omega)$ denote the power absorbed by the reference model and the hybrid model respectively. The constant labeled "Basic Rest." corresponds to the absorbed power density, $S_{\mathrm{ab}}(\omega)$, defined in [1] by the ICNIRP guidelines as a basic restriction (see Tab. 7.1). (b) Spectral analysis of the power reflection and the power transmission coefficients. $R$ and $T$ correspond to the reference model and $\tilde{R}(\omega)$ and $\tilde{T}(\omega)$ correspond to the hybrid model. (c) Relative deviation of $R(\omega)$ and $T(\omega)$ between the two skin models.

are observed, reaching a maximum of about 4.8 % and −4 % at 24 GHz for reflection and transmission respectively; ② an interval between 50 GHz and 100 GHz where negligible deviations can be observed; ③ an interval between 100 GHz and 300 GHz where significant deviations occur with increasing frequency reaching a maximum of about −56.4 % and 24.7 % at 280 GHz for reflection and transmission respectively.

Moving on to the dosimetric analysis of the epidermis in the next section, the power transfer to deeper sublayers of the skin and the power distribution across the epidermal cell layers are analyzed in the context of these subintervals.

## 10.4.2 Dosimetric Analysis of the Epidermis

The results of the power absorbed by the epidermis, $P_{\mathrm{ED}}(\omega)$, relative to the power transmitted in the skin, $P_{\mathrm{T}}(\omega)$, are shown in Fig. 10.6. In Fig. 10.6(a), solid black and red lines

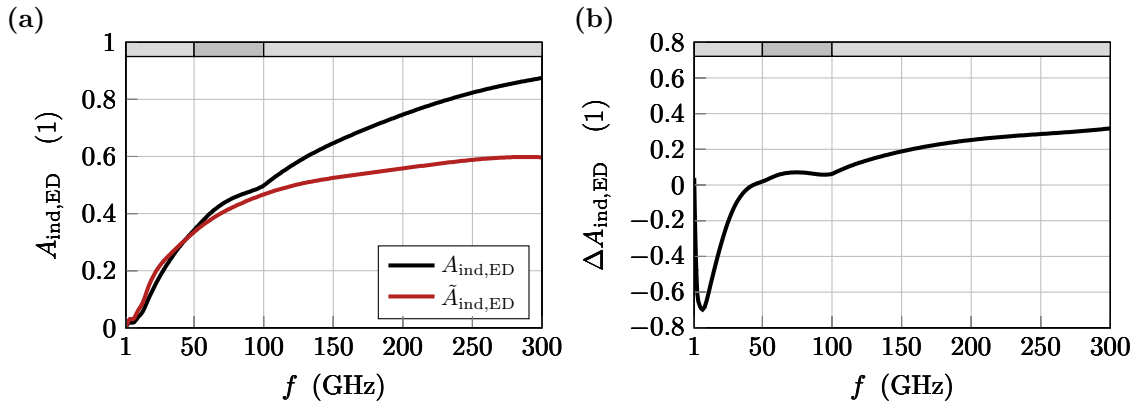


**Figure 10.6:** Overview of the power absorbed by the epidermis (ED), $P_{\mathrm{ED}}(\omega)$, relative to the power transmitted to the skin tissue, $P_{\mathrm{T}}$: (a) Spectral analysis of the absorption coefficients according to Eq. 10.4, where that of the reference model, $A_{\mathrm{ind,ED}}$, is shown as a solid black line and that of the hybrid model, $\tilde{A}_{\mathrm{ind,ED}}$, is shown as a solid red line. (b) Relative deviation between the two skin models.

illustrate the absorption coefficients of the epidermis as defined in Eq. 10.4 for the reference and hybrid model respectively. These are denoted by $A_{\mathrm{ind,ED}}$ and $\tilde{A}_{\mathrm{ind,ED}}$. Comparison of the two graphs shows that absorption within the epidermis at 1 GHz is only 0.5 % of the power transmitted to the skin tissue, but increases rapidly with increasing frequency, reaching 35 % at the upper end of interval ①, at 50 GHz. This trend continues at frequencies higher than 50 GHz, although the increase in absorption, especially in the hybrid model, is significantly lower, reaching about 60 % at 300 GHz. The absorption in the reference model increases to 87 % at 300 GHz and shows a discontinuity at 100 GHz, which is due to the decision to keep $\underline{\varepsilon}_{\mathrm{r,ED}}$ fixed at all for frequencies higher than 100 GHz. Moving on to Fig. 10.6(b), the relative differences in epidermal absorption between the two skin models, $\Delta A_{\mathrm{ind,ED}}$, are displayed in more detail. $\Delta A_{\mathrm{ind,ED}}$ is defined as

$$\Delta A_{\mathrm{ind,ED}} = \frac{A_{\mathrm{ind,ED}} - \tilde{A}_{\mathrm{ind,ED}}}{A_{\mathrm{ind,ED}}}. \tag{10.7}$$

It can be seen that the relative deviation is −65 % in interval ① increasing a moderate 8 % to 32 % in interval ② before increasing gradually after the discontinuity to a final value of 32 % in interval ③.

Having analyzed the power absorbed by the epidermis, its distribution within this skin layer is now examined. Following Eq. 10.5 above, the results of the power absorbed by the viable epidermis (vED) and the SC, $P_{\mathrm{vED}}$ and $P_{\mathrm{SC}}$, are shown in Fig. 10.7 relative to the

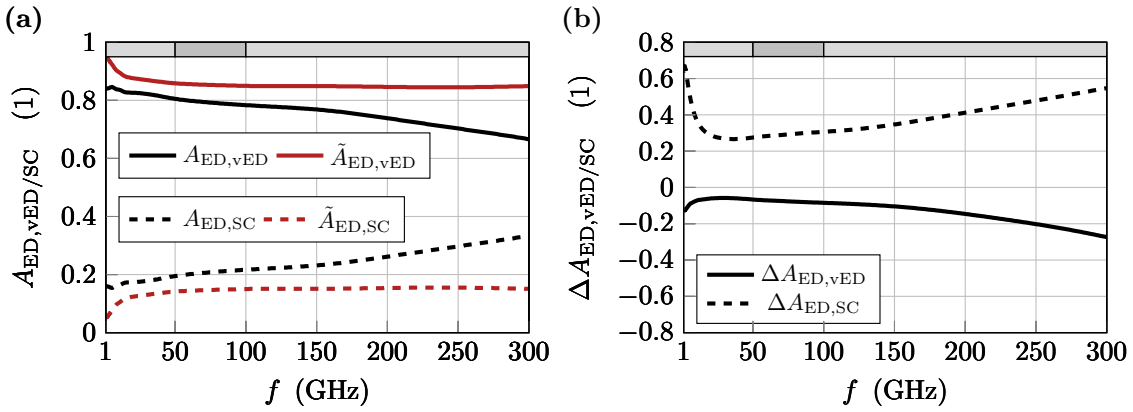


**Figure 10.7:** Analysis of the power distribution across the epidermis in accordance with Eq. 10.5: (a) Power absorbed by the epidermis in the reference and hybrid models, denoted by $A_{\mathrm{ED,vED/SC}}$ and $\tilde{A}_{\mathrm{ED,vED/SC}}$ respectively. (b) Relative deviation of $\Delta A_{\mathrm{ED,vED/SC}}$ between the two skin models.

total power absorbed by the epidermis, $P_{\mathrm{ED}}$. In Fig. 10.7(a), the solid black and red lines illustrate the fraction of power absorbed by the viable epidermis, $A_{\mathrm{ED,vED}}$ and $\tilde{A}_{\mathrm{ED,vED}}$, and the dashed black and red lines illustrate the fraction of power absorbed by the SC, $A_{\mathrm{ED,SC}}$ and $\tilde{A}_{\mathrm{ED,SC}}$. In addition, the corresponding relative deviations between the two skin models, $\Delta A_{\mathrm{ED,vED}}$ and $\Delta A_{\mathrm{ED,SC}}$, are shown in Fig. 10.7(b). It can be seen that the reference model predicts a significantly higher absorption within the SC and thus shows lower absorption within the viable epidermis.

Following these results, which only distinguishes between the larger-scale structures of the epidermis, a detailed analysis of the power distribution within the individual cell layers of the viable epidermis, $\mathrm{K}_p$, is now performed, the results of which are shown in Fig. 10.8. Following Eq. 10.6, the power absorbed by these cell layers, $P_{\mathrm{K}_p}$, relative to the total power absorbed by the epidermis, $P_{\mathrm{ED}}$, is shown in Figs. 10.8(a) and (b) for the reference and hybrid model respectively. The graphs corresponding to each of the examined cell layers are represented by solid, dashed, dotted, and dash-dotted lines. They are colored in magenta ($\mathrm{K}_1$ through $\mathrm{K}_4$), green ($\mathrm{K}_5$ through $\mathrm{K}_8$), and blue ($\mathrm{K}_9$ and $\mathrm{K}_{10}$), as indicated in the legend. The relative deviation between the two models, $\Delta A_{\mathrm{ED,K}_p}$, are displayed in Fig. 10.8(c). $\Delta A_{\mathrm{ED,K}_p}$ is defined as

$$\Delta A_{\mathrm{ED,K}_p} = \frac{A_{\mathrm{ED,K}_p} - \tilde{A}_{\mathrm{ED,K}_p}}{A_{\mathrm{ED,K}_p}}. \tag{10.8}$$

Focusing on the proliferative pool of the epidermis only, it being of particular interest in this thesis, $\Delta A_{\mathrm{ED,K}_1}$ and $\Delta A_{\mathrm{ED,K}_2}$ show deviations ranging between −29 % at the beginning of interval ① and −49 % at the end of interval ③. In addition, an overview of the power distribution across the SC is provided in Appendix C for completeness.

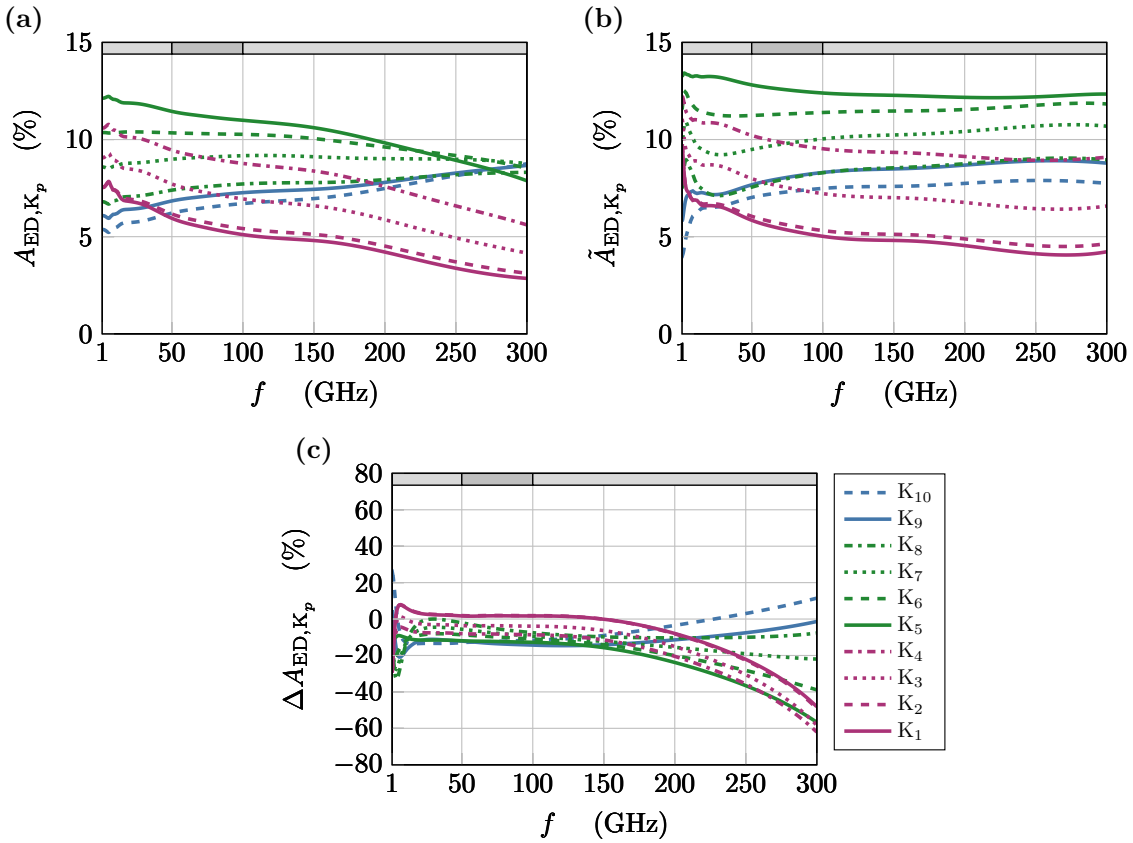


**Figure 10.8:** Analysis of the power distribution over the epidermal cell layers, $K_p$, according to Eq. 10.6: (a)-(b) Power absorbed by the epidermal cell layers, $K_p$, in the reference and hybrid models, denoted by $A_{\mathrm{ED,K}_p}$ and $\tilde{A}_{\mathrm{ED,K}_p}$, respectively. (c) Relative deviation of $\Delta A_{\mathrm{ED,K}_p}$ between the two skin models, $\Delta A_{\mathrm{ED,K}_p}$. The plots corresponding to each of the investigated cell layers are represented by solid, dashed, dotted and dash-dotted lines. They are colored in magenta ($K_1$ through $K_4$), green ($K_5$ through $K_8$), and blue ($K_9$ and $K_{10}$) as indicated in the legend.

## 10.5 Discussion

The comparison of the reflection and transmission properties of the two skin models in Sec. 10.4 shows significant differences at frequencies above 100 GHz. The power transmission coefficient calculated for the hybrid model is up to 24 % higher than that calculated for the reference model. This indicates a strong underestimation of the energy absorption of skin tissues using the reference model. With reference to the evaluation of the skin models performed in Sec. 10.3, it can be assumed that the imaginary part of the permittivity of the epidermis is significantly smaller than the extrapolated value used in the reference model. The extrapolation of the measured epidermal permittivity, $\underline{\varepsilon}_{\mathrm{r,ED}}(f > 100\,\mathrm{GHz}) = \underline{\varepsilon}_{\mathrm{r,ED}}(f = 100\,\mathrm{GHz})$, was performed to compensate for the missing data above the delimiting frequency. Consequently, the model based on [4] seems to require careful consideration in dosimetric studies of the skin above 100 GHz because of

this strong underestimation of the power transmitted to the tissue.

Another observation in the investigations performed in this study was the distribution of the power intake throughout the skin tissue. As shown in Fig. 10.6 (see Sec. 10.4.2), the epidermis initially absorbs only a small fraction of the power transmitted to the tissue between 1 GHz and 50 GHz (about 3 %), but dynamically increases to 38 % in both models. The close agreement continues for frequencies between 50 GHz and 100 GHz, with a more saturated increase in absorption. For frequencies above 100 GHz, however, the larger imaginary part of the epidermal permittivity of the reference model leads to strong deviations and an overestimation of the absorbed power by up to 35 %. This strong overestimation of the power absorbed in the epidermis naturally leads to a strong underestimation of the power absorbed in the dermis. Moving away from the simplified stratified representation of the skin chosen for exposure studies and interpreting this fact in the context of an anatomically correct representation of the skin, a higher induced power in the dermis would be expected to result in a higher temperature rise in this sublayer and thus a direct effect on the thermoreceptors located there. Targeted power induction in the tissue in which these receptors are embedded could, given a sufficient level and duration of exposure, result in a physiological response of the organism to the stress of the exposure and trigger thermoregulatory mechanisms, such as increased blood flow to the skin and activation of sweat glands.

An important objective of these studies is also to provide dosimetric information on the power input to the basal and subbasal cell layers of the epidermis (i.e., $K_1$ and $K_2$) necessary for skin renewal. Information on the power distribution within the epidermis can be obtained from Figs. 10.7 and 10.8. Here, Fig. 10.7 shows that absorption by the dead cells of the SC is significantly overestimated by the reference model and thus, the absorption within the viable epidermis is significantly underestimated. This overestimation of the power input at the body surface greatly biases the predictions of temperature evolution within the skin, as this power is much more easily dissipated to the environment by convection and evaporation due to transpiration. A more detailed analysis of the power distribution within the cell layers $K_1$ through $K_{10}$ in Fig. 10.8 shows that the absorption within the proliferative pool of the epidermis is underestimated by the reference model by up to 50 %. The use of the reference model for frequencies above 100 GHz thus leads to biased interpretations, especially at these cell locations.

## 10.6 Summary and Conclusions

In this study, extensive dosimetric investigations were conducted to assess the transmission and distribution of EM fields in the skin, taking into account physiological variations across the epidermis. The investigations compared a reference model, based on measured material properties reported in [4] and [5], with a hybrid model that combined the purely numerical tissue model of the epidermis and the existing measured models of the

other skin layers. Embedding the two skin models in a FEM-based simulation environment, a macroscopic exposure setup was established to simulate skin irradiation at frequencies between 1 GHz and 300 GHz. The macroscopic exposure setup allowed for the determination of local EM fields induced in the skin layers and thus enabled a comparative assessment of the two skin models considering both reflectometric and dosimetric aspects.

The evaluation of these skin models revealed biases in the reference model due to two factors: (1) an incorrect sectioning of the epidermis and likely inclusion of dermal components, and (2) the lack of epidermal measurements, $\underline{\varepsilon}_{\mathrm{r,ED}}$, at frequencies higher than 100 GHz. These biases necessitated the inclusion of the dermal permittivity, $\underline{\varepsilon}_{\mathrm{r,D}}$ which allowed the verification of the numerically determined permittivities of the individual epidermal cell layers, $\underline{\tilde{\varepsilon}}_{\mathrm{r,K}_p/\mathrm{C}_q}$. The verification performed on $\underline{\varepsilon}_{\mathrm{r,ED}}$, $\underline{\varepsilon}_{\mathrm{r,D}}$, and $\underline{\tilde{\varepsilon}}_{\mathrm{r,K}_p/\mathrm{C}_q}$ showed a strong correlation between all of these permittivities for frequencies up to 100 GHz. However, when extrapolating beyond 100 GHz, deviations occurred, especially between $\varepsilon''_{\mathrm{r,ED}}$ and the imaginary parts of the other permittivities, indicating a significant overestimation of this value in the reference model, calculated using dispersive complex material properties, $\underline{\tilde{\varepsilon}}_{\mathrm{r,K}_p,\mathrm{C}_q}$, as outlined in Chap. 9. Nevertheless, the dermal permittivity showed a substantial correlation, except for notable deviations found exclusively in the upper layers of the stratum corneum, which could be attributed to a reduction in water concentration. These results demonstrated the reliability of permittivities derived from the bottom-up model and its histochemical assumptions.

The significant overestimation of $\varepsilon''_{\mathrm{r,ED}}$ in the reference model had major consequences for both the power transmitted to the skin and the distribution of that power across its sublayers. One of these consequences was revealed by the reflectometric analysis performed in Sec. 10.4. There, significant differences in reflection and transmission properties were shown for frequencies above 100 GHz, with the transmitted power being underestimated by the reference model by up to 24 %. Consequently, the reference model must be carefully reevaluated for dosimetric studies above 100 GHz, as subtle changes in the material properties of the epidermis can have a major effect on the total transmission of EM energy to the skin. This has implications for the current ICNIRP restrictions [1] as the dosimetric assessment conducted in [4], leading to the reference model, was used to derive an absorbed power density of 200 $\frac{\mathrm{W}}{\mathrm{m}^2}$ which was set as an operational adverse health effect threshold (see Chap. 7). However, based on the reduction factor of 2 to 10 established for occupational and general exposure, respectively, no direct risks or potential adverse health effects can be inferred from the underestimated results given above.

Furthermore, the evaluation of the power absorbed by the epidermis in Sec. 10.4.2 showed that the larger imaginary part of the epidermal permittivity in the reference model yields an overestimation of the absorbed power by up to 35 % at frequencies above 100 GHz, resulting in a strong underestimation of the power absorption in deeper skin layers. When considering a more anatomically accurate representation of the skin, the induced power in the dermis would be expected to cause a more pronounced temperature increase within this layer. This, in turn, would have a direct effect on the thermoreceptors located there.

Consequently, if the tissue surrounding these receptors were exposed to a targeted power induction of sufficient intensity and duration, it would have the potential to trigger physiological responses in the organism. These responses might include increased blood flow to the skin and activation of sweat glands as a direct result of the exposure-induced stress.

In addition to the results recapitulated in the previous paragraph, the analysis of energy distribution in the epidermis underlines the importance of accurately representing physiological variations within this skin layer by using individual permittivities for each cell layer. The analysis, which divided the epidermis into the stratum corneum (SC) and the viable epidermis (see Fig. 10.7), revealed that the reference model significantly overestimated absorption by the dead cells of the stratum corneum, leading to a substantial underestimation of absorption within the living cells of the viable epidermis. This overestimation of power at the surface of the skin could introduce a significant bias in predicting the temperature evolution within the skin, as this power easily dissipates to the environment through convection and evaporation. Furthermore, the comprehensive analysis of power distribution across the individual cell layers, from $K_1$ to $K_{10}$ (as depicted in Fig. 10.8), revealed discrepancies in the estimation of absorption within the viable epidermis using the reference model. These discrepancies ranged from an overestimation of 20 % to an underestimation of 60 % depending on the specific location within the viable epidermis and the frequency. Notably, regarding the basal and subbasal cell layers of the epidermis (i.e., $K_1$ and $K_2$), which are crucial for skin renewal, the reference model underestimates the absorption in this layer by up to 50 % at 300 GHz. Importantly, this observation applies not only to frequencies above 100 GHz but also to frequencies below this threshold. Consequently, using the reference model leads to biased interpretations, particularly at these specific cell locations at frequencies above 100 GHz.

In conclusion, the reference model is clearly suitable for frequencies up to 100 GHz, but the extrapolation of the measured material parameters for frequencies above 100 GHz leads to a significant overestimation of the reflection of EM waves at the skin surface. This leads to an underestimation of the power transmitted to the skin tissue compared to the hybrid model. Comparing the results of the current study with those presented in [19], in which the SC was identified as an impedance matching layer, it appears that not only the thickness of the individual cell layers, but also the water concentration profile across the epidermis can lead to such an effect. Furthermore, the layer-by-layer representation of the epidermis in the hybrid model allows a detailed assessment of the power distribution within the epidermis. This shows the strong influence of the different permittivities within the individual cell layers corresponding to the water concentration profile profile and the metabolization of keratin. Thus, the hybrid model demonstrates that numerically derived material representations of tissue layers, which inhibit strong physiological variations, complement purely measurement-based skin models and allow for the targeted investigation of physiological structures that have been identified as important (such as the proliferative pool).

# 11 Scale-Back Projection

In the previous chapter, a comparison between the hybrid skin model and the reference model based on the work of Sasaki et al. [4] showed that physiological variations in the epidermis significantly affect the absorption properties of the skin. In this chapter, the consistent representation of the epidermis by the bottom-up model, encompassing both the macroscopic and microscopic scales, is used to develop a top-down multiscale approach, referred to as scale-back projection. This approach allows the projection of the macroscopically determined EM field distribution within the epidermis onto the microstructure of the underlying epidermal cell models. It is shown that scale-back projection provides a solid foundation for the determination of a measure that will be referred to as the statistical micro-SAR. This measure is derived from a statistical analysis of field variations due to the microstructure of epidermal cells, and represents a means to quantify EM absorption and its location in a realistic manner. This allows the investigation of three key aspects:

(1) The quantification of field variations resulting from the morphology and histological composition of the fully resolved epidermal cell structures using statistical analysis (arithmetical mean, standard deviation).

(2) The investigation of differences between the conventional SAR, as specified by ICNIRP, and the statistical micro-SAR proposed here at the microscopic scale.

(3) The introduction of parameters to quantify methodological consistency in the projection of field values at both the macroscopic and microscopic scales.

By considering currently accepted reference levels for exposure at the macroscopic scale, this study allows the assessment of the above aspects within the context of the ICNIRP guidelines, in two frequency intervals: $F_1$ (ranging from 1 GHz to 6 GHz) and $F_2$ (ranging from 24 GHz to 52 GHz) which are either currently in use or being considered for use in 5G telecommunication standards. Based on this, it is discussed whether and how scale-back projection can be integrated as a microdosimetric investigation tool into the repertoire of conventional multiphysics simulations.

Sec. 11.1 provides a comprehensive introduction to the implementation of the scale-back projection within the computational simulation environment, detailing the methods and measures used in the analysis. This is followed by Sec. 11.2, which provides a detailed examination of the key aspects outlined above. This includes a comparison of the statistical micro-SAR with the currently accepted SAR limits for local limb exposure as defined by ICNIRP. Finally, the main findings are summarized and discussed in Sec. 11.3.

## 11.1 Methodology

The methodology section of this chapter is structured into three parts. The first part provides a detailed explanation of the implementation of the scale-back projection, emphasizing the connection between the macroscopic and microscopic scales. In the second part, a thorough outline of the microdosimetric assessment conducted using the scale-back projection is presented, introducing the relevant measures involved. Lastly, an analytical approach is introduced to investigate the methodological consistency of the scale-back projection and propose measures to evaluate the quality of the linkage between the two hierarchical scales.

### 11.1.1 Implementation of the Scale-Back Projection

The methodology of the scale-back projection is illustrated in Fig. 11.1, and can be described as a two-fold procedure linking the representation of epidermal tissues at two hierarchical levels: (1) on a macroscopic scale, and (2) on a microscopic scale.

On a macroscopic scale, the spatial distribution of EM fields across the individual sublayers of the skin is determined using the macroscopic exposure setup introduced in Chap. 10 as illustrated in Fig. 11.1(a). Efficient numerical calculation is facilitated by the homogenized tissue representation of these layers using the hybrid skin model. The input power, $P_{\mathrm{inc}}(\omega)$, corresponds to the incident power density, $S_{\mathrm{inc}}(\omega)$, defined in the reference levels (see Tab.7.2). The EM wave is propagating along the z-direction, perpendicular to the skin surface, and polarized in the x-direction. By subdividing the epidermis into separate computational subdomains, it is possible to determine the induced volumetric loss densities, $p(\vec{r},\omega)$, within microvolumes corresponding to the specific size and location of individual epidermal cells (i.e., $\mathrm{K}_p$ and $\mathrm{C}_q$), as described in Chap. 9. The integration of $p(\vec{r},\omega)$ over these microvolumes yields the power induced in a single cell, denoted as $P_{\mathrm{ind,K}_p/\mathrm{C}_q}(\omega)$, as illustrated in Fig. 11.1(b).

At the microscopic scale, the epidermal cells are represented using the parametric cell models introduced in Chap. 9. These models are then incorporated into the virtual capacitor setup, initially introduced in Chap. 8 for quasi-static EM analysis of eukaryotic cells. This setup is referred to as the microscopic exposure setup in the following. The linkage between the macroscopic and microscopic exposure setups is achieved by converting $P_{\mathrm{ind,K}_p/\mathrm{C}_q}(\omega)$ into a voltage, $U_{\mathrm{ind,K}_p/\mathrm{C}_q}(\omega)$, representing an equivalent level of exposure on the microscopic scale.

The voltage $U_{\mathrm{ind,K}_p/\mathrm{C}_q}(\omega)$ is derived using the equivalent circuit representation of the virtual capacitor experiment, originally used to determine macroscopic material properties of individual epidermal cell layers (see Fig. 8.3 and Eq. 8.5 to 8.9), and is calculated as follows:

$$P_{\mathrm{ind,K}_p/\mathrm{C}_q}(\omega) = \tilde{G}_{\mathrm{K}_p/\mathrm{C}_q}(\omega) \cdot U_{\mathrm{ind,K}_p/\mathrm{C}_q}(\omega)^2 \tag{11.1}$$

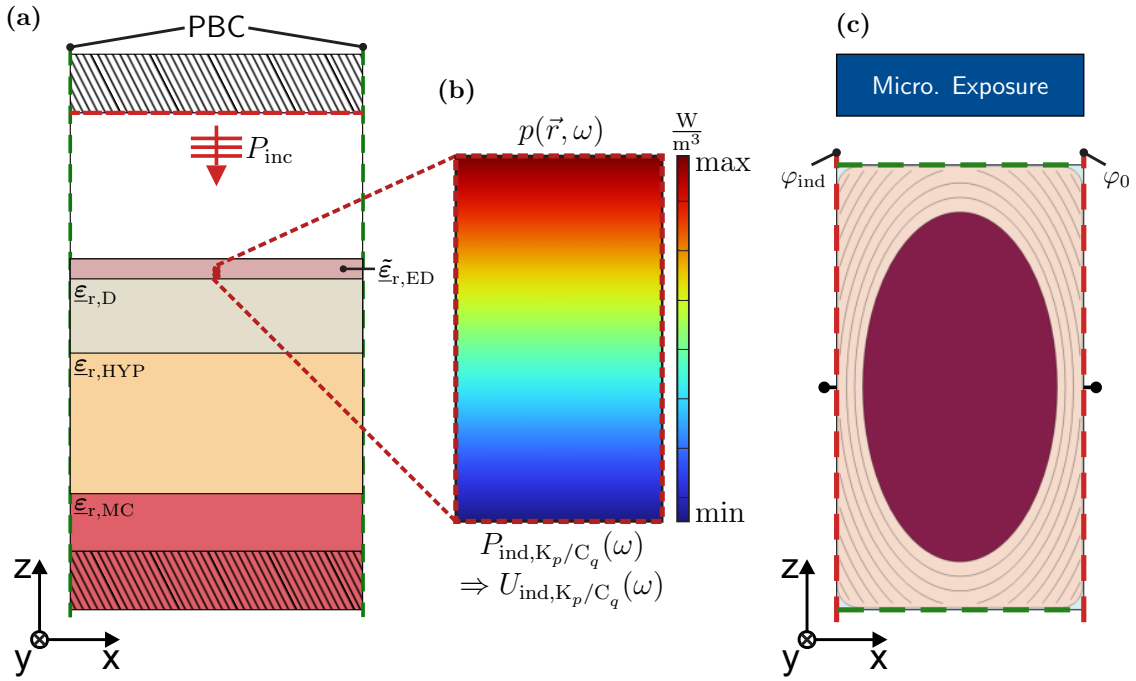


**Figure 11.1:** Conceptual overview of the scale-back projection: (a) Macroscopic exposure setup to determine EM fields induced in the hybrid skin model as introduced in Chap. 10. This setup allows the determination of the levels of exposure in each cell layer of the epidermis ($\text{K}_p$ and $\text{C}_q$). Considering only a single microvolume within each individual cell layer that corresponds to the specific size of the computational domain of its underlying parametric cell model, it is possible to determine the power induced in any of these microvolumes, $P_{\text{ind,K}_p/\text{C}_q}(\omega)$, as illustrated in (b). The induced power is then used to derive a voltage, $U_{\text{ind,K}_p/\text{C}_q}(\omega)$, which leads to an equivalent level of exposure on the microscopic scale (as outlined in Eq. 11.3). The corresponding potential difference, $\varphi_{\text{ind,K}_p/\text{C}_q}(\omega)$, is then applied across the microscopic exposure setup shown in (c).

where $\tilde{G}_{\text{K}_p/\text{C}_q}(\omega)$ represents the effective macroscopic conductance of the parametric cell models corresponding to the individual epidermal cell layers. By replacing $\tilde{G}_{\text{K}_p/\text{C}_q}(\omega)$ in Eq. 11.1 with the expression

$$\tilde{G}_{\text{K}_p/\text{C}_q}(\omega) = \frac{\tilde{\sigma}_{\text{K}_p/\text{C}_q}(\omega) \cdot A_{\text{YZ,K}_p/\text{C}_q}}{l_{\text{x,K}_p/\text{C}_q}}, \tag{11.2}$$

the voltage $U_{\text{ind,K}_p/\text{C}_q}(\omega)$ can be determined as follows:

$$U_{\text{ind,K}_p/\text{C}_q}(\omega) = \sqrt{\frac{P_{\text{ind,K}_p/\text{C}_q}(\omega) \cdot l_{\text{UC,x,K}_p/\text{C}_q}}{\tilde{\sigma}_{\text{K}_p/\text{C}_q}(\omega) \cdot A_{\text{YZ,K}_p/\text{C}_q}}} \tag{11.3}$$

where $A_{\text{YZ,K}_p/\text{C}_q} = l_{\text{UC,y,K}_p/\text{C}_q} \cdot l_{\text{UC,z,K}_p/\text{C}_q}$ denotes the cross-sectional area of the microvolume in the YZ plane and $\tilde{\sigma}_{\text{K}_p/\text{C}_q}(\omega) = \omega\varepsilon_0\tilde{\varepsilon}''_{\text{r,K}_p/\text{C}_q}(\omega)$ denotes the conductivity of any given homogenized epidermal cell layer. $U_{\text{ind,K}_p/\text{C}_q}(\omega)$ is now applicable to a microscopic

exposure setup by applying the corresponding potential difference, $\varphi_{\mathrm{ind,K}_p/\mathrm{C}_q}(\omega)$, to the Dirichlet boundary conditions considered in the quasi-static unit cell approach presented in Chap. 8. The application of $U_{\mathrm{ind,K}_p/\mathrm{C}_q}(\omega)$ in the x-direction is consistent with the polarization of the EM wave exposure at the macroscopic scale, as shown in Fig. 11.1(c).

### 11.1.2 Microdosimetric Assessment

The scale-back projection allows microdosimetric SAR assessments at both microscopic and macroscopic scales. At the macroscopic scale, it considers the homogeneous material representation of individual epidermal cell layers, while at the microscopic scale, it considers the fully resolved cell structure of individual epidermal cell models. SAR values at both scales can be determined using either the ICNIRP calculation rule (see Eq. 7.2), which relates the induced power within a microvolume to the mass contained in that volume, or by statistical analysis of field changes.

At the macroscopic scale, the specific absorption rate, denoted as $SAR_{\mathrm{ma,K}_p/\mathrm{C}_q}$, is calculated using the conventional definition (see Chap. 7):

$$SAR_{\mathrm{ma,K}_p/\mathrm{C}_q} = \frac{\iiint_{V_{\mathrm{UC}}} p(\vec{r},\omega)\,\mathrm{d}V}{\iiint_{V_{\mathrm{UC}}} \rho_{\mathrm{K}_p/\mathrm{C}_q}\,\mathrm{d}V} = \frac{P_{\mathrm{ind,K}_p/\mathrm{C}_q}(\omega)}{m_{\mathrm{K}_p/\mathrm{C}_q}} \tag{11.4}$$

where $p(\vec{r},\omega)$ and $\rho_{\mathrm{K}_p/\mathrm{C}_q}$ represent the volumetric loss densities induced in the individual microvolumes across the epidermal cell layers (see Fig. 11.1) and the volumetric mass densities of the homogeneous cell layers (see Fig. 9.11) respectively. The independent layer-wise values, $P_{\mathrm{ind,K}_p/\mathrm{C}_q}(\omega)$ and $m_{\mathrm{K}_p/\mathrm{C}_q}$, denote the corresponding induced losses and masses determined via integration over each microvolume, $V_{\mathrm{UC,K}_p/\mathrm{C}_q}$, for each cell layer. In contrast to this conventional assessment of the SAR, it is possible to perform a statistical analysis over these microvolumes that allows the quantification of field variations within the microvolume due to the attenuation of the penetrating wave. The results of this analysis are represented by the arithmetic mean value, denoted as $\mu_{\mathrm{SAR,ma,K}_p/\mathrm{C}_q}$, which is calculated as:

$$\mu_{\mathrm{SAR,ma,K}_p/\mathrm{C}_q} = \frac{1}{V_{\mathrm{UC,K}_p/\mathrm{C}_q}} \iiint_{V_{\mathrm{UC}}} \frac{p(\vec{r},\omega)}{\rho_{\mathrm{K}_p/\mathrm{C}_q}}\,\mathrm{d}V, \tag{11.5}$$

and the standard deviation, denoted as $s_{\mathrm{SAR,ma,K}_p/\mathrm{C}_q}$, calculated by

$$s_{\mathrm{SAR,ma,K}_p/\mathrm{C}_q} = \sqrt{\frac{1}{V_{\mathrm{UC,K}_p/\mathrm{C}_q}} \iiint_{V_{\mathrm{UC}}} \left(\frac{p(\vec{r},\omega)}{\rho_{\mathrm{K}_p/\mathrm{C}_q}} - \mu_{\mathrm{SAR,K}_p/\mathrm{C}_q}\right)^2 \mathrm{d}V}. \tag{11.6}$$

In this equation, the symbol $s$ has been chosen to represent the standard deviation instead of the commonly used $\sigma$ to avoid potential ambiguities with conductivity. Note that $\mu_{\mathrm{SAR,ma,K}_p/\mathrm{C}_q} = SAR_{\mathrm{ma,K}_p/\mathrm{C}_q}$.

At the microscopic scale, at which the individual epidermal cell layers are represented using their corresponding parametric cell models, it is also possible to determine a SAR that is calculated using the conventional definition:

$$SAR_{\mathrm{mi,K}_p/\mathrm{C}_q} = \frac{\iiint_{V_{\mathrm{UC}}} p(\vec{r},\omega)\,\mathrm{d}V}{\iiint_{V_{\mathrm{UC}}} \rho_{\mathrm{K}_p/\mathrm{C}_q}(\vec{r})\,\mathrm{d}V} = \frac{P_{\mathrm{ind,K}_p/\mathrm{C}_q}(\omega)}{m_{\mathrm{K}_p/\mathrm{C}_q}} \tag{11.7}$$

Here, it is important to note that even though $p(\vec{r},\omega)$ and $\rho_{\mathrm{K}_p/\mathrm{C}_q}(\vec{r})$ differ significantly from their corresponding values on the macroscopic scale, $P_{\mathrm{ind,K}_p/\mathrm{C}_q}$ and $m_{\mathrm{K}_p/\mathrm{C}_q}$ remain equal to their corresponding values, resulting in the fact that $SAR_{\mathrm{mi,K}_p/\mathrm{C}_q} = SAR_{\mathrm{ma,K}_p/\mathrm{C}_q}$. Consequently, the conventional representation of SAR at the microscopic scale does not offer any additional insights. However, it is now possible to use the results of a similar statistical analysis to define a new measure which demonstrates differences between the two scales, and thus the influences of cell morphology (size, shape, internal organization) and histochemical composition on field variations within the microstructure. This measure quantifies both the absorption and its location within the cell, leading to the redefinition of $SAR_{\mathrm{mi,K}_p/\mathrm{C}_q}$ (from Eq. 11.7) as a statistical micro-SAR:

$$SAR_{\mathrm{mi,K}_p/\mathrm{C}_q} = \mu_{\mathrm{SAR,mi,K}_p/\mathrm{C}_q} \pm s_{\mathrm{SAR,mi,K}_p/\mathrm{C}_q} \tag{11.8}$$

where the determination of the microscopic arithmetic mean value, $\mu_{\mathrm{SAR,mi,K}_p/\mathrm{C}_q}$, can be determined by

$$\mu_{\mathrm{SAR,mi,K}_p/\mathrm{C}_q} = \frac{1}{V_{\mathrm{UC,K}_p/\mathrm{C}_q}} \iiint_{V_{\mathrm{UC}}} \frac{p(\vec{r},\omega)}{\rho(\vec{r})}\mathrm{d}V \tag{11.9}$$

Due to the implementation of membranes as boundary conditions in the parametric models of individual epidermal cells, as defined in Eq. 8.2 and 8.3 in Chap. 8, the volumetric loss density, $p(\vec{r},\omega)$, is not defined within these cell structures and is thus not directly accessible for volume integration in the COMSOL software environment. To overcome this limitation, Eq. 11.9 needs to be rearranged to account for the individual cell structures:

$$\mu_{\mathrm{SAR,mi,K}_p/\mathrm{C}_q} = \frac{1}{V_{\mathrm{UC,K}_p/\mathrm{C}_q}} \sum_i \iiint_{V_{\mathrm{i}}} \frac{p(\vec{r},\omega)}{\rho(\vec{r})}\mathrm{d}V \tag{11.10}$$

$$= \frac{1}{V_{\mathrm{UC,K}_p/\mathrm{C}_q}} \sum_i \frac{1}{\rho_i} \iiint_{V_{\mathrm{i}}} p(\vec{r},\omega)\mathrm{d}V \tag{11.11}$$

$$\mu_{\mathrm{SAR,mi,K}_p/\mathrm{C}_q} = \frac{1}{V_{\mathrm{UC,K}_p/\mathrm{C}_q}} \sum_i \frac{P_i}{\rho_i} \tag{11.12}$$

In the above equations, the index $i$ represents the different cell structures, namely the extracellular medium (EC), the cytoplasm (CP), the nucleoplasm (NP), and the membranes (M). The variables $P_i$ and $\rho_i$ correspond to the power induced and the volumetric mass density assigned to each respective cell structure. By employing the concept of spatial segmentation as described in Chap. 8, it becomes possible to determine the power contributions $P_{\mathrm{EC}}$, $P_{\mathrm{CP}}$, and $P_{\mathrm{NP}}$ through volume integration within the epidermal cell models.

The associated membrane power contribution, denoted by $P_{\mathrm{M}}$, can also be obtained by subtracting the sum of $P_{\mathrm{EC}}$, $P_{\mathrm{CP}}$, and $P_{\mathrm{NP}}$ from $P_{\mathrm{tot}}$, where $P_{\mathrm{tot}}$ is the total induced power determined between the terminals (i.e. the electrodes) of the computational domain. In addition, the determination of $P_{\mathrm{tot}}$ in the microscopic exposure setup serves as a means to assess the consistency between the macroscopic and microscopic scales. This is evaluated by comparing the induced power $P_{\mathrm{Cell}}$ (macroscopic) and $P_{\mathrm{tot}}$ (microscopic), where the required condition $P_{\mathrm{Cell}} = P_{\mathrm{tot}}$ is checked and found to be satisfied. To solve Eq. 11.12,

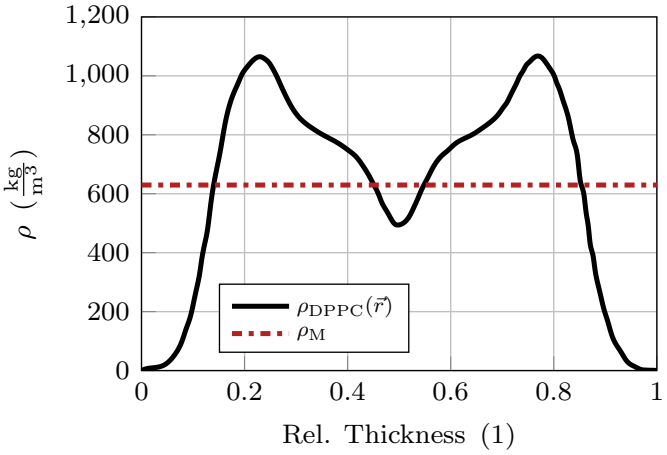


**Figure 11.2:** Profile of the volumetric mass density across membranes represented by an uncharged dipalmitoylphosphatidylcholine (DPPC) phospholipid bilayer, $\rho_{\mathrm{DPPC}}(\vec{r})$, adopted from [112], plotted against the relative thickness with respect to that of the membranes, which typically measures 6µm to 10µm. The average value, $\langle\rho_{\mathrm{DPPC}}(\vec{r})\rangle$, serves as $\rho_{\mathrm{M}}$ in Eq. 11.12 and represents the volumetric mass density of the membranes in the epidermal cell models.

it is necessary to specify the volumetric mass density of the membranes, $\rho_{\mathrm{M}}$. This is done by considering the volumetric mass density profile $\rho_{\mathrm{DPPC}}(\vec{r})$ across an uncharged dipalmitoylphosphatidylcholine (DPPC) phospholipid bilayer, as shown in Fig. 11.2. This density profile, which has been adopted from [112], provides an estimate of the average density of DPPC molecules in the bilayer, denoted as $\langle\rho_{\mathrm{DPPC}}(\vec{r})\rangle$. Thus, $\langle\rho_{\mathrm{DPPC}}(\vec{r})\rangle$ is used to approximate $\rho_{\mathrm{M}}$. These values are plotted against the relative thickness of the membranes, which typically ranges from 6µm to 10µm.

After obtaining $\mu_{\mathrm{SAR,mi,K}_p/\mathrm{C}_q}$ by solving Eq. 11.12, it becomes possible to determine the standard deviation of the SAR values across the computational domain using the following equation for the standard deviation:

$$s_{\mathrm{SAR,mi,K}_p/\mathrm{C}_q} = \sqrt{\frac{1}{V_{\mathrm{UC,K}_p/\mathrm{C}_q}} \iiint_{V_{\mathrm{UC}}} \left( \frac{p(\vec{r},\omega)}{\rho(\vec{r})} - \mu_{\mathrm{SAR,K}_p/\mathrm{C}_q} \right)^2 \mathrm{d}V} \tag{11.13}$$

However, it should be noted that due to the decision to implement membranes as boundary conditions, the integral in this equation does not consider field values within the membranes themselves. While this limitation does not render the analysis invalid, it needs

to be considered in the results section, as only an incomplete picture of the field and loss distribution is provided for the macroscopic exposure setup.

In order to provide a comprehensive statistical assessment of the distribution of $SAR_{\mathrm{mi}}(\vec{r},\omega)$, it is important to determine the minimum and maximum values occurring within the epidermal cell models. This can be achieved using the following equations:

$$SAR_{\mathrm{min,mi,K}_p/\mathrm{C}_q} = \min\left(\frac{p(\vec{r},\omega)}{\rho(\vec{r})}\right) \tag{11.14}$$

$$SAR_{\mathrm{max,mi,K}_p/\mathrm{C}_q} = \max\left(\frac{p(\vec{r},\omega)}{\rho(\vec{r})}\right) \tag{11.15}$$

By calculating these minimum and maximum values, a more comprehensive understanding of the range of SAR values within the cell models can be obtained. This evaluation is performed in two frequency intervals: $\mathrm{F}_1 \in [1\,\mathrm{GHz}, 6\,\mathrm{GHz}]$ and $\mathrm{F}_2 \in [24\,\mathrm{GHz}, 52\,\mathrm{GHz}]$.

### 11.1.3 Methodological Consistency of the Scale-Back Projection

In addition to the statistical analysis outlined above, the methodological consistency between the macroscopic and microscopic scales in the scale-back projection must be evaluated. The macroscopic exposure setup determines the distribution of EM fields within the skin using full-wave simulation. This even takes into account field variations within the investigated microvolumes themselves, which occur due to the attenuation of the penetrating wave within the tissues (see Fig. 11.1(b)). In contrast, the microscopic exposure setup uses a quasi-static capacitor approach, where the outer boundaries of the computational domain are assigned two numerical features: (1) periodic boundary conditions implemented to avoid fringing fields, and (2) Dirichlet boundary conditions used for the application of the voltage $U_{\mathrm{ind,K}_p/\mathrm{C}_q}$. The Dirichlet boundary conditions enforce a constant potential, $\varphi_{\mathrm{ind,K}_p/\mathrm{C}_q}$, resulting from the application of this voltage in the x-direction. This constant potential, however, is not consistent with the decay of EM waves penetrating the corresponding microvolume in the macroscopic exposure setup, leading to an inherent discrepancy between the macroscopic and microscopic scales in the scale-back projection. Nevertheless, considering both of these scales, this inherent methodological discrepancy becomes negligible when the variations of the EM field values observed in the microdosimetric exposure setup becomes significant in comparison to that in the microvolumes at the macroscopic scale. To quantify this, the agreement between the exposure setups at the two scales can be evaluated by considering the coefficient of variation, defined as:

$$CV_{\mathrm{SAR,ma/mi,K}_p/\mathrm{C}_q} = \frac{s_{\mathrm{SAR,ma/mi,K}_p/\mathrm{C}_q}}{\mu_{\mathrm{SAR,ma/mi,K}_p/\mathrm{C}_q}} \tag{11.16}$$

Here, "ma" and "mi" in the indices refers to statistical measures of microvolumes on the macroscopic and microscopic scales respectively. A low coefficient of variation in the

macroscopic setup and a high coefficient of variation in the microscopic setup indicate suitable methodological consistency between the two scales. To assess the coupling quality, the ratio of $CV_{\mathrm{SAR,mi,K}_p/\mathrm{C}_q}$ to $CV_{\mathrm{SAR,ma,K}_p/\mathrm{C}_q}$ is utilized, represented as:

$$\gamma_{\mathrm{SAR,K}_p/\mathrm{C}_q} = \frac{CV_{\mathrm{SAR,mi,K}_p/\mathrm{C}_q}}{CV_{\mathrm{SAR,ma,K}_p/\mathrm{C}_q}} \tag{11.17}$$

This ratio allows the assessment of the quality of coupling between the macroscopic and microscopic scales with a high value for $\gamma_{\mathrm{SAR,K}_p/\mathrm{C}_q}$ indicating strong coupling.

## 11.2 Results

The results derived from the application of the scale-back projection are presented in the following sections. First, the EM exposure in the epidermis is investigated by means of the statistical micro-SAR, which is used to quantify the variations of SAR values observed within the cellular microstructure of epidermal cells. In addition, the distribution of these values across the cell models is evaluated using histograms and field plots. Following this analysis, a comparison is made between the statistical micro-SAR and the conventional representation of the SAR on a macroscopic scale. The methodological consistency between the microscopic and macroscopic scales is then evaluated. Finally, the study examines how well the statistical micro-SAR conforms to current safety guidelines, particularly those defined in the basic restrictions for limiting local exposure in the extremities.

### 11.2.1 Microdosimetric Assessment of the Epidermis using Scale-Back Projection

The microdosimetric analysis of $SAR(\vec{r},\omega)$ using the statistical measures defined in Eqs. 11.9 to 11.15 is shown in Fig. 11.3 for basal keratinocytes (i.e. parametric cell model $\mathrm{K}_1$) as an illustrative example[1] because these cells are particularly important for skin resurfacing (see Chap. 3). The figure presents diagrams corresponding to frequency interval $\mathrm{F}_1$ in Figs. 11.3(a), (c), and (e), and frequency interval $\mathrm{F}_2$ in Figs. 11.3(b), (d), and (f).

In Figs. 11.3(a) and (b), the $SAR_{\mathrm{mi,K}_1}(\omega)$ is plotted on a semi-logarithmic scale for frequency intervals $\mathrm{F}_1$ and $\mathrm{F}_2$ respectively. The statistical mean, $\mu_{\mathrm{SAR,mi,K}_1}$, is represented by a solid black line. The dark-gray-shaded area surrounding $\mu_{\mathrm{SAR,mi,K}_1}$ corresponds to a range of values within one standard deviation of the mean, $\mu_{\mathrm{SAR,mi,K}_1} \pm s_{\mathrm{SAR,mi,K}_1}$. The upper and lower bounds of this range are indicated by dashed-dotted lines positioned above

[1] Appendix D complements the presented findings by including detailed statistical analysis of all epidermal cell models, $\mathrm{K}_p$ to $\mathrm{C}_q$, in Figs. D.1 to D.24.

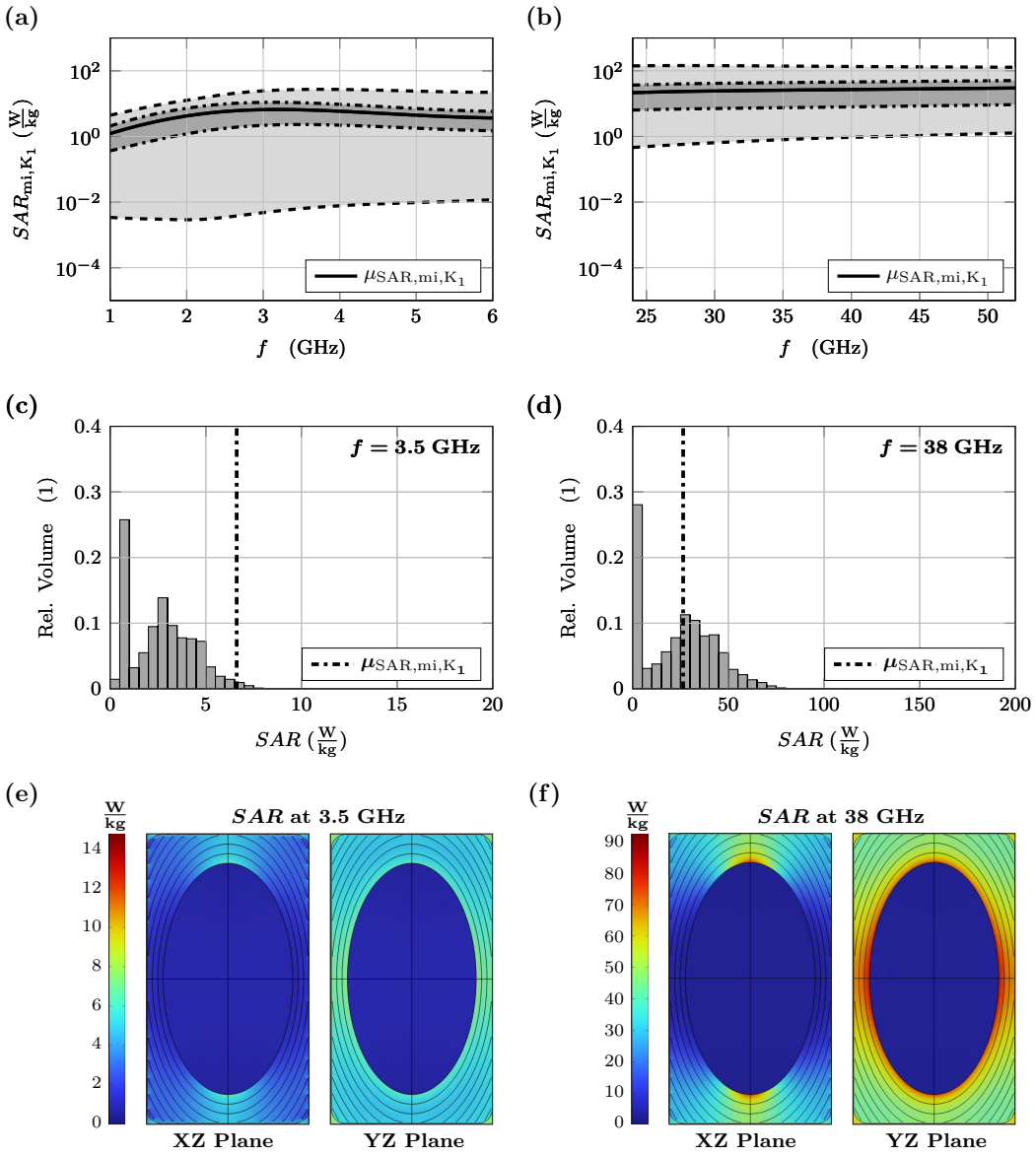


**Figure 11.3:** Microdosimetric analysis of $SAR(\vec{r},\omega)$ in basal keratinocytes. (a) Semi-logarithmic plot of $SAR_{\mathrm{mi,K_1}}(\omega)$ for frequency interval $\mathrm{F_1}$, illustrating the statistical measures. The solid black line represents the statistical mean ($\mu_{\mathrm{SAR,mi,K_1}}$), while the dark-gray-shaded area corresponds to values within one standard deviation of the mean, denoted as $\mu_{\mathrm{SAR,mi,K_1}} \pm s_{\mathrm{SAR,mi,K_1}}$. The dashed-dotted lines above and below the mean indicate the upper and lower bounds of this range. The light-gray-shaded area represents the entire range of values observed within the computational domain, bounded by the maximum value ($SAR_{\mathrm{max,mi,K_1}}$) at the top and the minimum value ($SAR_{\mathrm{min,mi,K_1}}$) at the bottom. (b) Similar plot as in (a), but for the frequency interval $\mathrm{F_2}$. (c) & (d) Histograms representing the distribution of $SAR(\vec{r},\omega)$ values at 3.5 GHz and 38 GHz. Note the discrepancy between $\mu_{\mathrm{SAR,mi,K_1}}$ and the central tendency of the histogram shown in (c), which is due to the implementation of membranes as boundary conditions, as explained in the methodology section of this chapter. (e) & (f) Field plots of $SAR(\vec{r},\omega)$ in basal keratinocytes illustrating the XZ and YZ planes for 3.5 GHz and 38 GHz, respectively.

and below the mean. To complete this statistical analysis, the light-gray-shaded area surrounding $\mu_{\mathrm{SAR,mi,K_1}} \pm s_{\mathrm{SAR,mi,K_1}}$ illustrates the entire range of values monitored within the computational domain of the microscopic exposure setup. This range is bounded at the top by the maximum value, $SAR_{\mathrm{max,mi,K_1}}$, and at the bottom by the minimum value, $SAR_{\mathrm{min,mi,K_1}}$. The SAR values shown here cover a large range, with the central frequencies of intervals $F_1$ and $F_2$ (3.5 GHz and 38 GHz respectively) being used as an illustrative example in Tab. 11.1.

**Table 11.1:** Illustrative overview of the variation of SAR values in basal keratinocytes for the central frequencies within intervals $F_1$ and $F_2$ at 3.5 GHz and 38 GHz.

| $f$ | $\mu_{\mathbf{SAR,mi,K_1}}$ | $s_{\mathbf{SAR,mi,K_1}}$ | $SAR_{\mathbf{max,mi,K_1}}$ | $SAR_{\mathbf{min,mi,K_1}}$ |
|---|---|---|---|---|
| 3.5 GHz | $6.4683\,\mathrm{W kg^{-1}}$ | $4.1594\,\mathrm{W kg^{-1}}$ | $27.0293\,\mathrm{W kg^{-1}}$ | $0.0063\,\mathrm{W kg^{-1}}$ |
| 38 GHz | $26.3634\,\mathrm{W kg^{-1}}$ | $18.5791\,\mathrm{W kg^{-1}}$ | $137.1015\,\mathrm{W kg^{-1}}$ | $0.8956\,\mathrm{W kg^{-1}}$ |

However, before moving on to a comprehensive analysis of the variations of SAR values across all of the cell models using $CV_{\mathrm{SAR,mi,K}_p/\mathrm{C}_q}$, which will be presented at the end of this subsection, it is important to first analyze the frequency of occurrence of SAR values across basal keratinocytes. This is illustrated using histograms in Figs. 11.3(c) and (d) for the two aforementioned sample frequencies. The histograms visually represent the distribution of $SAR(\vec{r},\omega)$ relative to the volume of the computational domain. Both histograms show that the majority of SAR values across this domain exhibit a unimodal distribution which is slightly skewed to the right. However, this general trend is disrupted by a significant accumulation of low values, which account for approximately 30 % of the cell volume forming a second peak in the data. This accumulation can be attributed to the nucleus, which occupies roughly 30 % of the cell volume, as shown in Fig. 9.3. This reasoning is supported by the field plots in Fig. 11.3(e) and (f), which show the SAR distribution in the XZ and YZ planes of the computational model of the basal keratinocytes for 3.5 GHz and 38 GHz respectively. These field plots illustrate low SAR values within the nucleus. This observation aligns with previous findings discussed in Chap. 8, which describe the electrical shielding provided by the nuclear envelope to the nucleoplasm. In summary, the significant accumulation of low values in the distribution of the specific absorption rate can be attributed to the SAR values within the nucleus, while the unimodal distribution of values corresponds to the SAR occurring in the cytoplasm and extracellular space. Upon closer analysis of the histograms shown in Figs. 11.3(c) and (d), it becomes evident that the calculated mean value, $\mu_{\mathrm{SAR,mi,K_1}}$, does not accurately represent the central tendency of the distribution resulting from the microscopic exposure setup at 3.5 GHz. This discrepancy can be attributed to the implementation of membranes as boundary conditions, as explained in the methodology section of this chapter. The histograms are determined using mathematical operations based on volume integration within the COMSOL Multiphysics software environment and values corresponding to the membranes, modeled as boundary conditions, are thus not captured. The large discrepancy between the expected mean value from the distribution of SAR values shown in the histogram and $\mu_{\mathrm{SAR,mi,K_1}}$ suggests a significant contribution to the SAR within the membranes.

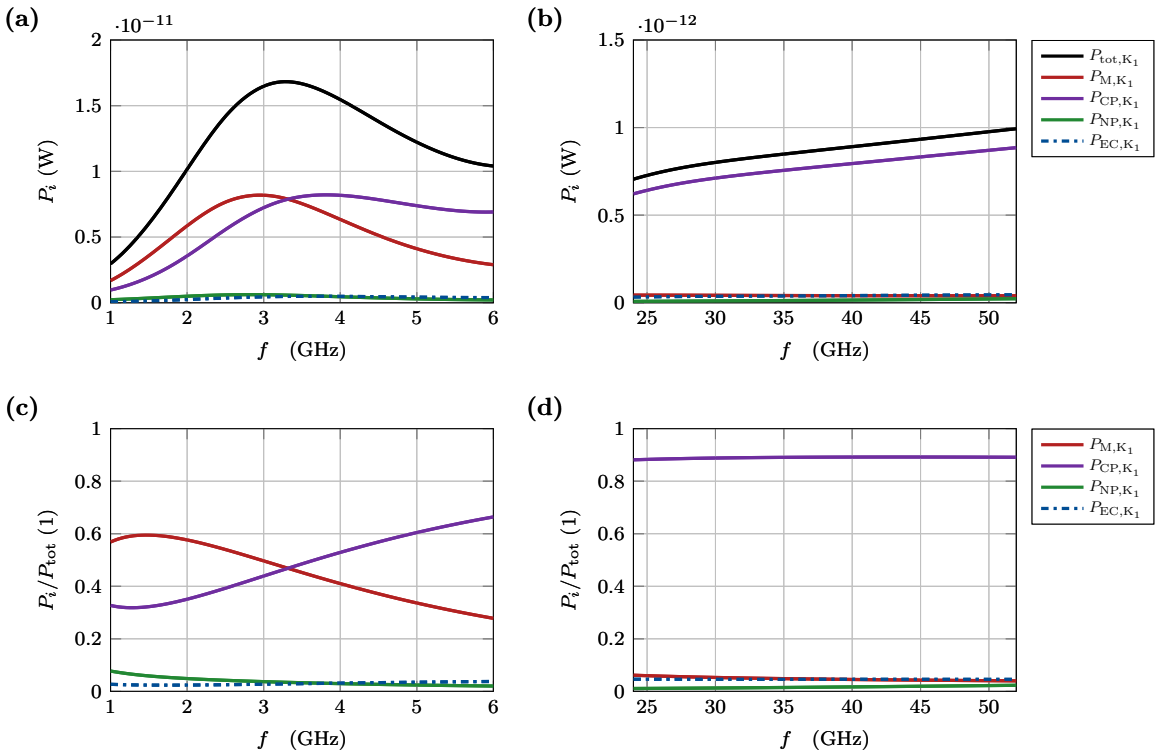


**Figure 11.4:** Power levels induced within each structure of the cell, represented by $P_{\text{tot}}$, $P_{\text{M}}$, $P_{\text{CP}}$, $P_{\text{NP}}$, and $P_{\text{EC}}$, depicted by black, red, purple, green, and blue lines, respectively. The analysis is performed separately for frequency intervals $\text{F}_1$ and $\text{F}_2$, as shown in (a) and (b). (c) and (d) show the relative cell losses expressed as $\frac{P_i}{P\text{tot}}$.

To investigate this missing contribution, the power levels induced in the membranes, cytoplasm, nucleoplasm and extracellular medium are shown in Fig. 11.4 represented by $P_{\text{M}}$, $P_{\text{CP}}$, $P_{\text{NP}}$, and $P_{\text{EC}}$ respectively. In addition, the power levels for the cell as a whole are given by $P_{\text{tot}}$. This is performed separately for each of the frequency intervals, $\text{F}_1$ and $\text{F}_2$, as shown in Figs. 11.4(a) and (b) respectively. Comparing Fig. 11.4(a) with Fig. 11.4(b), it can be seen that the membranes contribute significantly to absorption in frequency interval $\text{F}_1$, while their contribution in frequency interval $\text{F}_2$ is almost negligible. This observation is even more evident when considering the relative induced power, $\frac{P_i}{P_{\text{tot}}}$, shown in Figs. 11.4(c) and (d). There, it can be seen that the membrane losses account for approximately $30-60\,\%$ of the total cell losses in $\text{F}_1$, while accounting for less than $10\,\%$ in $\text{F}_2$.

As this comprehensive analysis demonstrates the variations of SAR values in basal keratinocytes, and acknowledges the computational constraints imposed by the built-in operations of the COMSOL Multiphysics software environment for capturing their distribution, the focus now shifts to quantifying the variations of SAR values across all epidermal

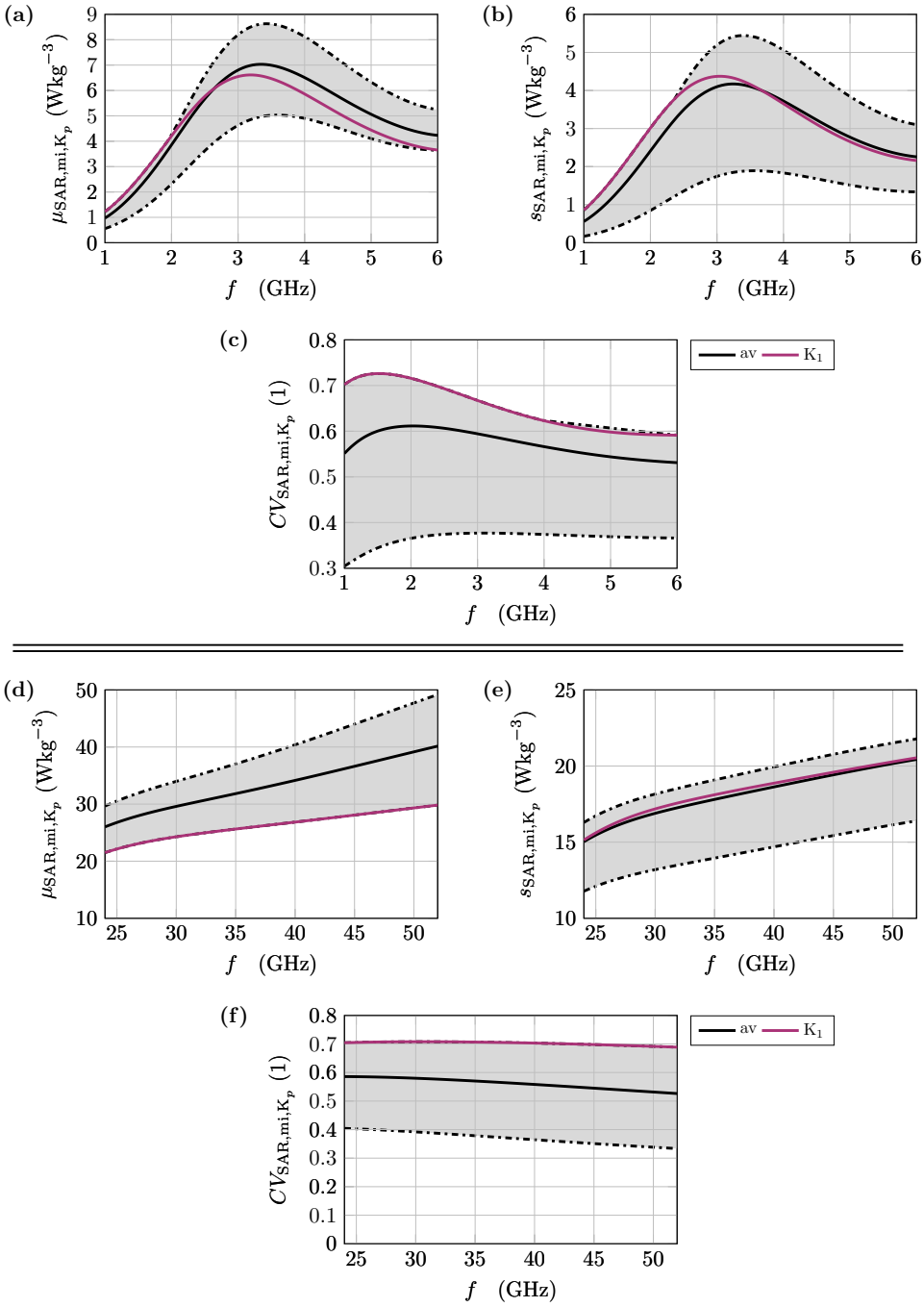


**Figure 11.5:** Viable Epidermis - Analysis of the variations of SAR values in the cell models of the viable epidermis ($K_1$ through $K_{10}$): Plots of the statistical parameters $\mu_{SAR,mi,K_p}$ and $s_{SAR,mi,K_p}$ are shown in (a) and (b), respectively, while (c) illustrates $CV_{SAR,mi,K_p}$ for quantification of SAR values within the frequency interval $F_1$. Correspondingly, Figs. 11.5(d)-(f) present these values for interval $F_2$. The plots visualize the range of values across all cell models by gray-shaded areas bordered by dashed black lines, with solid black lines representing their averages. Following the previous analysis of basal keratinocytes, the values for $K_1$ are additionally shown by magenta lines.

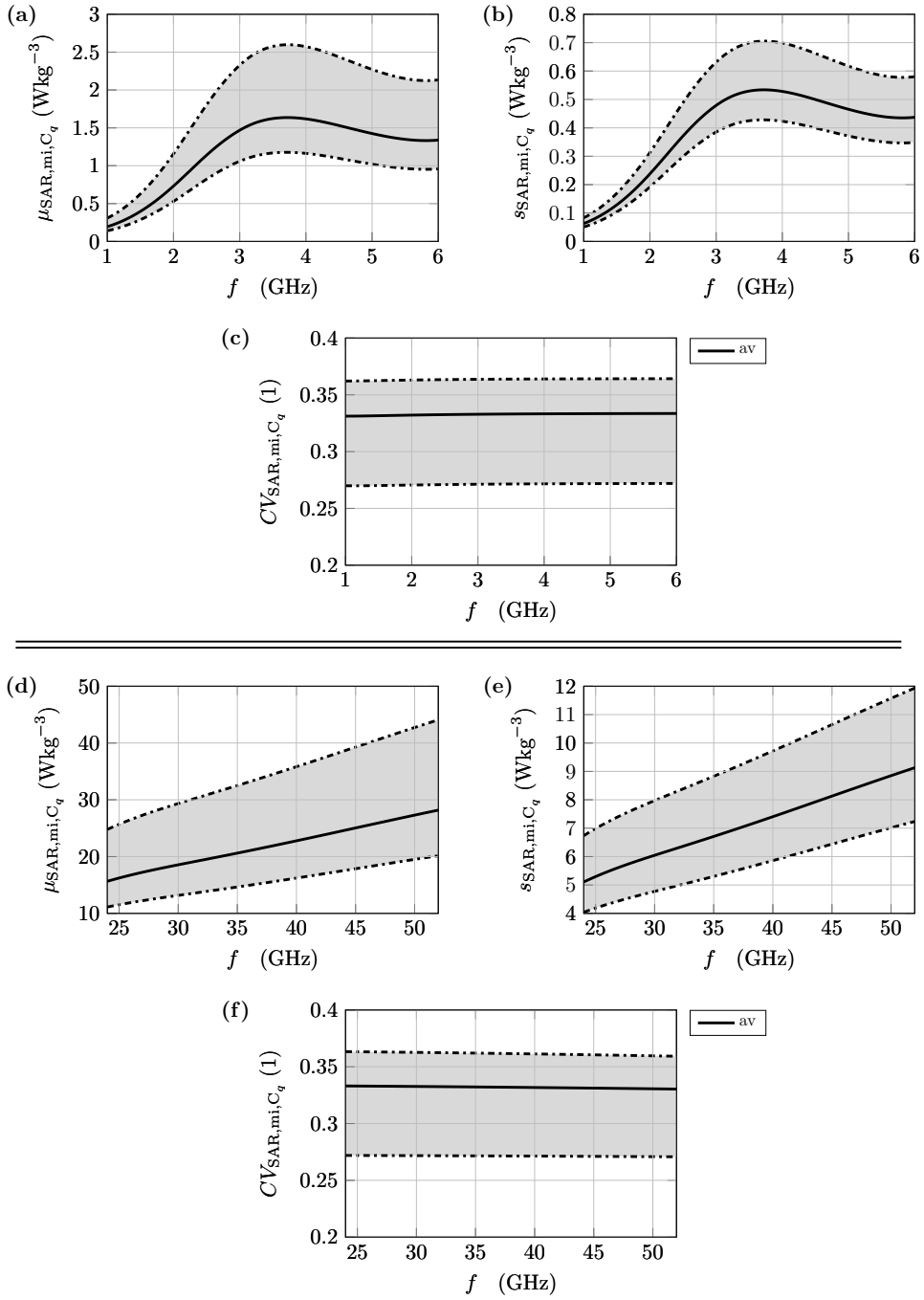


**Figure 11.6:** Stratum Corneum - Analysis of the variations of SAR values in the cell models of the SC $C_1$ through $C_{14}$: Plots of the statistical parameters $\mu_{\mathrm{SAR,mi,C}_q}$ and $s_{\mathrm{SAR,mi,C}_q}$ are shown in (a) and (b), respectively, while (c) illustrates $CV_{\mathrm{SAR,mi,C}_q}$ for quantification of SAR values within the frequency interval $F_1$. Correspondingly, Figs. 11.5(d)-(f) present these values for interval $F_2$. The plots visualize the range of values across all cell models by gray-shaded areas bordered by dashed black lines, with solid black lines representing their averages.

cell models with these issues in mind. This analysis is illustrated in Fig. 11.5 for the viable epidermis and in Fig. 11.6 for the SC.

In Fig. 11.5, $\mu_{\mathrm{SAR,mi,K}_p}$ and $s_{\mathrm{SAR,mi,K}_p}$ are shown in (a) and (b), while (c) shows $CV_{\mathrm{SAR,mi,K}_p}$ to quantify the variations of SAR values over interval $\mathrm{F}_1$. Similarly, Figs. 11.5(d)-(f) illustrate these values for interval $\mathrm{F}_2$. The plots illustrate the range of values across all cell models, $\mathrm{K}_1$ through $\mathrm{K}_{10}$, represented by gray-shaded areas bounded by dashed black lines, while solid black lines represent their averages. To maintain a connection with the detailed analysis of basal keratinocytes performed above, the values for $\mathrm{K}_1$ are additionally represented by magenta lines. In Figs. 11.5(c) and (f), it can be observed that the coefficient of variation ranges between 0.3 and 0.71 in both intervals. This wide range underlines the significant influence of cell morphology on the variations of SAR values within each cell model, and emphasizes the necessity to study each cell layer individually. However, by determining the arithmetic mean of $CV_{\mathrm{SAR,mi,K}_p}$, an average value for the variations within the viable epidermis can be given as a rough estimate, ranging from 0.53 to 0.62 in $\mathrm{F}_1$ and from 0.52 to 0.59 in $\mathrm{F}_2$.

To quantify the variations of SAR values across the cell models of the SC, $\mu_{\mathrm{SAR,mi,C}_q}$, $s_{\mathrm{SAR,mi,C}_q}$ and $CV_{\mathrm{SAR,mi,C}_q}$ are shown in Figs. 11.6(a)-(c) in interval $\mathrm{F}_1$ and in (d)-(f) in interval $\mathrm{F}_2$. The plots illustrate the range of values across all cell models, $\mathrm{C}_1$ through $\mathrm{C}_{14}$, in a manner corresponding to Fig. 11.5. In Figs. 11.6(c) and (f), a distinct observation arises: The coefficient of variation in the SC is almost frequency independent, displaying a much narrower range of values, spanning from 0.27 to 0.37, in both intervals. As a result, an almost constant average value of 0.33 emerges. The negligible frequency dependence and the much narrower range of values can be attributed to the much lower water content in the histochemical composition of the corneocytes and their much simpler geometric arrangement, lacking any intracellular compartmentalization and organelle membranes (see Chap. 9).

### 11.2.2 Comparison of the Statistical Micro-SAR and the Conventional Representation of the SAR at the Macroscopic Scale

After investigating the field variations of the SAR in the microstructure of a basal keratinocyte, it is now necessary to compare $\mu_{\mathrm{SAR,mi,K}_p/\mathrm{C}_q}$ with $SAR_{\mathrm{ma,K}_p/\mathrm{C}_q}$, conventionally determined by the homogeneous bulk representation of individual cell layers. This evaluation focuses on epidermal cells within the viable epidermis and the SC in Figs. 11.7 and 11.8, respectively.

In Fig. 11.7, $SAR_{\mathrm{ma,K}_p}$ and $\mu_{\mathrm{SAR,mi,K}_p}$ are shown in (a) and (b), while (c) shows the relative deviation between these values, denoted as $\Delta SAR_{\mathrm{K}_p}$, for frequency range $\mathrm{F}_1$. $\Delta SAR_{\mathrm{K}_p}$ is defined as

$$\Delta SAR_{\mathrm{K}_p} = \frac{SAR_{\mathrm{ma,K}_p} - \mu_{\mathrm{SAR,mi,K}_p}}{SAR_{\mathrm{ma,K}_p}}. \tag{11.18}$$

Similarly, Figs. 11.7(d)-(f) illustrate these values for the frequency range $\mathrm{F}_2$. The curves in each plot correspond to specific epidermal cell models, represented by solid, dashed, dotted, and dashed-dotted lines, and colored in magenta ($\mathrm{K}_1$ through $\mathrm{K}_4$), green ($\mathrm{K}_5$ through $\mathrm{K}_8$), and blue ($\mathrm{K}_9$ and $\mathrm{K}_{10}$) as indicated in the legend. Comparing $SAR_{\mathrm{ma,K}_p}$ and $\mu_{\mathrm{SAR,mi,K}_p}$ in Figs. 11.7(a) and (b), it can be seen that the curves for all cell models show the same basic trend with a maximum between 3 GHz and 4 GHz. However, the magnitude of this maximum is much smaller for $SAR_{\mathrm{ma,K}_p}$ than for $\mu_{\mathrm{SAR,mi,K}_p}$. This can be explained by the loss distribution within the epidermal cell models. As shown in the sectional images of the cell model of basal keratinocytes in Fig. 11.3(e) and indicated by the histogram in Fig. 11.3(d), the nucleus is largely shielded from EM radiation by the organelle membranes in the surrounding cytoplasm. In addition, the distribution of the power intake into the cell shown in Fig. 11.4 demonstrates that the total power of the cell forms a maximum at about 3.2 GHz, which is mainly split into equal parts of 45 % in the cytoplasm and the membranes. This underlines the usefulness of the piecewise determination of the SAR contributions of the individual cell structures in Eq. 11.12 for the calculation of $\mu_{\mathrm{SAR,mi,K}_p}$ as a means to quantify cell losses and their location within individual cells. Regarding $\Delta SAR_{\mathrm{K}_p}$ in Fig. 11.7(c), it can be seen that the SAR estimated from the graph, $SAR_{\mathrm{ma,K}_p}$, is up to 45 % lower than the microscopically measured $\mu_{\mathrm{SAR,mi,K}_p}$. These statements can also be applied to frequency range $\mathrm{F}_2$ shown in Figs. 11.7(d)-(f). Both $SAR_{\mathrm{ma,K}_p}$ and $\mu_{\mathrm{SAR,mi,K}_p}$ show the same monotonous slope in the plotted graphs, which essentially reflects the lower attenuation of the penetrating wave. The deviation of the two values, $\Delta SAR_{\mathrm{K}_p}$, is much smaller here than in $\mathrm{F}_1$ due to the smaller loss contribution of the membranes. However, it is still significant with a value of up to 13 %.

Moving on to the analysis of the individual cell layers of the SC, $SAR_{\mathrm{ma,C}_q}$, $\mu_{\mathrm{SAR,mi,C}_q}$ and $\Delta SAR_{\mathrm{C}_q}$ are illustrated in Figs. 11.8 (a)-(c) for frequency interval $\mathrm{F}_1$ and in (d)-(f) for frequency interval $\mathrm{F}_2$. The curves in each plot correspond to specific corneocyte models,

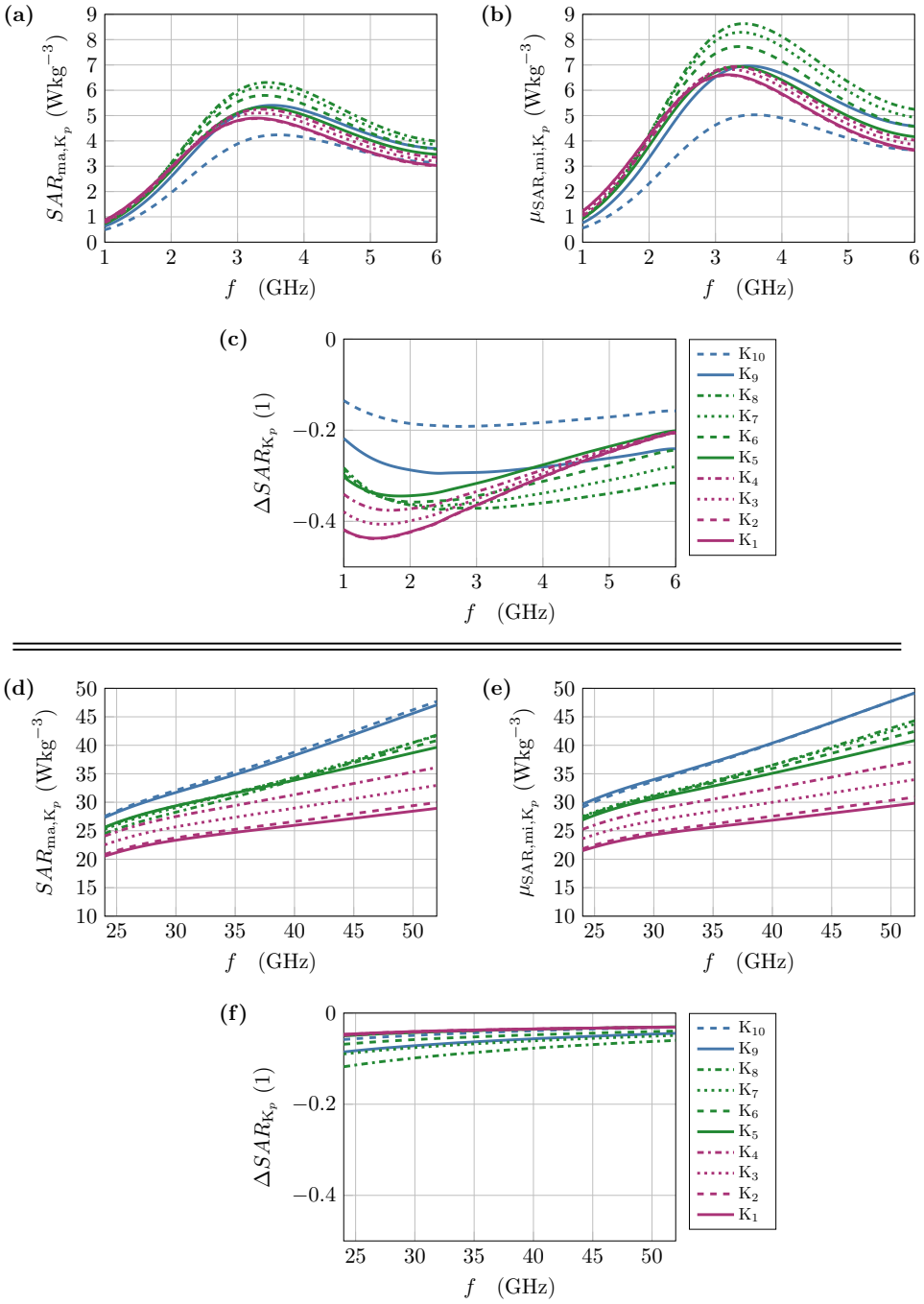


**Figure 11.7:** Viable Epidermis - Comparison between the SAR derived from the conventional representation of the microvolumes at a macroscopic scale, denoted as $SAR_{\mathrm{ma,K}_p}$ in (a) & (d), and the statistical micro-SAR, denoted as $\mu_{\mathrm{SAR,mi,K}_p}$ in (b) & (e), in the frequency interval $\mathrm{F}_1$ in (a)-(c), and $\mathrm{F}_2$ in (d)-(f): (a) & (d) show $SAR_{\mathrm{ma,K}_p}$ while (b) & (e) show $\mu_{\mathrm{SAR,mi,K}_p}$ for each frequency range; (c) & (f) depict the relative deviation between these values, denoted as $\Delta SAR_{\mathrm{K}_p}$. The plots corresponding to each of the investigated epidermal cell models are represented by solid, dashed, dotted, and dash-dotted lines. They are colored in magenta ($\mathrm{K}_1$ through $\mathrm{K}_4$), green ($\mathrm{K}_5$ through $\mathrm{K}_8$), and blue ($\mathrm{K}_9$ and $\mathrm{K}_{10}$) as indicated in the legend.

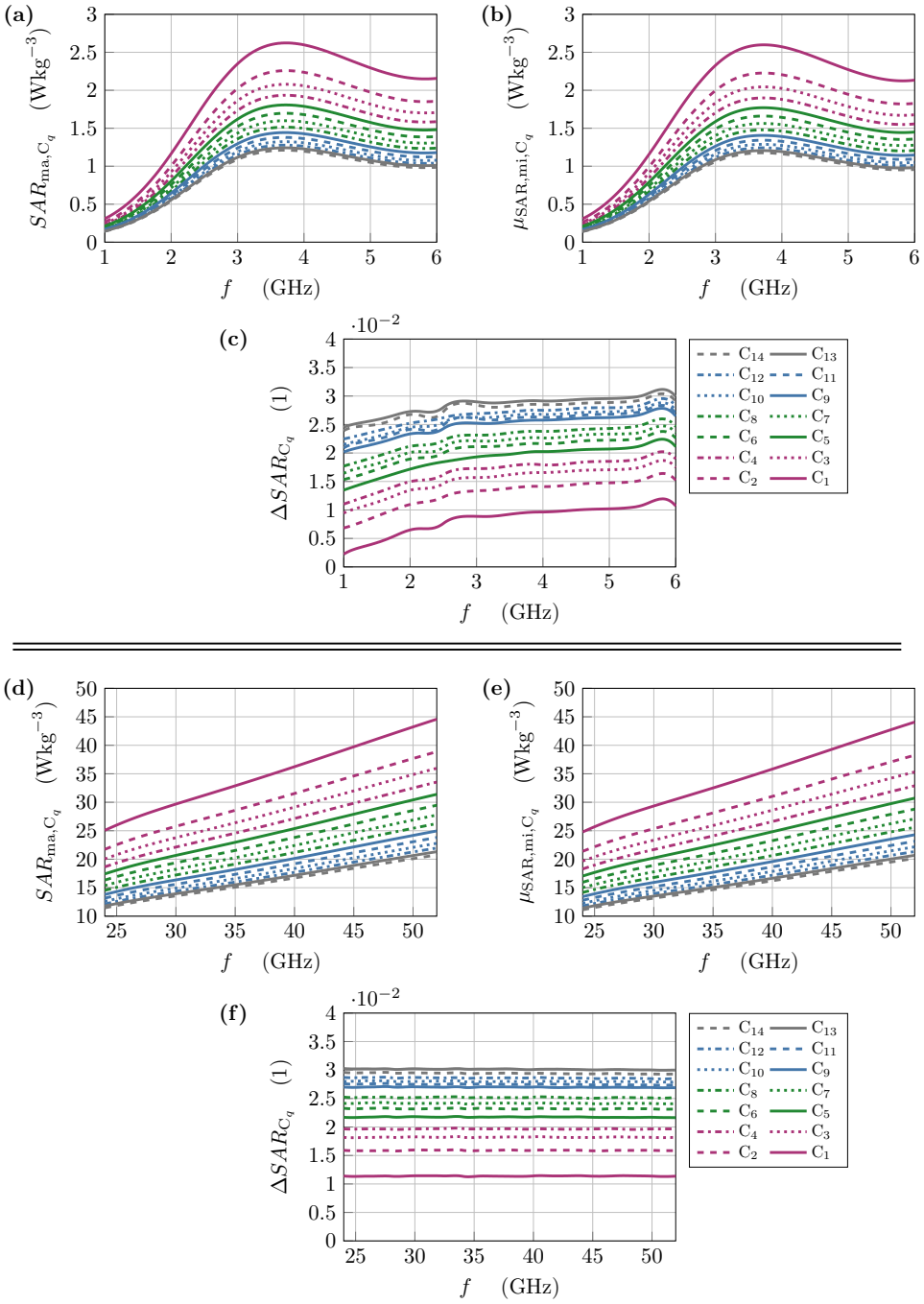


**Figure 11.8:** Stratum Corneum - Comparison between the SAR derived from the conventional representation of the microvolumes at a macroscopic scale, denoted as $SAR_{\mathrm{ma},C_q}$ in (a) & (d), and the statistical micro-SAR, denoted as $\mu_{\mathrm{SAR,mi},C_q}$ in (b) & (e), in the frequency interval $F_1$ in (a)-(c), and $F_2$ in (d)-(f): (a) & (d) show $SAR_{\mathrm{ma},C_p}$ while (b) & (e) show $\mu_{\mathrm{SAR,mi},C_p}$ for each frequency range; (c) & (f) depict the relative deviation between these values, denoted as $\Delta SAR_{C_q}$. The plots corresponding to each of the investigated cell layers are represented by solid, dashed, dotted and dashed-dotted lines. They are colored in magenta ($C_1$ through $C_4$), green ($C_5$ through $C_8$), blue ($C_9$ through $C_{12}$) and gray ($C_{13}$ and $C_{14}$) as indicated in the legend.

represented by solid, dashed, dotted, and dashed-dotted lines, and colored in magenta ($C_1$ through $C_4$), green ($C_5$ through $C_8$), blue ($C_9$ through $C_{12}$) and gray ($C_{13}$ and $C_{14}$) as indicated in the legend.It can be seen that $SAR_{\mathrm{ma,C}_q}$ and $\mu_{\mathrm{SAR,mi,C}_q}$ are almost identical with deviations, $\Delta SAR_{\mathrm{C}_q}$, ranging between 1 % and 3 % depending on the cell layer. The small deviations within the SC compared to the significant deviations within the viable epidermis are due to differences in the modeling of keratinocytes and corneocytes, or more specifically, the inclusion of organelle membranes. At the transition between the stratum granulosum and the stratum corneum, keratinocytes are metabolically deactivated, and their organelles and the nucleus dismantled. The lamellar bodies, which contain keratin and lipids in addition to organelles, fuse with the plasma membrane and shed their contents into the cell body [113]. Thus, the corneocytes, as described in detail in Chap. 9, are regarded as protein sacs that no longer contain organelles, and thus organelle membranes no longer need to be modeled. This leads to smaller differences between the SAR on a macroscopic and microscopic scale.

### 11.2.3 Methodological Consistency Between the Microscopic and Macroscopic Scales

The methodological consistency, evaluated by the coefficient $\gamma_{\mathrm{SAR,K}_p/\mathrm{C}_q}$, is examined in this subsection. The consistency analysis is presented for the cell models of the viable epidermis in Fig. 11.9(a) and (b) for the frequency ranges $F_1$ and $F_2$ respectively. Similarly, Figs. 11.9(c) and (d) display the consistency analysis for the cell layers of the SC covering the same frequency ranges. The plots depict the lowermost and uppermost cell models of the viable epidermis ($K_1$ and $K_{10}$) and SC ($C_1$ and $C_{14}$) as solid red and solid blue lines, respectively. The entire range of values is represented as a gray-shaded area bounded by dashed black lines.

It can be seen that $\gamma_{\mathrm{SAR,K}_p}$ is greater than 200 in $F_1$ and greater than 20 in $F_2$ in the viable epidermis, which means that the field variation in the cell models on a microscopic scale is at least 20 to 200 times greater than the field variations caused by the attenuation of the penetrating wave across the microvolumes in each cell layer on a macroscopic scale. In the SC, $\gamma_{\mathrm{SAR,C}_q}$ is greater that 10 in $F_1$ and greater than 200 in $F_2$. The methodological consistency of the scale-back projection is assured based on this factor, as the field variations within the microstructure of the cell are significantly larger than those within the microvolumes of the cell layers. This justifies the use of the scale-back projection for microdosimetric investigations.

In addition to this observation, some noticeable features in the presented curves need to be clarified. Particularly noticeable in frequency range $F_1$, a maximum is evident throughout the range of values in $\gamma_{\mathrm{SAR,K}_p}$, peaking at approximately 2.8 GHz. Additionally, there is a wide bandwidth of values in $\gamma_{\mathrm{SAR,C}_q}$, which also reaches a maximum around 2.8 GHz in the upper range of values. From the definition of $\gamma_{\mathrm{SAR,K}_p/\mathrm{C}_q}$ given in Eq. 11.17, it is inferred that the observed maximum and spread of data could be attributed to effects on either a

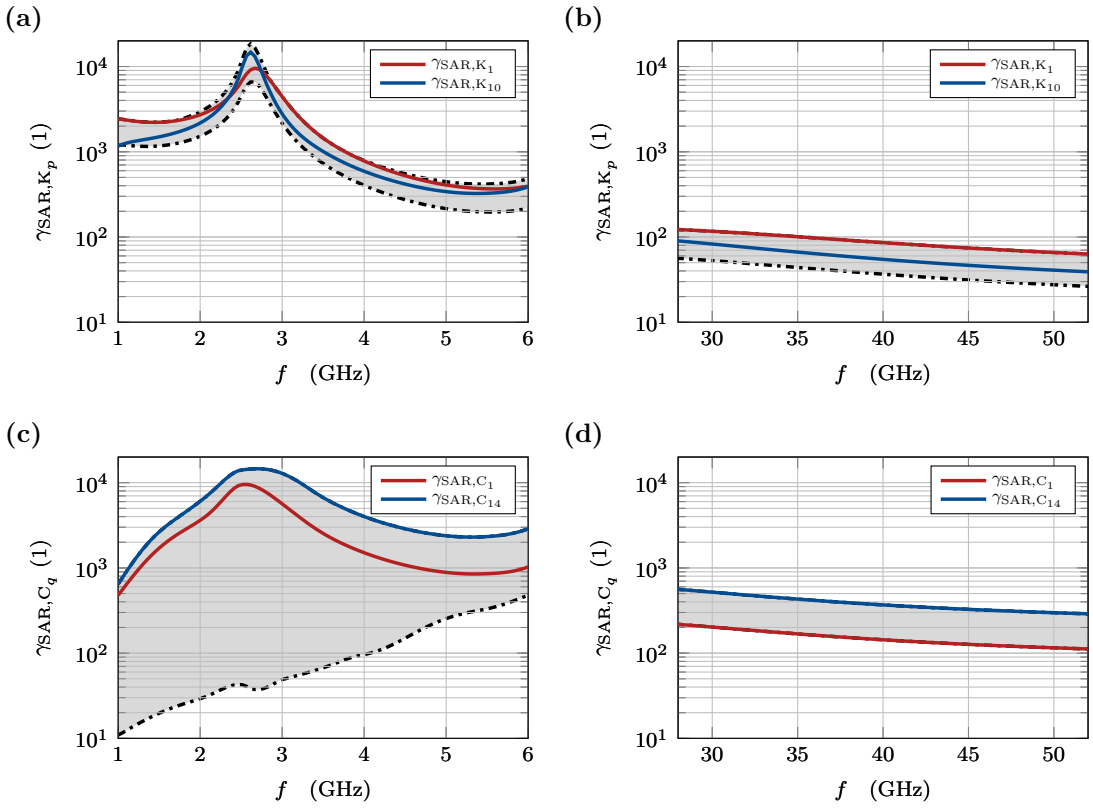


**Figure 11.9:** Consistency analysis of the methodological consistency, evaluated by the coefficient $\gamma_{\mathrm{SAR,K}_p/\mathrm{C}_q}$, for cell models of the viable epidermis and SC in different frequency ranges. Figures (a) and (b) present the consistency analysis for the viable epidermis in frequency ranges $\mathrm{F}_1$ and $\mathrm{F}_2$ respectively, while Figures (c) and (d) display the analysis for the SC covering the same frequency ranges. The plots show the lowermost and uppermost cell models of the viable epidermis ($\mathrm{K}_1$ and $\mathrm{K}_{10}$) and the SC ($\mathrm{C}_1$ and $\mathrm{C}_{14}$) as solid red and solid blue lines, respectively, with the entire range of values represented as a gray-shaded area bounded by dashed black lines.

microscopic scale (i.e., $CV_{\mathrm{SAR,mi,K}_p/\mathrm{C}_q}$) or a macroscopic scale (i.e., $CV_{\mathrm{SAR,ma,K}_p/\mathrm{C}_q}$). A decomposition of $CV_{\mathrm{SAR,mi,K}_p/\mathrm{C}_q}$ and $CV_{\mathrm{SAR,ma,K}_p/\mathrm{C}_q}$ into their respective arithmetic means, $\mu_{\mathrm{SAR,ma/mi,K}_p/\mathrm{C}_q}$, and standard deviations, $s_{\mathrm{SAR,ma/mi,K}_p/\mathrm{C}_q}$, on both the macroscopic and microscopic scales (while not explicitly shown here due to its irrelevance to the current investigation) shows that neither the observed maximum nor the spread of the data are due to phenomena in the microscopic exposure model, but can instead be attributed to $s_{\mathrm{SAR,ma,K}_p/\mathrm{C}_q}$. An explanation for this can be provided by considering the layered structure of the skin in which partial reflections and transmissions at the interfaces between these layers lead to superpositions that can yield two effects: (1) standing waves within the individual layers decreasing the variations of EM fields, and (2) dispersions in the reflectance and transmission of the overall skin structure. An indication of this hypothesis can be found in the spectral response of the power reflection coefficient of the macroscopic exposure setup, as shown in Fig. 11.10, which shows that a minimum in the total reflectance coincides with the maximum, as well as the spread of data, in $\gamma_{\mathrm{SAR,K}_p}$ and

$\gamma_{\mathrm{SAR,C}_q}$. This observation, alongside the impedance-matching properties of the epidermis mentioned in Chap. 10, could be further explored in a detailed analysis using the transfer matrix method. However, such an exploration is beyond the scope of the present investigations and is introduced here merely as an ancillary suggestion to consider the effects of multiple reflections within the skin as a layered medium.

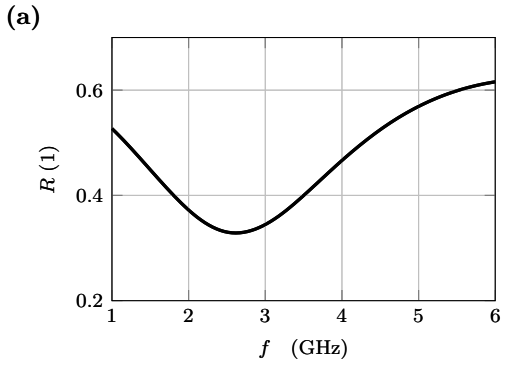


**Figure 11.10:** Power reflection coefficient, $R$, of the macroscopic exposure setup in the frequency interval $\mathrm{F}_1$.

### 11.2.4 The Statistical Micro-SAR compared to the Basic Restrictions for the Limitation of Local Exposure in the Limbs

Moving away from the analysis of the methodological consistency of the scale-back projection, Figs. 11.11(a) and (b) provide an overview of $\mu_{\mathrm{SAR,mi,K}_p}$ for all modeled keratinocytes of the viable epidermis for frequency intervals $\mathrm{F}_1$ and $\mathrm{F}_2$ respectively. The diagrams use the same labeling scheme for the cell models as used in Fig. 11.7. The bars displayed in red and green highlight values above and below $SAR_{10\mathrm{g}}$ as currently defined in the basic restrictions. In Fig. 11.11(a), it is observed that $\mu_{\mathrm{SAR,mi,K}_p}$ starts to exceed the threshold of $4\,\frac{\mathrm{W}}{\mathrm{kg}}$ from about 2 GHz and remains above this value throughout the entire interval $\mathrm{F}_1$. It can also be seen that $\mu_{\mathrm{SAR,mi,K}_p}$ forms a maximum at about 3.4 GHz across all cell models, varying between $5\,\frac{\mathrm{W}}{\mathrm{kg}}$ and $9\,\frac{\mathrm{W}}{\mathrm{kg}}$ depending on the cell model. However, in interval $\mathrm{F}_2$, $\mu_{\mathrm{SAR,mi,K}_p}$ increases monotonically with increasing frequency, and all values significantly exceed the threshold provided by the basic restrictions as illustrated in Fig. 11.11(b).

Similarly, Fig. 11.12 presents an overview of the mean exposure levels induced in the corneocytes, $\mathrm{C}_q$, for the same frequency intervals. The distribution of $\mu_{\mathrm{SAR,mi,C}_q}$ in the stratum corneum (SC) is shown in Figs. 11.12(a) and (b). Again, the same labeling scheme is used for the cell models as found in Fig. 11.8. Comparing Fig. 11.12 with Fig. 11.11, it can be observed that $\mu_{\mathrm{SAR,mi,C}_q}$ follows a similar general trend, with maxima developed at 3.4 GHz in interval $\mathrm{F}_1$ and a monotonic increase in interval $\mathrm{F}_2$. However, the average SAR

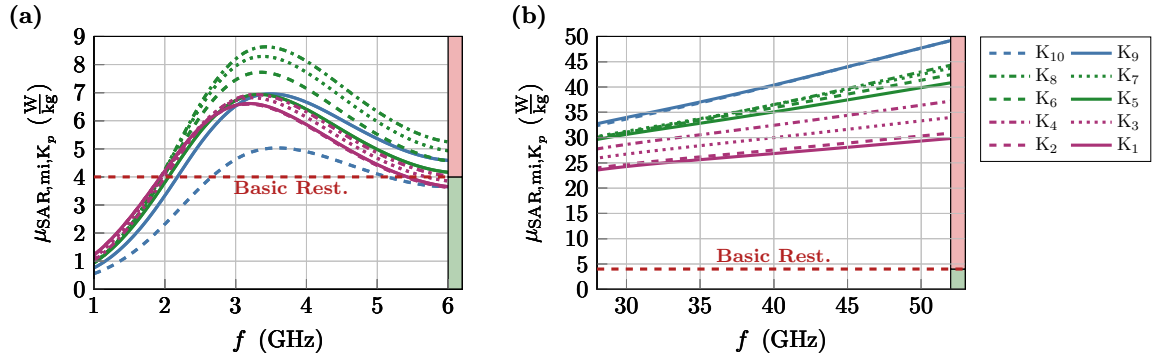


**Figure 11.11:** Viable Epidermis - Overview of $\mu_{\mathrm{SAR,mi,K}_p}$ within individual keratinocytes of the viable epidermis: (a) & (b) Distribution of $\mu_{\mathrm{SAR,mi,K}_p}$ in the viable epidermis for intervals $F_1$ and F2 respectively. The plots corresponding to each of the investigated cell models are represented by solid, dashed, dotted and dashed-dotted lines. They are colored in magenta ($K_1$ through $K_4$), green ($K_5$ through $K_8$), and blue ($K_9$ and $K_{10}$) as indicated in the legend.

values in the corneocytes are significantly lower, resulting in maximum values below 3 $\frac{\mathrm{W}}{\mathrm{kg}}$ in interval $F_1$ and maximum values below 45 $\frac{\mathrm{W}}{\mathrm{kg}}$ in interval $F_2$. In Fig. 11.12(b), it is evident that the threshold of 4 $\frac{\mathrm{W}}{\mathrm{kg}}$ is significantly exceeded in all of the cell models.

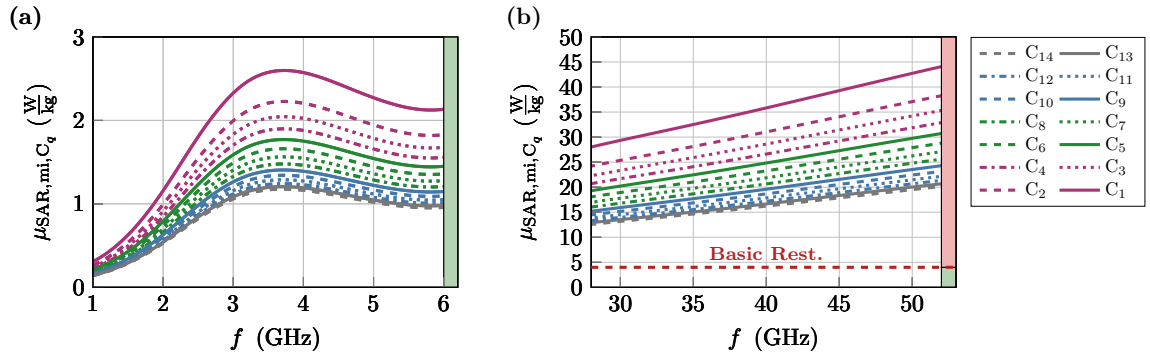


**Figure 11.12:** Stratum Corneum - Overview of $\mu_{\mathrm{SAR,mi,C}_q}$ within individual corneocyte models of the SC: (a) & (b) Distribution of $\mu_{\mathrm{SAR,mi,C}_q}$ in the SC for intervals $F_1$ and $F_2$ respectively. The plots corresponding to each of the investigated cell layers are represented by solid, dashed, dotted and dashed-dotted lines. They are colored in magenta ($C_1$ through $C_4$), green ($C_5$ through $C_8$), blue ($C_9$ through $C_{12}$) and gray ($C_{13}$ through $C_{14}$) as indicated in the legend.

## 11.3 Interpretation and Final Remarks

The application of scale-back projection to the bottom-up model of the epidermis has introduced a top-down multiscale approach, enabling a thorough investigation of the complex relationship between morphology, histochemical composition, and absorption behavior within epidermal cells. Conducted at two interrelated hierarchical scales, namely,

the macroscopic and microscopic scales, this investigation examined the level of EM exposure using the SAR within microvolumes that represent the smallest living units within the tissue (i.e., a cell) in each individual cell layer. At the macroscopic scale, these microvolumes constitute a homogeneous medium, representing individual epidermal cells through their effective material properties. This homogenization approach focuses on the broader aspects of cell behavior in relation to the overall skin structure. The SAR at this scale can be expressed in terms of $SAR_{\mathrm{ma,K}_p/\mathrm{C}_q}(\omega)$, following the conventional method of integrating the power density over the microvolume of interest and dividing by the integral of the volumetric mass density over the same volume (see Eq. 11.4). At the microscopic scale, the microvolumes encompass fully resolved cell models, wherein the morphology and histochemical composition of the cells are considered in great detail. This representation facilitates a comprehensive understanding of the influence of cellular structures on EM field absorption. For this, however, the SAR must be expressed in statistical terms, defining $SAR_{\mathrm{mi,K}_p/\mathrm{C}_q}(\omega) = \mu_{\mathrm{SAR,mi,K}_p/\mathrm{C}_q}(\omega) \pm s_{\mathrm{SAR,mi,K}_p/\mathrm{C}_q}(\omega)$, referred to as the micro-SAR. It is called this because its arithmetic mean, $\mu_{\mathrm{SAR,mi,K}_p/\mathrm{C}_q}(\omega)$, averages the SAR over the individual cell structures under consideration (see Eq. 11.12), allowing realistic consideration of EM absorption and its spatial distribution on the microscopic scale in a single representative scalar expression.

By using the micro-SAR to assess the variations of $SAR(\vec{r},\omega)$ in epidermal cells, Sec. 11.2.1 illustrated how the morphology and histochemical composition of these cells significantly shape the field distribution within the microstructure of the tissue. Using basal keratinocytes as an illustrative example, the detailed analysis of the field distribution based on sectional images and histograms showed that the membranes make a surprisingly large contribution to the absorption, especially in frequency interval $\mathrm{F}_1$, with a value of up to 60 %, while the nucleus, which is largely field-free due to the surrounding organelle membranes, contributed little to the absorption with a value of less than 10 %. This uneven distribution of loss contributions is all the more significant when one considers that the volumetric fraction of the computational domain comprising membranes is only 3 %, while that representing the nucleus is a much larger 30 %. In addition, these structures are assigned very different volumetric mass densities ($\rho_{\mathrm{M}} = 629\,\frac{\mathrm{kg}}{\mathrm{m}^3}$ and $\rho_{\mathrm{NP}} = 1094\,\frac{\mathrm{kg}}{\mathrm{m}^3}$). These differences in loss contributions, volumetric proportions, and mass densities further highlight the intricate relationship between morphology, composition, and absorption behavior within the epidermal cells and amplify the importance of considering these aspects combined in $\mu_{\mathrm{SAR,mi,K}_p/\mathrm{C}_q}(\omega)$.

In addition, the analysis of $CV_{\mathrm{SAR,mi,K}_p}$ showed that the variations of SAR values within the viable epidermis ranged in average between 30 % and 71 % within one standard deviation, $s_{\mathrm{SAR,mi,K}_p}$, around the respective mean value, $\mu_{\mathrm{SAR,mi,K}_p}$, in both frequency intervals $\mathrm{F}_1$ and $\mathrm{F}_2$. The corresponding analysis of $CV_{\mathrm{SAR,mi,C}_q}$ demonstrated an almost frequency-independent average variations of SAR values of 33 %.

The significant impact of neglecting the intricate structure of epidermal cells during SAR calculations was illustrated in Sec. 11.2.2, where it was shown to lead to a substantial underestimation of epidermal exposure. This was demonstrated by comparing $SAR_{\mathrm{ma,K}_p/\mathrm{C}_q}$

with $\mu_{\mathrm{SAR,mi,K}_p/\mathrm{C}_q}$. The comparison revealed that the macroscopic measure $SAR_{\mathrm{ma,K}_p/\mathrm{C}_q}$ underestimates the exposure of skin tissue by up to 45 %.

In Sec. 11.2.3, the methodological consistency of scale-back projection, as evaluated by the coefficient $\gamma_{\mathrm{SAR,K}_p/\mathrm{C}_q}$, revealed that the microscopic field variations in cell models are much greater than the macroscopic field variations within cell layers, thereby justifying the application of scale-back projection in microdosimetric investigations.

Sec. 11.2.4 demonstrated that $\mu_{\mathrm{SAR,mi,K}_p/\mathrm{C}_q}$ significantly exceeds the $SAR_{10\mathrm{g}}$ threshold of $4\,\frac{\mathrm{W}}{\mathrm{kg}}$ across both frequency ranges. However, a straightforward numerical comparison at this stage might lead to an oversimplified assumption that $SAR_{10\mathrm{g}}$ significantly underestimates the EM exposure of the skin. A nuanced interpretation of this result calls for a reassessment of the initial purpose behind the establishment of $SAR_{10\mathrm{g}}$ as a metric in the context of conventional dosimetric multiphysics simulations. Moreover, it requires a conceptual comparison of this intent with that of the scale-back projection approach.

Conventionally, the SAR is defined in terms of a generic cubic volume equivalent to a specific mass of water, in contact with the skin surface, encompassing all constituent tissue types. Within this paradigm, the spatially averaged SAR is related to the maximum temperature increase within this defined volume, serving as a mass-based EM exposure metric, and prescribes local exposure limits across a broad frequency spectrum from 100 kHz to 6 GHz. At the lower end of this spectrum, EM field attenuation within tissue can be considered negligible due to the extended wavelengths involved. At higher frequencies, however, the field attenuation becomes significant, resulting in a significant decrease in penetration depth with increasing frequency. This necessitates consideration of an optimal volume that provides a meaningful measure of EM exposure.

To reconcile the significant shift in field attenuation and penetration depth over the frequency range from 1 GHz to 6 GHz, Hirata et al. [9] examined the correlation between temperature distribution and mass-averaged SAR over a range of volumes. These volumes corresponded to water masses ranging from 0.1 g to 100 g. In the search for an optimal volume size, the challenge was to adequately capture a significant amount of data without including less significant trailing values, while at the same time avoiding smaller volumes that might capture only a fraction of the necessary data, thus providing an incomplete picture. To achieve this balance, they used the coefficient of determination, a statistical tool that assesses the quality of a best-fit line to data, which in this case was the predicted temperature increase derived from the multiphysics simulations. Their analyses identified a peak correlation at a 10 g water-equivalent volume, which represents a reliable relationship between the average SAR and the temperature distribution over the frequency range of 1 GHz to 6 GHz, as described in [9]. It is important to note, however, that this 10 g volume, encapsulates what appears to be the entire 'relevant' depth of the temperature profile, thereby providing the best balance within the 1 GHz to 6 GHz frequency range. As illustrated by the example of EM exposure of the human head by a dipole antenna in [8,9], $SAR_{10\mathrm{g}}$ proves to be an appropriate metric in scenarios where the

temperature profile is dominated by spatially variable irradiation patterns (such as an antenna aperture) and complex organ-scale geometries with heterogeneous tissue compositions, including the highly temperature-sensitive cerebral matter. Despite its suitability within these constraints, $SAR_{10g}$ serves as a statistical compromise, not an optimal solution, and may not provide the highest fidelity solution universally.

In contrast, scale-back projection examines EM exposure in distinct microvolumes, each of which represents the smallest living unit within the tissue, namely a cell. This approach allows a more precise quantification of EM absorption at individual depth levels, each corresponding to an individual cell layer. Thus, scale-back projection not only provides a high-resolution exposure profile across the skin, but also represents a potential tool for augmenting the methodological repertoire of conventional multiphysics simulations. When applying the absorption profile obtained by scale-back projection to subsequent thermal simulations, this approach allows for a much more accurate representation of the effects of EM irradiation on specific skin structures identified as thermally sensitive, in this case the proliferative pool of the epidermis. Thus, scale-back projection potentially provides more detailed access to thermal effects at the microstructural level and provides valuable insight into the complex interplay of EM exposure, absorption, and thermal response within the skin.

# 12 Conclusions and Outlook

In the context of this work, scale-back projection was introduced as an innovative top-down multiscale approach. This method allows the consideration of the complex interplay between morphology, histochemical composition and EM absorption at the cellular level, while taking into account the specific position of individual cells within the layered structure of the skin for accurate microdosimetric analyses. For its application, however, scale-back projection requires a comprehensive material description that must be tailored to the specific anatomical characteristics of the tissue under study.

Considering this requirement, a hierarchical bottom-up model of the epidermis was developed that offers a coherent description of the material properties both macroscopically and microscopically. Unlike earlier bottom-up models [45, 114], the epithelial tissue of the epidermis was regarded as a symbiotic biological system shaped by the life cycle of its predominant cell type, the keratinocytes (or corneocytes). By subdividing the epidermis into 24 cell layers, the differentiation of basal keratinocytes towards the skin surface is represented through gradual changes across these layers. This took into account two primary aspects: (1) alterations in cell geometry and internal structure, and (2) changes in the histochemical composition of the cells. The microstructure of the epidermal cells was represented using parametric CAD models. These models were adapted to the physiological conditions specific to each individual cell layer using geometric parameters derived from the literature, as outlined in detail in Chap. 9. Thanks to the adapted cell models, the thicknesses of individual epidermal layers were determined on a macroscopic scale, ensuring anatomical accuracy. As these thicknesses sum to the total thickness of the epidermis, the histochemical composition could be conceptually represented using concentration profiles, treating the tissue as a composite of water, lipids, keratin, and a general protein component. These concentration profiles were then used to derive the histochemical composition for each cell layer and project it onto individual cell compartments of the corresponding parametric cell models, treating their biochemical composition at a ”molecular scale". By employing mixing formulas in an incremental mixing procedure, the effective permittivities were determined and then set as material parameters for the compartments of the parameterized cell models. With the parametric cell models now fully realized, capturing detailed cytoanatomical features and ensuring accurate histochemical data when describing the permittivities of the cell compartments, it was possible to determine the effective material properties of each cell layer using numerical homogenization. With this innovative approach, the bottom-up model enables the reconstruction of the formation, maturation, and eventual death of epidermal cells, and seamlessly translates this life cycle into effective material properties, consistently

describing the epidermis at both the macroscopic and microscopic scale in a single integrated model.

The integration of the bottom-up model of the epidermis into a complete skin model is achieved by the simplified assumption that the individual sublayers of the skin are modular, i.e. that their exact modifications with respect to thickness and the choice of the underlying material parameters can be considered independently. Based on this assumption, two skin models could be implemented, the topological properties of which correspond to those of the skin of the thighs. The first model was denoted as the reference model and was based on metrologically derived tissue models published by Sasaki et al. in [4,5]. These studies formed the basis for exposure regulations as established by ICNIRP, thus allowing direct comparisons to be drawn between those guidelines and this study. In addition, having real measurements at the heart of its simulation models, Sasaki et al. provides the closest reference information available to a real case. The second model, referred to as the hybrid model, combined the bottom-up model of the epidermis with the metrologically derived tissue models of the other skin layers mentioned above. The material properties of the individual cell layers of the bottom-up model were validated by comparing them with the epidermal and dermal values found therein.

Embedding the two skin models in FEM-based simulations, a macroscopic exposure setup was established to simulate skin irradiation at frequencies between 1 GHz and 300 GHz. By analyzing the transmittance of EM waves to the skin models and assessing the EM absorption across the individual cell layers of the epidermis, the study revealed the following findings and associated conclusions:

- The assessment of the skin models highlighted biases in the metrological representation of the epidermis in the reference model. These biases can be attributed to: (1) missectioning of the epidermis, potentially incorporating dermal components, and (2) the absence of epidermal measurements for frequencies greater than 100 GHz.
- To address the aforementioned absence of data in the reference model, the extrapolation $\underline{\varepsilon}_{\mathrm{r,ED}}(f > 100\,\mathrm{GHz}) = \underline{\varepsilon}_{\mathrm{r,ED}}(f = 100\,\mathrm{GHz})$ was considered. As a result, deviations from the hybrid model were noted at frequencies above 100 GHz. Specifically: (1) The reference model underestimated the EM energy transmitted into the skin by as much as 24 %, and (2) overestimated the absorbed EM energy within the epidermis by up to 35 %.
- Regardless of these biases, the analysis of the energy distribution across the epidermis for the entire frequency range revealed: (1) overestimation of absorption by the dead cells of the stratum corneum by up to 70 %, and (2) underestimation of absorption by the living cells of the viable epidermis by up to 60 %, depending on the cell layer examined (i.e., $K_1$ through $K_{10}$ or $C_1$ through $C_{14}$). This demonstrated the importance of accurately representing physiological changes across the epidermis in dosimetric investigations, even at a macroscopic scale

After investigating the macrosopic effects of physiological changes across the epidermis, scale-back projection was applied to the hybrid model. In a twofold procedure, power

was first determined for cellular microvolumes on a macroscopic scale, with these microvolumes precisely corresponding to the size and specific location of individual epidermal cells. This data was then projected onto corresponding cell models on a microscopic scale, which capture the cellular structure and histochemical composition with high detail. Applying statistical analysis to the spatial SAR distribution in these parametric cell models, it was possible to define a statistical micro-SAR, $SAR_{\mathrm{mi,K}_p/\mathrm{C}_q} = \mu_{\mathrm{SAR,mi,K}_p/\mathrm{C}_q} \pm s_{\mathrm{SAR,mi,K}_p/\mathrm{C}_q}$. This enabled the precise determination of EM absorption using the statistical average, $\mu_{\mathrm{SAR,mi,K}_p/\mathrm{C}_q}$, and the estimation of the variation of this absorption across the cellular microstructure using the standard deviation, $s_{\mathrm{SAR,mi,K}_p/\mathrm{C}_q}$. Based on the extensive microdosimetric investigations conducted using scale-back projection within the 5G frequency ranges of $1-6\,\mathrm{GHz}$ and $24-52\,\mathrm{GHz}$, the following conclusions can be drawn:

- The comprehensive comparison between $\mu_{\mathrm{SAR,mi,K}_p/\mathrm{C}_q}$ and $SAR_{\mathrm{ma,K}_p/\mathrm{C}_q}$ revealed an underestimation of epidermal absorption using conventional methods by up to 45 %, especially between $1-6\,\mathrm{GHz}$ where the membranes significantly contribute to the total absorption.
- In addition, the analysis of the coefficients of variation showed a surprisingly high level of variation in the microstructure. For the viable epidermis, $CV_{\mathrm{SAR,mi,K}_p}$ showed that the variations of SAR values ranged between 30 % and 71 % of one standard deviation, $s_{\mathrm{SAR,mi,K}p}$, around the respective mean value, $\mu_{\mathrm{SAR,mi,K}_p}$. The corresponding analysis of $CV_{\mathrm{SAR,mi,C}_q}$ for the stratum corneum demonstrated an almost frequency-independent average variations of SAR values of 33 %, with an overall range from 27 % to 36 %.

Based on these findings, it has been demonstrated that scale-back projection allows the determination of more accurate exposure profiles of irradiated tissues by considering its underlying microstructure. The use of these profiles in conventional multiphysics simulations therefore has the potential to enhance the accuracy of EM dosimetry.

# Outlook

In the subsequent section, potential directions for future research and further refinements of the approaches presented are discussed along with any associated challenges.

The next logical step in research is to develop hierarchical bottom-up models for the other skin sublayers: the dermis and the hypodermis. However, there are two challenges, one minor and one major, in developing such models. The minor one is the design and implementation of a dedicated tissue scale in parametric tissue models that captures the amorphous histological organization of these tissues. This is a process which requires detailed histoanatomical knowledge, especially if physiological changes across these layers are to be captured. How the implementation of such a tissue scale in computational models could be achieved was discussed in [96] using the illustrative example of generic

hypodermis models. In these, the amorphous histological organization, i.e. the arrangement of cells relative to each other, was modeled using computational domains that confined a large number of randomly arranged cells. An excerpt from [96], adapted for this work, is given in Appendix E and should serve as inspiration for more realistic models. The major challenge is to develop methodological approaches that bridge the organ, tissue, and cellular scales. The strategy used for the epidermis, which exploited its regular, dense histological organization to approximate the tissue as a general cell arrangement based on a primitive orthorhombic unit cell, is not applicable to these other tissues. Consequently, the approach that allowed efficient numerical treatment using a detailed single cell model with boundary conditions that account for periodicity is no longer valid.

Another important endeavor is to extend the simulation environment to have multiphysics capabilities which can perform thermal simulations. A first step towards implementation would be to determine the temperature profile of the epidermis based on the micro-SAR, using $\mu_{\mathrm{SAR,mi,K}_p/\mathrm{C}_q}$ to quantify the absorption of the tissue microstructure along with the subsequent temperature increase. In the long term, the implementation of a multiscale approach to thermal simulation may also be a desirable goal to determine heat hotspots within single cells, especially in close proximity to organelle membranes.

A further aspect worthy of investigation would be to determine to what extent and in which frequency intervals physiological changes in the epidermis lead to impedance-matching effects that significantly influence the transmission behavior of the skin. A recent study by Christ et al. [19] has demonstrated the significance of impedance-matching properties at frequencies greater than 15 GHz. Specifically, this involves the interplay of the thickness and material properties of the stratum corneum (SC) in relation to the deeper sublayers of the skin, which can cause constructive interference, thereby reducing reflection from the skin surface. However, with the bottom-up model of the epidermis developed here, it would be possible to identify not only the thickness of the SC as the cause of such an effect, but also the gradual transition of the material properties from one cell layer to the next. One possible approach to investigate the impedance matching properties of the epidermis in greater detail would be to quantify partial reflectance and transmittance occurring at the interfaces defined by the layered topology of the individual epidermal cell layers. This method would allow the capture of the superposition of multiple reflections and transmissions at these interfaces considering the layered structure of the epidermis. Such an approach would elucidate whether impedance matching effects arise predominantly from the pronounced material contrast at the SG/SC interface - where water concentration drops most rapidly - or from combined interactions across all epidermal cell layer interfaces. From these insights, the necessary level of detail for modeling the epidermis to accurately simulate the transmission behavior of the skin on a macroscopic scale could be determined.

Finally, there are potential avenues for further developing the bottom-up model of the epidermis. One significant modification would be to account for glucose levels in the extracellular medium. Such an adaptation could facilitate non-invasive monitoring of

pathologies manifested by changes in the chemical composition of the extracellular medium, such as diabetes. Specifically, this would permit investigations into the sensitivity of metabolic changes to the effective macroscopic material properties within individual cell layers, paving the way for monitoring a range of pathologies non-invasively, such as novel glucose monitoring of the fingernail bed [115].

# Appendix A

In order to verify the computational model used to determine the macroscopic properties of the cells, the simulations considering the simple spherical cell model are compared with analytical mixing rules. As described in [66] and [61], the effective permittivity of the cell $\underline{\varepsilon}_{\mathrm{Cell}}$ is modelled as double-layered shell

$$\underline{\varepsilon}_{\mathrm{Cell}} = \underline{\varepsilon}_{\mathrm{PM}} \frac{2\,(1-\nu_1) + (1+2\,\nu_1)\,E_1}{(2+\nu_1) + (1-\nu_1)\,E_1} \tag{A.1}$$

where the geometrical parameter $\nu_1$ represents for the volume ratio between the plasma membrane and the inner layers and the intermediate parameter $E_1$ the effective permittivity of the lower layers weighted by the permittivity of the upper layer, which is in this case the plasma membrane. The parameters $\nu_1$ and $E_1$ is given by

$$\nu_1 = \left(1 - \frac{d_{\mathrm{PM}}}{r_{\mathrm{Cell}}}\right)^3 \tag{A.2}$$

and

$$E_1 = \frac{\underline{\varepsilon}_{\mathrm{CP}}}{\underline{\varepsilon}_{\mathrm{PM}}} \cdot \frac{2\,(1-\nu_2) + (1+2\,\nu_2)\,E_2}{(2+\nu_2) + (1-\nu_2)\,E_2}. \tag{A.3}$$

Similar to the calculation of the effective permittivity of the whole cell, the intermediate parameter $E_1$ itself is also calculated from the intermediate parameters $\nu_2$ and $E_2$. These can be calculated according to

$$\nu_2 = \left(\frac{r_{\mathrm{N}}}{r_{\mathrm{Cell}} - d_{\mathrm{PM}}}\right)^3 \tag{A.4}$$

and

$$E_2 = \frac{\underline{\varepsilon}_{\mathrm{NE}}}{\underline{\varepsilon}_{\mathrm{CP}}} \cdot \frac{2\,(1-\nu_3) + (1+2\,\nu_3)\,E_3}{(2+\nu_3) + (1-\nu_3)\,E_3} \tag{A.5}$$

The concatenation of intermediate parameters ends with the inner layer consisting of the nucleus and its envelope, expressed by:

$$\nu_3 = \left(1 - \frac{d_{\mathrm{NE}}}{r_{\mathrm{N}}}\right)^3 \tag{A.6}$$

and

$$E_3 = \frac{\underline{\varepsilon}_{\mathrm{NP}}}{\underline{\varepsilon}_{\mathrm{NE}}}. \tag{A.7}$$

After calculating the effective dielectric constant of the cell according to the above algorithm, the effective material parameters of the mixture are calculated based on the Hanai-Bruggeman equation as presented in [25]

$$0 = \frac{(\underline{\varepsilon}_{\mathrm{mix}} - \underline{\varepsilon}_{\mathrm{Cell}})}{(\underline{\varepsilon}_{\mathrm{EC}} - \underline{\varepsilon}_{\mathrm{Cell}})} \cdot \sqrt[3]{\left(\frac{\underline{\varepsilon}_{\mathrm{EC}}}{\underline{\varepsilon}_{\mathrm{mix}}}\right)} - (1 - c_{\mathrm{Cell}}). \tag{A.8}$$

# Appendix B

Cross-sections through the YZ plane of the cell models $K_{1\&2}$, $K_5$, $K_8$, $C_1$ and $C_{14}$ are illustrated in Fig. B.1. The cross-sections of the keratinocytes are each shown in the correct proportions to one another, and those of the corneocytes are also correct with respect to each other. Due to the large aspect ratio of the corneocyte model, it is not possible to show the two types of model in the correct size ratio to each other.

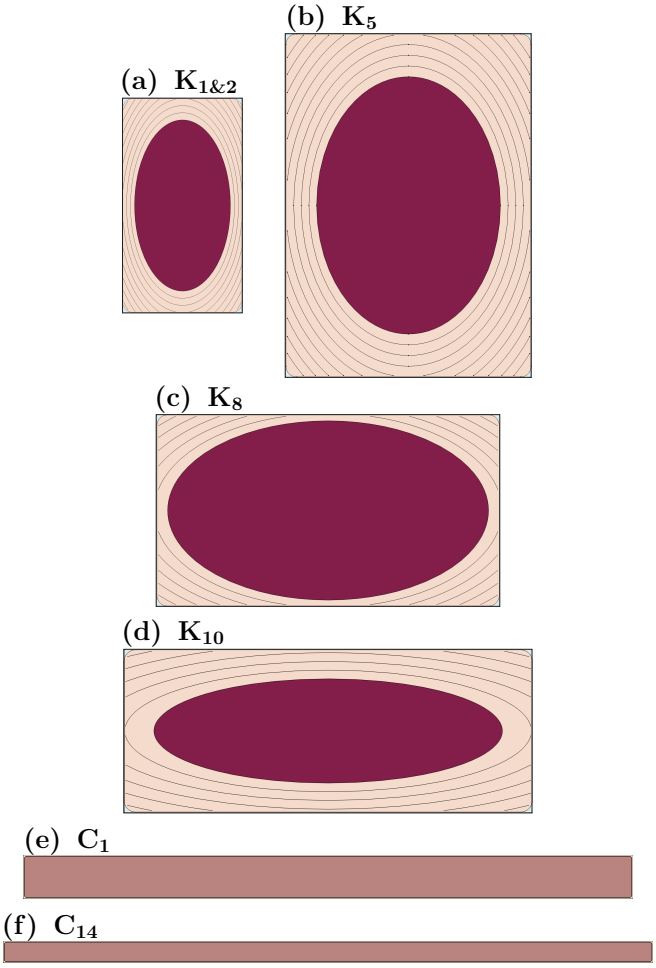


**Figure B.1:** Overview of the cross-sections through the YZ plane of the cell models $K_{1\&2}$, $K_5$, $K_8$, $C_1$ and $C_{14}$. The cross-sections of the keratinocytes and those of the corneocytes are each shown in the correct proportions to one another.

# Appendix C

Analysis of the power distribution over the epidermal cell layers, $C_q$, according to Eq. 10.6. Fig. C.1(a) shows that in the reference model, the power distribution within the SC is pri-

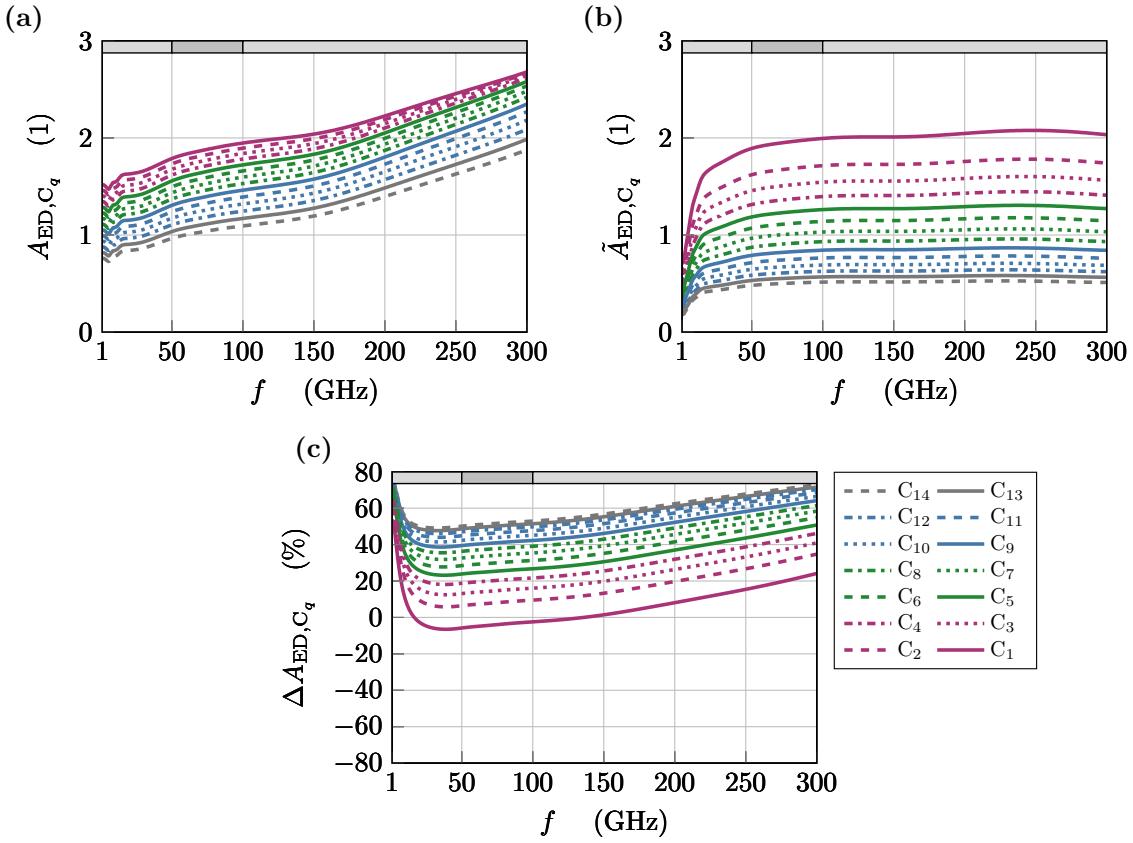


**Figure C.1:** Analysis of the power distribution over the epidermal cell layers, $C_q$, according to Eq. 10.6: (a)-(b) Power absorbed by the epidermal cell layers, $C_q$, in the reference and hybrid models, denoted by $A_{ED,C_q}$ and $\tilde{A}_{ED,C_q}$, respectively. (c) Relative deviation of $\Delta A_{ED,C_q}$ between the two skin models. The plots corresponding to each of the investigated cell layers are represented by solid, dashed, dotted and dashed-dotted lines. They are colored in magenta ($C_1$ through $C_4$), green ($C_5$ through $C_8$), blue ($C_9$ through $C_{12}$) and gray ($C_{13}$ through $C_{14}$) as indicated in the legend.

marily determined by the distance of the individual cell layers from the skin surface. The power distribution within the hybird model in Fig. C.1(b) shows that the level of hydration has a strong influence on the power distribution within the epidermis, as evidenced

by the significantly higher difference between the absorption in cell layer $C_1$ and $C_{14}$. The relative deviation depicted in Fig. C.1(c) shows that the absorption of the SC is overestimated by up to 70 % across the entire spectrum in all cell layers (with the exception of $C_1$).

# Appendix D

In this appendix, illustrations are provided to showcase the variability of SAR values. These are captured across the cell models of keratinocytes, as depicted in Fig. D.1 through Fig. D.10 (i.e., $K_1$ through $K_{10}$), and also across the cell models of corneocytes, as shown in Fig. D.11 through Fig. D.24 (i.e., $C_1$ through $C_{14}$). Within these figures, $SAR_{\mathrm{mi,K}_p/\mathrm{C}_q}(\omega)$ is illustrated on semi-logarithmic scales in subplots (a) and (b) for frequency intervals $F_1$ and $F_2$, respectively. The mean, $\mu_{\mathrm{SAR,mi,K}_p/\mathrm{C}q}$, is marked by a solid black line. A dark-gray area around this mean encompasses values within one standard deviation, specifically $\mu_{\mathrm{SAR,mi,K}_p/\mathrm{C}_q} \pm s_{\mathrm{SAR,mi,K}_p/\mathrm{C}_q}$, with dashed-dotted lines signify the bounds of this range. A light-gray area around $\mu_{\mathrm{SAR,mi,K}_p/\mathrm{C}_q} \pm s_{\mathrm{SAR,mi,K}_p/\mathrm{C}_q}$ reveals the full value range within the computational domains, bounded by $SAR_{\mathrm{max,mi,K}_p/\mathrm{C}_q}$ and $SAR_{\mathrm{min,mi,K}_p/\mathrm{C}_q}$. Additionally, a red dotted line denotes the local SAR exposure threshold, $SAR_{10\mathrm{g}}$, limiting induced power in limbs to below 4 $\frac{\mathrm{W}}{\mathrm{kg}}$ according to the basic restrictions (see Tab. 7.1).

## Cell Models of the Korneocytes $K_1$ through $K_{10}$

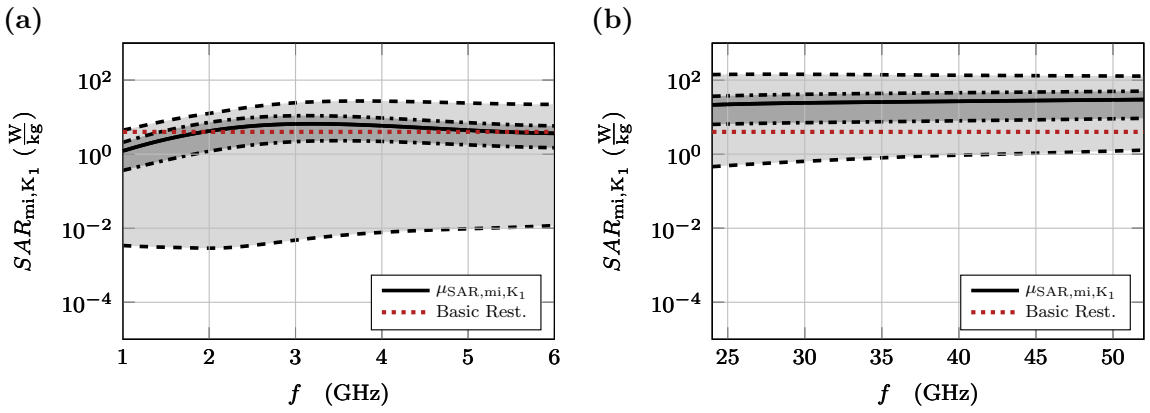


**Figure D.1:** $SAR_{\mathrm{mi,K_1}}(\omega)$ for cell model $K_1$: (a) Semi-logarithmic representation of SAR values for frequency interval $F_1$. The solid black line indicates the mean, $\mu_{\mathrm{SAR,mi,K_1}}$. A dark-gray area surrounds this mean, encompassing values within one standard deviation, $\mu_{\mathrm{SAR,K_1}} \pm s_{\mathrm{SAR,K_1}}$, demarcated by dashed-dotted lines. The light-gray area illustrates the full range of observed values within the computational domain, bounded by $SAR_{\mathrm{max,mi,K_1}}$ and $SAR_{\mathrm{min,mi,K_1}}$. A red dotted line marks the SAR exposure threshold for the public, $SAR_{10\mathrm{g}}$, set below 4 $\frac{\mathrm{W}}{\mathrm{kg}}$. (b) Plot analogous to (a) for frequency $F_2$.

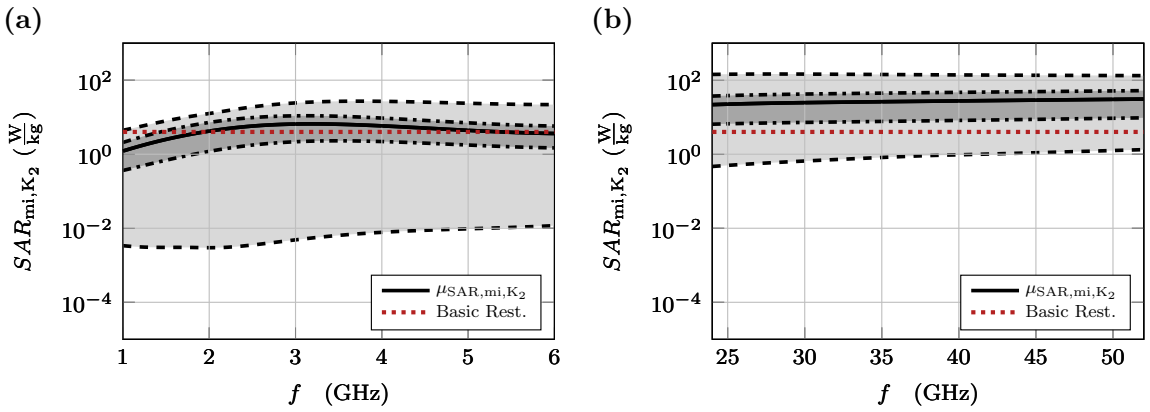


**Figure D.2:** $SAR_{\mathrm{mi,K_2}}(\omega)$ for cell model $\mathrm{K_2}$: (a) Semi-logarithmic representation of SAR values for frequency interval $\mathrm{F_1}$. The solid black line indicates the mean, $\mu_{\mathrm{SAR,mi,K_2}}$. A dark-gray area surrounds this mean, encompassing values within one standard deviation, $\mu_{\mathrm{SAR,K_2}} \pm s_{\mathrm{SAR,K_2}}$, demarcated by dashed-dotted lines. The light-gray area illustrates the full range of observed values within the computational domain, bounded by $SAR_{\mathrm{max,mi,K_2}}$ and $SAR_{\mathrm{min,mi,K_2}}$. A red dotted line marks the SAR exposure threshold for the public, $SAR_{10\mathrm{g}}$, set below $4\,\frac{\mathrm{W}}{\mathrm{kg}}$. (b) Plot analogous to (a) for frequency $\mathrm{F_2}$.

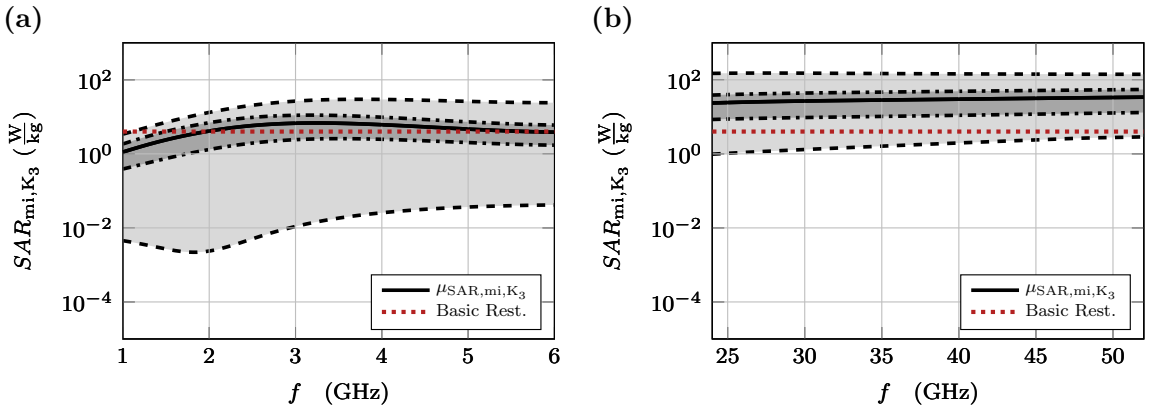


**Figure D.3:** $SAR_{\mathrm{mi,K_3}}(\omega)$ for cell model $\mathrm{K_3}$: (a) Semi-logarithmic representation of SAR values for frequency interval $\mathrm{F_1}$. The solid black line indicates the mean, $\mu_{\mathrm{SAR,mi,K_3}}$. A dark-gray area surrounds this mean, encompassing values within one standard deviation, $\mu_{\mathrm{SAR,K_3}} \pm s_{\mathrm{SAR,K_3}}$, demarcated by dashed-dotted lines. The light-gray area illustrates the full range of observed values within the computational domain, bounded by $SAR_{\mathrm{max,mi,K_3}}$ and $SAR_{\mathrm{min,mi,K_3}}$. A red dotted line marks the SAR exposure threshold for the public, $SAR_{10\mathrm{g}}$, set below $4\,\frac{\mathrm{W}}{\mathrm{kg}}$. (b) Plot analogous to (a) for frequency $\mathrm{F_2}$.

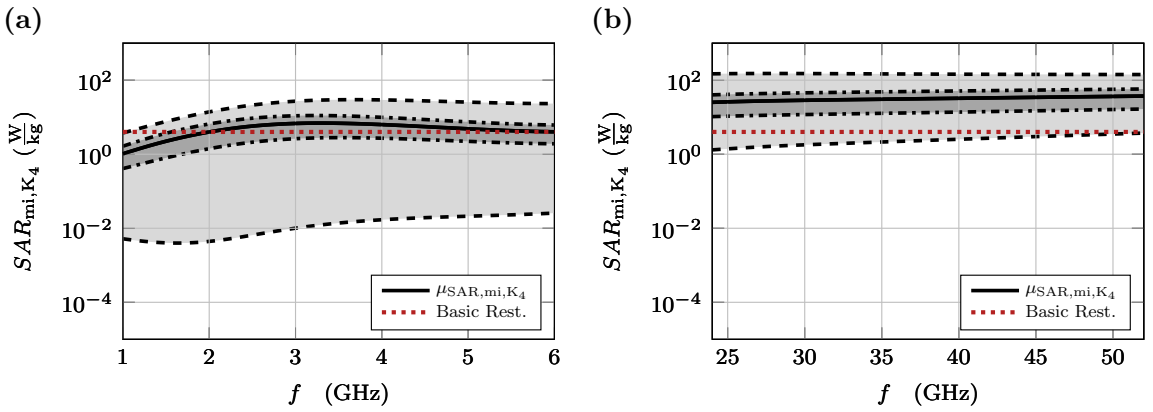


**Figure D.4:** $SAR_{\mathrm{mi,K_4}}(\omega)$ for cell model $\mathrm{K_4}$: (a) Semi-logarithmic representation of SAR values for frequency interval $\mathrm{F_1}$. The solid black line indicates the mean, $\mu_{\mathrm{SAR,mi,K_4}}$. A dark-gray area surrounds this mean, encompassing values within one standard deviation, $\mu_{\mathrm{SAR,K_4}} \pm s_{\mathrm{SAR,K_4}}$, demarcated by dashed-dotted lines. The light-gray area illustrates the full range of observed values within the computational domain, bounded by $SAR_{\mathrm{max,mi,K_4}}$ and $SAR_{\mathrm{min,mi,K_4}}$. A red dotted line marks the SAR exposure threshold for the public, $SAR_{10\mathrm{g}}$, set below $4\,\frac{\mathrm{W}}{\mathrm{kg}}$. (b) Plot analogous to (a) for frequency $\mathrm{F_2}$.

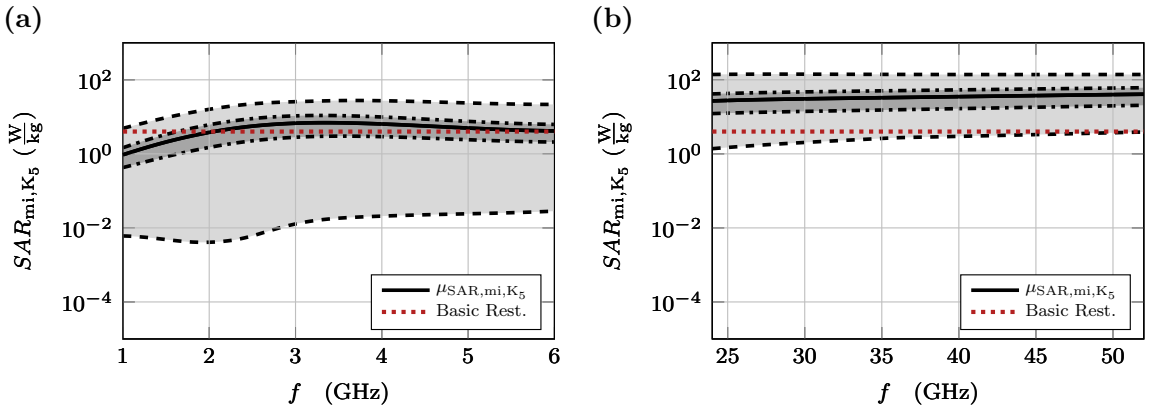


**Figure D.5:** $SAR_{\mathrm{mi,K_5}}(\omega)$ for cell model $\mathrm{K_5}$: (a) Semi-logarithmic representation of SAR values for frequency interval $\mathrm{F_1}$. The solid black line indicates the mean, $\mu_{\mathrm{SAR,mi,K_5}}$. A dark-gray area surrounds this mean, encompassing values within one standard deviation, $\mu_{\mathrm{SAR,K_5}} \pm s_{\mathrm{SAR,K_5}}$, demarcated by dashed-dotted lines. The light-gray area illustrates the full range of observed values within the computational domain, bounded by $SAR_{\mathrm{max,mi,K_5}}$ and $SAR_{\mathrm{min,mi,K_5}}$. A red dotted line marks the SAR exposure threshold for the public, $SAR_{10\mathrm{g}}$, set below $4\,\frac{\mathrm{W}}{\mathrm{kg}}$. (b) Plot analogous to (a) for frequency $\mathrm{F_2}$.

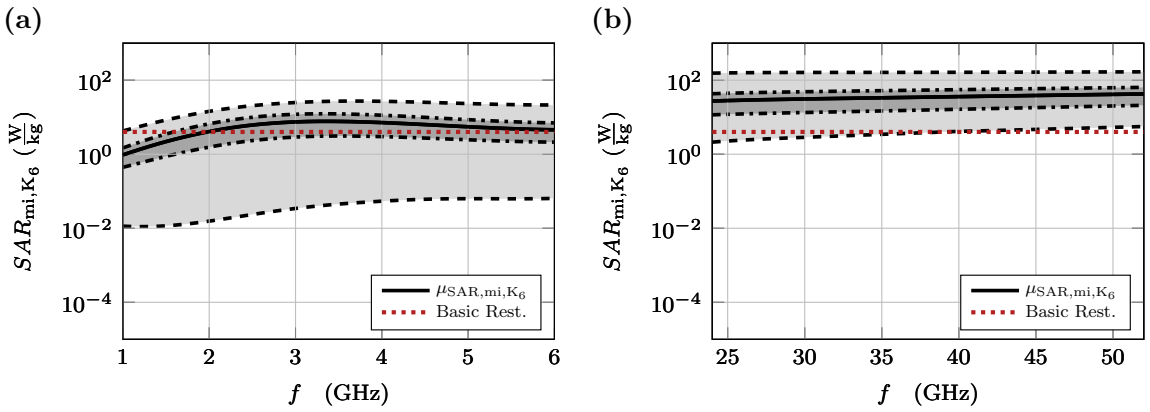


**Figure D.6:** $SAR_{\mathrm{mi,K_6}}(\omega)$ for cell model $\mathrm{K_6}$: (a) Semi-logarithmic representation of SAR values for frequency interval $\mathrm{F_1}$. The solid black line indicates the mean, $\mu_{\mathrm{SAR,mi,K_6}}$. A dark-gray area surrounds this mean, encompassing values within one standard deviation, $\mu_{\mathrm{SAR,K_6}} \pm s_{\mathrm{SAR,K_6}}$, demarcated by dashed-dotted lines. The light-gray area illustrates the full range of observed values within the computational domain, bounded by $SAR_{\mathrm{max,mi,K_6}}$ and $SAR_{\mathrm{min,mi,K_6}}$. A red dotted line marks the SAR exposure threshold for the public, $SAR_{10\mathrm{g}}$, set below $4\,\frac{\mathrm{W}}{\mathrm{kg}}$. (b) Plot analogous to (a) for frequency $\mathrm{F_2}$.

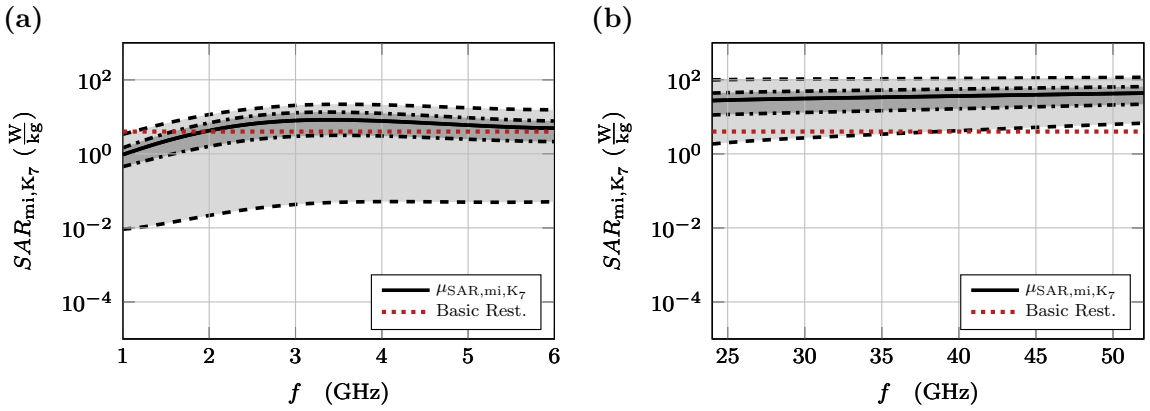


**Figure D.7:** $SAR_{\mathrm{mi,K_7}}(\omega)$ for cell model $\mathrm{K_7}$: (a) Semi-logarithmic representation of SAR values for frequency interval $\mathrm{F_1}$. The solid black line indicates the mean, $\mu_{\mathrm{SAR,mi,K_7}}$. A dark-gray area surrounds this mean, encompassing values within one standard deviation, $\mu_{\mathrm{SAR,K_7}} \pm s_{\mathrm{SAR,K_7}}$, demarcated by dashed-dotted lines. The light-gray area illustrates the full range of observed values within the computational domain, bounded by $SAR_{\mathrm{max,mi,K_7}}$ and $SAR_{\mathrm{min,mi,K_7}}$. A red dotted line marks the SAR exposure threshold for the public, $SAR_{10\mathrm{g}}$, set below $4\,\frac{\mathrm{W}}{\mathrm{kg}}$. (b) Plot analogous to (a) for frequency $\mathrm{F_2}$.

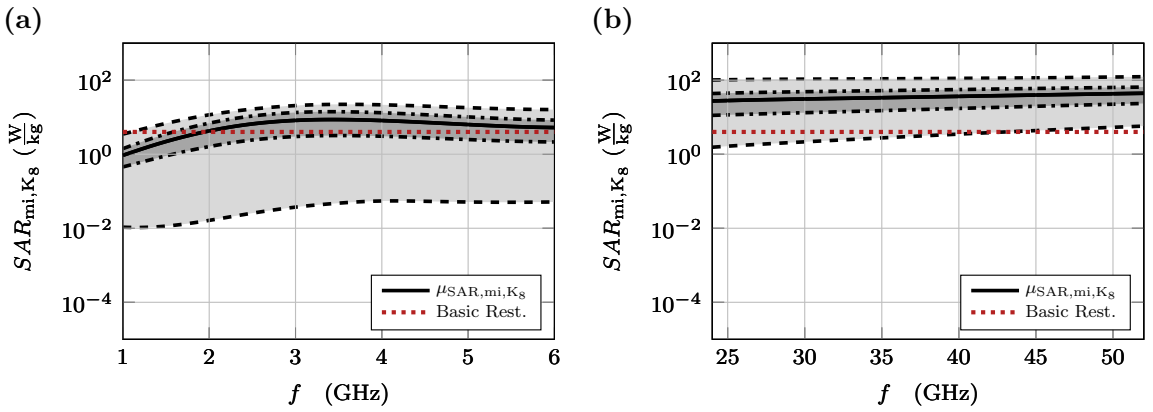


**Figure D.8:** $SAR_{\mathrm{mi,K_8}}(\omega)$ for cell model $\mathrm{K_8}$: (a) Semi-logarithmic representation of SAR values for frequency interval $\mathrm{F_1}$. The solid black line indicates the mean, $\mu_{\mathrm{SAR,mi,K_8}}$. A dark-gray area surrounds this mean, encompassing values within one standard deviation, $\mu_{\mathrm{SAR,K_8}} \pm s_{\mathrm{SAR,K_8}}$, demarcated by dashed-dotted lines. The light-gray area illustrates the full range of observed values within the computational domain, bounded by $SAR_{\mathrm{max,mi,K_8}}$ and $SAR_{\mathrm{min,mi,K_8}}$. A red dotted line marks the SAR exposure threshold for the public, $SAR_{10\mathrm{g}}$, set below $4\,\frac{\mathrm{W}}{\mathrm{kg}}$. (b) Plot analogous to (a) for frequency $\mathrm{F_2}$.

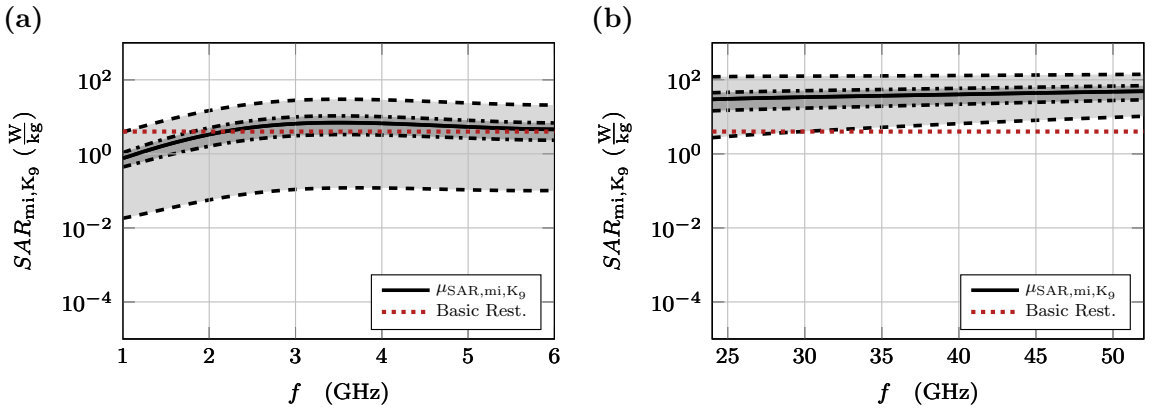


**Figure D.9:** $SAR_{\mathrm{mi,K_9}}(\omega)$ for cell model $\mathrm{K_9}$: (a) Semi-logarithmic representation of SAR values for frequency interval $\mathrm{F_1}$. The solid black line indicates the mean, $\mu_{\mathrm{SAR,mi,K_9}}$. A dark-gray area surrounds this mean, encompassing values within one standard deviation, $\mu_{\mathrm{SAR,K_9}} \pm s_{\mathrm{SAR,K_9}}$, demarcated by dashed-dotted lines. The light-gray area illustrates the full range of observed values within the computational domain, bounded by $SAR_{\mathrm{max,mi,K_9}}$ and $SAR_{\mathrm{min,mi,K_9}}$. A red dotted line marks the SAR exposure threshold for the public, $SAR_{10\mathrm{g}}$, set below $4\,\frac{\mathrm{W}}{\mathrm{kg}}$. (b) Plot analogous to (a) for frequency $\mathrm{F_2}$.

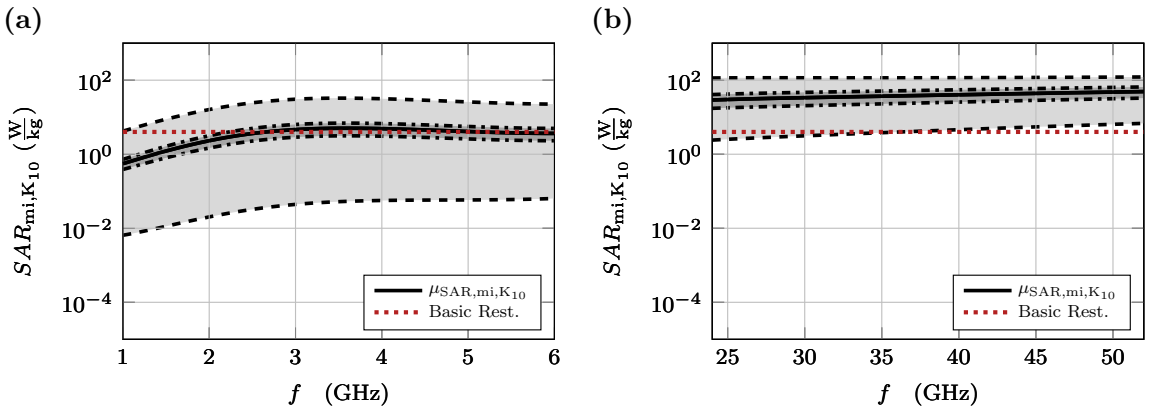


**Figure D.10:** $SAR_{\mathrm{mi,K_{10}}}(\omega)$ for cell model $\mathrm{K_{10}}$: (a) Semi-logarithmic representation of SAR values for frequency interval $\mathrm{F_1}$. The solid black line indicates the mean, $\mu_{\mathrm{SAR,mi,K_{10}}}$. A dark-gray area surrounds this mean, encompassing values within one standard deviation, $\mu_{\mathrm{SAR,K_{10}}} \pm s_{\mathrm{SAR,K_{10}}}$, demarcated by dashed-dotted lines. The light-gray area illustrates the full range of observed values within the computational domain, bounded by $SAR_{\mathrm{max,mi,K_{10}}}$ and $SAR_{\mathrm{min,mi,K_{10}}}$. A red dotted line marks the SAR exposure threshold for the public, $SAR_{\mathrm{10g}}$, set below $4\,\frac{\mathrm{W}}{\mathrm{kg}}$. (b) Plot analogous to (a) for frequency $\mathrm{F_2}$.

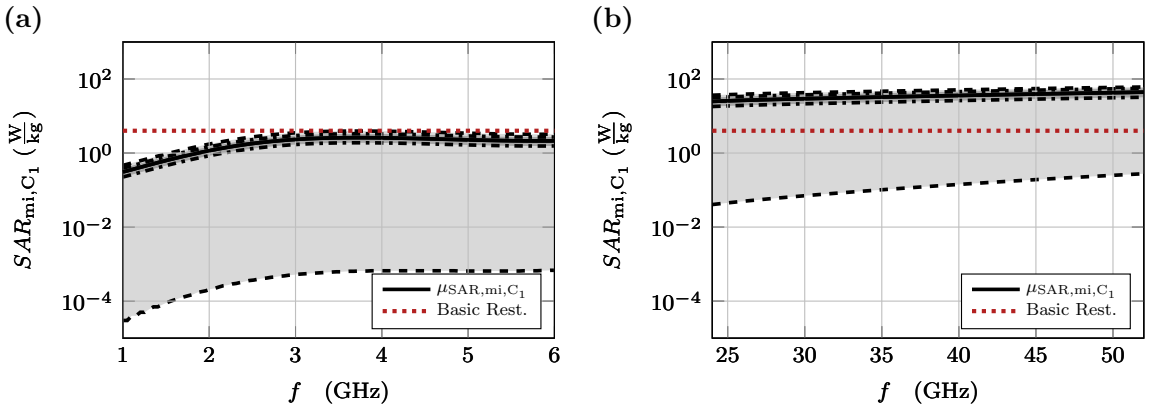


**Figure D.11:** $SAR_{\mathrm{mi,C_1}}(\omega)$ for cell model $C_1$: (a) Semi-logarithmic representation of SAR values for frequency interval $F_1$. The solid black line indicates the mean, $\mu_{\mathrm{SAR,mi,C_1}}$. A dark-gray area surrounds this mean, encompassing values within one standard deviation, $\mu_{\mathrm{SAR,C_1}} \pm s_{\mathrm{SAR,C_1}}$, demarcated by dashed-dotted lines. The light-gray area illustrates the full range of observed values within the computational domain, bounded by $SAR_{\mathrm{max,mi,C_1}}$ and $SAR_{\mathrm{min,mi,C_1}}$. A red dotted line marks the SAR exposure threshold for the public, $SAR_{10\mathrm{g}}$, set below $4\,\frac{\mathrm{W}}{\mathrm{kg}}$. (b) Plot analogous to (a) for frequency $F_2$.

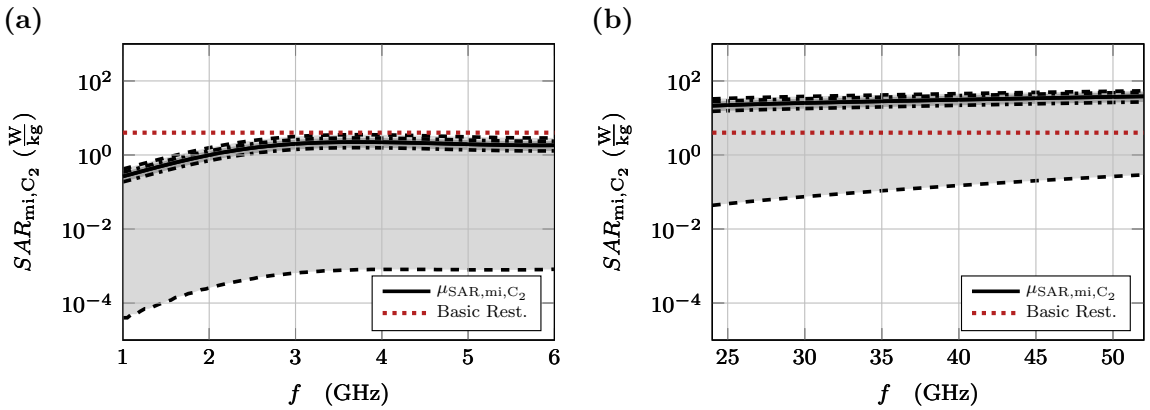


**Figure D.12:** $SAR_{\mathrm{mi,C_2}}(\omega)$ for cell model $C_2$: (a) Semi-logarithmic representation of SAR values for frequency interval $F_1$. The solid black line indicates the mean, $\mu_{\mathrm{SAR,mi,C_2}}$. A dark-gray area surrounds this mean, encompassing values within one standard deviation, $\mu_{\mathrm{SAR,C_2}} \pm s_{\mathrm{SAR,C_2}}$, demarcated by dashed-dotted lines. The light-gray area illustrates the full range of observed values within the computational domain, bounded by $SAR_{\mathrm{max,mi,C_2}}$ and $SAR_{\mathrm{min,mi,C_2}}$. A red dotted line marks the SAR exposure threshold for the public, $SAR_{10\mathrm{g}}$, set below $4\,\frac{\mathrm{W}}{\mathrm{kg}}$. (b) Plot analogous to (a) for frequency $F_2$.

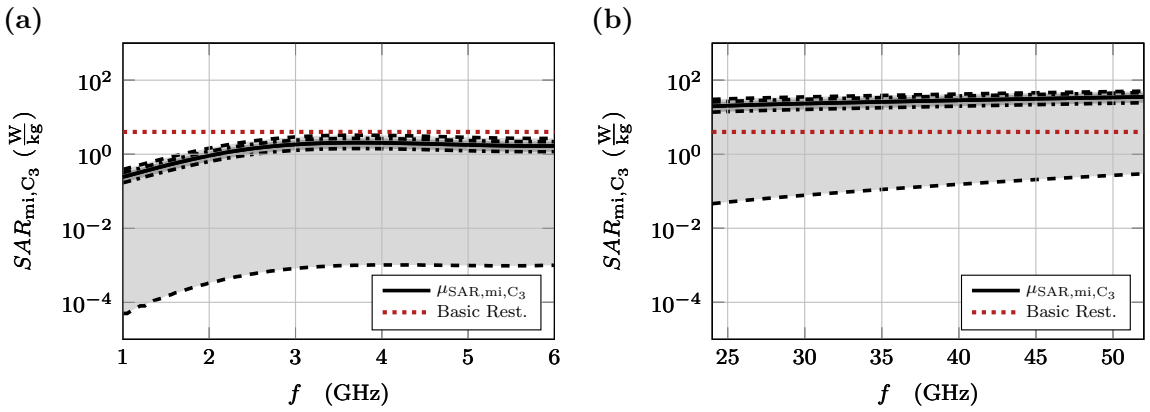


**Figure D.13:** $SAR_{\mathrm{mi,C_3}}(\omega)$ for cell model $\mathrm{C_3}$: (a) Semi-logarithmic representation of SAR values for frequency interval $\mathrm{F_1}$. The solid black line indicates the mean, $\mu_{\mathrm{SAR,mi,C_3}}$. A dark-gray area surrounds this mean, encompassing values within one standard deviation, $\mu_{\mathrm{SAR,C_3}} \pm s_{\mathrm{SAR,C_3}}$, demarcated by dashed-dotted lines. The light-gray area illustrates the full range of observed values within the computational domain, bounded by $SAR_{\mathrm{max,mi,C_3}}$ and $SAR_{\mathrm{min,mi,C_3}}$. A red dotted line marks the SAR exposure threshold for the public, $SAR_{10\mathrm{g}}$, set below $4\,\frac{\mathrm{W}}{\mathrm{kg}}$. (b) Plot analogous to (a) for frequency $\mathrm{F_2}$.

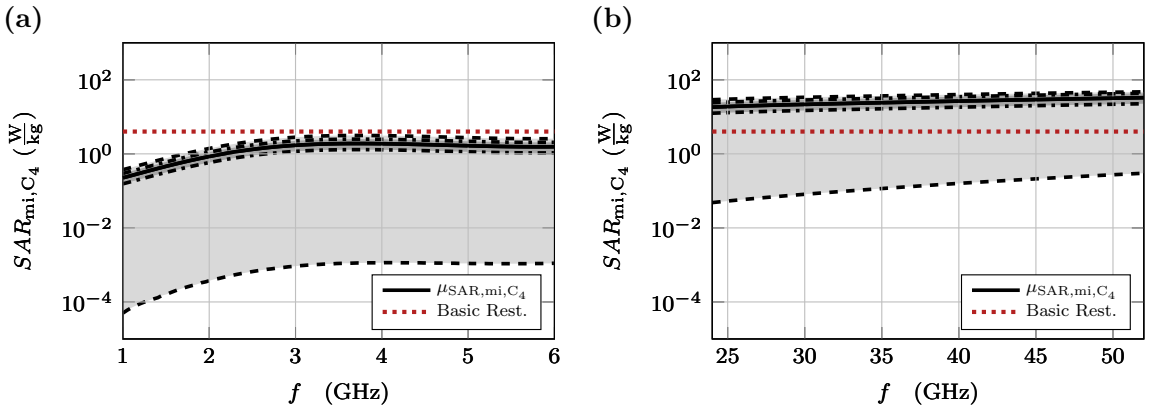


**Figure D.14:** $SAR_{\mathrm{mi,C_4}}(\omega)$ for cell model $\mathrm{C_4}$: (a) Semi-logarithmic representation of SAR values for frequency interval $\mathrm{F_1}$. The solid black line indicates the mean, $\mu_{\mathrm{SAR,mi,C_4}}$. A dark-gray area surrounds this mean, encompassing values within one standard deviation, $\mu_{\mathrm{SAR,C_4}} \pm s_{\mathrm{SAR,C_4}}$, demarcated by dashed-dotted lines. The light-gray area illustrates the full range of observed values within the computational domain, bounded by $SAR_{\mathrm{max,mi,C_4}}$ and $SAR_{\mathrm{min,mi,C_4}}$. A red dotted line marks the SAR exposure threshold for the public, $SAR_{10\mathrm{g}}$, set below $4\,\frac{\mathrm{W}}{\mathrm{kg}}$. (b) Plot analogous to (a) for frequency $\mathrm{F_2}$.

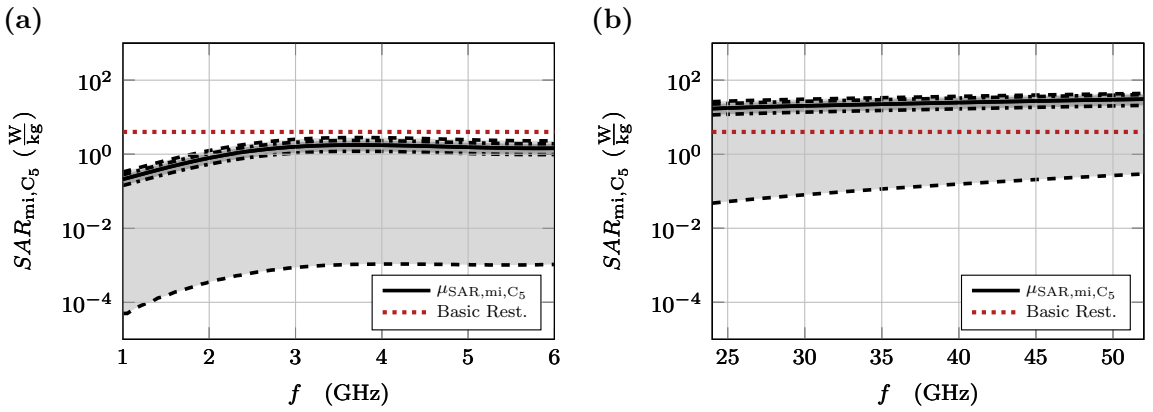


**Figure D.15:** $SAR_{\mathrm{mi,C_5}}(\omega)$ for cell model $\mathrm{C_5}$: (a) Semi-logarithmic representation of SAR values for frequency interval $\mathrm{F_1}$. The solid black line indicates the mean, $\mu_{\mathrm{SAR,mi,C_5}}$. A dark-gray area surrounds this mean, encompassing values within one standard deviation, $\mu_{\mathrm{SAR,C_5}} \pm s_{\mathrm{SAR,C_5}}$, demarcated by dashed-dotted lines. The light-gray area illustrates the full range of observed values within the computational domain, bounded by $SAR_{\mathrm{max,mi,C_5}}$ and $SAR_{\mathrm{min,mi,C_5}}$. A red dotted line marks the SAR exposure threshold for the public, $SAR_{10\mathrm{g}}$, set below $4\,\frac{\mathrm{W}}{\mathrm{kg}}$. (b) Plot analogous to (a) for frequency $\mathrm{F_2}$.

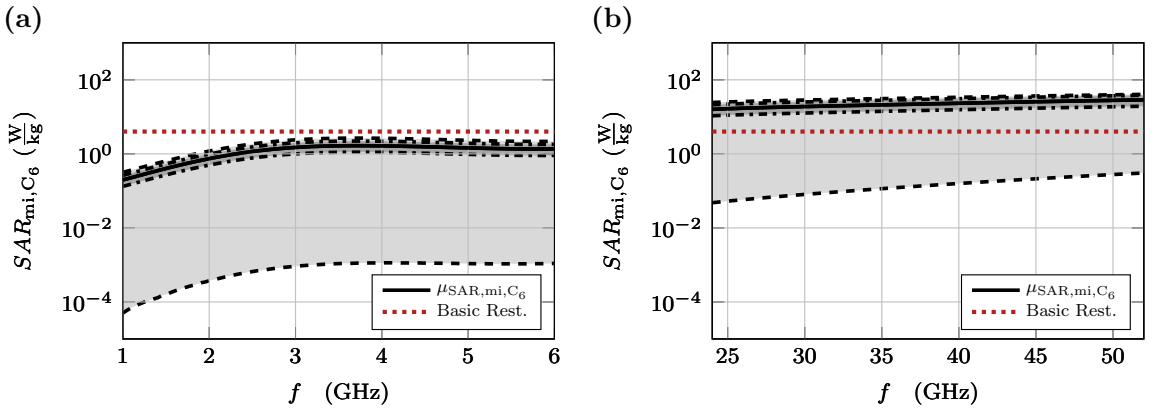


**Figure D.16:** $SAR_{\mathrm{mi,C_6}}(\omega)$ for cell model $\mathrm{C_6}$: (a) Semi-logarithmic representation of SAR values for frequency interval $\mathrm{F_1}$. The solid black line indicates the mean, $\mu_{\mathrm{SAR,mi,C_6}}$. A dark-gray area surrounds this mean, encompassing values within one standard deviation, $\mu_{\mathrm{SAR,C_6}} \pm s_{\mathrm{SAR,C_6}}$, demarcated by dashed-dotted lines. The light-gray area illustrates the full range of observed values within the computational domain, bounded by $SAR_{\mathrm{max,mi,C_6}}$ and $SAR_{\mathrm{min,mi,C_6}}$. A red dotted line marks the SAR exposure threshold for the public, $SAR_{10\mathrm{g}}$, set below $4\,\frac{\mathrm{W}}{\mathrm{kg}}$. (b) Plot analogous to (a) for frequency $\mathrm{F_2}$.

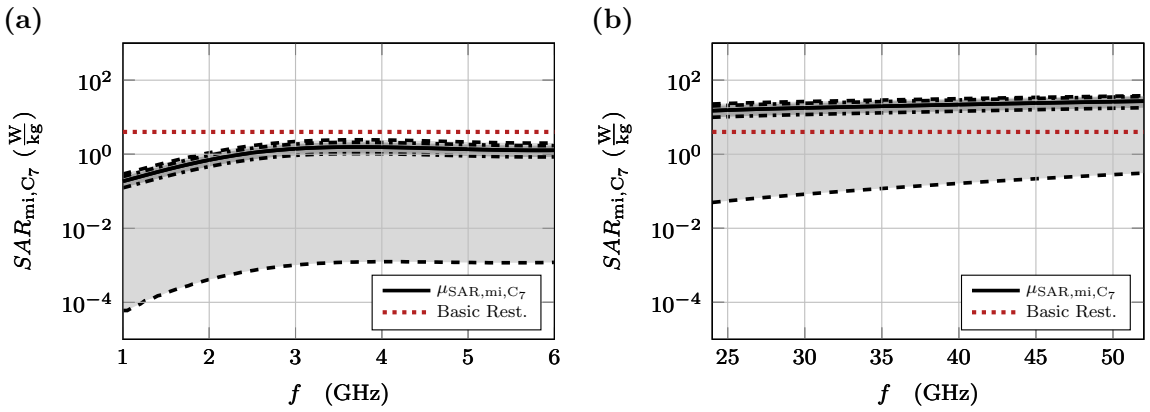


**Figure D.17:** $SAR_{\mathrm{mi,C_7}}(\omega)$ for cell model $\mathrm{C_7}$: (a) Semi-logarithmic representation of SAR values for frequency interval $\mathrm{F_1}$. The solid black line indicates the mean, $\mu_{\mathrm{SAR,mi,C_7}}$. A dark-gray area surrounds this mean, encompassing values within one standard deviation, $\mu_{\mathrm{SAR,C_7}} \pm s_{\mathrm{SAR,C_7}}$, demarcated by dashed-dotted lines. The light-gray area illustrates the full range of observed values within the computational domain, bounded by $SAR_{\mathrm{max,mi,C_7}}$ and $SAR_{\mathrm{min,mi,C_7}}$. A red dotted line marks the SAR exposure threshold for the public, $SAR_{10\mathrm{g}}$, set below $4\,\frac{\mathrm{W}}{\mathrm{kg}}$. (b) Plot analogous to (a) for frequency $\mathrm{F_2}$.

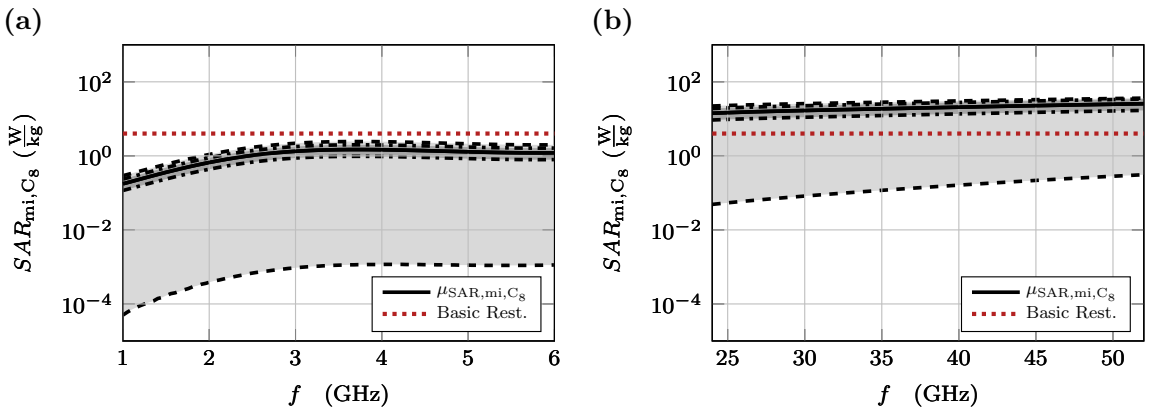


**Figure D.18:** $SAR_{\mathrm{mi,C_8}}(\omega)$ for cell model $\mathrm{C_8}$: (a) Semi-logarithmic representation of SAR values for frequency interval $\mathrm{F_1}$. The solid black line indicates the mean, $\mu_{\mathrm{SAR,mi,C_8}}$. A dark-gray area surrounds this mean, encompassing values within one standard deviation, $\mu_{\mathrm{SAR,C_8}} \pm s_{\mathrm{SAR,C_8}}$, demarcated by dashed-dotted lines. The light-gray area illustrates the full range of observed values within the computational domain, bounded by $SAR_{\mathrm{max,mi,C_8}}$ and $SAR_{\mathrm{min,mi,C_8}}$. A red dotted line marks the SAR exposure threshold for the public, $SAR_{10\mathrm{g}}$, set below $4\,\frac{\mathrm{W}}{\mathrm{kg}}$. (b) Plot analogous to (a) for frequency $\mathrm{F_2}$.

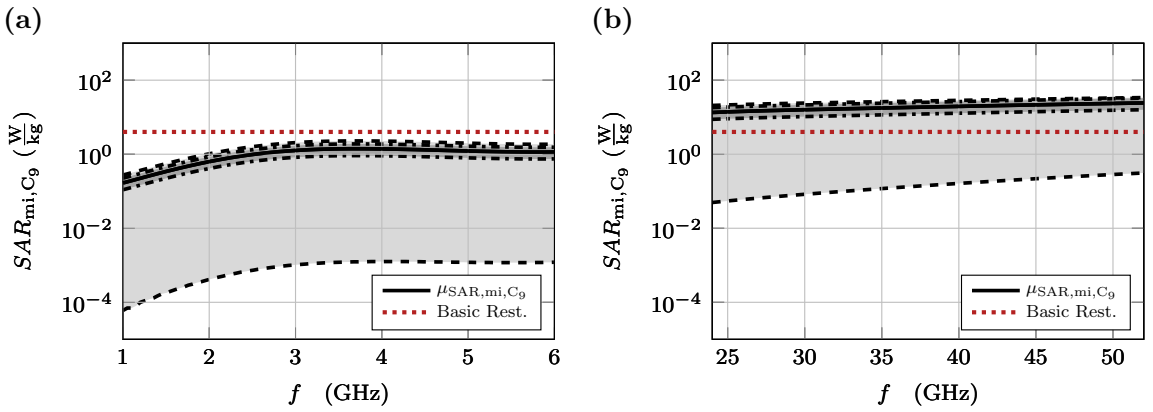


**Figure D.19:** $SAR_{\mathrm{mi,C_9}}(\omega)$ for cell model $\mathrm{C_9}$: (a) Semi-logarithmic representation of SAR values for frequency interval $\mathrm{F_1}$. The solid black line indicates the mean, $\mu_{\mathrm{SAR,mi,C_9}}$. A dark-gray area surrounds this mean, encompassing values within one standard deviation, $\mu_{\mathrm{SAR,C_9}} \pm s_{\mathrm{SAR,C_9}}$, demarcated by dashed-dotted lines. The light-gray area illustrates the full range of observed values within the computational domain, bounded by $SAR_{\mathrm{max,mi,C_9}}$ and $SAR_{\mathrm{min,mi,C_9}}$. A red dotted line marks the SAR exposure threshold for the public, $SAR_{10\mathrm{g}}$, set below $4\,\frac{\mathrm{W}}{\mathrm{kg}}$. (b) Plot analogous to (a) for frequency $\mathrm{F_2}$.

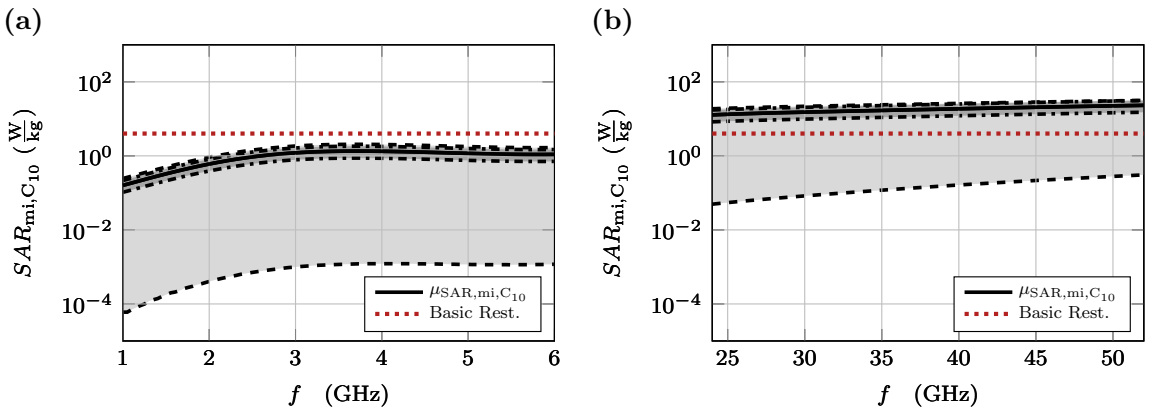


**Figure D.20:** $SAR_{\mathrm{mi,C_{10}}}(\omega)$ for cell model $\mathrm{C_{10}}$: (a) Semi-logarithmic representation of SAR values for frequency interval $\mathrm{F_1}$. The solid black line indicates the mean, $\mu_{\mathrm{SAR,mi,C_{10}}}$. A dark-gray area surrounds this mean, encompassing values within one standard deviation, $\mu_{\mathrm{SAR,C_{10}}} \pm s_{\mathrm{SAR,C_{10}}}$, demarcated by dashed-dotted lines. The light-gray area illustrates the full range of observed values within the computational domain, bounded by $SAR_{\mathrm{max,mi,C_{10}}}$ and $SAR_{\mathrm{min,mi,C_{10}}}$. A red dotted line marks the SAR exposure threshold for the public, $SAR_{10\mathrm{g}}$, set below $4\,\frac{\mathrm{W}}{\mathrm{kg}}$. (b) Plot analogous to (a) for frequency $\mathrm{F_2}$.

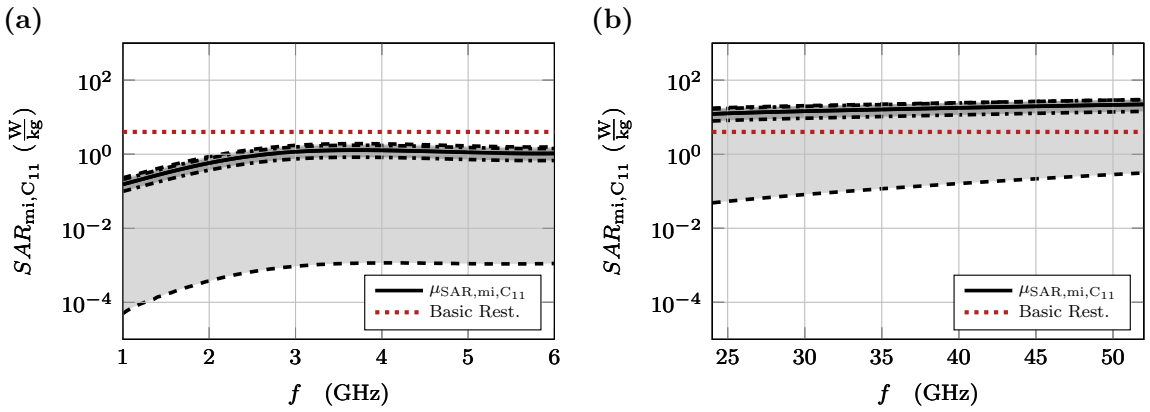


**Figure D.21:** $SAR_{\mathrm{mi,C_{11}}}(\omega)$ for cell model $\mathrm{C_{11}}$: (a) Semi-logarithmic representation of SAR values for frequency interval $\mathrm{F_1}$. The solid black line indicates the mean, $\mu_{\mathrm{SAR,mi,C_{11}}}$. A dark-gray area surrounds this mean, encompassing values within one standard deviation, $\mu_{\mathrm{SAR,C_{11}}} \pm s_{\mathrm{SAR,C_{11}}}$, demarcated by dashed-dotted lines. The light-gray area illustrates the full range of observed values within the computational domain, bounded by $SAR_{\mathrm{max,mi,C_{11}}}$ and $SAR_{\mathrm{min,mi,C_{11}}}$. A red dotted line marks the SAR exposure threshold for the public, $SAR_{10\mathrm{g}}$, set below $4\,\frac{\mathrm{W}}{\mathrm{kg}}$. (b) Plot analogous to (a) for frequency $\mathrm{F_2}$.

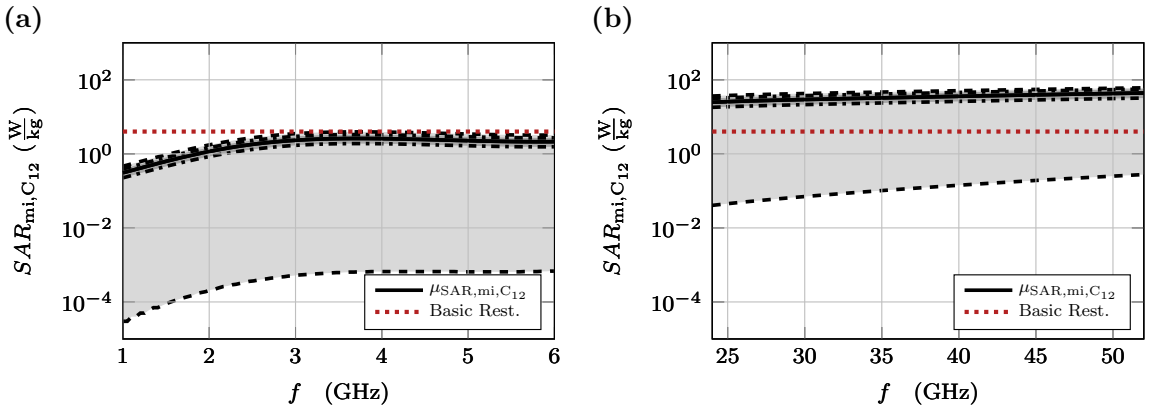


**Figure D.22:** $SAR_{\mathrm{mi,C_{12}}}(\omega)$ for cell model $\mathrm{C_{12}}$: (a) Semi-logarithmic representation of SAR values for frequency interval $\mathrm{F_1}$. The solid black line indicates the mean, $\mu_{\mathrm{SAR,mi,C_{12}}}$. A dark-gray area surrounds this mean, encompassing values within one standard deviation, $\mu_{\mathrm{SAR,C_{12}}} \pm s_{\mathrm{SAR,C_{12}}}$, demarcated by dashed-dotted lines. The light-gray area illustrates the full range of observed values within the computational domain, bounded by $SAR_{\mathrm{max,mi,C_{12}}}$ and $SAR_{\mathrm{min,mi,C_{12}}}$. A red dotted line marks the SAR exposure threshold for the public, $SAR_{10\mathrm{g}}$, set below $4\,\frac{\mathrm{W}}{\mathrm{kg}}$. (b) Plot analogous to (a) for frequency $\mathrm{F_2}$.

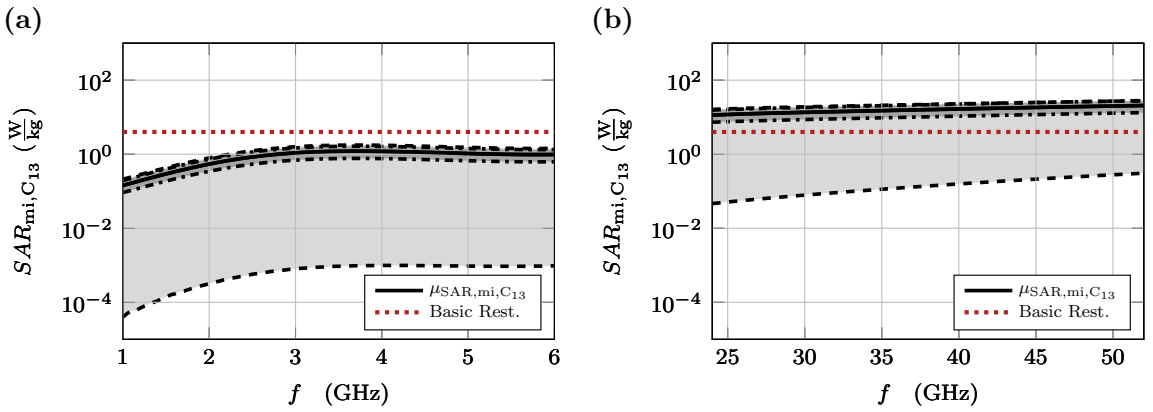


**Figure D.23:** $SAR_{\mathrm{mi,C_{13}}}(\omega)$ for cell model $\mathrm{C_{13}}$: (a) Semi-logarithmic representation of SAR values for frequency interval $\mathrm{F_1}$. The solid black line indicates the mean, $\mu_{\mathrm{SAR,mi,C_{13}}}$. A dark-gray area surrounds this mean, encompassing values within one standard deviation, $\mu_{\mathrm{SAR,C_{13}}} \pm s_{\mathrm{SAR,C_{13}}}$, demarcated by dashed-dotted lines. The light-gray area illustrates the full range of observed values within the computational domain, bounded by $SAR_{\mathrm{max,mi,C_{13}}}$ and $SAR_{\mathrm{min,mi,C_{13}}}$. A red dotted line marks the SAR exposure threshold for the public, $SAR_{10\mathrm{g}}$, set below $4\,\frac{\mathrm{W}}{\mathrm{kg}}$. (b) Plot analogous to (a) for frequency $\mathrm{F_2}$.

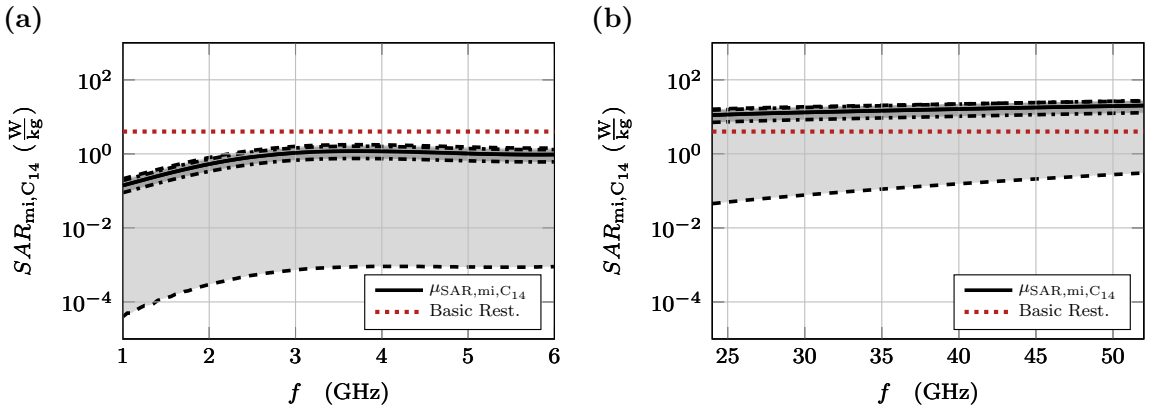


**Figure D.24:** $SAR_{\mathrm{mi,C_{14}}}(\omega)$ for cell model $\mathrm{C_{14}}$: (a) Semi-logarithmic representation of SAR values for frequency interval $\mathrm{F_1}$. The solid black line indicates the mean, $\mu_{\mathrm{SAR,mi,C_{14}}}$. A dark-gray area surrounds this mean, encompassing values within one standard deviation, $\mu_{\mathrm{SAR,C_{14}}} \pm s_{\mathrm{SAR,C_{14}}}$, demarcated by dashed-dotted lines. The light-gray area illustrates the full range of observed values within the computational domain, bounded by $SAR_{\mathrm{max,mi,C_{14}}}$ and $SAR_{\mathrm{min,mi,C_{14}}}$. A red dotted line marks the SAR exposure threshold for the public, $SAR_{10\mathrm{g}}$, set below $4\,\frac{\mathrm{W}}{\mathrm{kg}}$. (b) Plot analogous to (a) for frequency $\mathrm{F_2}$.

# Appendix E

**Preface:** *The following appendix, adapted from the journal article published in [96], serves as an illustrative example of the implementation of a dedicated tissue scale. This scale addresses the histological organization of an amorphous tissue structure in the context of the multiscale classification scheme as originally discussed in Chap. 4. While the generic representation of the hypodermis given here allows for the identification and quantification of the limits of applicability of analytical and numerical homogenization methods over a frequency range from* 10 MHz *to* 200 GHz*, it lacks the level of realism necessary for full integration into this thesis. It is important to note that nomenclature and indexing of values might differ between the main body of the thesis and this appendix.*

This appendix covers the computer-aided investigation of randomized composites. Here, these are generalized microstructures which, in a broader sense, represent the hypodermis (HYP), i.e. the subcutaneous adipose tissue of humans. In the context of this investigation, Sec. E.1 "Concept and Methodology" first presents a formalism that allows the generation of virtual randomized microstructures, represents them in a numerically efficient manner by means of a homogenized surrogate material, and then investigates the spectral response of the reflection from both the original (sub-)surface material system and the homogenized surrogate in a broad-band frequency investigation covering a range from 10 MHz to 200 GHz. This formalism is used to determine the validity of the homogenization of an individual microstructure by setting a validity boundary and thus dividing the investigated frequency range into a valid range and a forbidden range.

Subsequently, this formalism is applied to a large number of parameterized randomized microstructures in a Monte Carlo analysis. In the context of this study, the statistical evaluation of the validity limits of the individual microstructures is then used to determine the validity limit of an entire class of realized microstructures defined by common parameter settings that determine their morphology.

Finally, the graphical evaluation of the electromagnetic fields within the microstructures is used to estimate the information content of the forbidden region in order to determine its potential for the classification of structural features.

# E.1 Concept and Methodology

## E.1.1 Random Sequential Addition

The heterogeneous material structures under investigation, which mimic a realistic HYP microstructure, are generated using the random sequential addition (RSA) algorithm [116]. This algorithm allows the randomized placement of spherical inclusions for a given volume fraction $c_v = \frac{V_{inc}}{V_{supercell}}$, a given inclusion diameter $d_{inc}$ and a minimum separation distance $d_d$ to avoid contact between inclusions and their merging. $d_d$ defines the minimum radius around an inclusion where no further adjacent inclusion may be placed. In the version of the algorithm re-implemented in this study, $d_d$ is a dimensionless coefficient greater than 1, which must be multiplied by the inclusion diameter to determine the prohibited area around an inclusion. In addition, the algorithm has been modified to enable the periodic continuation of the microstructure, defining it as a computational supercell. This allows the use of periodic boundary conditions both for numerical homogenization and for the subsequent numerical backscatter analysis (see section E.1.2 and section E.1.4, respectively).

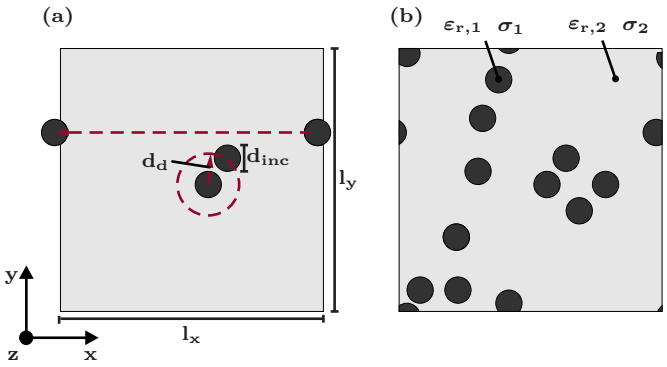


**Figure E.1:** Random sequential addition algorithm for the generation of heterogeneous material structures: (a) overview of the adjustable parameters; (b) generalized example for a generalized parameter setup. In this study: $d_{inc} = 50\,\mu$m, $\varepsilon_{r,1} = 80$, $\sigma_1 = 0.53\,\frac{S}{m}$, $\varepsilon_{r,2} = 50$ and $\sigma_2 = 0.12\,\frac{S}{m}$.

The dimensions of the computational supercell were chosen to be $l_x = 1$ mm and $l_y = 1$ mm in order to represent a structure on the same scale as the thickness of the hypodermis. Fig. E.1 shows a generalized 2D representation of the microstructure of this layer with adipose cells represented by monodisperse spherical inclusions with a diameter $d_{inc} = 50\,\mu$m , $\varepsilon_{r,1} = 80$, and $\sigma_1 = 0.53\,\frac{S}{m}$ that are embedded in a homogeneous extracellular material with $\varepsilon_{r,2} = 50$, and $\sigma_2 = 0.12\,\frac{S}{m}$. Due to the lack of dispersive material parameters in the investigated frequency range, constant material parameters are applied using the estimations provided by [45], even though the dispersive nature of extracellular and intracellular media would have to be considered for a more realistic tissue representation (see Chap. 8.2.2.2). Since the main objective is the evaluation of validity limits in

the context of multiscale modelling, the constant material parameters help to ascribe the validity limits more clearly to volume scattering.

## E.1.2 Numerical Homogenization

For homogenization, the 2D supercell contains the heterogeneous 2D composite microstructure (cf. Fig. E.1(b)). This is then placed between the plates of an idealized virtual capacitor. As depicted in Fig. E.2, a time-harmonic voltage with constant amplitude $\underline{\hat{u}} = \underline{\varphi}_1 - \underline{\varphi}_2$ is applied between these opposing plates (i.e Dirichlet boundary conditions). Periodic boundary conditions (PBC) are then defined along the remaining two edges in order to suppress fringing fields and reduce the memory resources of the subsequent quasi-static EM simulation. Using different boundary conditions, previous investigations have quantified the influence of Maxwell-Wagner interfacial polarization in composite materials in comparison to results calculated using classical mixing rule [97]. Anisotropy in the underlying microstructure is taken into consideration by exchanging the virtual electrodes and the PBCs as seen in Fig. E.2. The capacitor setup is implemented in the finite-element-method-based (FEM) software package COMSOL Multiphysics [95]. Each 2D simulation model can be interpreted as an infinitely extended 3D capacitor of finite thickness in one of two ways. Firstly, due to the PBCs outlined above, and secondly, due to translational invariance normal to the plane visible in Fig. E.2.

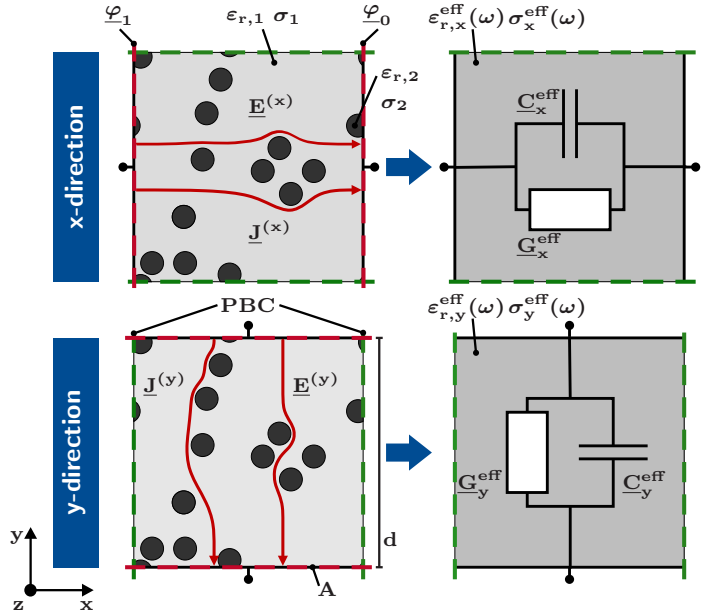


**Figure E.2:** Schematic of the numerical homogenization procedure: For the tensorial acquisition of the material parameters, the effective material properties are determined successively with respect to the individual spatial directions.

From the time-harmonic quasi-static EM analysis of the supercell as a capacitor, an effective admittance is retrieved that is represented by the equivalent electrical parallel circuit

consisting of the elements $G^{\text{eff}}$ and $C^{\text{eff}}$. This is given by

$$\underline{Y}^{\text{eff}}(\omega) = \frac{\hat{\underline{i}}(\omega)}{\hat{\underline{u}}} = G^{\text{eff}}(\omega) + j\omega C^{\text{eff}}(\omega). \tag{E.1}$$

where the applied voltage $\hat{\underline{u}}$ and the resulting current $\hat{\underline{i}}(\omega)$ can be directly exported from COMSOL Multiphysics. The effective material properties $\varepsilon^{\text{eff}}$ and $\sigma^{\text{eff}}$ are thus easily deduced according to

$$\underline{Y}^{\text{eff}}(\omega)\frac{d}{A} = \frac{\hat{\underline{i}}(\omega)}{\hat{\underline{u}}} \cdot \frac{d}{A} = \underbrace{\sigma^{\text{eff}}(\omega) + j\omega\varepsilon_0\varepsilon_{\text{r}}^{\text{eff}}(\omega)}_{\underline{\sigma}^{\text{eff}}(\omega)} \tag{E.2}$$

where $d$ is the distance between the parallel plates and $A$ is the area of the electrode. In Eq. E.2, the right-hand term can be interpreted as the complex effective conductivity $\underline{\sigma}^{\text{eff}}(\omega)$ of the homogenized effective material. The required material parameters can then be derived directly:

$$\sigma^{\text{eff}}(\omega) = \Re\{\underline{\sigma}^{\text{eff}}\} \tag{E.3}$$

and

$$\varepsilon_{\text{r}}^{\text{eff}}(\omega) = \frac{\Im\{\underline{\sigma}^{\text{eff}}\}}{\omega\varepsilon_0}. \tag{E.4}$$

Excitation in both the x and the y directions (cf. Fig. E.2) allows the consideration of anisotropies in the effective material properties and yield the corresponding frequency-dependent second-rank tensors for the effective permittivity and effective conductivity, respectively.

For the conductivity

$$\overleftrightarrow{\sigma}^{\text{eff}}(\omega) = \begin{pmatrix} \sigma_{\text{x}}^{\text{eff}}(\omega) & 0 \\ 0 & \sigma_{\text{y}}^{\text{eff}}(\omega) \end{pmatrix} \tag{E.5}$$

and for the permittivity

$$\overleftrightarrow{\varepsilon}_{\text{r}}^{\text{eff}}(\omega) = \begin{pmatrix} \varepsilon_{\text{r,x}}^{\text{eff}}(\omega) & 0 \\ 0 & \varepsilon_{\text{r,y}}^{\text{eff}}(\omega) \end{pmatrix}. \tag{E.6}$$

These homogenized, frequency-dependent effective material representations are integrated in the simulation model of the generalized reflectometry setup in accordance with the multiscale modeling approach.

### E.1.3 Homogenization Using Mixing Rules

Despite the application of analytical mixing rules from EMT [23] being a potential alternative to the numerical homogenization procedure presented in Sec. 3.1.2, the latter is superior and thus implemented due to a variety of differences discussed in the following.

Classical mixing rules such as Maxwell-Garnett (MG), Bruggemann (B) [117] or Landau-Lifshitz-Looyenga (LLL) [118], [119] consider two-phase composites as inclusions embedded in a dielectric host material. The derivation of classical mixing rules, which analytically describe the macroscopic material properties of such a material mixture, is based on the following assumptions: the EM field solution is curl-free ($\nabla \times \underline{\vec{E}} = 0$) and all interactions between adjacent inclusions are neglected [24]. Strictly speaking, these assumptions mean that the application of the mixing rules is limited to quasi-static conditions in diluted mixtures. As a rule of thumb, the relation $\frac{\lambda_\mathrm{m}}{2\pi} > d_\mathrm{inc}$, where $\lambda_\mathrm{m}$ denotes the wavelength within the material, can be used to estimate the upper applicable frequency of the mixing rules for sparse microstructures ($c_\mathrm{v}$ up to 10 %).

In [120], Bruggeman's mixing rule was extended to the Hanai-Bruggeman (HB) formula to approximate denser mixtures ($c_\mathrm{v}$ up to 40 % [25]). The macroscopic material properties according to HB can be determined by:

$$0 = \frac{(\varepsilon_{\mathrm{r,BG}}^{\mathrm{eff}} - \varepsilon_{\mathrm{r,2}}^{\mathrm{eff}})}{(\varepsilon_{\mathrm{r,1}}^{\mathrm{eff}} - \varepsilon_{\mathrm{r,2}}^{\mathrm{eff}})} \cdot \left( \frac{\varepsilon_{\mathrm{r,2}}^{\mathrm{eff}}}{\varepsilon_{\mathrm{r,BG}}^{\mathrm{eff}}} \right)^{A} - (1 - c_\mathrm{v}) \tag{E.7}$$

where $\varepsilon_{\mathrm{r,1}}^{\mathrm{eff}}$ and $\varepsilon_{\mathrm{r,2}}^{\mathrm{eff}}$ denote the effective complex permittivity of the host and inclusion material respectively. The depolarization factor, $A = 0.5$ accounts for composites consisting of rods embedded in a dielectric host material. According to MG, the effective material parameters can be determined by

$$\varepsilon_{\mathrm{r,MG}}^{\mathrm{eff}} = \varepsilon_{\mathrm{r,1}}^{\mathrm{eff}} \cdot \frac{(\varepsilon_{\mathrm{r,1}}^{\mathrm{eff}}(1 - c_\mathrm{v})(1 - A) + \varepsilon_{\mathrm{r,2}}^{\mathrm{eff}}(c_\mathrm{v} + A(1 - c_\mathrm{v})))}{\varepsilon_{\mathrm{r,2}}^{\mathrm{eff}} + A(1 - c_\mathrm{v})(\varepsilon_{\mathrm{r,2}}^{\mathrm{eff}} - \varepsilon_{\mathrm{r,1}}^{\mathrm{eff}})} \tag{E.8}$$

and according to LLL by

$$\varepsilon_{\mathrm{r,LLL}}^{\mathrm{eff}} = \varepsilon_{\mathrm{r,1}}^{\mathrm{eff}\,(1-c_\mathrm{v})} \cdot \varepsilon_{\mathrm{r,2}}^{\mathrm{eff}\,c_\mathrm{v}}. \tag{E.9}$$

In Fig. E.3, the spectra of the permittivity and conductivity calculated by MG, HB and LLL mixing rules are compared with those determined by numerical simulations. Fig. E.3 (a) and (c) show the permittivity and conductivity of a microstructure with the parameter set $d_\mathrm{d} = 1.05$, $d_\mathrm{inc} = 50\,\mu$m and $c_\mathrm{v} = 0.45$ and (b) and (d), one with the parameter set $d_\mathrm{d} = 1.05$, $d_\mathrm{inc} = 100\,\mu$m and $c_\mathrm{v} = 0.35$. Examples of the analyzed HYP realizations are shown in (e) and (f). These cases represent extremes in terms of the volume fraction or density applied to the mixing rules.

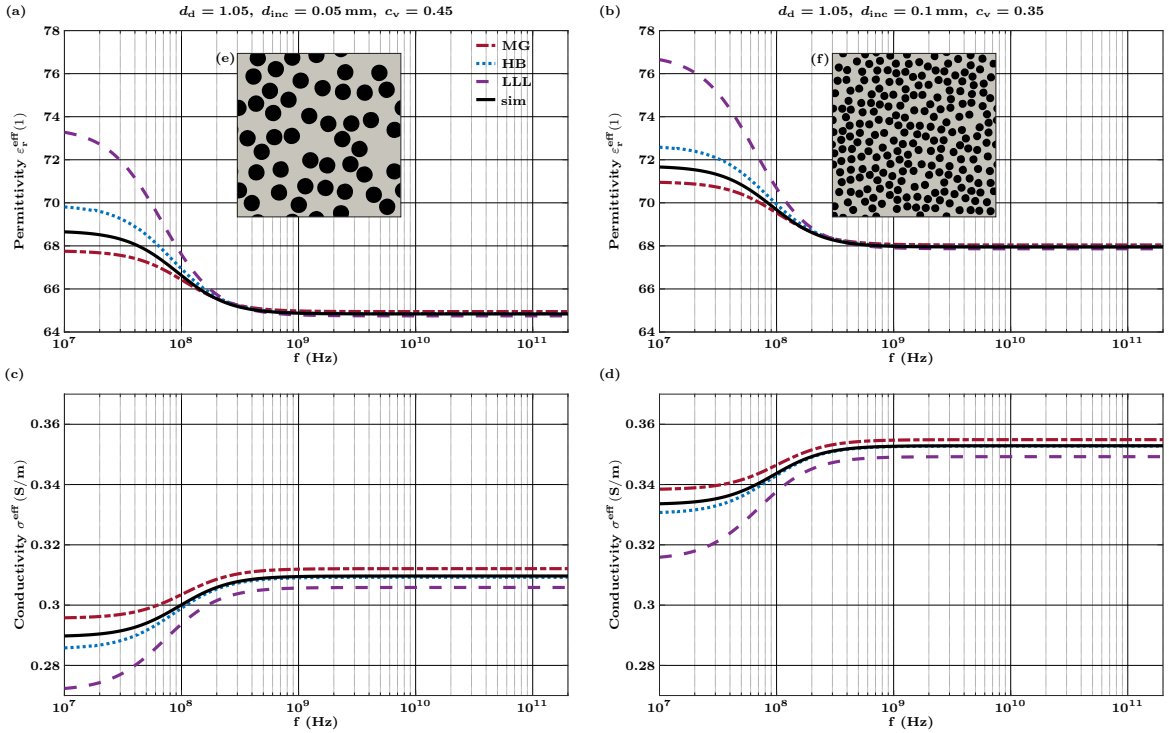


**Figure E.3:** Spectral response of the permittivity and conductivity of two illustrative microstructures in the frequency range from 10 MHz to 200 GHz. The spectra are calculated by analytical mixing rules such as Maxwell-Garnett (MG), Hanai-Bruggemann (HB) and Landau-Lifshitz-Looyenga (LLL) as well as by using numerical simulations. (a) and (c) correspond to the structural parameters $d_\mathrm{d} = 1.05, d_\mathrm{inc} = 50\,\mu$m, $c_\mathrm{v} = 0.45$ and (b) and (d) to $d_\mathrm{d} = 1.05, d_\mathrm{inc} = 100\,\mu$m, $c_\mathrm{v} = 0.35$. Examples for the analyzed HYP realizations are shown in (e) and (f).

Common to all spectra is a low-frequency roll-off of permittivity, or a increase of conductivity, at about 100 MHz, which is associated with the decay of the Maxwell-Wagner effect. In the lower frequency range, the simulated spectra are between those of MG and HB. The calculations according to the MG formula represent a lower estimate and the HB an upper estimate of the electromagnetic material properties. The calculations according to the LLL formula seem to overestimate the influence of interfacial polarization and, thus, are not appropriate to represent the macroscopic material properties in the lower frequency range. At high frequencies, however, the deviation between the simulation results and any of the mixing rules is marginal.

This result is in accordance with [97], where the dielectric spectra obtained by simulations and mixing rules have been compared. The investigations showed that only numerical simulations which could be considered as the multipole representation of the EM problem were able to determine the influence of interactions between adjacent particles correctly at low frequencies. In [14] and more comprehensively in [45], numerical homogenization has been extensively investigated and validated using skin measurements, in the context of multi-scale modelling of the skin at microwave frequencies in comparison with classical mixing rules. It has been shown that the shape of cells has a significant influence on the macroscopic material properties due to interfacial polarization, especially at low frequencies and high volume densities.

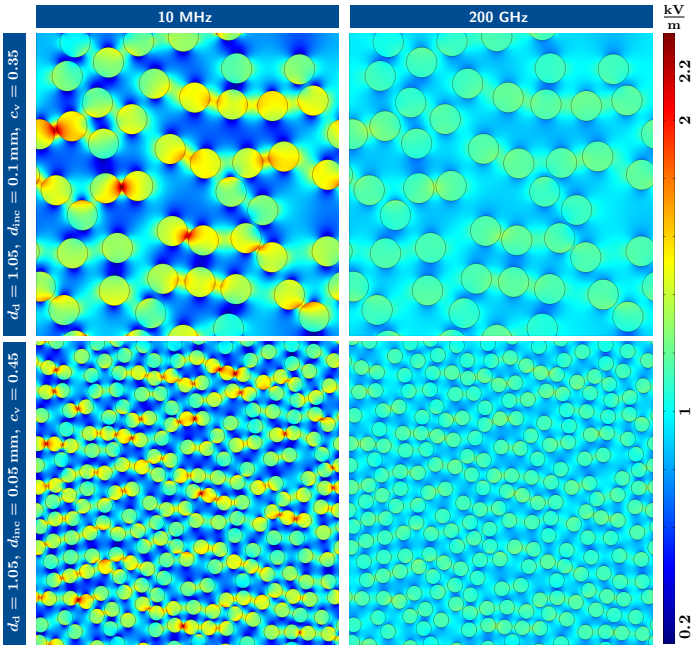


**Figure E.4:** Graphical evaluation of the electric field within the microstructures under investigation at 10 MHz and 200 GHz (i.e. with and without the influence of charge carriers between the material boundaries). The images all demonstrate rotation-free yet divergent electric fields.

The effect of interfacial polarization is illustrated in Fig. E.4 using the electric field strength distribution at 10 MHz and 200 GHz within the illustrative microstructures considered in Fig. E.3. Even though the numerical FEM solver uses all of Maxwell's equations, the excitation of the composite by two electrodes means that the images all demonstrate rotation-free yet divergent electric fields. Compared to classical mixing rules at frequencies lower than the roll-off frequency of the interfacial polarization, numerical homogenization can therefore still be regarded as the more reliable calculation method, as it considers field interactions between adjacent inclusions, but still provides a quasi-static solution.

Nevertheless, MG and HB mixing rules can be used to estimate the validity at low frequencies and can calculate the macroscopic material properties with high accuracy for

high frequencies even for dense composites when compared to numerical simulations.

In summary, at frequencies lower than the expected Maxwell-Wagner roll-off, while MG and HB can be considered as upper and lower bounds to verify numerical simulation, LLL overestimates the interfacial polarization. Only at frequencies lower than the expected Maxwell-Wagner roll-off, are the differences between the spectra obtained by simulations and those determined by mixing rules are negligible, so that the calculation methods are interchangeable.

### E.1.4 Reflectometry

After determining the effective macroscopic material properties of the microstructures, a generalized reflectometry setup is used to analyze the reflection of an incident EM plane wave from a (sub)surface system of structures. This system is defined by a plane boundary between air and either the original heterogeneous composite material or its homogenized EMT representation (cf. Fig. E.5). The plane wave is emitted from a non-reflective port at an angle of incidence, $\alpha_{\mathrm{inc}}$, (here 0 °) having either s or p-polarization with respect to the reflection plane (i.e. x-y plane). The amplitude of the incident plane wave corresponds to a constant input power, $P_0$, whereas the reflected power, $P_{\mathrm{R}}$, is detected by the same non-reflective port. From these values, the desired measure, namely the power reflection coefficient, $R = \frac{P_{\mathrm{R}}}{P_0}$, is calculated. The absorption coefficient, $A = \frac{P_{\mathrm{A}}}{P_0}$, is determined by a corresponding volume integration of the material losses, $P_{\mathrm{A}}$, within the material structure. The top and bottom of the computational domain are terminated with perfectly matched layers (PML). The upper layer is assigned the material parameters of air, and the lower those defined by $\overleftrightarrow{\varepsilon}_{\mathrm{r}}^{\mathrm{eff}}(\omega)$ and $\overleftrightarrow{\sigma}^{\mathrm{eff}}(\omega)$. Similar to the capacitor setup, PBCs are also introduced into the reflectometry model to omit fringing fields while extending the randomized super cell to a periodic representation of the composite surface layer.

The simulation was performed on a PC equipped with an Intel i7-6700k processor (4 cores) and 64 GB DDR4 RAM. In the given frequency interval, 260 frequency points were simulated with a multifrontal massively parallel sparse direct solver (MUMPS) where the density of the frequency points increased for higher frequencies. This increasing density can be interpreted as a frequency-dependent sampling rate to investigate interference patterns within the forbidden range with sufficiently high resolution. The simulation for each frequency point lasted 21 s and included the simulation of the heterogeneous microstructure and its homogenized representation in s and p-polarization.

A first example for analyzing the breakdown of the effective material representation is given in Fig. E.5(c) for HYP tissue with a cell volume fraction of $c_{\mathrm{v}} = 0.45$. The blue curve represents the power reflection coefficient of the heterogeneous composite model and the dotted red curve that of the homogeneous EMT model for p-polarized excitation in a frequency range from 10 MHz to 200 GHz. The comparison between the reflectance of the heterogeneous material structure and its homogenized representation is only carried

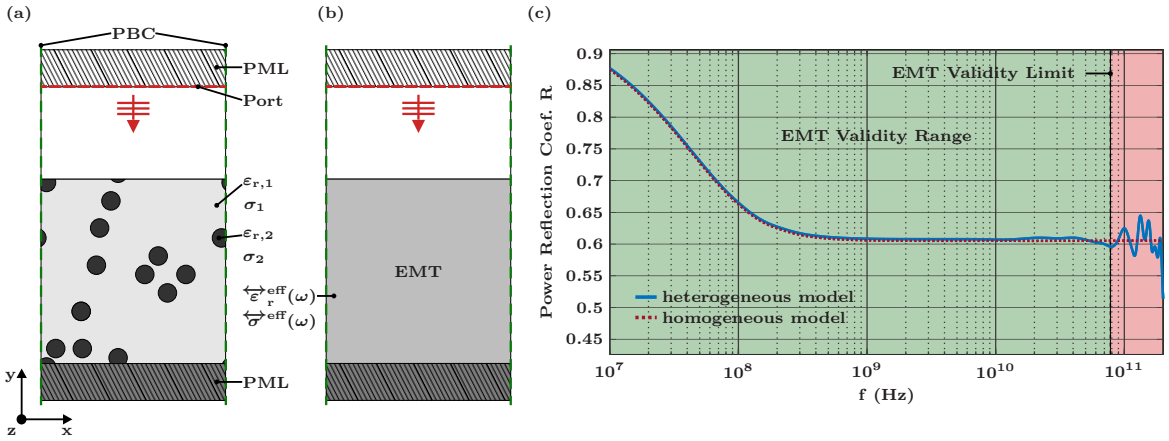


**Figure E.5:** Comparison between the heterogeneous and homogenized (EMT) representation of a generalized HYP model: (a) heterogeneous simulation setup; (b) homogeneous simulation setup; (c) spectral responses of the reflectance (showing the typical Maxwell-Wagner roll-off in the MHz range) for $\varepsilon_{r,1} = 80$, $\sigma_1 = 0.53\,\frac{S}{m}$, $\varepsilon_{r,2} = 50$, $\sigma_2 = 0.12\,\frac{S}{m}$, $d_{inc} = 50\,\mu$m, and $c_v = 0.452$.

out for p-polarization. This is due to the fact that, for s-polarization, the electric field is aligned in the translation-invariant direction of the composite and therefore, homogenization is not defined according to the numerical homogenization procedure stated earlier. The validity limit of the EMT representation for a deviation of 2 % between the two frequency responses is located at $f_{val} = 78\,$GHz for this particular HYP tissue realization. The validity range of the homogenized EMT representation therefore extends below the validity limit. However, the forbidden range found above this limit is characterized by strong variations in the frequency response. These are associated with the heterogeneous tissue model which defines a characteristic fingerprint which can be exploited for material classification.

### E.1.5 Transferability to Three-Dimensional Simulations

Since the validity limits of the microstructure are to be studied in the context of a Monte Carlo simulation, it is necessary that large amounts of data be generated using simulations. In order to limit the numerical effort to a manageable level, the Monte Carlo study presented in Sec. E.2 is based on the 2D reflectometry setup presented above (see Sec. E.1.4). In order to assess the transferability of the study for 3D microstructures that more realistically approximate HYP, two 3D microstructures are simulated: one with a volume coefficient of $c_v = 0.2$ and the other with $c_v = 0.35$. As shown in Fig. E.6(c) and (f), microstructures with spherical inclusions embedded in a cubic supercell are investigated. While the material parameters and the diameter of the inclusion, $d_{inc} = 50\,\mu$m, remain unchanged to those introduced in Sec. E.1.1, the edge length of the cubic supercell is now reduced to 0.25 mm. To reduce the numerical demands of the simulation, an auxiliary layer is inserted between the supercell and the PML. Just like the bottom PML, the

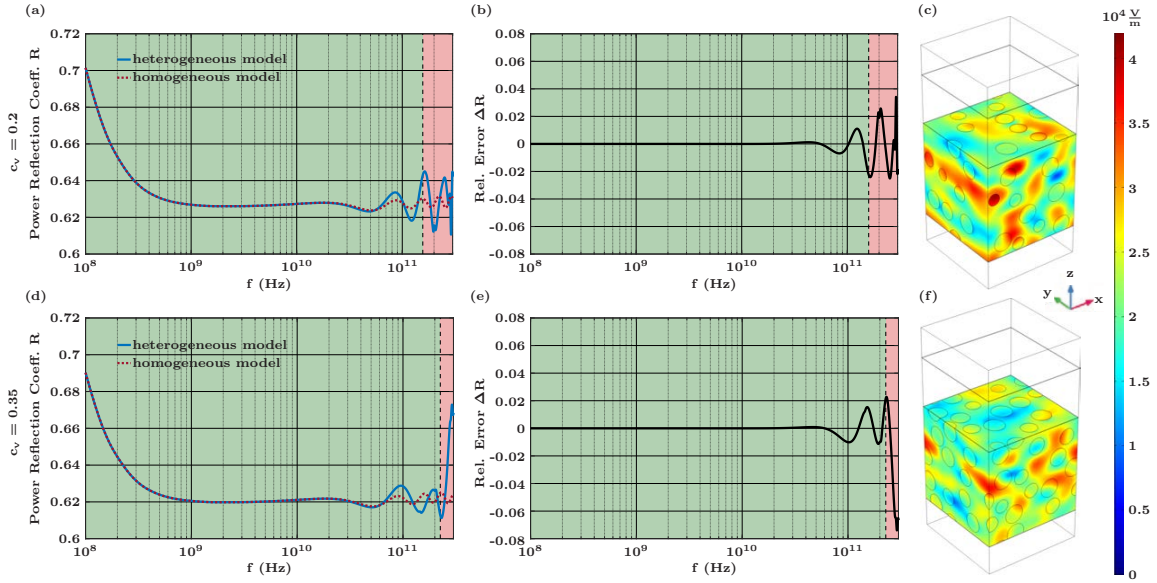


**Figure E.6:** Overview of two 3D simulations of a generalized HYP structure (i.e. for $\varepsilon_{r,1} = 80$; $\sigma_1 = 0.53\,\mathrm{S/m}$; $\varepsilon_{r,2} = 50$; $\sigma_2 = 0.12\,\mathrm{S/m}$; $d_{inc} = 50\,\mu\mathrm{m}$). The edge length of the simulated supercell is 0.25 mm. The upper row contains simulation results for a structure with a volume fraction of $c_v = 0.2$ and the bottom row those of a structure with a volume fraction of $c_v = 0.35$. (a) and (d) show the frequency-dependent power reflection coefficient, $R$, of the heterogeneous (blue) and the homogeneous model (red). (b) and (e) provide an overview of the relative error between both models. The validity range is highlighted in green and the forbidden frequency range in red. (c) and (f) show the field distribution of the magnitude of the electric field within the supercell embedded in the simulation setup at 300 GHz.

effective material parameters of the composite are assigned to this auxiliary layer. Note that this separation of the supercell by this auxiliary layer is mainly due to numerical reasons as the direct termination of the heterogeneous layer by the PML poses some numerical challenges given complex morphology of the layer.

Due to the high numerical demand and, thus, to the high simulation time, this investigation could not be performed with a larger set of implementations. The simulations were performed on a PC equipped with two Intel Xeon E5-2697 V4 processors (36 cores) and 512 GB of RAM. Between 0.1 GHz and 300 GHz, 200 frequency points were simulated with a MUMPS solver with the density of these points increasing with frequency. The simulation for each frequency point lasted 2 hours and included the full-wave simulation of the heterogeneous microstructure and its homogenized representative in p and s-polarization.

The spectral response of the power reflection coefficient $R$ is shown for the heterogeneous (blue) and homogeneous model (red) in the given frequency interval in Fig. E.6(a) and (d). Based on the 2 % deviation criterion, the validity of the homogeneous material model is retrieved from the relative deviation (i.e. relative error) between the models This collapses at 156 GHz for the material structure with a volume coefficient of $c_v = 0.2$ and

at 225 GHz for $c_v = 0.35$. The validity range of the homogeneous model is again marked green and the forbidden range red.

The observed periodic oscillations in the simulated spectral response of the power reflection are due to Fabry-Perot resonances in both the heterogeneous and homogeneous layer. These oscillations are determined by the finite thickness of the auxiliary layers and are thus not present in our prior 2D simulations. This is because we have dealt with a numerically infinite half-space system in those cases. However, the evaluation of the validity limit is not affected by the Fabry-Perot resonances since they are present in both models and thus assumed to be balanced out in the analysis of the relative error. To underline this, Figs. E.6(b) and (e) show the relative errors between the reflection coefficients of both models in the same frequency range.

The field strength distributions within the heterogeneous models at 300 GHz illustrated in Figs. E.6(c) and (f) show that the breakdown of the validity of the EMT model and the associated interference patterns in the reflection response are accompanied by strong field inhomogeneities within the microstructure. A core statement of this thesis concerning the correlation between interference patterns in the spectral response and morphological peculiarities of the microstructure can thus be transferred to randomized 3D cases. This is clearly indicated by two observations stated above and summarised here: (a) the separation of the investigated spectrum into a valid and a forbidden range, and (b) the interference patterns associated with inhomogeneous field distributions in the microstructure in the forbidden range. Due to the limited number of 3D simulations performed here, the transferability of these statements can only be given qualitatively.

## E.2 Monte-Carlo Analysis of Validity Limits

**Table E.1:** Overview of the material and structural parameters of parameter sets $P_1$ to $P_9$.

| $\varepsilon_{r,1} = 80$; $\sigma_1 = 0.53\,S/m$; $\varepsilon_{r,2} = 50$; $\sigma_2 = 0.12\,S/m$ | | | | |
|---|---|---|---|---|
| 260 sampled frequency points (10 MHz to 200 GHz) | | | | |
| $P_i$ | $d_d$ | $d_{inc}$ | $c_v$ | realizations |
| $P_1$ | 1.05 | 50 $\mu$m | 0.05 | 220 |
| $P_2$ | 1.05 | 50 $\mu$m | 0.1 | 220 |
| $P_3$ | 1.05 | 50 $\mu$m | 0.15 | 220 |
| $P_4$ | 1.05 | 50 $\mu$m | 0.2 | 220 |
| $P_5$ | 1.05 | 50 $\mu$m | 0.25 | 220 |
| $P_6$ | 1.05 | 50 $\mu$m | 0.3 | 220 |
| $P_7$ | 1.05 | 50 $\mu$m | 0.35 | 220 |
| $P_8$ | 1.05 | 50 $\mu$m | 0.4 | 220 |
| $P_9$ | 1.05 | 50 $\mu$m | 0.45 | 220 |

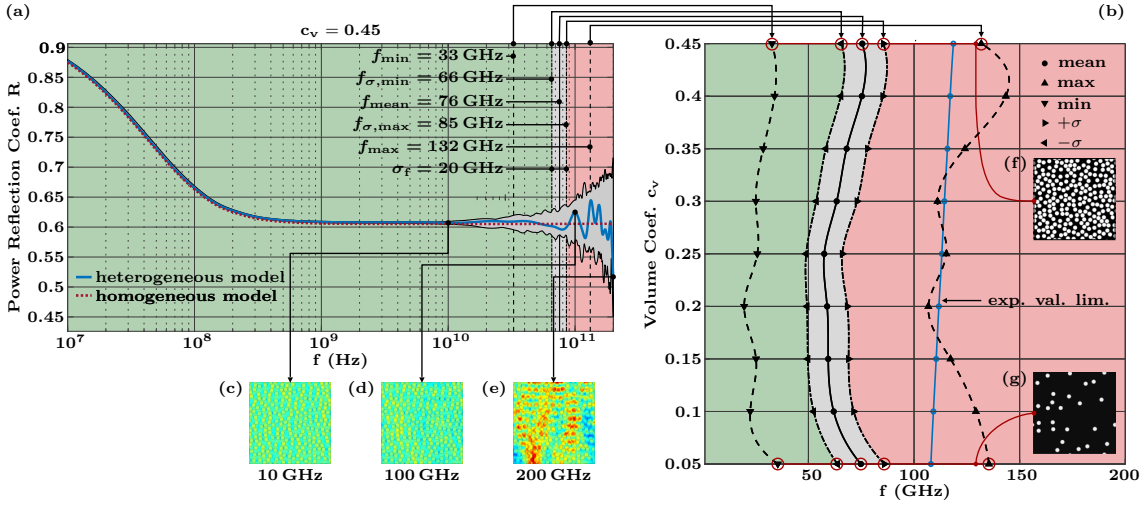


**Figure E.7:** Validity limits for several generalized HYP derivatives: (a) spectral responses of the reflectance (showing the typical Maxwell-Wagner roll-off in the MHz range) of 220 implementations (for $\varepsilon_{r,1} = 80$; $\sigma_1 = 0.53\,\mathrm{S/m}$; $\varepsilon_{r,2} = 50$; $\sigma_2 = 0.12\,\mathrm{S/m}$; $d_{inc} = 50\,\mu\mathrm{m}$; and volume fraction $c_v = 0.45$); (b) Validity limits of the derivatives of a heterogeneous material structure (here the HYP tissue), the blue line indicates the expected validity limit based on classical considerations; (c), (d), (e) examples of the electric field distribution $|\underline{\vec{E}}|$ at various frequencies (i.e. at 10 GHz, 100 GHz, 200 GHz, respectively); (f), (g) examples of the analyzed microstructures (i.e. for $c_v = 0.45$ and $c_v = 0.05$ respectively). The validity range of the EMT material model is colored in green while the forbidden range is marked red.

The analysis of a single HYP tissue structure has only minor significance for the reliable determination of the validity limit of the associated EMT representation. Therefore, the procedure presented in Sec. E.1.4 is performed for a large number of randomly generated realizations of the same HYP tissue based on a corresponding structural parameter set labelled $P_i$. Each set, $P_i$, contains fixed values for both the minimal separation distance, $d_d = 1.05$, and the diameter of the spherical inclusions in the HYP, $d_{inc} = 50\,\mu$m. These fixed values are augmented by one of nine volume fractions, $c_{v,i} \in \{0.05, 0.1, \ldots, 0.45\}$, resulting in 9 different HYP tissue types, corresponding to parameter sets $P_1, \ldots, P_9$ (cf. Table E.1). Within the framework of a Monte-Carlo analysis, 220 statistically independent microstructures with randomly distributed inclusions were created for each $P_i$ and corresponding $c_{v,i}$. These are considered in the following as realizations of the parameter set $P_i$. Examples of such microstructures are shown in Fig. E.7(f) and E.7(g) for the parameter sets $P_9 := (d_d = 1.05, \quad d_{inc} = 50\,\mu\mathrm{m}, \quad c_v = 0.45)$ and $P_1 := (d_d = 1.05, \quad d_{inc} = 50\,\mu\mathrm{m}, \quad c_v = 0.05)$ respectively. As an example, the statistical analysis for HYP sample $P_9$ ($c_v = 0.45$) with 220 randomly generated realizations is illustrated in Fig E.7(a). The frequency responses of the simulated power reflection coefficient of all of the realizations are confined to the grey-shaded area between the top and bottom envelope, with the blue curve labelling a single representation of this spectral set, which has already been depicted in Fig. E.5(c). The red-dotted curve shows the performance of the homogenized EMT model of the HYP tissue. The validity limits of the EMT homogenization are de-

termined as the frequency above which the power reflection of the homogeneous EMT model and the heterogeneous composite model deviate by more than 2 %. This yields a frequency value for each of the realizations at which this deviation first occurs. For the example of $P_9$, this yields a corresponding data set of 220 values with a mean frequency of $f_{\mathrm{mean}} = 76\,\mathrm{GHz}$, which in the following is defined as the representative value for the validity limit. The associated standard deviation is $\sigma_{\mathrm{f}} = 20\,\mathrm{GHz}$ leading to a first upper and lower bound of $f_{\sigma,\mathrm{min}} = 66\,\mathrm{GHz}$ and $f_{\sigma,\mathrm{max}} = 86\,\mathrm{GHz}$, whereas the absolute minimum and maximum of this limit for this data set corresponds to $f_{\mathrm{min}} = 33\,\mathrm{GHz}$ and $f_{\mathrm{max}} = 132\,\mathrm{GHz}$ as depicted in Fig. E.7(a). The validity range of the EMT material model is coloured green while, the forbidden range, in which the EMT representation breaks down, is coloured red.

As a last stage, the overall Monte-Carlo analysis was carried out for all parameter sets, $P_1, \ldots, P_9$, and their respective volume fractions, $c_{\mathrm{v},1}, \ldots, c_{\mathrm{v},9}$ (cf. Fig. E.7(b)). This revealed validity limits for HYP tissues at astonishingly low frequencies around $60 - 80\,\mathrm{GHz}$. In contrast, the classical estimation of validity limits according to EMT [23] using $\frac{\lambda_{\mathrm{m}}}{2\pi} > d_{\mathrm{inc}}$, where $\lambda_{\mathrm{m}}$ denotes the wavelength within the material, is significantly higher, with values between 110 GHz and 120 GHz (see Fig. E.7(b) blue line). This is an interesting result as it may challenge assumptions made in commonly used tissue models for mm-wave [58] and THz frequencies [121]. In addition, the statistical evaluation of all nine parameter sets also led to validity limits with only weak dependence on the volume fraction of the lipid droplets (i.e. inclusions) in the adipose HYP tissue. Fig. E.7(c)-(e) depict the electric field distributions, $|\underline{\vec{E}}|$, within the microstructure of the heterogeneous composite for three distinct frequencies along the blue curve. As expected from EMT, these field profiles are mostly homogeneous at frequencies within the validity range (e.g. 10 GHz), but display interference patterns at forbidden frequencies (e.g. 100 GHz and 200 GHz) with emerging spatial correlations to the underlying microstructure. In the context of reflectometry-based tissue classification, these correlations will in Sec. E.3 be used to establish the possibility of classifying microscopic features of the heterogeneous microstructure using spectral fingerprints in the forbidden range, an example of which is shown by the blue curve in Fig. E.7(a). In contrast, the well-behaved frequency response in the validity range allows for the extraction of macroscopic quantities such as the underlying volume fraction of the inclusions.

## E.3 Information Content of the Forbidden Range

The existence of validity limits has direct consequences on the use of EMT-based multi-scale models for multi-layered tissue systems such as skin. In such models the maximum frequency is determined by the tissue layer with the lowest validity limit, thus yielding an allowed operating frequency band which becomes specific to the overall skin model. At higher frequencies outside this band, the described homogenization of the particular

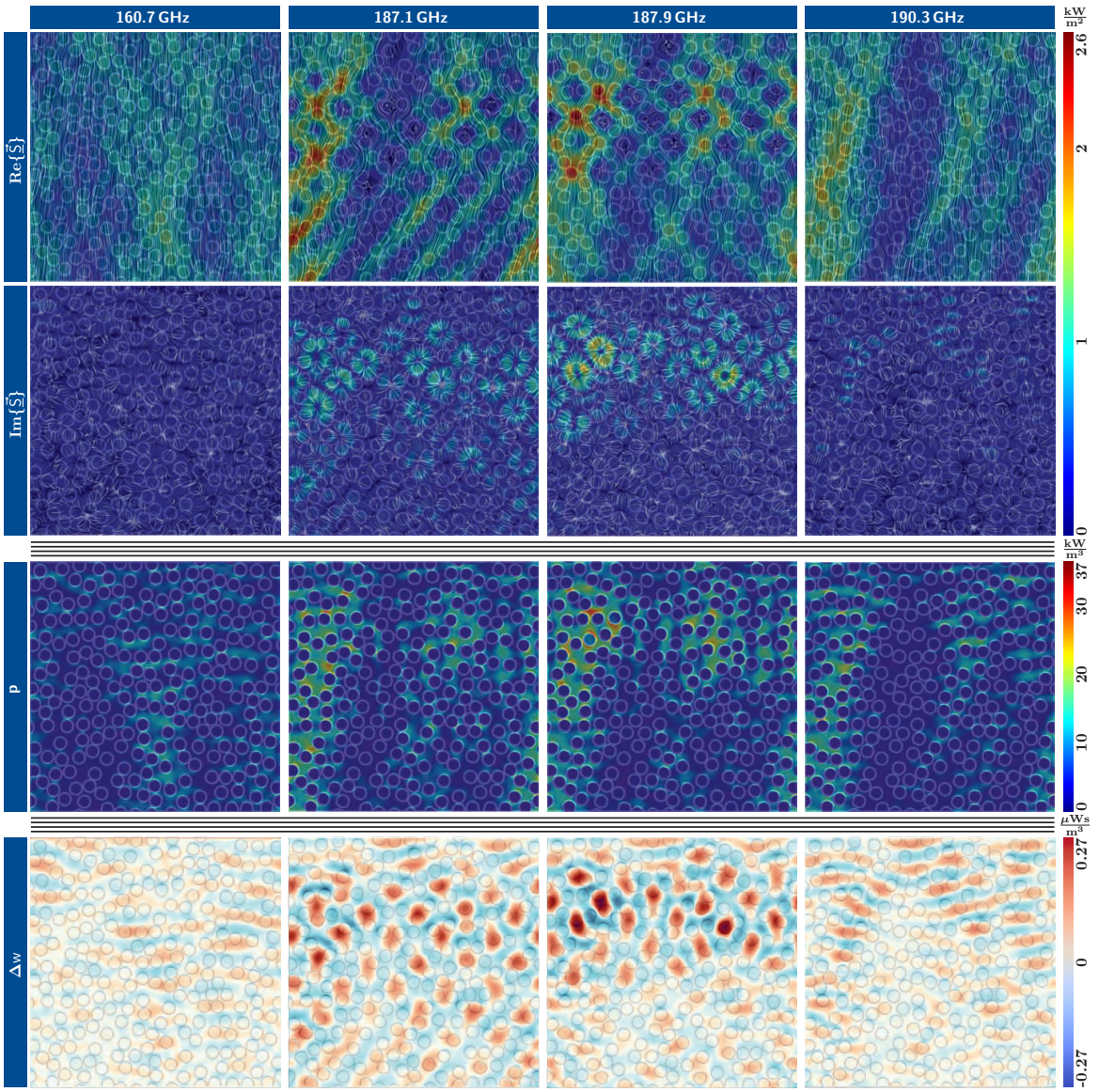


**Figure E.8:** Graphical evaluation of the EM fields within the microstructure for the frequency points 160.7 GHz, 187.1 GHz, 187.9 GHz and 190.3 GHz (i.e. for $\varepsilon_{r,1} = 80$; $\sigma_1 = 0.53\,\mathrm{S/m}$; $\varepsilon_{r,2} = 50$; $\sigma_2 = 0.12\,\mathrm{S/m}$; $d_{inc} = 50\,\mu\mathrm{m}$; and volume fraction $c_v = 0.45$). From the top to the bottom row: the real part of the Poynting vector $\mathrm{Re}\{\underline{\vec{S}}\}$, the imaginary part $\mathrm{Im}\{\underline{\vec{S}}\}$, the loss density $p$, and the difference of energy densities $\Delta w$.

tissue layer is not applicable anymore and its further analysis requires accurate modelling of its proper microstructure, which actually leads to a modified multiscale skin model. An ultra-broadband tissue analysis must therefore consider simultaneous structural changes in the tissue models during the frequency-domain simulation while relying on an appropriately prepared set of multiple model representations. These multiple representations can be set up prior to numerical analysis, e.g. when using machine learning-based predictions of the validity limits involved.

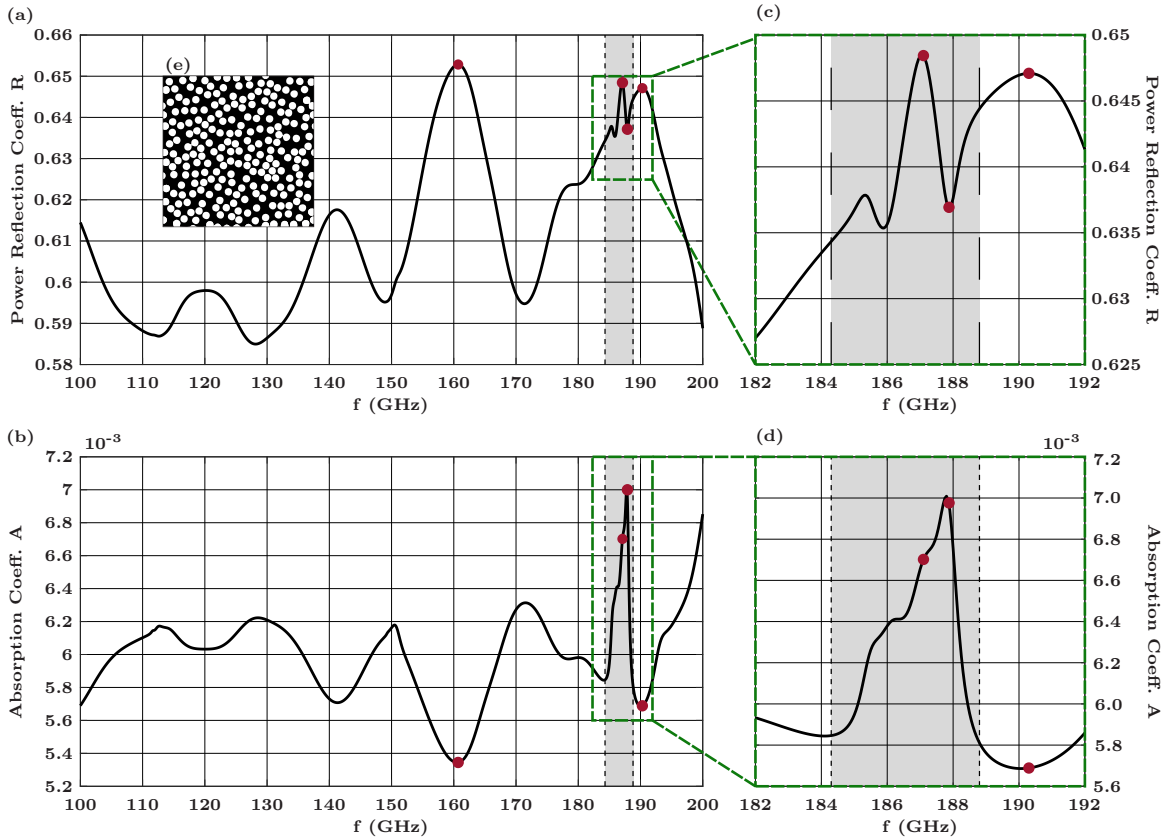


**Figure E.9:** Spectral response in the forbidden frequency range between 100 GHz and 200 GHz: (a) reflectance; (b) absorptance; (c), (d) detailed enlargements of the reflectance and absorptance in the subinterval between 182 GHz and 188 GHz; (e) example of the analysed HYP realization (i.e. for $\varepsilon_{r,1} = 80$; $\sigma_1 = 0.53\,\mathrm{S/m}$; $\varepsilon_{r,2} = 50$; $\sigma_2 = 0.12\,\mathrm{S/m}$; $d_{inc} = 50\,\mu\mathrm{m}$; and volume fraction $c_v = 0.45$).

As indicated in the previous section, the increasing impact of the microscopic properties on the frequency response beyond the validity limit opens up the possibility to identify and classify specific features of the tissue's microstructures based solely on the associated spectral fingerprint in the forbidden frequency range. This reasoning can be underpinned by correlating characteristic features in this spectral fingerprint with interference patterns emerging from the microstructure. In an illustrative example, specific frequency points in the spectral fingerprints of the power reflection, $R$, and absorption, $A$, between 100 GHz and 200 GHz were studied for a single HYP tissue realization ($c_v = 0.45$) in conjunction with the associated EM field patterns in the microstructure.

A field quantity of particular significance here is the difference between electric and magnetic energy density, $\Delta w$. This measure has already proven successful in the assessment of advanced MRI coils [122]. It is derived from the time-harmonic version of the Poynting theorem, represents the conservation of EM energy flux, $\underline{\vec{S}}$ (i.e. the Poynting vector), as shown in Eq. E.10, where $\underline{\vec{S}}$ has to fuel areas with dissipation loss and at the same time

compensate for temporal changes in the reactive power.

$$\nabla \cdot \underline{\vec{S}} = -\underbrace{\frac{1}{2}\sigma|\underline{\vec{E}}|^2}_{p} - j2\omega \underbrace{\frac{1}{4}\left(\mu|\underline{\vec{H}}|^2 - \varepsilon_0\varepsilon_\mathrm{r}|\underline{\vec{E}}|^2\right)}_{\Delta w = w_\mathrm{m} - w_\mathrm{e}}, \tag{E.10}$$

The reactive power term contains the difference, $\Delta w$, between the electric and magnetic energy density, where $\Delta w$ emerges only if the energy density distributions of both field quantities are spatially separated. The quantity $\Delta w$ thus indicates a locally confined resonant enhancement of reactive fields in the very microstructure of the tissue while also highlighting potential "hot spots" in the loss density, $p$. This is mainly due to oscillating balancing currents between these separated energy densities. The dissipated power in the tissue, $P_\mathrm{A}$, results from integrating the power loss density, $p$, over the tissue volume yielding the absorption, $A$.

Applied to the proper heterogeneous material representation of an illustrative HYP realization, Eq. E.10, and its derived measures, can be used to investigate correlations between the spatial field distribution within the microstructure and the spectral fingerprint in the forbidden range. In this case, the local electric and magnetic field strengths, $\underline{\vec{E}}(\vec{r}) = (\underline{E}_\mathrm{x}(\vec{r})\ \underline{E}_\mathrm{y}(\vec{r})\ \underline{E}_\mathrm{z}(\vec{r}))^\mathrm{T}$ and $\underline{\vec{H}}(\vec{r}) = (\underline{H}_\mathrm{x}(\vec{r})\ \underline{H}_\mathrm{y}(\vec{r})\ \underline{H}_\mathrm{z}(\vec{r}))^\mathrm{T}$ respectively, are used for calculation, where $\vec{r}$ denotes the spatial position. As depicted in Fig. E.8, $\Delta w$ provides the most selective map of the resonant loss enhancement which is highly correlated to the tissue microstructure and thus to the randomized HYP cell distribution. With this connection between microstructure, affine field patterns and specific signatures in the spectral fingerprint, the spectral responses in the forbidden frequency range are reasoned to contain enough information for the classification of the underlying microstructure. In the following, the spectral responses of both power reflection, $R$, and absorption, $A$, of the given HYP tissue are plotted in Fig. E.9 for the previously mentioned region of interest in the forbidden frequency range. Apart from the expected opposing behavior of the frequency responses of $R$ and $A$ (see Figs. E.9(a) and (b)), where a reflection maximum is accompanied by an absorption minimum, there are distinct subintervals demonstrating different behavior, such as that between 184 GHz and 188 GHz (shaded grey). An enlarged view of this specific region is plotted in Figs. E.9(c) and E.9(d) and shows both $R$ and $A$ forming unique spectral substructures. In the following, local extrema located both within and outside the sub-interval will be analyzed. This will be performed at the frequency values of 160.7 GHz, 187.1 GHz, 187.9 GHz and 190.3 GHz labelled by red dots.

The associated field patterns regarding flowing, dissipating and stored energy are depicted in Fig. E.8 partly using a generalized field line representation provided by the line integral convolution (LIC) method [123]. Comparing these fields inside the subinterval (at 187.1 GHz and 187.9 GHz) with those outside (at 160.7 GHz and 190.3 GHz) indicates that the imaginary part of the energy flux, $\underline{\vec{S}}$, yields the most distinct correlations to the underlying microstructure. This is even more distinct when using $\Delta w$, which is actually derived from $\mathrm{Im}\{\underline{\vec{S}}\}$. It can therefore be assumed that these unique spectral substructures in the spectral responses may contribute particularly significantly to the information

content about the tissue microstructure. This makes it easy to understand that promising tissue classification schemes based on skin surface reflectometry could implicitly use such unique spectral features and eventually exploit them in the framework of a supervised learning-based classification approach. For a more detailed discussion of this topic, see [96].

## E.4 Conclusions

In Sec. E.1, the basic assumption and the methodology of the numerical study conducted was introduced. This introduction included the generation of semi-periodic microstructures using a modified parameterizable version of the RSA algorithm. Subsequently, the effective macroscopic material properties of these structures were determined using either a numerical FEM-based homogenization approach or analytical mixing rules. Finally, the validity limits of these microstructures were evaluated by comparing the original heterogeneous (bio)composite with its homogenized surrogate material in a generalized reflectometry setup.

The comparison between the numerical and analytical homogenization approaches performed in Sec. E.1.3 showed that, at frequencies below the expected Maxwell-Wagner roll-off, only numerical homogenization accounts for the interaction between depolarization fields of adjacent inclusions correctly. This is of particular importance in the case of random, dense material composites, such as those investigated in this study, and would be even more important if more complex irregular inclusion shapes were considered. The reason is that only numerical homogenization provides a correct multipole representation of the EM problem and is able to determine a rotation-free yet divergent quasi-static solution for the electric field with respect to the interactions between adjacent inclusions. This is not possible when using mixing rules, since these make approximate assumptions to account for the proximity of adjacent inclusions (e.g. the HB mixing rule) or to neglect them completely (e.g. the MG mixing rule). Therefore, at low frequencies, these mixing formulas can only be used to estimate upper and lower limits for the expected effective macroscopic material parameters. For frequencies above the expected Maxwell-Wagner polarization, both the MG and the HB mixing formulas allow the exact determination of the effective material parameters.

In Sec. E.1.4, a formalism to investigate the validity limit of each homogenized surrogate material by means of a generalized reflectometry setup was introduced. The validity limit was defined at the lowest frequency value with a 2 % deviation between the reflection of an incoming plane wave from the heterogeneous subsurface system and its homogenized representation. Thus, a validity range was defined below this limit. Above this validity range, the spectral response of the reflection of the heterogeneous material system showed oscillations caused by Fabry-Perot resonances. To check the transferability of these observations to more realistic representations of HYP tissue, the formalism was also applied to two 3D supercells containing spherical inclusions. This investigation

showed the same oscillation pattern as observed before, thus allowing the same classification of the spectral response of the system into validity and forbidden ranges. Due to the high numerical demand of these simulations, the subsequent Monte-Carlo analysis was performed in 2D only.

In Sec. E.2, a comprehensive Monte-Carlo analysis was conducted to investigate the validity limits of several HYP tissue derivatives. These HYP derivatives were defined by parameter sets describing their structural particularites in terms of the separation distance between the inclusions, $d_\mathrm{d}$, their diameter, $d_\mathrm{inc}$, and their volume fraction, $c_\mathrm{v}$. In this particular analysis, nine parameter sets were defined resulting in generalized HYP tissue derivatives with various volume fractions of the inclusions with $c_{\mathrm{v,i}} \in \{0.05, \ldots, 0.45\}$ alongside constant $d_\mathrm{d} = 1.05$ and $d_\mathrm{inc} = 50\,\mu$m. For each of these parameter sets, 220 randomized realizations were generated, homogenized and evaluated in terms of their individual validity limits using the virtual reflectometry setup. The analysis of the validity limits of the individual realizations of each parameter set, $\mathrm{P_i}$, showed that the validity limit of an entire parameter set must be defined by statistical measures such as the mean validity frequency, $f_{\mathrm{mean,i}}$, and the corresponding standard derivation, $\sigma_{\mathrm{f,i}}$. In addition, the statistical analysis showed an astonishingly low onset of the EMT validity limits between 60 GHz - 80 GHz while classical estimations forecasted a limit between 110 GHz - 120 GHz.
Furthermore, it could be observed that the EMT validity limits and the Fabry-Perot oscillations in the forbidden range corresponded to the structural particularities of the underlying parameter set, while the roll-off of the reflection coefficient in the validity range corresponded to the volume fraction of the underlying material composition.

To validate the applicability of the forbidden frequency range for classification of the underlying microstructure, the reflection in the forbidden range was investigated for an arbitrary tissue representation as an illustrative example. The analysis of the spectral response was complemented by a graphical evaluation of the electromagnetic fields within the microstructure. In this graphical evaluation, four measures were illustrated: the real and imaginary part of the Poynting vector, $\mathrm{Re}\,\underline{\vec{S}}$ and $\mathrm{Im}\,\underline{\vec{S}}$, the loss density, $p$, and the difference between the energy densities, $\Delta w$. The analysis of these fields regarding energy flow, dissipation and storage showed locally confined resonant enhancement of reactive fields and also highlighted local hot spots in the loss density. It could be shown that these field effects corresponded to maxima and minima in the spectral response of the reflection coefficient. Based on this finding, it can be assumed that these locally confined resonant enhancements contribute to the information content of the forbidden range and can thus be used to classify structural particularities of the underlying microstructure under investigation.

# List of Figures

# List of Tables

# Abbreviations

CAD ..... Computer Aided Design
CP ..... Cytoplasm
D ..... Dermis
DPPC ..... Dipalmitoylphosphatidylcholine
EC ..... Extracellular Space
ED ..... Epidermis
EM ..... Electromagnetic
EMT ..... Effective Material Theory
ER ..... Endoplasmic Reticulum
FEM ..... Finite Element Method
HB ..... Hanai-Bruggeman
HYP ..... Hypodermis
ICNIRP ..... International Commission on Non-Ionizing Radiation Protection
LLL ..... Landau-Lifshitz-Looyenga
M ..... Mitochondria
MC ..... Muscle Tissue
MM ..... Millimeter-Wave Frequencies
MR ..... Material Range
MUMPS ..... Multifrontal Massively Parallel Sparse Direct Solver
MG ..... Maxwell-Garnett
N ..... Nucleus
NP ..... Nucleoplasm
OS ..... Optical Spectrum
PBC ..... Periodic Boundary Conditions

PBS ..... Phosphate-Buffer Saline Solution
PM ..... Plasma Membrane
RSA ..... Random Sequential Addition
RF ..... Radio Frequencies
SC ..... Stratum Corneum
SG ..... Stratum Granulosum
SS ..... Stratum Spinosum
SB ..... Stratum Basale
TMP ..... Transmembrane Potential
UC ..... Unit Cell
vED ..... Viable Epidermis

# Bibliography


[1] "Guidelines for limiting exposure to electromagnetic fields (100 kHz to 300 GHz)," Int. Comm. on Non-Ionizing Radiation Protection, ICNIRP Publication, *Health. Phys.*, vol. 118, no. 5, pp. 483-524, 2020, doi: 10.1097/HP.0000000000001210.

[2] "Guidelines for limiting exposure to time-varying electric and magnetic fields (1 Hz to 100 kHz)," Int. Comm. on Non-Ionizing Radiation Protection, ICNIRP Publication, *Health. Phys.*, vol. 99, no. 6, pp. 818-836, 2010, doi: 10.1097/HP.0b013e3181f06c86.

[3] "IEEE Standard for Safety Levels with Respect to Human Exposure to Electric, Magnetic, and Electromagnetic Fields, 0 Hz to 300 GHz," *in IEEE Std C95.1-2019 (Revision of IEEE Std C95.1-2005/ Incorporates IEEE Std C95.1-2019/Cor 1-2019)*, pp. 1–312, 2019.

[4] K. Sasaki, M. Mizuno, K. Wake, and S. Watanabe, "Monte Carlo simulations of skin exposure to electromagnetic field from 10 GHz to 1 THz," *Phys. Med. Biol.*, vol. 62, no. 17, p. 6993–7010, 2017, doi: 10.1088/1361-6560/aa81fc.

[5] K. Sasaki, K. Wake, and S. Watanabe, "Measurement of the dielectric properties of the epidermis and dermis at frequencies from 0.5 GHz to 110 GHz," *Phys. Med. Biol.*, vol. 59, no. 16, p. 4739–4747, 2014, doi: 10.1088/0031-9155/59/16/4739.

[6] A. Hirata, M. Morita, and T. Shiozawa, "Temperature increase in the human head due to a dipole antenna at microwave frequencies," *IEEE Trans. Electromagn. Compat.*, vol. 45, no. 1, pp. 109–116, 2003, doi: 10.1109/TEMC.2002.808045.

[7] A. Hirata and T. Shiozawa, "Correlation of maximum temperature increase and peak SAR in the human head due to handset antennas," *IEEE Trans. Microw. Theo. Techn.*, vol. 51, no. 7, pp. 1834–1841, 2003, doi: 10.1109/TMTT.2003.814314.

[8] A. Hirata, M. Fujimoto, T. Asano, J. Wang, O. Fujiwara, and T. Shiozawa, "Correlation Between Maximum Temperature Increase and Peak SAR with Different Average Schemes and Masses," *IEEE Trans. Electromagn. Compat*, vol. 48, no. 3, pp. 569–578, 2006, doi: 10.1109/TEMC.2006.877784.

[9] A. Hirata and O. Fujiwara, "The correlation between mass-averaged SAR and temperature elevation in the human head model exposed to RF near-fields from 1 to 6 GHz," *Phys. Med. Biol.*, vol. 54, no. 23, pp. 7227–7238, 2009, doi: 10.1088/0031-9155/54/23/013.

[10] A. Hirata, I. Laakso, T. Oizumi, R. Hanatani, K. H. Chan, and J. Wiart, "The relationship between specific absorption rate and temperature elevation in anatomically based human body models for plane wave exposure from 30 MHz to 6 GHz," *Phys. Med. Biol.*, vol. 58, no. 4, pp. 903–921, 2013, doi: 10.1088/0031-9155/58/4/903.

[11] Y. Hashimoto, A. Hirata, R. Morimoto, S. Aonuma, I. Laakso, K. Jokela, and K. R. Foster, "On the averaging area for incident power density for human exposure limits at frequencies over 6 GHz," *Phys. Med. Biol.*, vol. 62, no. 8, pp. 3124–3138, 2017, doi: 10.1088/1361-6560/aa5f21.

[12] D. Funahashi, A. Hirata, S. Kodera, and K. R. Foster, "Area-Averaged Transmitted Power Density at Skin Surface as Metric to Estimate Surface Temperature Elevation," *IEEE Access*, vol. 6, pp. 77 665–77 674, 2018, doi: 10.1109/ACCESS.2018.2883733.

[13] H. Kitano, "Computational systems biology," *Nature*, vol. 420, no. 6912, pp. 206–210, 2002.

[14] S. Huclova, D. Erni, and J. Froehlich, "Modelling and validation of dielectric properties of human skin in the MHz region focusing on skin layer morphology and material composition," *J. Phys. D: Appl. Phys.*, vol. 45, no. 2, pp. 025 301–1–17, 2012, doi: 10.1088/0022-3727/45/2/025301.

[15] ——, "Modelling effective dielectric properties of materials containing diverse types of biological cells," *J. Phys. D: Appl. Phys.*, vol. 43, no. 36, pp. 365 405–1–10, 2010, doi: 10.1088/0022-3727/43/36/365405.

[16] T. Kotnik and D. Miklavčič, "Theoretical evaluation of the distributed power dissipation in biological cells exposed to electric fields," *Bioelectromagnetics*, vol. 21, no. 5, pp. 385–394, 2000.

[17] M. Saviz and R. Faraji-Dana, "A multiscale approach to terahertz electric field estimation in corneal issues," *EEE J. Multisc. Multiphys. Comp. Tech.*, vol. 5, pp. 167–175, 2020, doi: 10.1109/JMMCT.2020.3018298.

[18] K. Jerbic, J. T. Svejda, B. Sievert, A. Rennings, J. Fröhlich, and D. Erni, "The Importance of Subcellular Structures to the Modeling of Biological Cells in the Context of Computational Bioelectromagnetics Simulations," *Bioelectromagnetics*, 2022, doi: 10.1002/bem.22436.

[19] A. Christ, T. Samaras, E. Neufeld, and N. Kuster, "RF-induced temperature increase in a stratified model of the skin for plane-wave exposure at 6-100 GHz," *Rad. Prot. Dos.*, vol. 188, no. 3, p. 350–360, 2020, doi: 10.1093/rpd/ncz293.

[20] K. S. Cole and R. H. Cole, "Dispersion and Absorption in Dielectrics I. Alternating Current Characteristics," *J. Chem. Phys.*, vol. 9, no. 4, pp. 341–351, 1941, doi: 10.1063/1.1750906.

[21] D. W. Davidson and R. H. Cole, "The Differentiation of White Adipose Cells - An Electron Microscope Study," *J. Chem. Phys.*, vol. 19, no. 12, pp. 1484–1490, 1951, doi: 10.1063/1.1748105.

[22] S. Havriliak and S. Negami, "A complex plane representation of dielectric and mechanical relaxation processes in some polymers," *Polymer*, vol. 8, pp. 161–210, 1967, doi: 10.1016/0032-3861(67)90021-3.

[23] A. H. Sihvola, *Electromagnetic mixing formulas and applications*, ser. IEEE electromagnetic waves series. London: Institution of Electrical Engineers, 2008, vol. 47.

[24] A. H. Sihvola and J. A. Kong, "Effective permittivity of dielectric mixtures," *IEEE Trans. Geosci. Remote Sensing*, vol. 26, no. 4, pp. 420–429, 1988.

[25] K. Asami, "Characterization of heterogeneous systems by dielectric spectroscopy," *Prog. Polym. Sci.*, vol. 27, no. 8, pp. 1617–1659, 2002, doi:https://doi.org/10.1016/0925-2312(93)90006-O.

[26] Y. Gilaberte, L. Prieto-Torres, I. Pastushenko, and A. Juarranz, *book chapter 1 "Anatomy and Function of the Skin," pp. 1-14, in Nanoscience in Dermatology, M. R. Hamblin, P. Avci, and T. W. Prow, 1st Ed.*, San Diego, CA, USA: Academic Press, 2016.

[27] W. Wiegers and S. Wolf, *Haut.de*, [accessed Jan. 9 2023]. [Online]. Available: https://www.haut.de/haut/grundlagen/haut/

[28] Y. Lee and H. K., "Skin thickness of Korean adults," *Surg. Radiol. Anat.*, vol. 24, no. 3-4, pp. 183–189, 2002, doi: 10.1007/s00276-002-0034-5.

[29] Y. Ishida, J. F. Carroll, M. L. Pollock, J. E. Graves, and S. H. Leggett, "Reliability of B-mode ultrasound for the measurement of body fat and muscle thickness," *Am. J. Hum. Bio.*, vol. 4, no. 4, pp. 511–520, 1992, doi: 10.1002/ajhb.1310040410.

[30] J. S. Barbieri, K. Wanat, and J. Seykora, *"Skin: Basic Structure and Function," pp. 1134-1144, in Pathobiology of Human Disease - A Dynamic Encyclopedia of Disease Mechanisms, L. M. McManus, and R. N. Mitchell, 1st Ed.*, San Diego, CA, USA: Academic Press, 2014.

[31] R. S. Moreci and T. Lechler, "Epidermal structure and differentiation," *Current Biol.*, vol. 30, no. 4, pp. R144–R149, 2020, doi: 10.1016/j.cub.2020.01.004.

[32] H. Jastrow, *Workshop Anatomy for the Internet*, [accessed Dec. 2021] http://www.drjastrow.de.

[33] G. Kroemer, L. Galluzzi, P. Vandenabeele, J. Abrams, E. S. Alnemri, E. H. Baehrecke, M. V. Blagosklonny, W. S. El-Deiry, P. Golstein, D. R. Green, M. Hengartner, R. A. Knight, S. Kumar, S. A. Lipton, W. Malorni, G. Nuñez, M. E. Peter, J. Tschopp, J. Yuan, M. Piacentini, B. Zhivotovsky, and M. G., "Classification of cell death: recommendations of the Nomenclature Committee on Cell Death 2009," *Cell Death & Differentiation*, vol. 16, no. 1, pp. 3–11, 2009, doi: 10.1038/cdd.2008.150.

[34] L. Chrit, P. Bastien, G. D. Sockalingum, D. Batisse, F. Leroy, M. Manfait, and H. C., "An in vivo randomized study of human skin moisturization by a new confocal Raman fiber-optic microprobe: assessment of a glycerol-based hydration cream," *Skin Pharm. Phys.*, vol. 19, no. 4, pp. 207–215, 2006, doi: 10.1159/000093116.

[35] P. W. Wertz, "Stratum corneum Lipids and Water," *Exog. Dermat.*, vol. 3, no. 2, pp. 53–56, 2004, doi: 10.1159/000086155.

[36] L. Chen, G. Lian, and L. Han, "Use of bricks and mortar model to predict transdermalpermeation: Model development and initial validation," *Exog. Dermat.*, vol. 47, no. 17, pp. 6465–6472, 2008, doi: 10.1021/ie701711v.

[37] G. D. Weinstein, J. L. McCullough, and P. Ross, "Cell proliferation in normal epidermis," *J. Invest. Dermat.*, vol. 82, no. 6, pp. 623–628, 1984, doi: 10.1111/1523-1747.ep12261462.

[38] P. Corcuff, C. Bertrand, and J. L. Leveque, "Morphometry of human epidermis in vivo by real-time confocal microscopy," *Arch. Dermat. Res.*, vol. 285, no. 8, pp. 475–481, 1993, doi: 10.1007/BF00376820.

[39] H. Pinkus, "Examination of the epidermis by the strip method of removing horny layers. I. Observations on thickness of the horny layer, and on mitotic activity after stripping," *J. Invest. Dermat.*, vol. 16, no. 6, pp. 383–386, 1951, doi: 10.1038/jid.1951.45.

[40] N. S. Penneys, "Location of proliferating cells in human epidermis," *Arch. Dermat.*, vol. 101, no. 3, pp. 323–327, 1970.

[41] M. R. Gdula, K. Poterlowicz, A. N. Mardaryev, A. A. Sharov, Y. Peng, M. Y. Fessing, and V. A. Botchkarev, "Remodeling of three-dimensional organization of the nucleus during terminal keratinocyte differentiation in the epidermis," *J. Invest. Dermat.*, vol. 133, no. 9, pp. 2191–2201, 2013, doi: 10.1038/jid.2013.66.

[42] H. Yousef, M. Alhajj, and S. Sharma, *Anatomy, Skin (Integument), Epidermis*, [accessed Dec. 4, 2022] https://www.ncbi.nlm.nih.gov/books/NBK470464.

[43] N. G. and G. C., "Variability of fibroblast morphology in vivo: A silver impregnation study on human digital dermis and subcutis," *J. Anat.*, vol. 177, p. 195, 1991.

[44] T. Tamura, M. Tenhunen, T. Lahtinen, T. Repo, and H. P. Schwan, "Modeling of the dielectric properties of normal and irradiated skin," *Phy. Med. Biol.*, vol. 39, p. 927–936, 1994, doi: 10.1088/0031-9155/39/6/001.

[45] S. Huclova, "Modeling of cell suspensions and biological tissue for computational electromagnetics," Ph.D. dissertation, ETH Zurich, Zurich, Switzerland, 2011.

[46] L. Napolitano, "The Differentiation of White Adipose Cells - An Electron Microscope Study," *J. Cell Biol.*, vol. 18, pp. 663–679, 1963, doi: 10.1083/jcb.18.3.663.

[47] J. Despr'es, R. Savard, A. Tremblay, and C. Bouchard, "Adipocyte diameter and lipolytic activity in marathon runners: Relationship with body fatness," *Europ. J. App. Phys. Occup. Phys.*, vol. 51, no. 2, pp. 223–230, 1983, doi: 10.1007/BF00455185.

[48] Z. Haider, Y. Le Drean, G. Sacco, D. Nikolayev, R. Sauleau, and M. Zhadobov, "High-Resolution Model of Human Skin Appendages for Electromagnetic Dosimetry at Millimeter Waves," *IEEE J. Microw.*, vol. 2, no. 1, pp. 214–227, 2022, doi: 10.1109/JMW.2021.3126712.

[49] N. Betzalel, Y. Feldman, and P. Ben Ishai, "The Modeling of the Absorbance of Sub-THz Radiation by Human Skin," *IEEE Trans. THz Sci. Technol.*, vol. 7, no. 5, pp. 521–528, 2017, doi: 10.1109/TTHZ.2017.2736345.

[50] N. Betzalel, P. Ben Ishai, and Y. Feldman, "The human skin as a sub-THz receiver - Does 5G pose a danger to it or not?" *Environ. Res.*, vol. 163, 2018, doi: 10.1016/j.envres.2018.01.032.

[51] O. Spathmann, M. Zang, J. Streckert, V. Hansen, M. Saviz, K. Statnikov, U. Pfeiffer, and M. Clemens, "Numerical computation of temperature elevation in human skin due to electromagnetic exposure in the THz frequency Range," *IEEE Trans. Terahertz Sci. Technol.*, vol. 5, no. 6, pp. 978–989, 2015, doi: 10.1109/TTHZ.2015.2476962.

[52] M. C. Ziskin, S. I. Alekseev, K. R. Foster, and Q. Balzano, "Tissue models for RF exposure evaluation at frequencies above 6 GHz," *Bioelectromagnetics*, vol. 41, no. 1, pp. 173–189, 2018, doi: 10.1002/bem.22110.

[53] K. Li, K. Sasaki, S. Watanabe, and H. Shirai, "Relationship between power density and surface temperature elevation for human skin exposure to electromagnetic waves with oblique incidence angle from 6 GHz to 1 THz," *Phys. Med. Biol.*, vol. 64, no. 6, p. 065016, 2019, doi: 10.1088/1361-6560/ab057a.

[54] G. Sacco, S. Pisa, and M. Zhadobov, "Age-dependence of electromagnetic power and heat deposition in near-surface tissues in emerging 5G bands," *Sci. Rep.*, vol. 11, no. 1, p. 3983, 2021, doi: 10.1038/s41598-021-82458-z.

[55] C. Gabriel, S. Gabriel, and E. K. Corthout, "The dielectric properties of biological tissues: I. Literature survey," *Phys. Med. Biol.*, vol. 41, no. 11, pp. 2231–2249, 1996, doi: 10.1088/0031-9155/41/11/001.

[56] S. Gabriel, R. W. Lau, and C. Gabriel, "The dielectric properties of biological tissues: II. Measurements in the frequency range 10 Hz to 20 GHz," *Phys. Med. Biol.*, vol. 41, no. 11, pp. 2251–2269, 1996, doi: 10.1088/0031-9155/41/11/002.

[57] ——, "The dielectric properties of biological tissues: III. Parametric models for the dielectric spectrum of tissues," *Phys. Med. Biol.*, vol. 41, no. 11, pp. 2271–2293, 1996, doi: 10.1088/0031-9155/41/11/003.

[58] S. I. Alekseev and M. C. Ziskin, "Human skin permittivity determined by millimeter wave reflection measurements," *Bioelectromagnetics*, vol. 28, no. 5, pp. 331–339, 2007.

[59] R. Clausius, *Die Mechanische Behandlung der Electricität*. Wiesbaden, Germany: Springer, 1879.

[60] L. Lorenz, "Ueber die Refractionsconstante," *Ann. Phys. Chem.*, vol. 247, no. 9, pp. 70–103, 1880, doi: 10.1002/andp.18802470905.

[61] Y. Feldman, I. Ermolina, and Y. Hayashi, "Time domain dielectric spectroscopy study of biological systems," *IEEE Trans. Dielect. Electr. Insul.*, vol. 10, no. 5, pp. 728–753, 2003.

[62] T. Kotnik and D. Miklavčič, "Theoretical evaluation of voltage inducement on internal membranes of biological cells exposed to electric fields," *Biophys. J.*, vol. 90, no. 2, pp. 480–491, 2006, doi: 10.1529/biophysj.105.070771.

[63] V. Vajrala, J. R. Claycomb, H. Sanabria, and J. H. S. Miller, "Effects of oscillatory electric fields on internal membranes: an analytical model," *Biophys. J.*, vol. 94, no. 6, pp. 2043–2052, 2008, doi: 10.1529/biophysj.107.114611.

[64] H. Ye, M. Cotic, E. E. Kang, M. G. Fehlings, P. Carlen, and L. Peter, "Transmembrane potential induced on the internal organelle by a time-varying magnetic field: a model study," *J. Neuroeng. Rehabilitation*, vol. 7, p. 12, 2010, doi: 10.1186/1743-0003-7-12.

[65] K. Asami, T. Hanai, and N. Koizumi, "Dielectric properties of yeast cells," *J. Membrane Biol.*, vol. 28, no. 2-3, pp. 169–180, 1979.

[66] K. Asami, Y. Takahashi, and S. Takashima, "Dielectric properties of mouse lymphocytes and erythrocytes," *BBA Mol. Cell Res.*, vol. 1010, no. 1, pp. 49–55, 1989.

[67] R. Lisin, B. Z. Ginzburg, M. Schlesinger, and Y. Feldman, "Time domain dielectric spectroscopy study of human cells. i. erythrocytes and ghosts," *BBA Biomembranes*, vol. 1280, no. 1, pp. 34–40, 1996.

[68] Y. Polevaya, I. Ermolina, M. Schlesinger, B. Z. Ginzburg, and Y. Feldman, "Time domain dielectric spectroscopy study of human cells ii. normal and malignant white blood cells," *BBA Biomembranes*, vol. 1419, no. 2, pp. 257–271, 1996.

[69] I. Ermolina, Y. Polevaya, and Y. Feldman, "Analysis of dielectric spectra of eukaryotic cells by computer modeling," *Euro. Biohphys. J.*, vol. 29, no. 2, pp. 141–145, 2000.

[70] I. Ermolina, Y. Polevaya, Y. Feldman, B. Z. Ginzburg, and M. Schlesinger, "Study of normal and malignant white blood cells by time domain dielectric spectroscopy," *IEEE Trans. Dielect. Electr. Insul.*, vol. 8, no. 2, pp. 253–261, 2001.

[71] C. Merla, M. Liberti, F. Apollonio, and G. d'Inzeo, "Quantitative assessment of dielectric parameters for membrane lipid bi-layers from RF permittivity measurements," *Bioelectromagnetics*, vol. 30, no. 4, pp. 286–298, 2009. [Online]. Available: https://onlinelibrary.wiley.com/doi/abs/10.1002/bem.20476

[72] J. Gielis, "A generic geometric transformation that unifies a wide range of natural and abstract shapes," *Am. J. Bot.*, vol. 590, no. 3, p. 333–338, 2003, doi: 10.3732/ajb.90.3.333.

[73] L. Mescia, M. A. Chiapperino, P. Bia, J. Gielis, and D. Caratelli, "Modeling of electroporation induced by pulsed electric fields in irregularly shaped cells," *IEEE Trans. Biomed. Eng.*, vol. 65, no. 2, pp. 414–423, 2018, doi: 10.1109/TBME.2017.2771943.

[74] J. Dermol-Cerne and D. Miklavcic, "From Cell to Tissue Properties-Modeling Skin Electroporation With Pore and Local Transport Region Formation," *IEEE Trans. Biomed. Eng.*, vol. 65, no. 2, pp. 458–468, 2018, doi: 10.1109/TBME.2017.2773126.

[75] C. Merla, M. Liberti, P. Marracino, A. Muscat, A. Azan, F. Apollonio, and L. M. Mir, "A wide-band bio-chip for realtime optical detection of bioelectromagnetic interactions with cells," *Sci. Rep.*, vol. 8, no. 1, p. 5044, 2018.

[76] T. García-Sánchez, C. Merla, J. Fontaine, A. Muscat, and L. M. Mir, "Sine wave electropermeabilization reveals the frequency-dependent response of the biological membranes," *BBA Biomembranes*, vol. 1860, no. 5, pp. 1022–1034, 2018.

[77] Y. Feng, L. Huang, P. Zhao, F. Liang, and W. Wang, "A microfluidic device integrating impedance flow cytometry and electric impedance spectroscopy for high-efficiency single-cell electrical property measurement," *Anal. Chem.*, vol. 91, no. 32, pp. 15 204–15 212, 2019.

[78] C. Merla, M. Liberti, C. Consales, A. Denzi, F. Apollonio, C. Marino, and B. Benassi, "Evidences of plasma membrane-mediated ROS generation upon ELF exposure in neuroblastoma cells supported by a computational multiscale approach," *BBA Biomembranes*, vol. 1861, no. 8, pp. 1446–1457, 2019.

[79] Y. Guo, I. Yagi, S. Uchida, F. Tochikubo, M. Takano, Y. Wakizaka, and T. Enjoji, "Basic study of dielectric properties of cancer cells by dielectrophoretic velocimetry," *Electron. Comm. Jpn*, vol. 104, no. 2, pp. 15 204–15 212, 2021.

[80] A. Denzi, J. A. A. Escobar, C. Nasta, C. Merla, B. Benassi, C. Consales, F. Apollonio, and M. Liberti, "A microdosimetry study for a realistic shaped nucleus," in *2016 38th Annual International Conference of the IEEE Engineering in Medicine and Biology Society (EMBC)*, 2016, pp. 4189–4192.

[81] A. Denzi, H. Hanna, F. M. Andre, L. M. Mir, F. Apollonio, and M. Liberti, "Microdosimetry for pulsed E fields in a realistic models of cells and endoplasmic reticulum," in *2017 14th International Conference on Synthesis, Modeling, Analysis and Simulation Methods and Applications to Circuit Design (SMACD)*, 2017, pp. 1–3.

[82] A. Denzi, C. Merla, F. Andre, T. Garcia-Sanchez, L. Mir, F. Apollonio, and M. Liberti, "Shared knowledge, gaps and challenges of microdosimetry: Realistic models of cells and endoplasmic reticulum," in *2018 IEEE International Microwave Biomedical Conference (IMBioC)*, 2018, pp. 19–21.

[83] A. De Angelis, A. Denzi, C. Merla, F. Andre, T. Garcia-Sanchez, L. Mir, F. Apollonio, and M. Liberti, "A microdosimetric realistic model to study frequency-dependent electroporation in a cell with endoplasmic reticulum," in *2019 49th European Microwave Conference (EuMC)*, 2019, pp. 212–215.

[84] G. Pucihar, T. Kotnik, B. Valic, and D. Miklavci, "Numerical determination of transmembrane voltage induced on irregular shaped cells," *Ann. Biomed. Eng.*, vol. 43, no. 4, pp. 642–652, 2006.

[85] L. Towhidi, T. Kotnik, G. Pucihar, S. M. P. Firoozabadi, H. Mozdarani, and D. Miklavčič, "Variability of the minimal transmembrane voltage resulting in detectable membrane electroporation," *Electromag. Biol. Med.*, vol. 27, no. 4, pp. 372–385, 2008.

[86] A. De Angelis, A. Denzi, C. Merla, F. M. Andre, L. M. Mir, F. Apollonio, and M. Liberti, "Confocal Microscopy Improves 3D Microdosimetry Applied to Nanoporation Experiments Targeting Endoplasmic Reticulum," *Front. Bioeng. Biotec.*, vol. 8, 2020.

[87] M. W. Dewhirst, B. L. Viglianti, M. Lora-Michiels, M. Hanson, and P. J. Hoopes, "Basic principles of thermal dosimetry and thermal thresholds for tissue damage from hyperthermia," *Int. J. Hypoth.*, vol. 19, no. 3, pp. 267–294, 2003, doi: 10.1080/0265673031000119006.

[88] P. S. Yarmolenko, E. J. Moon, C. Landon, A. Manzoor, D. W. Hochman, B. L. Viglianti, and M. W. Dewhirst, "Thresholds for thermal damage to normal tissues: an update," *Int. J. Hypoth.*, vol. 27, no. 4, pp. 320–343, 2011, doi: 10.3109/02656736.2010.534527.

[89] G. C. van Rhoon, T. Samaras, P. S. Yarmolenko, M. W. Dewhirst, E. Neufeld, and N. Kuster, "CEM43°C thermal dose thresholds: a potential guide for magnetic resonance radiofrequency exposure levels?" *Europ. Radiol.*, vol. 23, no. 8, pp. 2215–2227, 2013, doi: 10.1007/s00330-013-2825-y.

[90] A. Peyman, C. Gabriel, and E. Grant, "Complex permittivity of sodium chloride solutions at microwave frequencies," *Bioelectromagnetics*, vol. 28, no. 4, pp. 264–274, 2007.

[91] A. Denzi, C. Merla, C. Palego, A. Paffi, Y. Ning, C. R. Multari, X. Cheng, F. Apollonio, J. C. M. Hwang, and M. Liberti, "Assessment of cytoplasm conductivity by nanosecond pulsed electric fields," *IEEE Trans. Biomed. Eng.*, vol. 62, no. 6, pp. 1595–1603, 2015.

[92] J. Weaver, "Electroporation of biological membranes from multicellular to nano scales," *IEEE Transactions on Dielectrics and Electrical Insulation*, vol. 10, no. 5, pp. 754–768, 2003.

[93] T. R. Gowrishankar, A. T. Esser, Z. Vasilkoski, K. C. Smith, and J. C. Weaver, "Microdosimetry for conventional and supra-electroporation in cells with organelles," *Biochem. Biophys. Res. Com.*, vol. 341, no. 4, pp. 1266–1276, 2006.

[94] T. Gowrishankar and J. C. Weaver, "Electrical behavior and pore accumulation in a multicellular model for conventional and supra-electroporation," *Biochemical and Biophysical Research Communications*, vol. 349, no. 2, pp. 643–653, 2006.

[95] *COMSOL Multiphysics*® (v. 5.6), COMSOL AB, [online] Available: www.comsol.com.

[96] K. Jerbic, K. Neumann, J. T. Svejda, B. Sievert, A. Rennings, and D. Erni, "Limits of effective material properties in the context of an electromagnetic tissue model," *IEEE Access*, vol. 8, pp. 223 806–223 826, 2020, doi: 10.1109/ACCESS.2020.3045327.

[97] I. Krakovský and V. Myroshnychenko, "Modeling dielectric properties of composites by finite-element method," *J. Appl. Phys.*, vol. 92, no. 11, pp. 6743–6748, 2002.

[98] J. Froelich, S. Huclova, C. Beyer, and D. Erni, *book chapter 12 "Accurate multi-scale skin model suitable for determining sensitivity and specificity of changes of skin components," pp. 353-394, in Computational Biophysics of the Skin, Bernard Querleux, Ed.*, Singapore: Pan Stanford Publishing Pte. Ltd., 2014.

[99] J.-C. Chien, A. Ameri, E.-C. Yeh, A. N. Killilea, M. Anwar, and A. M. Niknejad, "A high-throughput flow cytometry-on-a-CMOS platform for single-cell dielectric spectroscopy at microwave frequencies," *Lab Chip*, vol. 18, pp. 2065–2076, 2018.

[100] *MATLAB*® (R2020b), The MathWorks Inc., Available: www.mathworks.com.

[101] K. A. Holbrook and G. F. Odland, "Regional differences in the thickness (cell layers) of the human stratum corneum: an ultrastructural analysis," *J. Inv. Derm.*, vol. 62, no. 4, pp. 415–422, 1974, doi: 10.1111/1523-1747.ep12701670.

[102] A. J. Klein-Szanto, "Clear and dark basal keratinocytes in human epidermis. A stereologic study," *J. Cut. Path.*, vol. 4, no. 5, pp. 275–280, 1977, doi: 10.1111/j.1600-0560.1977.tb00916.x.

[103] R. R. Warner, M. C. Myers, and D. A. Taylor, "Electron probe analysis of human skin: determination of the water concentration profile," *J. Inv. Derm.*, vol. 90, no. 2, pp. 218–224, 1988, doi: 10.1111/1523-1747.ep12462252.

[104] S. Grayson and P. M. Elias, "Isolation and lipid biochemical characterization of stratum corneum membrane complexes: implications for the cutaneous permeability barrier," *J. Inv. Derm.*, vol. 78, no. 2, pp. 128–135, 1982, doi: 10.1111/1523-1747.ep12505953.

[105] H. Fischer, I. Polikarpov, and A. F. Craievich, "Average protein density is a molecular-weight-dependent function," *Histoch. and Cell Bio.*, vol. 13, no. 10, pp. 2825–2828, 2004, doi: 10.1110/ps.04688204.

[106] R. Moll, M. Divo, and L. Langbein, "The human keratins: biology and pathology," *Protein Sci.*, vol. 129, no. 6, pp. 705–733, 2008, doi: 10.1007/s00418-008-0435-6.

[107] T. Gouw and J. C. Vlugter, "Physical Properties of Triglycerides. I. Density and Refractive Index," *Europ. J. Lipid Sci. Tech.*, vol. 68, no. 7, pp. 544–549, 1966, doi: 10.1002/lipi.19660680705.

[108] T. Z. Rizvi and M. A. Khan, "Temperature-dependent dielectric properties of slightly hydrated horn keratin," *Int. J. Biol. Macromol.*, vol. 42, no. 3, pp. 292–297, 2008, doi: 10.1016/j.ijbiomac.2008.01.001.

[109] C. Reid, "Spectroscopic methods for medical diagnosis at terahertz wavelengths," Ph.D. dissertation, University College London, London, UK, 2006.

[110] M. Saviz, L. Mogouon Toko, O. Spathmann, J. Streckert, V. Hansen, M. Clemens, and R. Faraji-Dana, "A new open-source toolbox for estimating the electrical properties of biological tissues in the terahertz frequency band," *J. Infrared Millim. Terahertz Waves*, vol. 34, no. 9, pp. 529–538, 2013, doi: 10.1007/s10762-013-9997-z.

[111] M. Khiao-In, "From porcine skin samples in situ to three-dimensional human skin constructs in vitro. Studying skin with a focus on the 3R principles," Ph.D. dissertation, Freie Universität Berlin, Berlin, Germany, 2022.

[112] R. R. Gullapalli, M. C. Demirel, and P. J. Butler, "Molecular dynamics simulations of dii-c18(3) in a dppc lipid bilayer," *Phys. Chem. Chem. Phys.*, vol. 10, no. 24, pp. 3548–3560, 2008, doi: 10.1039/b716979e.

[113] S. Lippens, G. Denecker, P. Ovaere, P. Vandenabeele, and W. Declercq, "Death penalty for keratinocytes: apoptosis versus cornification," *Cell Death Differ.*, vol. 12, no. 2, pp. 1497–1508, 2005, doi: 10.1038/sj.cdd.4401722.

[114] O. Spathmann, M. Zang, J. Streckert, V. Hansen, M. Saviz, T. M. Fiedler, K. Statnikov, U. R. Pfeiffer, and M. Clemens, "Numerical Computation of Temperature Elevation in Human Skin Due to Electromagnetic Exposure in the THz Frequency Range," *IEEE Trans. THz Sci. Technol.*, vol. 5, no. 6, pp. 978–989, 2015, doi: 10.1109/TTHZ.2015.2476962.

[115] M. Jalali, A. Prokscha, Y. Yan, T. Kubiczek, J. T. Svejda, S. Preu, J. Balzer, T. Kaiser, and D. Erni, "Non-invasive glucose sensing via the fingernail bed using THz radiation," *Biomed. Eng. Biomed. Techn.*, 2023, (accepted).

[116] H. Richter, "Mote3D: an open-source toolbox for modelling periodic random particulate microstructures," *Model. Simul. Mat. Sci. Eng.*, vol. 25, no. 3, p. 035011, 2017.

[117] D. A. G. Bruggeman, "Berechnung verschiedener physikalischer Konstanten von heterogenen Substanzen," *Annalen der Physik*, vol. 416, no. 7, pp. 636–664, 1935.

[118] L. D. Landau, E. M. Lifshits, and L. P. Pitaevskiĭ, *Electrodynamics of continuous media*, ser. Course of theoretical physics. Oxford: Pergamon, 1984, vol. 8.

[119] H. Looyenga, "Dielectric constants of heterogeneous mixtures," *Physica*, vol. 31, no. 3, p. 401–406, 1965.

[120] T. Hanai, "Theory of the dielectric dispersion due to the interfacial polarization and its application to emulsions," *J. Appl. Phys.*, vol. 171, no. 1, p. 23–31, 1960.

[121] K. I. Zaytsev, I. N. Dolganova, N. V. Chernomyrdin, G. M. Katyba, A. A. Gavdush, O. P. Cherkasova, G. Komandin, M. A. Shchedrina, A. N. Khodan, D. S. Ponomarev, I. V. Reshetov, V. Karasik, M. Skorobogatiy, V. N. Kurlov, and V. V. Tuchin, "The progress and perspectives of terahertz technology for diagnosis of neoplasms: A review," *J. Opt.*, vol. 22, no. 1, pp. 1–44, 2019.

[122] G. Solomakha, J. T. Svejda, C. van Leeuwen, A. Rennings, A. J. Raaijmakers, S. Glybovski, and D. Erni, "A self-matched leaky-wave antenna for ultrahigh-field MRI with low SAR," *arXiv:2001.10410 [physics.app-ph], Bibcode: 2020arXiv200110410S*, 2020.

[123] B. Cabral and L. C. Leedom, "Imaging vector fields using line integral convolution," in *Proc. of the 20th Ann. Conf. on Comput. Graph. and Interactive Techn.*, M. C. Whitton, Ed. New York, NY: ACM, 1993, pp. 263–270.

# List of Publications

This chapter lists the publications that have emerged as a direct result of the research conducted for this thesis.

**Journal papers:**

P1 K. Jerbic, J. T. Svejda, B. Sievert, A. Rennings, J. Fröhlich, and D. Erni, "The importance of subcellular structures to the modeling of biological cells in the context of computational bioelectromagnetics simulations," *Bioelectromagnetics*, vol. 44, no. 1-2, pp. 26-46, 2023, doi: 10.1002/bem.22436.

P2 K. Jerbic, K. Neumann, J. T. Svejda, B. Sievert, A. Rennings, and D. Erni, "Limits of effective material properties in the context of an electromagnetic tissue model," *IEEE Access*, vol. 8, pp. 223806-223826, 2020, doi: 10.1109/ACCESS.2020.3045327

**Conference contributions:**

P3 K. Jerbic, J. T. Svejda, B. Sievert, X. Liu, K. Kolpatzeck, M. Degen, A. Rennings, A. Czylwik, J. Balzer and D. Erni, "The identification of spectral signatures in randomized
(sub-)surface material systems," presented at the *5th Int. Workshop on Mobile THz Systems (IWMTS 2022)*, Duisburg, Germany, July 4-6, 2022, pp. 1-5, doi: 10.1109/IWMTS54901.2022.9832449

P4 K. Jerbic, J. T. Svejda, B. Sievert, A. Rennings, J. Froehlich, and D. Erni, "The role of organelles in electromagnetic microdosimetry based on broadband multiscale skin models of eukaryotic cells," presented at *BioEM 2022*, Nagoya, Japan, Session 14: 'S14: Computational Dosimetry', June 19-24, 2022, pp. 337-340.

P5 K. Jerbic, B. Sievert, J. T. Svejda, J. Jebramcik, J. Barowski, A. Rennings, I. Rolfes, and D. Erni, "Limits of homogenization in electromagnetic composite material models: A show case in tissue analysis," in *SENSORICA 2020*, Mülheim a. d. Ruhr, Germany, May 14-15, 2020, pp. 28- 29.

P6 K. Jerbic, B. Sievert, J. T. Svejda, A. Rennings, and D. Erni, "On the applicability of homogenization in composite material models for tissue analysis in the mm-wave range," presented at *PIERS 2019*, Rome, Italy, Session 3P3 - SC1 & SC2: 'Computational Bioelectromagnetics: from Single Molecule to Human Body', June 17-20, 2019, pp. 1717-1718.

# Acknowledgements

I would like to begin my acknowledgments by expressing my gratitude to Prof. Dr. sc. techn. Daniel Erni, who gave me the opportunity to start my Ph.D. program as well as teaching me important scientific and personal lessons along the way. I would also like to thank Prof. Dr.-Ing. Jan Balzer for co-examining my thesis.

In addition, I would like to thank Dr.-Ing. Andreas Rennings for his untiring commitment, patience and far-sightedness, which have contributed significantly to the fact that I was able to bring my research project to a successful conclusion. My gratitude also extends to Dr.-Ing. Christian Thiel and Mr. Claas Bröcheler for the cherished friendship we share.

Looking back on my first three years of research within the MARIE transregional research project, I would like to thank my colleagues Mr. Peng-Yuan Wang, Dr.-Ing. Mohamed Haj Hassan, and Dr.-Ing. Benedikt Sievert. The camaraderie and fun that we shared during this intensive research phase were of inestimable value to me. I extend special thanks to Dr.-Ing. Benedikt Sievert for his scientific support. His technical and scientific brilliance, coupled with his wise counsel in personal conversations, greatly enriched my experience. I particularly cherish our tradition of exchanging interesting and inspiring books at Christmas, which has deepened our mutual esteem and friendship.

I would also like to thank Dr.-Ing. Kevin Kolpatzeck and especially Dr.-Ing. Xuan Liu for the fruitful collaboration in investigating spectral signatures in randomized (sub-)surface systems. It was a pleasure to work with you.

Having become acquainted with Mr. Barry Morley during language courses as part of my undergraduate studies, I would like to thank him for his patience and dedication in teaching and refining my academic writing skills through private tutoring during my Ph.D. period. Valuing the educational support with which he provided me with, I am even more grateful for the friendship that developed over the past six years and the enjoyable conversations we had discussing the philosophical concepts behind Frank Herbert's fabulous Dune series.

In addition, I am grateful to Dr.-Ing. Jan Taro Svejda, Mr. Viktor Gerhardt, and Ms. Katja Johrendt for their scientific, technical, and organizational support, respectively. Furthermore, I appreciate Ms. Cornelia Schwering and Dr.-Ing. Norbert Koster for their experienced advice during my doctoral studies. While we are considering valuable advice, I would also like to thank Dr.-Ing. Jörg Stammen for his support and mentorship during my undergraduate studies, which significantly influenced my decision to study for a doctorate.

My thanks also go to all the undergraduate students who have entrusted me with their final theses. I hope that I was able to provide you not only with important knowledge and methods, but also with a rich and fulfilling experience of scientific growth. From my side, the experience of supervision has enriched my view of the world.

Last but not least, I would like to extend my deepest gratitude to my family and friends for their unwavering emotional and moral support during challenging times. Special thanks go to my parents Andre and Heike, my sister Chantal, my grandmother Hannelore, my uncle Guido, and my cousin Vanessa for their enduring support and love. I am equally grateful to my close friends Florian, Nikolai, Benjamin, and Gerome for their camaraderie and encouragement. Finally, I send my heartfelt thanks to my partner, Parinaz, for her profound support and love throughout this journey.